Direct Visualisation of the Surface Chemistry of Tin Dioxide Nanoparticles

Arthur N. Moya



Linacre College

University of Oxford

Supervisors:

Angus I. Kirkland

Emanuela Liberti (Co-supervisor)

A thesis submitted for the degree of

Doctor of Philosophy

Trinity 2022

To my family and friends

for

my wife, Mbali, and our Siso and little Thala.

'Dominus Illuminatio Mea'

'The LORD is my light'- **Psalm 27:1**

Acknowledgements

I am grateful to my supervisors Prof Angus Kirkland and Dr Emanuela Liberti. Their guidance, wisdom and patience have been indispensable to my academic journey.

I am also thankful to past and present members of the Electron Image Analysis group and electron Physical Sciences Imaging Centre (ePSIC) that have widened my scope of what is possible on the microscope. I am thankful for the camaraderie, drinks, engaging scientific discussions and back-and-forth emails as I pestered you.

Special mention goes to Kevin Treder, Xiaonan Luo and Ofentse Makgae, Colum O'Leary, James Sode, Alex Sheader and many more that lit up room 30.16 in the Holder Building with their presence, work and conference stories.

I am also grateful to my family in Christ at Magdalen Road Church. Their prayers, love, support, and communion have been a great balm to my weary spirit all the way through. I am thankful to the Westons, Brittendens, Curries, Carrolls, Dunnes, Dents, Martins, Londons, Fennings, Baileys and Jill Bain.

I am indebted to my wife, Mbali. Her patience, love and support in the ebb and flow of research have been essential to its success. I cannot articulate the gift and blessing you and our little ones have been to me.

To my family and all my friends and those who have contributed directly and indirectly to the success of this project - thank you.

To the Commonwealth Scholarship Commission, the Department of Materials, Linacre College and many others who have funded various aspects of my research - thank you. Above all, I give thanks to my Lord and Saviour Jesus Christ through whom I have enjoyed the privilege, joy, and love of meeting many people who have made this a success.

Conference Presentations

'Exit wavefunction reconstruction of beam-sensitive photonic SnO_2 nanoparticles', **A.N. Moya**, E. Liberti & A.I. Kirkland, *Electron Microscopy and Analysis Group Conference 2018* (EMAG 2018), Warwick, UK, (Session 6), Oral

'A semi-quantitative predictive model for SnO_2 adatom diffusion and its application to exit wave reconstruction', **A.N. Moya**, O. Makgae, E. Liberti & A.I. Kirkland, *Microscience Microscopy Congress 2019* (MMC 2019), Manchester, UK, Oral

'A semi-quantitative predictive model for SnO_2 adatom diffusion and its application to exit wave reconstruction', **A.N. Moya**, O. Makgae, E. Liberti & A.I. Kirkland, *Microscopy & Microanalysis 2019* (M&M 2019), Portland, Oregon, USA, Poster (MSA scholar award and MSA Student Poster Award)

'Activation of Co Fischer-Tropsch Catalyst: Exploring Co Valence State under Different Reduction Conditions Using STEM-EELS'. O. Makgae, **A.N. Moya**, E. Liberti & A.I. Kirkland, *Microscopy & Microanalysis 2019* (M&M 2019), Portland, Oregon, USA, Poster

Publications

Moya, A.N, Makgae, O., Liberti, E., & Kirkland, A. (2019). *A semi-quantitative predictive model for SnO_2 adatom diffusion and its application to exit wave reconstruction*. **Microscopy & Microanalysis**, 25(S2), 108-109. doi:10.1017/S1431927619001272

Makgae, O., **Moya, A.N**, Yao, B., Schuster, M., Edwards, P., Liberti, E., & Kirkland, A. (2019). *Activation of Co Fischer-Tropsch Catalyst: Exploring Co Valence State under Different Reduction Conditions Using STEM-EELS*. **Microscopy & Microanalysis**, 25(S2), 668-669. doi:10.1017/S1431927619004070

Makgae, O., **Moya, A.N**, Huang, C., Liberti, E., & Kirkland, A.I. (2022) *Direct Visualisation of the Surface Atomic Active Sites of Carbon-Supported Co_3O_4 Nanocrystals via High-Resolution Phase Restoration.* **ChemPhysChem**, 23, 15, 1-7, doi.org/10.1002/cphc.202200031

Liberti, E., **Moya, A. N**, Treder, K. P., O'Leary, C. M., Kim, J. S., Nellist, P. D. & Kirkland, A. I. (2021). *Quantitative electron ptychography for simultaneous light and heavy elements atom counting.* **Acta Crystallographica, A**. A77, C235.

Moya, A.N, Makgae, O., Liberti, E., & Kirkland, A. (2022). Direct visualisation of the surface chemistry of nominally Pd-doped SnO_2 sub-10 nm nanoparticles. (in preparation)

Moya, A.N, Liberti, E., & Kirkland, A. (2022). Atomically resolved surface reconstructions of {110} facets on sub-10 nm nominally Pd-doped SnO_2 nanoparticles. (in preparation)

Disclaimer

The work presented in this thesis is my own original work and has not been submitted to any institution for examination. Work by other authors has been properly acknowledged in the main text and in the reference list.

The nominally doped 0.5 wt% Pd-SnO_2 nanoparticles used in this work were provided by Prof Mike Bowker from the University of Cardiff. The original MTF inclusion code, used in Chapters 4 and 5, was provided by Dr Konstantin Borisenko (former research group member). I adapted the code to include the NPS as well as the finite dose noise.

Dr Emanuela Liberti acquired the fast focal series data restored in Figure 5.8 (d-f). The fast focal series approach was developed in collaboration with Dr Mohsen Danaie from ePSIC. I performed all the data processing and analysis.

The code used to plot the ECTF was developed by Dr Ali Mostaed and packaged by Dr Jingjing Zhao.

List of Figures

Figure 2.1: Atomic model of a [100] oriented unit cell of SnO_2 showing the shared O atoms on the {001} faces and its [001] zone axis projection with a small angle tilt along [100] showing SnO_6 distorted octahedra (red and grey atoms are O and Sn, respectively). 7

Figure 2.2: Atomic models of stoichiometric and reduced surfaces of SnO_2 as predicted by DFT. The grey and red spheres represent Sn and O atoms, respectively. For all the atomic models, the stoichiometric surfaces are terminated by $O_{\mathbf{br}}$ atoms and O atoms in the second atomic plane for the {110} surfaces are referred to as in-plane O ($O_{\mathbf{ip}}$). 13

Figure 2.3: Theoretically predicted adsorption and substitutional sites of Pd atom dopants on (a) stoichiometric, (b) partially and, (c) significantly reduced {110} facets of SnO_2. (a) was adapted with permission from Springer Nature [22] and (b) was adapted from ref [24] with permission from Elsevier. 16

Figure 2.4: A Pd_5 cluster coordinated to a bulk terminated facet through $O_{\mathbf{br}}$ atoms as proposed by Germán et al. (2019) [22]. 16

Figure 2.5: Earlier SnO_2 (110) surface reconstruction atomic models derived from correlative LEED and surface spectroscopy studies. Only one or two atomic planes are shown depending on the reconstruction. The orange boxes indicate the respective surface unit cells, and the red, black, and grey atoms

show O atoms and vacancies as well as Sn atoms, respectively. The (4x1) surface reconstruction is adapted from ref[64](c) (1982) with permission from Elsevier. The other reconstructions are adapted from ref[36]© (1991) IOP Publishing. Reproduced with permission. All rights reserved. 22

Figure 2.6: The formation energy of various SnO_2 surface defects as a function of $\Delta\mu_O$. The insert corresponds to the Sn_2O_2 defect which has the lowest formation energy at $\Delta\mu_O$ <-1.91 eV. Adapted from ref[56] © (2011) with permission from Elsevier. 24

Figure 2.7: (a) Simulated STM image based on the model proposed by Merte et al. (2017) with an atomic model overlay of the model proposed by Jones et al. (1997). (b) An experimental high resolution STM image of the (4x1) surface reconstruction imaged by Batzill et al. (2003). In (a) the red, and black atoms indicate O atoms and O in-plane vacancies, while the grey spheres correspond to Sn atoms. The black borders indicate the (4x1) surface unit cell. The STM simulated image in (a) is adapted with permission from ref [65] © (2017) by the American Physical Society and the atomic model in (a) is adapted from ref[70] © (1997) with permission from Elsevier, while (c) was adapted from ref[34] © (2003) with permission from Elsevier. 26

Figure 2.8: The atomic model of the first atomic plane of the (110) (4x1) reconstruction proposed by (a) Merte et al. (2017) and (b) Batzill et al. (2003) projected in the [110] direction.(c) and (d) show multiple atomic planes

corresponding to the [001] projected views for (a) and (b), respectively. In (a) and (c) the surface has an Sn_3O_3 overlayer that has interstitial Sn atoms (grey atoms) bonded to the bulk through bridging (labelled as b), coordinately unsaturated (labelled as c) and, 'apex' (labelled as a) O atoms (red spheres). While in (b) and (d) the surface is composed of Sn interstitials coordinated to the bulk through 2 bridging and 2 coordinately unsaturated O atoms. The orange boxes indicate the (4x1) surface unit cell in the presented projections. (a,c) Adapted with permission from ref [65] © (2017) by the American Physical Society and (b,d) were adapted from ref[34] © (2003) with permission from Elsevier. 28

Figure 2.9: Sn-terminated (a) (101) and (b) (100) surfaces of a nanobelt and lamella of SnO_2 oriented in the [100] direction. The corresponding atomic models are overlain on the micrographs and Sn and O are represented by grey and red spheres, respectively. The scale bar is 10 Å. (a) and (b) are adapted with permission from ref[39] and ref[40]. © 2010 and 2020 American Chemical Society. 32

Figure 2.10: (a) A restored phase of a (001) facet on a TiO_2 nanoparticle oriented in the [100] direction exhibiting a (1x4) surface reconstruction. The inset in (a) is the adatom row model predicted through DFT. (b) The template averaged motif of the atomic arrangement of the surface reconstruction obtained from the restored phase in (a). The separation between each adatom

row is 4**a**, corresponding to the distance measured from the STM image of the (001) surface of a bulk single crystal in (c) and on its magnified counterpart (d). The scale bars shown in (a) and (b) correspond to a distance of 10 Å. Adapted from ref.[94] with permission from the Royal Society of Chemistry. . 34

Figure 2.11: HAADF and BF images of the (1x2) surface reconstruction on the (110) facet of a cuboctahedron of SnO_2 along with the DFT calculated model of the surface in the [001] and [110] directions. The green boxes show the dimensions of the (1x2) reconstructions in both projections. Adapted with permission from ref[31] © (2021) American Chemical Society. 37

Figure 3.1: A schematic diagram of a TEM equipped with an image aberration corrector in the post-field of the objective lens including key instrumental parameters that limit the resolution of the microscope..... 40

Figure 3.2: A schematic diagram of a cold FEG source assembly. Adapted by permission from Springer Nature: Springer US, by ref [102] © (2009)..... 42

Figure 3.3: A ray diagram illustrating the phase shift (ϱ) introduced by the objective lens (OL) aberrations on an ideal spherical wavefront in the back focal plane (BFP). The overall effect is that a point object in the object plane (OP) becomes a disk whose radius is equal to the ray aberration, (ω), in the image plane (IP). 46

Figure 3.4: Calculated PCTF of a thermionic LaB_6 source (red) and a Schottky FEG source (blue) for 200 kV instruments which have 1 eV and 0.7 eV energy

spreads, respectively. Both PCTFs were calculated with C_3= 0.5 mm and C_c= 1 mm. The point resolution (p) and the information limit(i) are also indicated for both highlighting the significant contrast reversals for a FEG source past the point resolution and its extended information limit (adapted by permission from ref [108] © (2012) John Wiley & Sons, Ltd.). 49

Figure 3.5: A schematic diagram of a hexapole-based aberration corrector with two hexapoles (Hex 1 & 2) linked to each other and to the objective lens (OL) through a pair of transfer doublets (TL*nm*) (adapted from ref [113] © (2011) John Wiley & Sons, Ltd., and ref [112] © (2005) IEEE..... 50

Figure 3.6: An experimental Zemlin tableau acquired using a JEOL aberration corrector with tilt azimuths ranging from 14-40 mrad with an inset of the numerical phase plate showing a $\pi 4$ phase shift limit at a radius of 27 mrad with a corresponding resolution of 0.7 Å. 53

Figure 3.7: The normalised experimental MTF and NPS of a 4kx4k Gatan OneView detector acquired at 300 kV. 55

Figure 3.8: A micrograph of a 2.62×10^3 Å latex sphere acquired at a magnification of x200k measuring an average diameter of 3480 pixels as indicated by the corresponding line profiles (blue double arrow line = 3530 pixels and yellow double arrow line = 3437 pixels). 57

Figure 3.9: Power spectrum of gold nanoparticles acquired at 300 keV at a magnification of x300k showing reflections corresponding to the {111}, {200},

{220}, {311}, and {222} lattice spacings. In real space, these correspond to distances of 2.36 Å, 2.04 Å, 1.44 Å, 1.23 Å and 1.18 Å, respectively..... 58

Figure 3.10: A magnification calibration curve for the JEOL ARM 300CF acquired at 300 keV..... 59

Figure 3.11: A simplified schematic diagram indicating the multislice simulation method (adapted by permission from Springer Nature: Springer US, by ref [131] © (2010). 63

Figure 3.12: A flow diagram showing the essential steps of the focal series exit wave reconstruction method adopted in FTSR (adapted from ref[144] © (2002) with permission from Elsevier). 70

Figure 4.1: Histogram of the length (orange) and width (green) of the 0.5 wt% Pd-SnO_2 nanoparticles. $N_{l/w}$, $Mean_{l/w}$ represent the number of measurements for the length and width, respectively and the measured average length and width of the nanoparticles, respectively..... 76

Figure 4.2: Representative 0.5 wt% Pd-SnO_2 nanoparticles samples, oriented along the (a) [100], (b) [001], (c) [110], (d) [101] and (e) [111] projection. In (e), representative measurements for the length (orange) and width (green) are also shown. The scale bar is 50 Å in all cases. 77

Figure 4.3: (a-e) Projected Wulff models, oriented along several zone axes and corresponding experimental images oriented along the same directions. Facets (f-j) overhanging vacuum are indicated with dashed blue lines, while those in

contact with other nanoparticles or the amorphous carbon are indicated with dashed yellow lines. The scale bars correspond to 10 Å in all cases..... 81

Figure 4.4: A restored phase quantification workflow employed in this study, showing: (1) focal series computation, (2) a restored wave phase, (3) atom position extraction and (4) phase quantification. The grey and blue atoms correspond to Pd and Sn atoms..... 84

Figure 4.5: Simulated noiseless images before (a) and after (b) MTF convolution for a [101] SnO_2 model nanoparticle, and respective power spectra (c) and (d). In (c) the highest spatial frequency transferred goes up to the (505) Fourier reflection which is close to the information limit of the microscope (blue circle), as opposed to the case where signal is damped by the MTF beyond the (404) Fourier reflection (see (d)). 89

Figure 4.6: Intensity profiles obtained from simulated power spectra before and after MTF convolution, showing the decay of the signal intensity from the (000) to the (505) reflections. 90

Figure 4.7: 2kx2k images of Poisson noise for an electron dose of 1000 $e/Å^2$ (a) before and (b) after convolution by the NPS. Respective power spectra are shown in the inserts..... 91

Figure 4.8: (a) Simulated image of a [101] oriented nanoparticle with a 1000 $e/Å^2$ dose and corresponding power spectrum (b) showing spatial frequency dependent transfer of signal and noise..... 92

Figure 4.9: Simulated focal series data for a [001] oriented nanoparticle. The electron dose per image ranges from 100 $e/Å^2$ to 3000 $e/Å^2$. From top to bottom, the defocus ranges from -300 Å, -190 Å and 130 Å, respectively. The scale bar is 10 Å. 95

Figure 4.10: Selected images from the focal series of the [001] projected nanoparticle with defoci of (a) -526 Å, -467 Å, -399 Å, and -340 Å, (b) -274 Å, (c) -235 Å. The red arrows in (b) and (c) show the appearance of contrast motif that deviates from the one observed in the bulk of the nanoparticle. An atomic model is overlain in (b) and (c). (d) Orange and blue line profiles acquired with 8-pixel wide integration from dashed ROIs shown in (b) and (c), respectively. The four O atoms in the line profiles acquired in (b) and (c) have average distances of 3.48 (0.75) Å and 3.39 (0.26) Å, respectively. The scale bar is 20 Å. 97

Figure 4.11: Restored phase of a [100] oriented SnO_2 model nanoparticle obtained from a simulated focal series of 30 images with electron doses per frame of 100 $e/Å^2$, 300 $e/Å^2$, 1000 $e/Å^2$, 2000 $e/Å^2$ and 3000 $e/Å^2$. The region marked by the orange box highlights the same areas of the nanoparticle surface. The blue box highlights O atom columns of interest (shown in Figure 4.13). The scale bar is 10 Å. 101

Figure 4.12: Vacuum noise standard deviation measurements as a function of cumulative dose for phases obtained from complex exit waves restored from

focal series data calculated using the Multiplicative (thesis approach) and the Vulovic et al. (2013) [154] method. 102

Figure 4.13: (a) A magnified view of the ROI marked in blue in Figure 4.11. Three atom columns (indicated with squares in a dashed blue line) are selected for quantification of the oxygen phase shift at the surface. For each highlighted atom column, the maximum pixel value was taken as the maximum phase value within the marked region. (b) and (c) are line profiles across the atom column from which the average 'valley' wave minimum phase shift values are obtained and used to normalise the maximum phase shift at the atom column. 105

Figure 4.14: (a) Experimental phase of a [110] oriented 0.5 wt% Pd-SnO_2 nanoparticle showing a vacuum exposed stepped (110) surface. Yellow arrows indicate undercoordinated Sn/O surface atoms (see false colour insert in (a)). The interplanar spacings $d_{\{110\}}$ and $d_{\{002\}}$ are also shown. (b) False colourmap of the phase in (a). The white arrows indicate atom columns of mixed Sn and O occupancy. (c) Stoichiometric (left) and reduced (right) reconstructed phases, obtained from the simulated focal series. Atomic model overlays of the stoichiometric (O-terminated) and reduced surfaces are also shown in (c). The scale bar represents 10 Å in all cases. 109

Figure 4.15: (a) Experimental phase of a [111] oriented 0.5 wt% Pd-SnO_2 nanoparticle exposing a stepped (110) surface. The $2d_{\{110\}}$ and $2d_{\{112\}}$

interplanar spacings are also shown. (b) False colourmap of (a) with white arrows showing a possible Sn/O monolayer. (c) Stoichiometric (left) and reduced (right) phase images, obtained from the simulated focal series. Atomic model overlays of stoichiometric (O-terminated) and reduced surfaces are also shown in (c). The scale bars represent 10 Å in all cases. 111

Figure 4.16: (a) Experimentally restored phase of a 0.5 wt% Pd-SnO_2 nanoparticle oriented in a [001] direction exhibiting a surface reconstruction composed of Sn_i atoms. The false colourmap is shown in (b). Contrast in the red ROI in (b) is not fully consistent with the (2x1) motif observed on the right surface. (c) Stoichiometric (left, O-terminated) and fully reduced (right, SnO-terminated) reconstructed phases, obtained from simulated focal series data. Atomic models are overlaid on both terminations in (c). The scale bar is 10 Å in all cases. 115

Figure 4.17: Atomic models of the [001] projected (110) (4x1) (a) and (2x1) (b) surface reconstructions. In (a), a Sn_3O_3 overlayer has interstitial Sn atoms (blue spheres) bonded to the bulk through bridging (labelled as br), 'coordinately unsaturated' (labelled as cus) and, 'apex' O (labelled as ap) (red spheres). In (b), Sn_i atoms (grey spheres) are bonded to the bulk through $O_{\mathbf{cus}}$ and $O_{\mathbf{br}}$ atoms. The model in (a) was proposed by Merte et al. (2017) and that in (b) is consistent with that of Li et al. (2021) and Ágoston and Albe (2011). (a) has been adapted with permission from ref [65] © (2017) by the American Physical

Society and (b) is adapted from refs [37,167] © (2011) and (2021) with permission from Elsevier and the American Chemical Society, respectively. 117

Figure 4.18: (a) Experimental reconstructed phase of a 0.5 wt% Pd-SnO_2 nanoparticle oriented along [100] exposing a stepped (011) facet, and false colourmap image (b). The yellow dashed line indicates a grain boundary. In (b) the white dashed circles indicate bridging O vacancies. (c) Stoichiometric (left) and reduced (right) reconstructed phases, obtained from simulated focal series. Atomic model overlays of the stoichiometric (O-terminated) and reduced (Sn-terminated) surfaces are also shown in (c). The scale bars represent 10 Å in all cases. 119

Figure 4.19: (a) Experimental reconstructed phase of a 0.5 wt% Pd-SnO_2 nanoparticle oriented along [101] exposing a Sn-terminated stepped (101) facet and its (b) false colourmap. The dashed white circles and arrows in (b) show bridging O vacancy positions and three-fold coordinated O atoms, respectively. (c) Stoichiometric (left) and reduced (right) reconstructed phases, obtained from simulated focal series. Atomic model overlays of the stoichiometric (O-terminated) and reduced (Sn-terminated) surfaces are also shown in (c). The scale bars represent 10 Å in all cases. 120

Figure 4.20: (a) Experimental reconstructed phase of a 0.5 wt% Pd-SnO_2 nanoparticle oriented along [101] exposing a reduced stepped (010) facet and its false colourmap (b). In (b), in the upper left region of the nanoparticle, a

diffuse layer of Sn atoms is shown indicated by white arrows, while oxygen surface atoms are indicated by yellow arrows. (c) Simulated phases of O-terminated (stoichiometric) and Sn-terminated (reduced) surfaces and corresponding atomic model overlays. The scale bars represent 10 Å in all cases. 122

Figure 4.21: (a) Plots of the average phase shifts from single O atoms obtained from noiseless focal series data damped by the MTF (dashed lines), for different facets in projection of a SnO_2 model nanoparticle. For the $(110)^{13}_{[001]}$ and $(110)^{3}_{[110]}$ facets, the phase shifts of single O atoms from the O sub-lattice only are also shown as solid lines. (b) Data points showing the phase shifts obtained for a single O atom at finite doses. The colour of the data points corresponds to the same projection in the infinite dose calculations. To aid visibility only the positive error bars of the data points are shown.....128

Figure 4.22: SNFR for a single O atom as a function of cumulative dose for the facets of interest in the respective zone axis. The black dashed horizontal lines signify the range of the minimum SNFR values greater than 3 required for single atom visibility.....130

Figure 4.23: False colourmap reconstructed phase of the $(110)_{[001]}$ surface as in Figure 4.16. The red arrows indicate contrast above bridging O ($O_{\mathbf{br}}$) and on-top O ($O_{\mathbf{cus}}$) atom columns, contrary to reports in the literature[31,156]. The scale bar is 10 Å.....133

Figure 4.24: Phases of a [001] oriented nanoparticle restored using the first (a), second (b), and third (c) third of the 30-image focal series. The cumulative dose at a given point in time is shown as well as Sn atoms in bulk lattice positions (grey), interstitial positions (yellow/ orange arrows) as well as O atoms (yellow dashed circles) and their vacancies (white dashed circles) that progressively appear compared to the previous phase. Each restoration had a cumulative dose of 45.7x10^3 $e/Å^2$(O SNFR = 6). Below each phase is the log modulus of the Fourier transform of the restored complex exit wave. These indicate that the nanoparticle did not rotate but underwent some slight tilting with time as seen in the asymmetry of the Fourier components (d-f).....136

Figure 5.1: Full schematic workflows of (a) CFS1, and (b) FFS scripts. For all scripts, the processes that take place in the main *for loops* are automated and script driven whereas steps that require manual input are blue-bordered. However, the *for loop* indicating the automatic acquisition (continuous image capture) of images in a FFS is directly performed by the detector and not script driven. Refer to the main text for further details on pre-image acquisition parameters.....148

Figure 5.2: (a) Variation of the O_{tp} as a function of binning, (b) OL settling time and (c) step size during CFS.....150

Figure 5.3: The influence of varying binning, focal step, OL settling time and SPEC on the blanking (top value) and exposure (bottom value) times during CFS. 152

Figure 5.4: (a) A stepwise calibration defocus profile of a FFS acquired on amorphous carbon. The points labelled as n_i and n_f correspond to the first and last images of the FFS. Each step size is 60 bits and 4 images per step were acquired during OL settling at a frame rate of 2 fps. The last and first images of the pre- and post-focal series defocus plateaus are labelled as n_{01} and n_{02}, respectively. (b) A comparison between simulated CTFs from the Gctf software and LAS calculated from experimental micrographs for the points labelled in (a).....155

Figure 5.5: A schematic diagram of an FFS defocus profile plot indicating sharp contrast changes between the last image of the pre-focal series plateau (n_{01}) and the first image of the focal series (n_i) as well as that between the image at the end of the focal series (n_f) and the first image of the post-focal series plateau (n_{02}). The latter were used to determine the beginning and end of the focal series. 158

Figure 5.6: Comparison of (a) single (70 $e/Å^2$), (b) 5-sum (349 $e/Å^2$), and 27-sum images (1890 $e/Å^2$) obtained from the 7th focal plane of the focal series whose transition points are shown in Figure 5.5. The defocus in a single image was approximated based on the expected defocus calculated using equation 5.1.

The defocus values of (b) and (c) were obtained from values estimated by FTSR. The dotted line at the top of this figure represents a focal plane with the dots representing individual images. The brackets show the number of images that were summed to produce the respective images. The scale bar corresponds to 10 Å. 161

Figure 5.7: A schematic diagram showing images included in the cumulative dose (CD) calculation for the (a) first and (b) second focal series for a given nanoparticle. The red defocus pathways show the number of images added in the cumulative dose calculation while the blue defocus pathways show the images that are excluded. 165

Figure 5.8: (a-i) Restored phases of ≈4 nm-sized nanoparticles, acquired at increasing dose rate (down column) and cumulative dose (left to right). The red, black, orange, and blue lines represent facets with stoichiometric, (4x2), (2x1) and (1x2) surface reconstructions, respectively. The grey lines show isolated strands of Sn_xO_y units. The grey, orange, and red arrows show Sn_b, Sn_i and O surface atoms in that order. The scale bar represents 20 Å. 168

Figure 5.9: (a) Phase of the stoichiometrically terminated $(110)_t$ facet, at a cumulative dose of 264 798 $e/Å^2$, for the nanoparticle shown in Figure 5.8 (a-c). (b) Line profiles acquired from its surface at increasing cumulative doses. The phase shifts induced by O atoms are shown with black dashed arrows. The

integration width of the line profiles was 8 pixels (orange box with dashed lines). The scale bar corresponds to 20 Å. 170

Figure 5.10: (a) Phase of the stoichiometrically terminated $(110)_l$ facet, at a cumulative dose of 220 652 e/Å^2, for the nanoparticle shown in Figure 5.8 (a-c) and (b) line profiles acquired from its surface at increasing cumulative dose. The phase shifts induced by O atoms is shown with black dashed arrows and that of the Sn_i atom column by a red arrow. The integration width of the line profiles was 8 pixels (orange box with dashed lines). The scale bar corresponds to 20 Å. 171

Figure 5.11: (a) Phases of the $(110)_t$ facet of the nanoparticle shown in Figure 5.8 (a-c) at cumulative doses of 308 807 e/Å^2 and 398 568 e/Å^2. Line profiles (8-pixels wide) are shown as insets in (a) for O atoms, while traces in (b) indicate pairs of Sn_i atoms coordinated to O_{cus}. (c) Line profiles acquired in the yellow ROI in (a) showing the stability of the facet with increasing cumulative dose. The scale bar corresponds to 20 Å. 174

Figure 5.12: (a) Phase of the $(110)_t$ facet of the nanoparticle shown in Figure 5.8 (a-c) at a cumulative dose of 450 102 e/Å^2. (b) 8 pixel wide line profiles obtained from the region shown in (a) at a cumulative dose of 450 102 e/Å^2 (blue) and 540 690 e/Å^2 (red), respectively. The scale bar represents 20 Å.176

Figure 5.13: (a) Phase of the $(110)_l$ facet at a cumulative dose of 308 807 e/Å^2. (b) Line profiles were acquired from the ROI in dashed orange borders indicate

a relative Sn_b atom loss and Sn_i gain (red arrow) from a cumulative dose of 41 343 $e/Å^2$ to 308 807 $e/Å^2$. The scale bar in (a) corresponds to a length of 20 Å.....178

Figure 5.14: (a) Phase of the $(110)_t$ facet shown in Figure 5.8 (i) at a cumulative dose of 63 967 $e/Å^2$. The region where line profiles were acquired is shown by the orange dashed ROI. (b) Line profiles of the reconstructed surface layer shown at increasing cumulative doses. The dashed black arrows indicate phase shifts by Sn_i atoms from the overlayer. Areas without Sn_i atoms are shown with red crosses. The scale bar corresponds to 20 Å.....182

Figure 5.15: Graphical summary of the experimentally observed surface reconstruction pathways for 0.5 wt% Pd-doped SnO_2 nanoparticles as a function of electron dose.....184

Figure 5.16: Magnified ROI shown on the surface of the [001] nanoparticle from Figure B.5 (h) and (b) that of a nanoparticle projected in a [110] direction acquired under comparable dose conditions. The nanoparticle was acquired with a dose rate of 5450 $e/Å^2s$. The grey and red atoms in the atomic model overlays represent Sn and O atoms, respectively. In (c) and (d) phases restored from simulated focal series of ≈10 Å thick atomic models of the (2x1) reconstruction model proposed by Li et al. (2021) [31] in the [001] and [110] projections are shown. The scale bar represents 10 Å.....189

List of Tables

Table 2.1: Surface energies of stoichiometrically terminated SnO_2 surfaces[32,50,52] and resultant relative ratios determined by normalisation with respect to the (001) surface energy..... 12

Table 3.1: Properties of electron sources (adapted by permission from Springer Nature: Springer US, by ref [102] © (2009).)..... 42

Table 3.2: Axial aberration coefficients up to the 3rd order in the Typke and Dierksen and Krivanek notations (Adapted by permission from Springer Nature: Springer Nature, by ref [104] © (2012).)..... 47

Table 4.1: Experimentally observed crystallographic facets of a 0.5 wt% Pd-SnO_2 nanoparticle sample..... 78

Table 4.2: Summary of the mean phase shifts per pixel (in rad/pixel) for pristine and doped Sn atom columns of equal occupancy (8 atoms) oriented in the [001] direction..... 85

Table 4.3: A tabulated summary of experimental and simulated mean pixel counts ($\boldsymbol{\mu}$) obtained in vacuum at various electron doses per frame..... 93

Table 4.4: Summary of the exit wave restoration parameters used in this study. 99

Table 4.5: Summary of the cumulative dose, C_3 and detector sampling for the experimental data in this study. The cumulative dose corresponds to that of a

30-image focal series data set and the total cumulative dose at the sample is shown in parenthesis.....107

Table 4.6: Measured average projected distances for surface and bulk Sn atom columns spacings along the [110] and [111] zone axes.....112

Table 4.7: Facets observed in this study for 0.5 wt% Pd-SnO_2 nanoparticles along with their terminations. A comparison with DFT and STM/LEED surfaces reported in the literature is also shown. The Sn_i atoms are related to (110) surface reconstructions. 123

Table 4.8: A summary of the signal-to-noise fluctuation ratios (**SNFR**) at the vacuum/nanoparticle surface interface for different nanoparticles projections and cumulative doses in the simulated focal series. 125

Table 4.9: Comparison between the interatomic distances measured from bulk and surface atomic planes for the (2x1) surface reconstruction observed in this study and that of Li et al. (2021)[37].....139

Table 5.1: Summarised parameters used for restoring complex exit waves from FFS data. 162

Table 5.2: Dose parameters for the nanoparticles examined in this thesis. In order the dose parameters shown are the cumulative focal series dose (FSD), dose rate (DR), the number of consecutive focal series (No. FS) and the total dose (TD) at the end of the FFS and CFS acquisition. Here, the third dataset corresponds to the CFS data while the first and second are FFS. 166

Table 5.3: Comparison of interatomic distances for surface atomic planes and bulk, obtained for the (2x1) surface reconstruction on the nanoparticles in Figure 5.8 and the results reported by Li et al. (2021)[37].....172

Table 5.4:A summary of the stability of the observed surface reconstructions as a function of cumulative dose and dose rate.....185

Abstract

The presence of O vacancies and subsequent undercoordinated Sn atoms on the surface of pure or doped SnO_2 nanomaterials is known to enhance their efficiency in catalysis and for sensing applications. Furthermore, the surface reconstructions that occur under reducing environments can be up to four orders of magnitude more conductive than their stoichiometric counterparts. However, research on both the surface chemistry as well as the reconstructions of SnO_2 facets has been mostly limited to bulk single crystals and theoretical calculations. To date, there is very limited direct evidence on the local surface chemistry of native and reconstructed facets of sub-10 nm, catalytically-relevant, SnO_2 nanoparticles.

In this thesis, aberration corrected electron microscopy with exit wave restoration are used to reveal the surface chemistry of low energy facets of nominally 0.5 wt% Pd-doped SnO_2 nanoparticles. The atomically resolved surface chemistry is studied on sub-10 nm nanoparticles projected in different orientations. For the first time, it is demonstrated, as expected from theory, that the {100} and {101} facets are largely reduced and Sn-terminated, without complex surface reconstructions, under the influence of the electron beam and low $O_{2(g)}$ pressures in the microscope. The {110} facets in the [110] and [111] directions were shown to have a non-stoichiometric SnO-terminated surface.

However, the [001] projected {110} facets are shown to undergo complex surface reconstructions in agreement with theoretical predictions and previous experimental findings.

Further investigation into the (110) surface reconstructions, reveals that, the initial surface chemistry of the [001] projected {110} facets and their reconstruction pathways are dependent on the imaging dose rate. It is shown for the first time that the initial surface chemistry is stoichiometric at dose rates below 1200 $e/Å^2s$, while the (2x1) surface reconstruction has the least surface energy at 2000 $e/Å^2s$ to 7000 $e/Å^2s$. Above this dose rate, the nanoparticles form a (2x1) surface reconstruction but undergo bulk reduction.

Contents

List of Figures ..... **vi**

List of Tables ..... **xxiii**

1. Introduction **1**

1.1. Rationale 1

1.2. Thesis outline 4

2. Literature Review: SnO_2 surface chemistry **7**

2.1. Introduction 7

2.2. Chemistry of stoichiometric and reduced surfaces 10

2.2.1. Pd doping effects 15

2.3. Chemistry of reconstructed surfaces 18

2.4. Electron microscopy surface characterisation 29

3. Theory and Methods **39**

3.1. Introduction 39

3.2. Electron Sources 41

3.2.1. Partial coherence 44

3.3. The Imaging system 46

3.4. Aberration Correction 49

3.5. Electron detection 53

3.5.1. MTF and NPS calculation 54

3.5.2. Magnification calibration 56

3.5.3. Electron dose measurement 60

3.6. Specimen-electron interactions 61

3.6.1. Multislice simulations 62

3.7. Exit wave restoration 65

4. Surface chemistry of nominally Pd-doped SnO_2 nanoparticles 72

4.1. Introduction 72

4.2. Theoretical and experimental methods 74

4.2.1. Sample preparation and imaging 74

4.2.2. Morphological and crystallographic properties 75

4.2.3. Model construction 78

4.2.4. Finite electron dose focal series simulations 86

4.2.5. Focal series exit wave restoration 96

4.2.6. Quantification of surface O atom SNFR as a function of dose and occupancy 102

4.3. Results 106

4.3.1. Experimental focal series 106

4.3.2. Single O atom sensitivity study: simulated focal series 123

4.3.3. Surface dynamics 131

4.4. Conclusions 142

5. Surface chemistry of beam-induced surface reconstructions on {110} facets 143

5.1. Introduction 143

5.2. Experimental methods 146

5.2.1. Effects of overhead time on dose and temporal resolution 146

5.2.2. Post-acquisition image processing and calibrations 153

5.2.3. Exit wave restoration 159

5.2.4. Electron dose properties 163

5.3. Results and discussion 167

5.3.1. Dose rate and cumulative dose dependence 167

5.1. Conclusions 191

6. Conclusions and Recommendations 192

6.1. Conclusions 192

6.1.1. Surface chemistry of nominally Pd-doped SnO_2 nanoparticles 192

6.1.2. Surface chemistry of beam-induced surface reconstructions on {110} facets 195

6.2. Recommendations and Future Work 197

Appendix A 203

Appendix B 222

Appendix C 232

Glossary 234

References 236

1. Introduction

1.1. Rationale

Tin dioxide (SnO_2) is one of the most widely studied metal oxides [1–6], both in its native and doped state. It possesses the unique property of being 97% optically transparent in the visible light region and electrically conducting [7]. Optical transparency is attributed to a wide bandgap (3.6 eV) while electrical conductivity is related to non-stoichiometric surfaces stabilised by the bivalence of Sn (4+/2+ oxidation states) [7]. These two factors have made it a material of interest in opto-electronics[8], sensing[9], photovoltaics[10], energy-storage[11], and catalysis[12].

Compositing[12–14], has been employed to enhance the intrinsic properties of SnO_2-based nanomaterials. Synthesis research has matured such that rational synthetic techniques can be employed to reproducibly engineer particles at the nanoscale with specific high energy facets, shapes and sizes[15–17]. Additionally, doping[18–20] has also been used to enhance the surface properties of SnO_2

nanoparticles. Particularly, Pd doping, relevant to this study, has been shown both theoretically and experimentally to either lower or close the bandgap of SnO_2, subsequently enhancing its conductivity significantly [21–25]. Experimental evidence has demonstrated that Pd incorporates into the SnO_2 surface as single dopants on sub-10 nm nanoparticles when the nominal doping concentration is lower than 1 wt% [26]. At higher nominal doping concentrations and on larger particles it forms clusters composed of Pd^0/Pd^{2+} [26].

There is limited understanding of the native and dopant-induced active sites, their distribution on the low energy facets as well as the fundamental mechanistic processes which take place on them under various experimental conditions. This is because spectroscopic or diffraction-based bulk structural characterisation techniques lack the capability to probe individual sites with high spatial resolution necessary to enable the exact correlation of active sites, their distribution, as well as their dynamic activity under various environmental conditions [27,28].

Our current understanding of the surface chemistry of SnO_2 materials under oxidising and reducing conditions is largely derived from scanning tunnelling microscopy (STM) combined with low energy electron diffraction (LEED) and surface spectroscopic techniques on bulk single crystals. These findings have been substantiated through theoretical calculations (see reviews by Batzill et al. (2005, 2006)[29,30] and Das (2014)[31]). Valuable insights have been gained

through these characterisation techniques. For example, the relative stability of the various low energy facets of SnO_2 has been established unambiguously both experimentally and theoretically as well as the surface chemistry of {100} and {101} facets under reducing and oxidising conditions [32,33]. For the {110} facets, there is general agreement about the stoichiometric termination and, to a less degree, its reduced termination chemistry. Unlike other SnO_2 facets, under progressively reducing conditions, {110} surfaces undergo complex surface reconstructions, which have been difficult to resolve through STM imaging [34].

These reconstructions remain an area of research interest since they have been shown to enhance the conductivity of bulk single crystal {110} surfaces by up to four orders of magnitude, for the (4x1) surface reconstruction for example, compared to the stoichiometric surface [35,36]. Their metastability under ambient temperatures[37] or high $O_{2(g)}$ conditions[38], despite being formed at high temperatures and low pressures, suggests that once formed, they may be suitable for heterogeneous catalysis applications in an oxygen atmosphere (see section 2.4)[37].

Aberration-corrected (scanning) transmission electron microscopy (AC-(S)TEM) is routinely employed to study the surface chemistry of oxide materials. To date, for SnO_2, it has been used to determine the reduced surface chemistry of the {100} and {101} facets on thin films[39] and nanobelts[40]

,respectively. Similarly, *in situ* and room temperature reconstructions of the {110} facets on micron-sized cuboctahedra[37] and thin films[41] have also been imaged at atomic resolution. However, no comparable research has been conducted for sub-10 nm, catalytically relevant, nanoparticles.

In this thesis, the application of AC-TEM for determining the surface chemistry of SnO_2 materials will be extended to nanoparticle sizes (sub-10 nm[26]). Specifically, AC-TEM in conjunction with exit wave restoration (EWR), will be used for the first time, to determine the surface chemistry of nominally doped 0.5 wt% Pd-SnO_2 nanoparticles imaged along various low-order zone axis projections. Furthermore, the structure and chemistry of reconstructed {110} facets will be studied as a function of electron dose. These and the stoichiometric/reduced surface chemistries will be compared to theoretical and experimental findings.

1.2. Thesis outline

Chapter 2 outlines the surface chemistry of stoichiometric, reduced, and reconstructed surfaces as deduced from theoretical and experimental findings on bulk single crystals. It then highlights the relevance and use of AC-(S)TEM as a tool suitable for studying the surface chemistry of SnO_2 materials at atomic resolution.

Chapter 3 provides an overview of CTEM image formation theory, aberration correction, and the advanced AC-TEM imaging techniques used in this thesis. The latter include conventional focal series (CFS) EWR, and the methods employed to measure the instrumental parameters for EWR. In addition, computational methods used for physics-based image simulations are also discussed.

Chapter 4 examines the physicochemical properties of nominally doped 0.5 wt% Pd-SnO_2 nanoparticles using conventional focal series (CFS) EWR. Specifically, the morphological and crystallographic properties as well as the surface chemistry of these nanoparticles, are studied at atomic resolution. Wulff constructed 3D SnO_2 models with theoretically predicted stoichiometric and reduced terminations are used as input for detector-representative finite dose simulations for comparison with experimental observations. In addition, the effect of the electron beam on the surface chemistry is also studied by temporal segmentation of the focal series.

Chapter 5 investigates the dependence of the reconstruction pathway of {110} facets on the dose rate and cumulative doses employed for imaging. Herein, imaging parameters that limit the time resolution of CFS are also quantified

and an alternative time-resolved focal series acquisition method called fast focal series (FFS) is developed.

Chapter 6 gives general conclusions and future research recommendations.

2. Literature Review: SnO_2 surface chemistry

2.1. Introduction

Tin dioxide (SnO_2) naturally occurs as a tetragonal-rutile crystal structure ($P4_2/mnm$) with 2 Sn and 4 O atoms per unit cell[42]. The O atoms occupy tetrahedral voids in the Sn sublattice and form distorted octahedral coordination around the central Sn atom (Figure 2.1)[43].

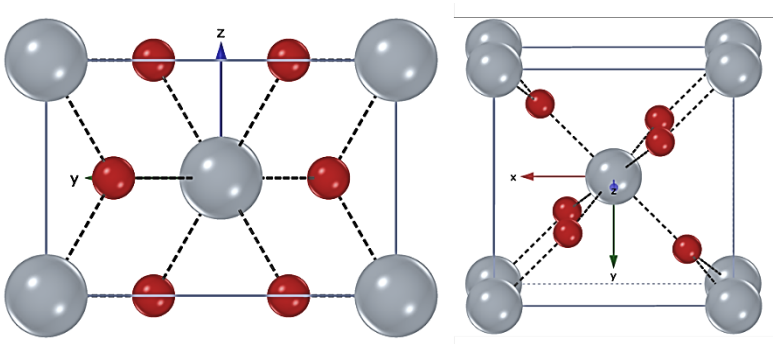

Figure 2.1: Atomic model of a [100] oriented unit cell of SnO_2 showing the shared O atoms on the {001} faces and its $[00\bar{1}]$ zone axis projection with a small angle tilt along [100] showing SnO_6 distorted octahedra (red and grey atoms are O and Sn, respectively).

It is one of the most studied oxides both in its native and doped states[1–6,44–46]. Its bandgap of 3.6 eV, is larger than the highest visible light energy of 3.1 eV, making it optically transparent[7]. The bivalence of Sn atoms in SnO_2 accommodates its nonstoichiometry resulting in defect-induced surface states that make it conductive[7]. These property combinations make it viable for a wide range of applications in opto-electronics[8], sensing[9], photovoltaics[10], energy-storage[11] and photocatalysis[12].

In general, the surface chemistry of nanoparticles is probed through bulk averaging techniques. Insightful characteristics of the surface of SnO_2 nanoparticles such as crystalline phase, defect type and density have been characterised through X-ray diffraction[47], surface spectroscopies[48] and molecular probe temperature-programmed desorption studies[48], respectively. The novel characteristics of SnO_2 nanoparticles, relative to their bulk counterparts, are associated with their surface properties, which can be modified through variations of size[26] and morphological properties[9] as well as doping[18,19] and compositing[12–14]. Specifically, their performance in gas sensing and heterogeneous catalysis applications is strongly correlated to the presence of O vacancies and the subsequent undercoordinated surface Sn atoms. However, there is a lack of direct evidence correlating these defects to the surface structure of specific facets of SnO_2, especially for nanoscale 0D materials.

Linking specific defect types and their distributions to specific facets has the potential to enable the engineering of nanoparticle facets for specific functional enhancement. Insights into such links have been determined for bulk single crystal and have also been verified theoretically. However, the surface features observed on single crystals, or their lamellae may not directly correlate with surface features of catalytically relevant materials. For example, bulk-to-surface ratios of nanoscale materials are different from those of macroscale SnO_2[26]; thus, surface relaxation processes may occur more complexly than observed at macroscale or predicted theoretically. For example, for the {100} facets of CeO_2 nanocuboids, Lin et al. (2014), showed that the O-row removal termination models generated theoretically and or those obtained on single bulk crystals using scanning tunnelling microscopy (STM) were not consistent with their observations on nanoparticle surfaces using aberration-corrected high resolution transmission electron microscopy (AC-HRTEM)[49]. They demonstrated that the same surface possessed reconstructions, O, Ce and CeO terminated regions in proximity. They postulated that the presence of this mixed termination indicated that, at the nanoscale, the various terminations had small energy differences such that their locally ordered structure overall resulted in a low energy surface. Hence, it remains critical to provide direct evidence of the surface terminations of nanoscale SnO_2 facets, despite the general consistency between theoretically and experimentally observed

terminations and reconstructions on bulk single crystals as will be discussed subsequently.

In this review, current insights on the stoichiometric, reduced, and reconstructed termination chemistry of SnO_2, as derived from scanning probe microscopy (SPM) of bulk single crystals and theoretical calculations will be discussed. Using other nanosized oxide nanoparticles, as examples, it is also demonstrated that aberration-corrected (scanning) transmission electron microscopy (AC-(S)TEM) is a suitable tool for providing direct evidence of the local surface chemistry of stoichiometric, reduced, and reconstructed facets of SnO_2 nanoparticles. Furthermore, insights on the termination chemistry of reduced and reconstructed SnO_2 surfaces attained with AC-(S)TEM imaging on micron-sized particles as well as on lamellae will also be discussed.

2.2. Chemistry of stoichiometric and reduced surfaces

The surface chemistry of stoichiometric and reduced low-index surfaces of SnO_2, which will be briefly reviewed below, is well characterised experimentally on bulk single crystals[1,29,30,34,38] and theoretically[3,32,33,50,51]. For more details refer to the comprehensive reviews by Das (2014)[31] and Batzill et al. (2005)[29,38].

It is known that the low energy surfaces of SnO_2 in their relative surface energy order are: (110)<(100)<(101)<(001). This surface energy trend remains valid irrespective of the choice of functional in density functional theory (DFT)

calculations [32]. For example, the theoretically predicted surface energies of the stoichiometric (*bulk terminated*) surfaces by Oviedo et al. (2000)[50], Beltrán et al. (2003)[52] and Xu et al. (2012)[32] are shown in Table 2.1 and the absolute surface energy (γ_{hkl}) values in this table are different across different studies. However, the resultant relative surface energies are largely comparable. This is particularly helpful when calculating the equilibrium shape of nanoparticles, as in Wulff analysis[53]. It means that in most instances, the same equilibrium shape can be obtained irrespective of the choice of the theoretically calculated γ_{hkl} values employed because relative surface energies are similar across multiple studies[32,50,52,53]. However, it must be noted that under experimental conditions the interaction of the nanoparticle with the substrate, neighbouring nanoparticles as well as surface reconstructions will simultaneously alter the relative surface energies of the equilibrium shape such that modified Wulff model approaches need to be employed [54,55] (see section 4.2.3 for more details).

Table 2.1: Surface energies of stoichiometrically terminated SnO_2 surfaces[32,50,52] and resultant relative ratios determined by normalisation with respect to the (001) surface energy.

Authors	**Surface energy (J/m^2)**			
	(110)	(100)	(101)	(001)
Xu et al. (2012)[32]	1.00-1.38	1.07-1.55	1.42-1.79	1.83-2.23
Beltrán (2003)[52]	1.20	1.27	1.43	1.84
Oviedo (2000)[50]	1.04	1.14	1.33	1.72
Authors	**Relative surface energy**			
	(110)	(100)	(101)	(001)
Xu et al. (2012)	0.55-0.62	0.58-0.69	0.78-0.8	1
Beltrán (2003)	0.65	0.69	0.78	1
Oviedo (2000)	0.6	0.66	0.77	1

Theoretical calculations also indicate that under highly oxidising conditions, the stoichiometric termination is the most stable[32,56]. However, under reducing conditions all these surfaces undergo the loss of surface O atoms. Figure 2.2 illustrates the most accepted surfaces of SnO_2 predicted theoretically for the stoichiometric (left) and reduced (right) cases, along low-index zone axis. In Figure 2.2 the {001} facets of SnO_2 are not included because they only have a stoichiometric termination with no reduced counterparts. This surface, unlike other SnO_2 surfaces, is classified as Type-I and not Type-II, according to Tasker's classification[57]. It is composed of charge-neutral atomic planes that have bulk stoichiometry, SnO_2. While Type-II surfaces are composed of symmetric charged trilayers with a zero-dipole moment perpendicular to the surface. They are composed of either O(2-)-Sn(4+)-O(2-) units for the {100} and {101} surfaces or O(2-)-[Sn_2(8+)O_2(4-)]-O(2-) layers for the {110} surfaces.

Additionally, the (001) surface is unlikely to be observed experimentally since it has the highest surface energy relative to other facets [32,34,50]. Stoichiometric terminations of {101} and {100} surfaces are all terminated by 2-fold coordinated bridging O (O_{br}) atoms bonded to 5-fold coordinated Sn atoms.

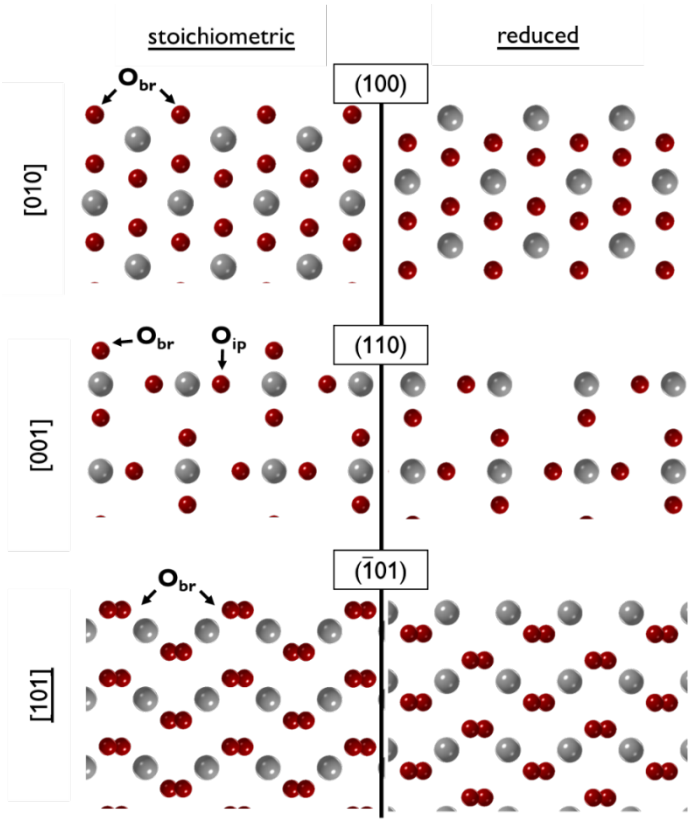

Figure 2.2: Atomic models of stoichiometric and reduced surfaces of SnO_2 as predicted by DFT. The grey and red spheres represent Sn and O atoms, respectively. For all the atomic models, the stoichiometric surfaces are terminated by O_{br} atoms and O atoms in the second atomic plane for the {110} surfaces are referred to as in-plane O (O_{ip}).

On reduction, bridging O vacancies are formed, and the resulting surface is composed of a charge-neutral SnO layer of stable tri-coordinated Sn atoms in the 2+ oxidation state [29]. DFT, low energy electron diffraction (LEED) and STM confirm that the {101} and {010} bulk single crystal surfaces are typically

either stoichiometric or reduced with a SnO overlayer [29,33,38]. The reduced surfaces do not undergo reconstruction even under low $O_{2(g)}$ partial pressures and high-temperature conditions[29].

From Figure 2.2 the stoichiometric (110) facet is terminated by $O_{\mathbf{br}}$ atoms (red spheres) doubly coordinated to Sn atoms (grey spheres) which form a distorted octahedron. The O atoms one atomic layer below are referred to as in-plane O ($O_{\mathbf{ip}}$) atoms and these are tri-coordinated to unsaturated Sn atoms (5-fold coordinated) forming a square-pyramidal geometry.

Surface techniques and theoretical studies agree on the same stoichiometric model for this surface. Similarly, there is general agreement, but to a lesser degree, about the reduced model of this surface due to its tendency to undergo surface reconstruction with reduction. However, theoretically, it is generally accepted that at low O chemical potentials ($\Delta\mu_O$), full reduction of the stoichiometric surface occurs in 2 steps: the bridging atoms are removed first because they have the lower energy of O vacancy formation, secondly, every other in-plane O row is removed [33,34,58]. Stoichiometric and fully reduced surfaces, therefore, have six or three-fold coordinated Sn atoms in the 4+ and 2+ oxidation states, respectively.

2.2.1. Pd doping effects

The functionality of nanosized SnO_2 can be enhanced through compositing [12–14] and doping [18–20]. The doping effect is of interest in this study, as the SnO_2 nanoparticles have a nominal doping concentration of 0.5 wt% Pd. Hence, the following discussion will be limited to the effects of Pd doping on the properties of SnO_2.

Theoretical calculations have shown that Pd doping enhances the electronic properties[26] of SnO_2, in both its stoichiometric or reduced state, by introducing surface states which either cover or decrease the band gap significantly [21–25]. Furthermore, it has also been shown to provide additional adsorption sites[21,22]. Both these factors have been subsequently used to explain the experimentally observed enhancement of the gas sensing and catalytic properties of SnO_2 with Pd doping[19,59–61]. However, the incorporation of Pd on reduced and stoichiometric/bulk terminated facets is predicted to be different.

On bulk terminated facets single Pd atoms are shown to have preferential adsorption to the surface through O_{br} atoms[21–24] as shown in Figure 2.3 (a). The incorporation of a single Pd dopant introduces surface states in the gap and in the case of CO sensing, it also increases the number of adsorption sites to three compared to one for the pure bulk terminated facet[21].

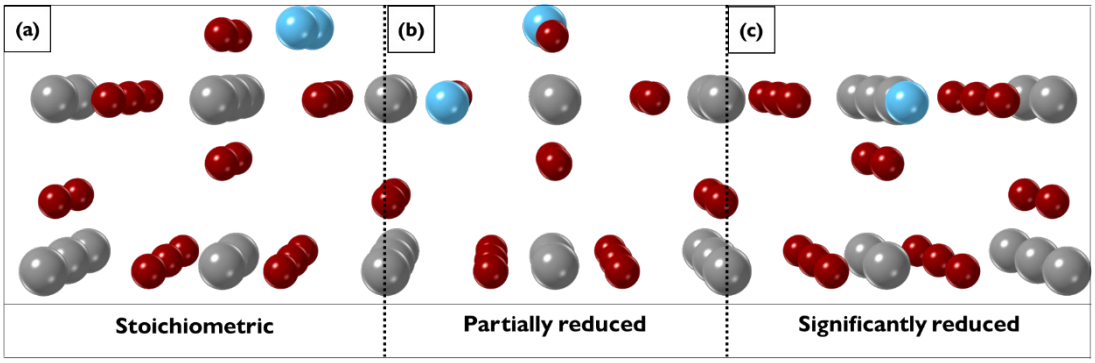

Figure 2.3: Theoretically predicted adsorption and substitutional sites of Pd atom dopants on (a) stoichiometric, (b) partially and, (c) significantly reduced {110} facets of SnO_2. (a) was adapted with permission from Springer Nature [22] and (b) was adapted from ref [24] with permission from Elsevier.

Furthermore, Pd clusters have also been shown to be stable on bulk terminated facets than on their reduced counterparts by Robina et al. (2014) and more recently by Germán et al. (2019). The interaction of the Pd clusters with the stoichiometric surface is mostly through O_{br} as stated above. According to the findings of Germán et al. (2019), the cluster with n=5, shown in Figure 2.4, is the most energetically favourable compared to all the other configurations composed of n≤10 atoms[22].

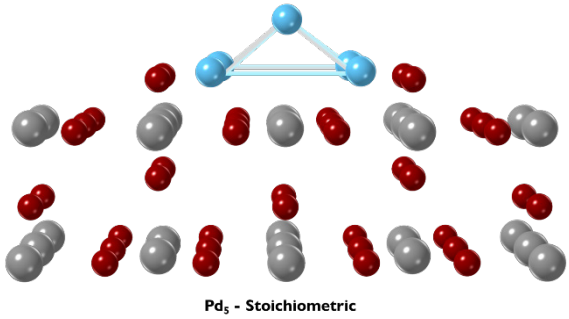

Figure 2.4: A Pd_5 cluster coordinated to a bulk terminated facet through O_{br} atoms as proposed by Germán et al. (2019) [22].

Compared to the pristine stoichiometric SnO_2 (110) facet, the stoichiometric SnO_2 (110) facet with the Pd_5 cluster had better H_2(g) adsorption. Nonetheless

its dissociative capacity was lesser than the former's. Overall, however, the bulk terminated facet with the Pd_5 cluster had 11 more sites for $H_{2(g)}$ dissociation compared to the pristine SnO_2 facet. In addition, Robina et al. (2014) also showed theoretically that Pd clusters on reduced facets, for Pd_4 for example, had more negative sintering energies (-0.77 eV) than on bulk terminated facets (1.43 eV). This implies that there is more energy required to decompose a Pd cluster into individual Pd atoms on a stoichiometric surface while it is more preferable for the cluster to decompose on the reduced surface[23].

Little research has been conducted on the effect of Pd on reduced SnO_2 facets[23,24]. The most extensive work has been conducted by Mäki-Jaskari et al. (2003)[24]. They proposed that the distribution of Pd on reduced SnO_2 surfaces is strongly dependent on their degree of defectivity. For moderately reduced surfaces (where the surface still has some O_{br}), the binding energy of Pd on an O_{ip} atom site (3.5 eV) is slightly larger than that on an O_{br} atom site (3.3 eV) (Figure 2.3 (b)). Moreover, when the surface has no O_{br}, the binding energy of Pd on the O_{ip} site increases to 4.3 eV. Additionally, Mäki-Jaskari (2003) also showed that for significantly defective facets (surfaces that have lost all O_{br} and some Sn and O_{ip} surface atoms), Pd substitutes for the 4-fold coordinated surface Sn atom which has lost coordination to O_{br} atoms (Figure 2.3 (c)). However, it must be noted that Robina et al. (2014) suggested that Pd does not substitute for either Sn or O surface atoms, on surfaces that have lost all

O_{br} atoms, but rather it binds strongly to surface Sn atoms resulting in surface strain[23]. Despite some discrepancies between these two studies, both demonstrate that the incorporation of Pd also induces surface states in the band gap which improves the conductivity of SnO_2 nanoparticles, consistent with what is predicted for the bulk terminated SnO_2/Pd system and experimental observations. The oxidation state of the Pd is dependent on its size. When it is incorporated into the SnO_2 lattice as a single atom dopant it adopts an Pd^{2+} state. However, when it is clustered, it can exist as Pd^0 and Pd^{2+} [26]. To the best of my knowledge, no studies have elucidated the chemical and physical behaviour of Pd dopant atoms during the surface reconstructions of SnO_2 surfaces.

2.3. Chemistry of reconstructed surfaces

The reconstructions of low energy surfaces of SnO_2 have also been studied extensively on bulk single crystals through surface diffraction and spectroscopy in conjunction with DFT calculations[29,34–36,38,56,62–65]. The findings between theory and experimental analysis agree for the {100} and {101} surfaces. For example, these surfaces are characterised by simple reconstruction pathways with sputtering and annealing up to 1000 K through LEED and STM studies[30,38]. Herein, reconstruction pathway refers to the order of the transformation of the chemistry and atomic rearrangement of the surface as a

function of controlled stimulation i.e., variation of temperature or charged particle sputtering i.e., from an initial state/reconstruction to another. For the {100} and {101} facets there is no qualitative change in the periodicity observed in LEED i.e., retains its (1x1) surface periodicity. Similarly, the unit cell dimensions of these surfaces remain consistent with that of the initially stoichiometrically terminated surface based on STM analysis. Nonetheless, low energy ion spectroscopy (LEIS) indicated that a sharp decrease in the O/Sn ratio occurs at 610-660 K and 600-810 K for the {100} and {101} surfaces, respectively[38]. This reduction in the O/Sn ratio is ascribed to the desorption of bridging O atoms from the surface to form a stable overlayer of tri-coordinated Sn atoms with a stable SnO composition [38,62]. In fact, the {100} reduced surfaces remain stable even after exposure to high levels of $O_{2(g)}$ under ambient conditions[38]. As shown above, there is consistency between these experimental findings with DFT calculations.

The {110} surfaces are of interest because several studies on bulk single crystals have demonstrated that reconstructed {110} surfaces are up to four orders of magnitude more conductive than their nearly stoichiometric counterparts[35,36,38]. In general, conductivity increases with reduction. De Frésart et al. (1982) and Shen et al. (2000) and Batzill et al. (2003), showed that the highest level of conductivity is associated with the (4x1) surface

reconstruction and thereafter decreases slightly with the subsequent formation of high-temperature reconstructions (> ≈900 K) [35,36,38].

There is general agreement about the order in which the SnO_2 {110} surfaces undergo surface reconstructions. This has been clearly elucidated using LEED studies. The {110} surfaces that are repeatedly sputtered and annealed, as in STM, undergo surface reconstructions as follows: (1x1) (300 K), diffuse c(2x2) (500-870 K) [34,66], c(2x2) and (4x1) (850-980K) [34,36,67], (4x1) (900-1200 K)[34], (1x1) (975 – 1230 K)[34,36] and (1x2) (1075-1100 K)[36]. For bulk single crystals, consensus between theoretically and experimentally proposed models is only being established more recently despite the known order of surface reconstructions.

It must be noted, however, that the reconstruction pathway of purely annealed, initially oxidised, SnO_2 {110} bulk surfaces occurs differently compared to the one that occurs on surfaces that have undergone cycles of annealing and sputtering. With annealing, oxidised surfaces are shown to transform their (1x1) partially stoichiometric termination to a high temperature (1x1) reconstruction with a lower O/Sn ratio as evidenced through LEIS[30]. This surface subsequently transforms to the high temperature (1x2) surface reconstruction at >≈900 K. This indicates that the high temperature (1x1) and (1x2) surface reconstructions are the low energy reconstructions of SnO_2, unlike

the (4x1) surface reconstruction which is only observed during sputtering and annealing cycles.

From the 80s to the 90s, the surface periodicity of these surfaces was thought to be driven by the periodic desorption of O atoms in various multiplicities (<900 K) and their bulk to surface diffusion (>≈900 K)[36]. Figure 2.5 shows the subsequent atomic models that were approximated through the correlation of O/Sn ratios and surface periodicity. For example, for the high temperature (1x1) surface reconstruction, earlier studies on bulk single crystals, attributed its surface periodicity to that of a stoichiometric surface that has lost all its O_{br} atoms [36,67,68]. While the high temperature (1x2) surface reconstruction model comprised of a stoichiometric surface with every other surface bridging atom removed in the [001] direction[36]. This was corroborated by the O/Sn ratios obtained through surface spectroscopies. In these studies, the O/Sn ratio of the high-temperature (>≈900 K) surface reconstructions, was shown to be higher than that of the (4x1) surface reconstruction. Hence, the model of the (4x1) reconstruction was thought to be highly O-deficient and composed of differently ordered in-plane O vacancies[64]. The mechanism at low temperatures was driven by O desorption while at higher temperatures bulk diffusion of O atoms to the surface accounted for the increase in the O/Sn ratio.

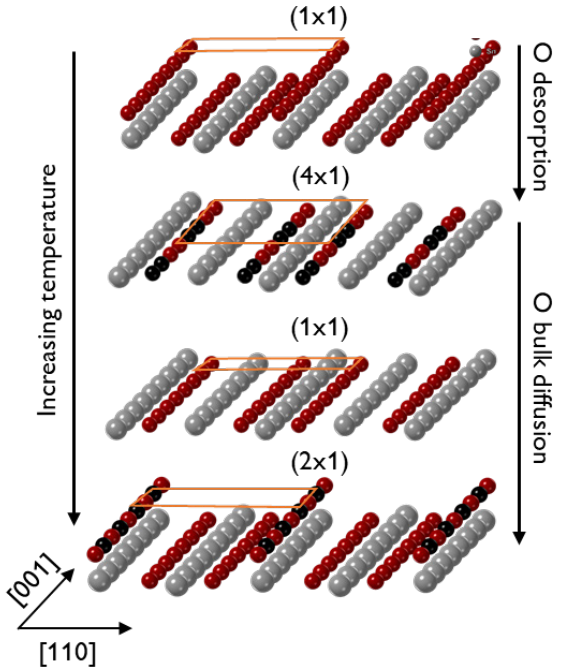

Figure 2.5: Earlier SnO_2 (110) surface reconstruction atomic models derived from correlative LEED and surface spectroscopy studies. Only one or two atomic planes are shown depending on the reconstruction. The orange boxes indicate the respective surface unit cells, and the red, black, and grey atoms show O atoms and vacancies as well as Sn atoms, respectively. The (4x1) surface reconstruction is adapted from ref[64](c) (1982) with permission from Elsevier. The other reconstructions are adapted from ref[36]© (1991) IOP Publishing. Reproduced with permission. All rights reserved.

Nonetheless, in the late 90s, it was demonstrated that these models were generally not consistent with observations made using real space surface imaging techniques such as STM. It was observed that the high temperature (1x1) surface reconstruction had a combination of short-range order and complete disorder through STM analysis[34,36,66,69]. Pang et al. (2000) showed, through STM, that the surface had no evident 1x1 periodicity but was characterised by featureless terraces, which they assigned to disorder. With atomically resolved STM, Batzill et al. (2003) and Sinner-Hettenbach et al. (2001) demonstrated that, although largely disordered, this reconstruction has

some zigzag (2x1) and (4x1) local ordering, respectively[34,69]. In fact, Batzill et al. (2003), postulated that the (1x1) periodicity may be coming from the bulk of the crystal[34].

Similarly, the high-temperature (1x2) reconstruction was also shown to have poor long-range order, like the (1x1) reconstruction[38]. It was shown through STM that it was composed of discontinuous, local atomic rows separated by twice the surface unit cell length in the [110] direction, giving the diffuse (1x2) periodicity observed in LEED [38,66]. Other models, such as the added Sn_2O_3 row model derived from the research on the (1x2) surface reconstruction of TiO_2 {110} surfaces were also proposed[66] but DFT calculations showed that the surface was not stable compared to the stoichiometric termination even at extremely low $\Delta\mu_O$ making the structure unlikely to be observed experimentally [38].

These STM findings have been largely corroborated by DFT models that consider the role of surface O vacancies as well as Sn surface 'interstitials' (Sn_i). Ágoston and Albe (2011), examined nearly 200 possible defect models that can form under various $\Delta\mu_O$ on the {110} surfaces of SnO_2 and determined that under reducing conditions ordered structures composed of Sn_2O_2 units had the lowest energy relative to other single and clustered defects of SnO_2[56]. The Sn_2O_2 defect model they propose comprises a pair of Sn_i atoms coordinated to

the bulk through coordinately unsaturated O (O_{cus}) and O_{br}/O_{ip} atoms (see insert in Figure 2.6).

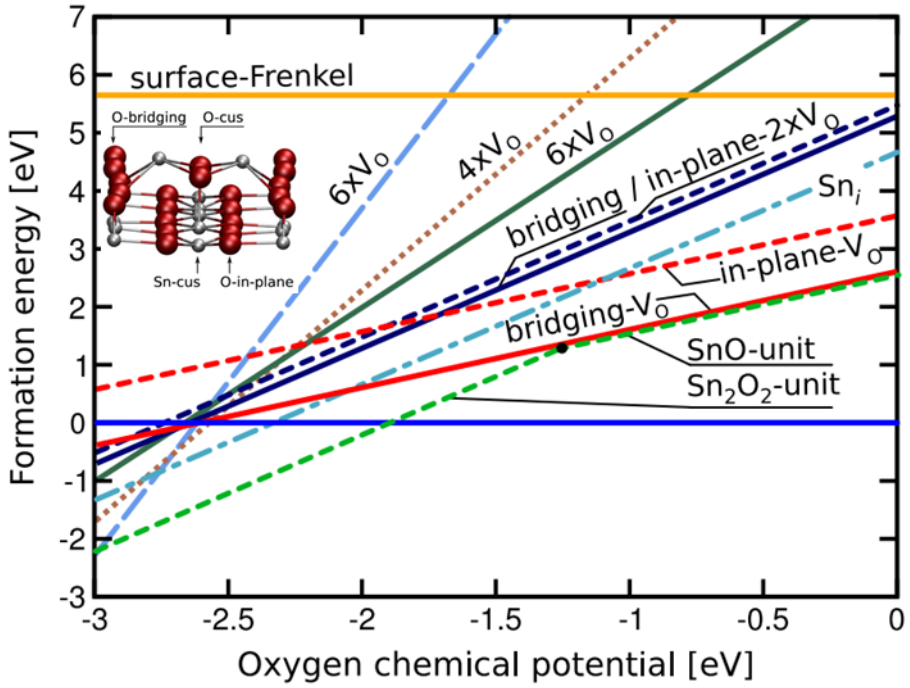

Figure 2.6: The formation energy of various SnO_2 surface defects as a function of $\Delta\mu_O$. The insert corresponds to the Sn_2O_2 defect which has the lowest formation energy at $\Delta\mu_O$ <-1.91 eV. Adapted from ref[56] © (2011) with permission from Elsevier.

They successfully constructed various surface models with experimentally verified periodicities of SnO_2 using Sn_2O_2 units as building blocks. They were able to account for both the local symmetry and long-range disorder of the high-temperature reconstructions. In particular, they demonstrated that the disorder can be attributed to the low energetic cost (≈0.07 eV) of the flipping and gliding of thermally activated Sn_i atoms in Sn_2O_2 units along the [110] and [001] directions, respectively. Effectively, the low energetic cost of these processes means that at high temperatures used in STM the Sn_i are thermally

activated to acquire almost an infinite number of configurations which have comparable energies, leading to poor long-range order[56]. Furthermore, as will be demonstrated in the next section, atomically resolved AC-(S)TEM images of the high-temperature surface reconstructions validate the presence of local ordering of pairs of Sn_i atoms coordinated to the bulk through $O_{\mathbf{cus}}$ and $O_{\mathbf{br}}/O_{\mathbf{ip}}$ atoms.

Although the (1x1) and (1x2) reconstructions are said to be the low energy reconstructions of SnO_2, the (4x1) reconstruction is easily reproducible and has wider temperature stability and long-range order[34,56]. Thus, more research has been conducted to understand its properties. It has also been shown to be highly conductive and stable once formed even after exposure to 200 mbar of $O_{2(g)}$ at room temperature, making it more interesting for potential sensing and catalysis applications[34,56]. Several models were proposed for this surface reconstruction beginning in the early 1980s. Like the previous reconstructions, models derived from surface diffraction and spectroscopy involved the removal of $O_{\mathbf{ip}}$ atoms in various multiplicities without accounting for any relaxations in the Sn sublattice that may be induced by O loss [64,67]. Using surface diffraction and spectroscopy, de Fresart et al. (1981) proposed one of many motifs that could form a (4x1) periodicity by the removal of $O_{\mathbf{ip}}$ atoms from every 3rd unit cell in the [001] direction as shown in Figure 2.5[64].

Unlike for the previously mentioned reconstructions, atomically resolved STM imaging did not establish a widely accepted model for the (4x1) reconstruction. Contrary to de Fresart et al. (1981), Jones et al. (1997) proposed that the (4x1) motif was formed by the alternate removal of in-plane O atoms based on the contrast observed in atomically resolved STM images[70]. They intuitively interpreted the depressions observed on experimental STM data as O_{ip} vacancies as shown in the atomic model in Figure 2.7(a).

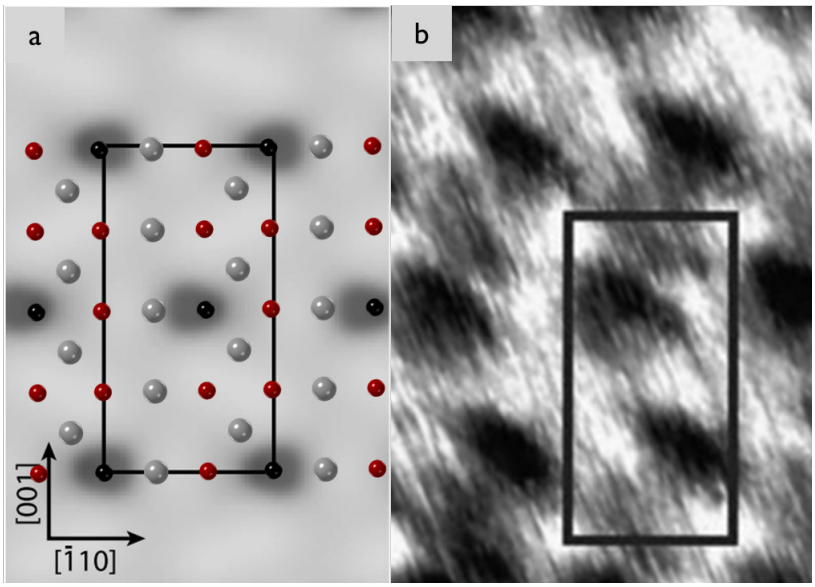

Figure 2.7: (a) Simulated STM image based on the model proposed by Merte et al. (2017) with an atomic model overlay of the model proposed by Jones et al. (1997). (b) An experimental high resolution STM image of the (4x1) surface reconstruction imaged by Batzill et al. (2003). In (a) the red, and black atoms indicate O atoms and O in-plane vacancies, while the grey spheres correspond to Sn atoms. The black borders indicate the (4x1) surface unit cell. The STM simulated image in (a) is adapted with permission from ref [65] © (2017) by the American Physical Society and the atomic model in (a) is adapted from ref[70] © (1997) with permission from Elsevier, while (c) was adapted from ref[34] © (2003) with permission from Elsevier.

However, subsequent simulations of STM images revealed that the correlation between the observed contrast and the specimen topology was more complex

due to the convolution of topographical and electronic information[34]. Through DFT, Oviedo and Gillan (2002), re-examined the model proposed by Jones et al. (1997) and found inconsistencies in their interpretation of STM contrast and their subsequently proposed atomic model of the (4x1) reconstruction[51]. They showed that surface Sn atoms would undergo notable relaxation with the loss of in-plane O atoms and that surface Sn atoms and O vacancies exhibited bright contrast, while O atoms next to the O vacancies produced dark contrast. Based on these observations, Batzill et al. (2003) were the first to propose a tentative model of the (4x1) surface composed of Sn_i and O vacancies by reinterpreting STM contrast[34]. They proposed a (4x1) surface reconstruction with an SnO stoichiometry with every Sn_i bound to 2 $O_{\mathbf{cus}}$ and 2 $O_{\mathbf{br}}$ atoms (Figure 2.8). However, later DFT calculations by Ágoston and Albe (2011) and Merte et al. (2017) showed that the surface was highly unstable relative to other possible surface terminations under the same conditions[56,65]. Although Ágoston and Albe (2011) did not find a suitable alternative model based on Sn_2O_2 units, Merte et al. (2017) were able to propose a model composed of an overlayer of Sn_3O_3 clusters bound to the bulk through $O_{\mathbf{cus}}$ and $O_{\mathbf{br}}$ atoms, and an additional O atom referred to as an 'apex' O_a atom (Figure 2.8). Their

model produced simulated contrast that is consistent with experimental STM observations (compare Figure 2.7 (a) and (b)).

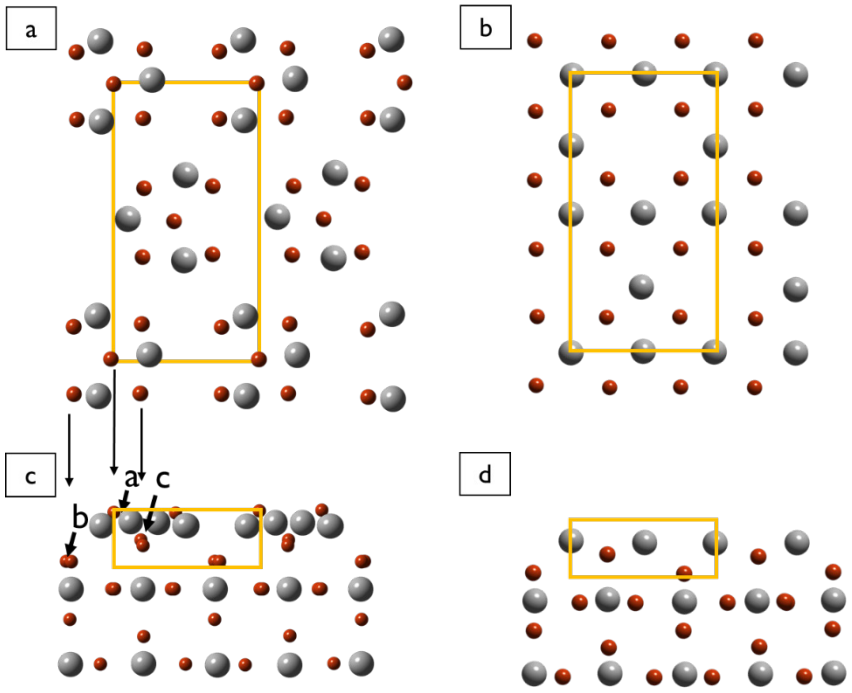

Figure 2.8: The atomic model of the first atomic plane of the (110) (4x1) reconstruction proposed by (a) Merte et al. (2017) and (b) Batzill et al. (2003) projected in the [110] direction.(c) and (d) show multiple atomic planes corresponding to the [001] projected views for (a) and (b), respectively. In (a) and (c) the surface has an Sn_3O_3 overlayer that has interstitial Sn atoms (grey atoms) bonded to the bulk through bridging (labelled as b), coordinately unsaturated (labelled as c) and, 'apex' (labelled as a) O atoms (red spheres). While in (b) and (d) the surface is composed of Sn interstitials coordinated to the bulk through 2 bridging and 2 coordinately unsaturated O atoms. The orange boxes indicate the (4x1) surface unit cell in the presented projections. (a,c) Adapted with permission from ref [65] © (2017) by the American Physical Society and (b,d) were adapted from ref[34] © (2003) with permission from Elsevier.

Above it is shown that for bulk single crystal surfaces, except for the {110} surfaces, theoretical and experiment-derived surface models of the reconstructions agree. It is also shown that the reconstruction pathways on the {110} surfaces are more complex. They have multiple surface periodicities with

increasing annealing temperature unlike that of the other facets which retain a single periodicity i.e., (1x1). Furthermore, the surface reconstructions of the {110} surfaces of SnO_2 are associated with improved electrical conductivity. However, there is no direct evidence to reveal their presence on and their subsequent impact on catalytically relevant nanoparticles (≈tens of nanometres in diameter). The methods through which these surface reconstructions are formed i.e., thermal annealing and sputtering are also well established and the relative stability of these reconstructions under ambient conditions is also known for bulk single crystals. It remains critical, nonetheless, to clarify the role, if any, of these reconstructions on the observed superior conductivity of SnO_2 nanoparticles during catalytic processes such as aqueous CO_2 electroreduction[71].

2.4. Electron microscopy surface characterisation

AC-(S)TEM with its analytical capabilities is a powerful characterisation tool that is routinely employed to characterise the physical and chemical properties of oxide facets, interfaces, and their transformation both *ex-situ* and *in situ* at atomic resolution[72–74]. DFT-corroborated surface terminations of catalytically relevant nanoparticle systems such as CeO_2, their active sites, dose sensitivity and the subsequent formation and annihilation of surface defects have been established through AC-(S)TEM[75–80]. In addition, advanced numerical post-

acquisition processing techniques that enable the extraction of 3D data from 2D images or in-line holograms continue to be developed[81–85].

Nevertheless, for nanoscale SnO_2 in its pure or doped state, little atomic resolution work has been conducted to determine the chemistry of the facets. Studies that have been conducted are largely limited to low-resolution TEM studies to elucidate faceting, morphological and size properties [9,86]. Stroppa et al (2009, 2011) used a combination of HRTEM, Wulff analysis and DFT to elucidate the shape of native and Sb-doped SnO_2 nanoparticles[86,87]. They revealed that preferential substitution of Sb on specific facets of the nanoparticles as a function of dopant concentration modified their surface energy and subsequently the morphology of the nanoparticles. Nonetheless, their focus was limited to morphological features and not facet chemistry nor were they able to visualise O atoms.

To correlate the function and structure of nanoparticles it is necessary to determine the sites associated with each facet at a local scale. This enables the engineering of facets for increased catalytic specificity and selectivity enhancement. Synthesis approaches are sufficiently advanced to generate monodisperse particles with specific morphologies and facets for heterogeneous catalysis, gas, and ion sensing applications[16,17,88,89]. To fully exploit this development, the native local surface chemistry must be known to correlate function with structure.

To date, two studies have unambiguously revealed the atomic configuration of the {100} and {101} surfaces on lamellae [39] and zigzag nanobelts[40] of SnO_2 under low $O_{2(g)}$ partial pressures using negative spherical aberration imaging (NCSI)[90,91]. In this technique, the contrast of all atoms, and especially light atoms, is enhanced by employing a negative C_3 value with an appropriate positive defocus during imaging. This enables the visualisation of both light and heavy elements. Both studies indicated, in agreement with theoretical calculations, that at low $O_{2(g)}$ partial pressures the surfaces lose their bridging O atoms and are terminated by Sn atom columns with a 2+ oxidation state. As iterated above, to date, no studies have been conducted on SnO_2-based nanoparticles that are relevant in catalysis to examine their surface properties. Particularly, there is no atomic resolution work reported on the pristine termination chemistry of {110} facets.

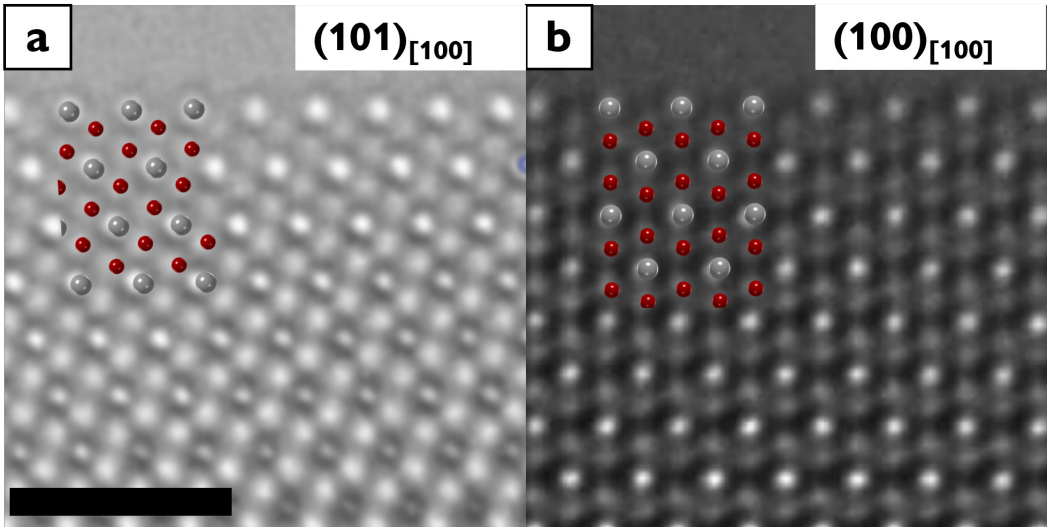

Figure 2.9: Sn-terminated (a) (101) and (b) (100) surfaces of a nanobelt and lamella of SnO_2 oriented in the [100] direction. The corresponding atomic models are overlain on the micrographs and Sn and O are represented by grey and red spheres, respectively. The scale bar is 10 Å. (a) and (b) are adapted with permission from ref[39] and ref[40]. © 2010 and 2020 American Chemical Society.

Furthermore, surface reconstructions on the {110} surfaces formed through annealing and /or particle bombardment are known to further enhance the conductivity of SnO_2[35,38]. The highly conductive (4x1) surface reconstruction has been shown to be stable under ambient conditions post-formation, despite being exposed to 200 mbar of $O_{2(g)}$, indicating that it may be employed for catalytic processes under $O_{2(g)}$[38]. Moreover, the (1x2) surface reconstruction has also been shown to be stable at room temperature, although it is typically formed at temperatures >1100 K. Moreover, DFT calculations, show that the dissociation of adsorbed O_2 molecules on the (1x2) surface reconstruction has a low energy barrier of 0.36 eV. This makes it suitable for catalytic processes, such as ***low-temperature oxidation of CO***, that depend on the adsorption

and activation of O_2 molecules[37]. As shown above, the sequence of surface reconstructions formed on bulk single crystals with annealing and sputtering is largely characterised, but there is little direct evidence to demonstrate their occurrence on catalytically active nanoparticles[56,65] and hence their demonstrated enhancement of electronic properties on bulk crystals cannot be simply extrapolated to nanoparticles.

On the other hand, for TiO_2 nanoparticles, AC-(S)TEM work has been successfully used to corroborate theoretical and STM-derived atomic models of its surface reconstructions. The 3D structure of the (1x2) surface reconstruction was resolved at atomic resolution using high angle annular dark field (HAADF) STEM imaging[92] by Shibata et al. (2008). In this study, they revealed the structure of the (1x2) surface reconstruction of the (110) facet by imaging it in 2 orthogonal directions, namely the [110] and [001] directions. Through their observations, they clarified ambiguity relating to the 3D position of the surface interstitial Ti atoms that was not resolved theoretically. Similarly, *in situ* HAADF and bright field (BF) STEM imaging have also been used to demonstrate the sequence of surface reconstructions that occur at atomic resolution on the {001} surfaces of TiO_2[93]. Additionally, Ek et al. (2018) also observed excellent agreement between theoretical models, and the [001] projected atomic structure of the (1x4) surface reconstruction obtained through focal series exit wave restoration[94]. This indicates that AC-(S)TEM is an

indispensable tool for the elucidation of the local atomic configuration of nanoparticles. However, it has been seldom employed for SnO_2-based nanoparticle systems.

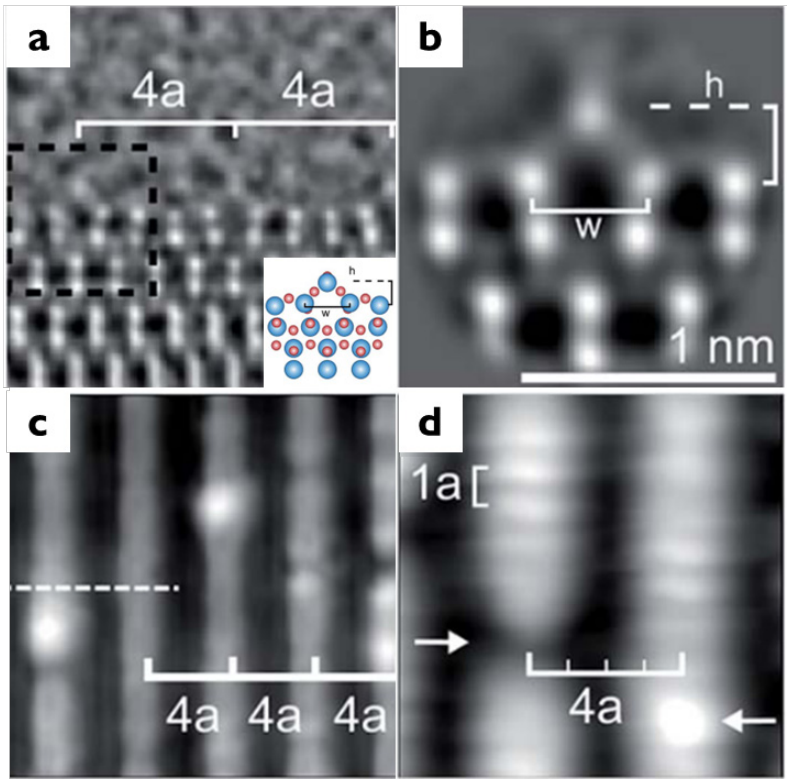

Figure 2.10: (a) A restored phase of a (001) facet on a TiO_2 nanoparticle oriented in the [100] direction exhibiting a (1x4) surface reconstruction. The inset in (a) is the adatom row model predicted through DFT. (b) The template averaged motif of the atomic arrangement of the surface reconstruction obtained from the restored phase in (a). The separation between each adatom row is 4**a**, corresponding to the distance measured from the STM image of the (001) surface of a bulk single crystal in (c) and on its magnified counterpart (d). The scale bars shown in (a) and (b) correspond to a distance of 10 Å. Adapted from ref.[94] with permission from the Royal Society of Chemistry.

It is only recently that the sequence of the surface reconstructions that occur on the {110} facets of micron-sized cuboctahedra of SnO_2 has been demonstrated at atomic resolution through a combination of *in situ* HAADF/BF AC-STEM and DFT[37]. The {110} facets of the cuboctahedra were

found to possess bulk termination at room temperature and progressively formed (2x1) (573-1073 K) and subsequently (1x2) (>1073 K) surface reconstructions with annealing. The abovementioned reconstructions are composed of rows of pairs of Sn_i atoms centred on $O_{\mathbf{cus}}$ atoms and coordinated to $O_{\mathbf{br}}$ atoms[37,56].

In particular, the (2x1) surface reconstruction model Li and co-workers proposed has an identical surface periodicity to that proposed by Ágoston and Albe (2011) and is also consistent with the zigzag (2x1) motif observed locally on the (1x1) reconstructed single crystal surface by Sinner-Hettenbach (2001). However, the coordination environment of the Sn_i atoms in their models is slightly different. Ágoston and Albe (2011), propose a (2x1) model with Sn_i coordinated to $O_{\mathbf{cus}}$ and $O_{\mathbf{ip}}$, with a Sn_2O_2 stoichiometry while that of Li et al. (2021) has Sn_i also coordinated to $O_{\mathbf{br}}$ with a $SnO_{1.89}$ stoichiometry. The projected geometric atomic arrangement of these models in the [001] and [110] directions would qualitatively look identical. Unlike Li et al. (2021), Ágoston and Albe (2011) do not provide the DFT-relaxed atomic coordinates of their models to enable quantitative differentiation between the two models based on the degree of atom relaxation since their coordination environments are different.

Despite the findings by Li et al. (2021), a recent computational study showed conditions where a (2x1) model composed of Sn_2O_2 units (as suggested by

Ágoston and Albe (2011)), is stable. Liu et al. (2022), used DFT to corroborate observations made using the NCSI technique of the projected structure of a room-temperature (2x1) (110) surface reconstruction of SnO_2 in the [110] direction[41]. Their calculations showed that under mildly reducing conditions the Sn_2O_2-based (2x1) model similar to the one proposed by Ágoston and Albe (2011) is more stable than that proposed by Li et al. (2021).

By annealing the cuboctahedra to 1200 K, Li et al. (2021), revealed a surface motif with a (1x2) periodicity in the [001] direction. They were able to precisely locate the position of the Sn_i and O atoms through HAADF and BF imaging, respectively (see Figure 2.11). They observed rows of pairs of Sn_i atoms that were coordinated to the bulk through $O_{\mathbf{cus}}$ and $O_{\mathbf{br}}$ atoms and separated by a distance of ≈13.4 Å, consistent with observations made in STM on bulk single crystals[38,69].

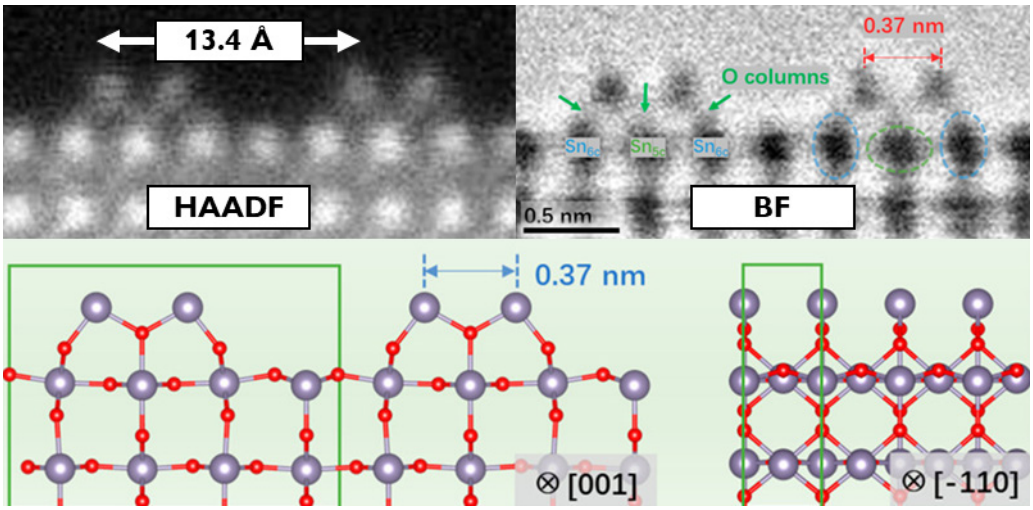

Figure 2.11: HAADF and BF images of the (1x2) surface reconstruction on the (110) facet of a cuboctahedron of SnO_2 along with the DFT calculated model of the surface in the [001] and [$\bar{1}$10] directions. The green boxes show the dimensions of the (1x2) reconstructions in both projections. Adapted with permission from ref[31] © (2021) American Chemical Society.

Subsequently, they generated 8 models by varying the positions of the Sn_i atoms and the stoichiometry of the Sn_2O_x units. Values of x ranged from 0 to 4. In the [110] projection, the Sn_i atoms have two sites that they can occupy, namely above pure Sn or above mixed Sn-O atom columns. These sites are referred to as the interstitial-vertical (*iv*) and the interstitial-horizontal (*ih*) sites, respectively[82]. Their calculations revealed that the surface composed of the Sn_2O-*iv* surface stoichiometry was the most stable and generated simulated BF and HAADF contrast that was consistent with their experiments. The stability of this model under highly reducing conditions has also recently been confirmed independently through DFT calculations by Liu et al. (2022)[41].

Another factor that remains ignored or is not explicitly accounted for carefully during electron microscopy imaging of SnO_2 surfaces when they are undergoing

surface reconstructions is their sensitivity to the electron beam and its subsequent influence on the reconstruction pathway[93,95]. Li et al. (2021), and Liu et al. (2022) attribute the surface reconstruction pathway solely to thermal annealing and the low $O_{2(g)}$ partial pressure in the microscope, respectively. Nonetheless, the effect of the electron beam must be considered as will be done in this study. Yuan et al. (2016), demonstrated that surface reconstructions observed on nanoparticles and nanosheets of TiO_2 degrade rapidly under the influence of the electron beam if they are not protected by an $O_{2(g)}$ environment[95].

3. Theory and Methods

3.1. Introduction

'There is plenty of room at the bottom... if only the electron microscopes could be 100 times better', said Richard Feynman in the 1960s, when he considered the possibilities of observing and manipulating matter at atomic level through the aid of better electron microscopes[96]. Significant progress has been made since then to improve the resolution of electron microscopes by 20-fold from 1000 pm, at best, to about 50 pm in the latest aberration corrected instruments[97–99].

In this chapter, imaging theory in the transmission electron microscope (TEM) and instrumental properties which limit the attainable resolution will be discussed briefly (Figure 3.1). The instrument effects on the imaging process will be discussed including the influence of the electron source, objective lens, multipole corrector, and detector according to the schematic diagram in Figure 3.1.

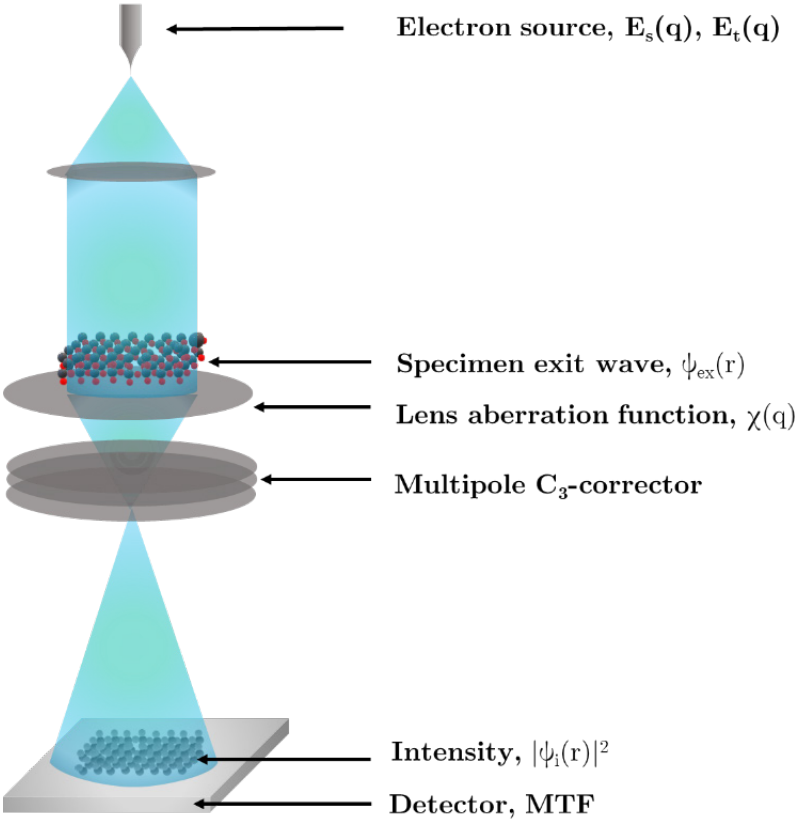

Figure 3.1: A schematic diagram of a TEM equipped with an image aberration corrector in the post-field of the objective lens including key instrumental parameters that limit the resolution of the microscope.

The methods employed to experimentally calibrate some of these instrument properties will then be described. Thereafter, a brief introduction to the theoretical framework of specimen-electron interactions will be given including a brief discussion of HRTEM simulation strategies with emphasis on the multislice approach. Finally, the theory of numerically inverting the imaging process by EWR will be discussed along with its experimental implementation as used in this thesis.

3.2. Electron Sources

Electron sources can be classified according to the method by which electrons overcome the source material's work function. Sources emit electrons by overcoming their work function by the assistance of either a strong electric field (field emission) or heat (thermionic). For HRTEM imaging, field emission gun (FEG) sources are most employed and can be thermally assisted or cold. The thermally assisted FEG, (Schottky FEG), is operated at 1472 °C and consists of a single crystal of W [100] with a coating of ZrO to lower its work function to 2.7 eV from 4.6 eV [100]. A cold FEG operated at room temperature is similarly made from a single crystal of W without any coating, typically oriented along a [111] or [310] directions[101].

The microscope used in this study was equipped with a cold FEG. Hence, the following discussion will focus on this source type and only draw comparisons with other sources where useful. For a comparative summary of electron source parameters refer to Table 3.1.

Table 3.1: Properties of electron sources (adapted by permission from Springer Nature: Springer US, by ref [102] © (2009).

Property	Units	W_{hp}	LaB_6	Schottky	Cold FEG
Work function	eV	4.6	2.6	2.8	4.6
Operating temperature	°C	2427	1427	1427	30
Current density, j	A/m^2	5	10^2	10^5	10^6
Cross over size, d_0	Å	$>10^6$	10^5	150	30
Brightness, β	A/m^2sr	10^{10}	5 x 10^{11}	5 x 10^{12}	10^{13}
Energy spread	eV	3	1.5	0.7	0.3
Emission current stability	%/hr	<1	<1	<1	5
Vacuum	Pa	10^{-2}	10^{-4}	10^{-6}	10^{-9}

Cold FEG sources have a nanosized tip and the electrons are extracted from this using two anodes (Figure 3.2). An extraction voltage (V_1) of a few keV is applied to the first anode to generate an intense field which induces electron tunnelling at the tip.

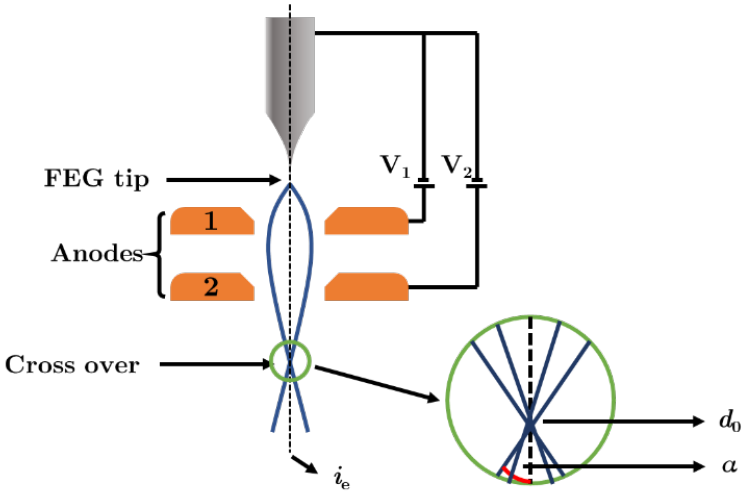

Figure 3.2: A schematic diagram of a cold FEG source assembly. Adapted by permission from Springer Nature: Springer US, by ref [102] © (2009).

The electric field (E) is most intense at the tip and is inversely proportional to its radius (r) as shown in equation 3.1:

$$E = \frac{V_1}{r} \qquad 3.1$$

In this study, the extraction voltage was about 3.6 keV. The extracted electrons are focused by the second anode and are subsequently accelerated to the desired voltage. In this study an accelerating voltage of 300 keV was used for all experiments unless stated otherwise. There are four important source properties for high resolution imaging namely, brightness, coherence, energy spread and stability. The brightness (β) is the current density per unit area per unit solid angle[103]. In equation 3.2 β is expressed to demonstrate the dependence of the source size:

$$\beta = \frac{i_e}{\pi^2 r^2 \alpha^2} \qquad 3.2$$

Here i_e, α and, $r = \left(\frac{d_0}{2}\right)$ are the emission current, divergence semi-angle and the radius of the cross over, correspondingly as shown in Figure 3.2.

Cold FEG sources have small gun crossovers and consequently are the brightest electron sources currently available.

FEG sources must be operated under ultra-high vacuum (UHV) conditions to ensure a stable emission current over time as contamination leads to a decrease in the emission current. It is common practice to flash the tip by heating it to high temperatures for a few seconds (~2 s) after prolonged use to decontaminate the surface. Flashing is not necessary for Schottky FEGs as they are constantly heated during operation. Although this ensures better emission

current stability, it comes at a cost of higher energy spread compared to a cold FEG [102].

3.2.1. Partial coherence

Electron sources are not monochromatic point sources and produce partially coherent electrons due to their finite size and energy spread. The finite size of the electron source results in electrons that are partially spatially uncorrelated. By approximating the intensity profile for the source as a Gaussian, the partial spatial coherence can be defined as in equation 3.3 [104]:

$$E_s(q) = e^{\{(-\pi^2 s_g{}^2 (C_1 \lambda q + C_3 \lambda^3 q^3)^2\}} \qquad 3.3$$

where s_g is the standard deviation of the Gaussian modelling the cone of illumination at the surface of the specimen, typically 0.1 mrad for a FEG [104] , C_1 and C_3 are the defocus and the spherical aberration coefficients, **q** is a general 2D reciprocal vector and λ is the wavelength of the incident electrons. Partial spatial coherence results in a point in the object plane being illuminated from a range of different angles leading to a damping of high spatial frequency information.

The emitted electrons are also partially temporally coherent due to their energy spread. The partial temporal coherence can similarly be defined by (equation 3.4), assuming a Gaussian energy distribution[105] :

$$E_t(q) = e^{-\frac{1}{2}(\pi \lambda \Delta)^2 q^4} \qquad 3.4$$

In equation 3.4, Δ, the focal spread of the source, can be expressed in terms of the dependence of the partial temporal coherence on instabilities in the accelerating voltage, objective lens current and the intrinsic energy spread of the electron source as:

$$\Delta = C_c \sqrt{\left(\frac{\delta V}{V}\right)^2 + 4\left(\frac{\delta I}{I}\right)^2 + \left(\frac{\delta E}{E}\right)^2} \qquad 3.5$$

where C_c is the chromatic aberration coefficient of the objective lens, typically a few mm in modern instruments. A cold FEG double-aberration corrected JEOL ARM 300 CF was used in this study. At 300 keV the value of C_c is 2.14 mm, $\frac{\delta I}{I}$ is $5x10^{-7}$, $\frac{\delta E}{E}$ is $4x10^{-7}$and $\frac{\delta V}{V}$ is $1.3x10^{-6}$. Substituting these values into equation 3.5 results in a focal spread of 36 Å. This value was subsequently used in image simulations and experimental EWR. The effect of temporal partial coherence produces an image formed by an incoherent superposition of images with slightly differing defoci, thus also blurring high spatial frequency information. Monochromation is a viable option for lowering the energy spread of partially coherent electrons[106]. However, although the energy spread would be improved by monochromation, it reduces the beam current at the specimen significantly[106]. In combination these two damping envelopes determine the information limit of a TEM which will be discussed further in the next section.

3.3. The Imaging system

A perfect optical system would transfer a point in the object plane to a spherical wavefront in the back focal plane which subsequently contracts into a point in the image plane (red ray path in Figure 3.3).

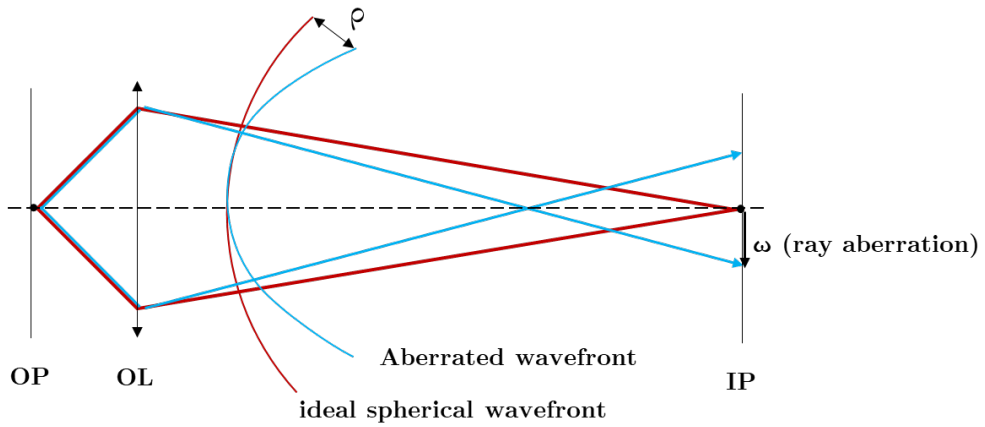

Figure 3.3: A ray diagram illustrating the phase shift (ρ) introduced by the objective lens (OL) aberrations on an ideal spherical wavefront in the back focal plane (BFP). The overall effect is that a point object in the object plane (OP) becomes a disk whose radius is equal to the ray aberration, (ω), in the image plane (IP).

However, due to objective lens imperfections, in the back focal plane, the actual electron wavefront (blue ray path) deviates from the ideal wavefront by a distance ρ(q), known as the wave aberration function. This deviation produces an aberrated image disk whose radius is equal to the ray aberration, ω, in the image plane.

A general treatment of ρ(q) would include its dependence on image plane position (*x,y*) and energy spread E of the electrons. However, the energy dependence is ignored in the *isochromatic* approximation due to the very small

energy spreads i.e., 0.3 eV for a cold FEG source. The positional dependence is also ignored at the very high magnifications typically used for HRTEM in the *isoplanatic* approximation [104].

The wave aberration function, $\rho(q)$, can be Taylor expanded to fourth order as shown in equation 3.6 [104] (also refer to Table 3.2).

$$\rho(q) = \Re\Big\{ A_0\lambda q^* + \frac{1}{2}A_1\lambda^2 q^2 + \frac{1}{2}\lambda^2 C_1 qq^* + \frac{1}{3}A_2\lambda^3 q^{*3} + \frac{1}{3}B_2\lambda^3 q^* q^2 + \frac{1}{4}A_3\lambda^4 q^{*4} + \frac{1}{4}S_3\lambda^4 q^{*3} q + \frac{1}{4}C_3\lambda^4 q^{*2} q^2 \ldots \Big\} \qquad 3.6$$

Table 3.2: Axial aberration coefficients up to the 3rd order in the Typke and Dierksen and Krivanek notations (Adapted by permission from Springer Nature: Springer Nature, by ref [104] © (2012).

Aberration Coefficient	**Typke & Dierksen**	**Krivanek**	**Order (q)**	**Azimuthal symmetry**
Image shift	A_0	$C_{0,1}$	1	1
2-fold Astigmatism	A_1	$C_{1,2}$	2	2
Defocus	C_1	$C_{1,0}$	2	∞
3-fold Astigmatism	A_2	$C_{2,3}$	3	3
Axial coma	B_2	$C_{2,1}$	3	1
4-fold Astigmatism	A_3	$C_{3,4}$	4	4
Star aberration	S_3	$C_{3,2}$	4	2
Spherical aberration	C_3	$C_{3,0}$	4	∞

For phase contrast imaging, the effect of the coherent aberrations is to increase the distance travelled by the electron wave, which is equivalent to a phase shift, $\chi(q)$, [104] given by equation 3.7:

$$\chi(q) = \frac{2\pi}{\lambda}\rho(q) \qquad 3.7$$

For a well-aligned uncorrected TEM $\chi(q)$ can be expressed as a function of the defocus C_1 and the C_3. In this case higher order aberrations remain negligible to a degree as the effect of C_1 and especially C_3 is much more significant. The combined phase shift due to C_1 and C_3 can then be expressed as a phase contrast transfer function (PCTF) (equation 3.8)[104]:

$$\mathrm{PCTF} = \sin(\chi(q)) = \sin\{\tfrac{1}{2}C_1\lambda^2 qq^* + \tfrac{1}{4}C_3\lambda^4 q^{*2}q^2\} \qquad 3.8$$

The C_3 coefficient of an uncorrected microscope is fixed but the defocus value can be adjusted by changing the strength of the objective lens or the specimen height. Scherzer derived an optimum defocus ($C_{1,Sc}$) setting which gives the widest flat passband in the PCTF[107]. A commonly used modified Scherzer defocus is given in equation 3.9 below:

$$C_{1,Sc} = -\tfrac{6}{5}\sqrt{C_3\,\lambda} \qquad 3.9$$

This equation results in a local minimum in the passband of the PCTF. The original definition of the Scherzer defocus does not have the -6/5 pre-factor, ($C_{1,Sc} = \sqrt{C_3\lambda}$), to avoid the local minimum in the passband of the PCTF but this results in a slightly poorer point resolution [105].

In Figure 3.4 the first zero intersection of this passband at spatial frequency $\mathbf{q_{max}} = 1.6(C_3\lambda^3)^{-1/4}$ can be used to define a real space point resolution $p = 0.625\sqrt[4]{C_3\lambda^3}$. HRTEM images of thin specimens acquired at Scherzer defocus will have features that are interpretable up to p[105]. Beyond p, the PCTF

oscillates rapidly up to the highest spatial frequency transferred from the specimen to the image- information limit. The contrast reversals prevent simple image interpretation of high-resolution spatial frequency information past *p*.

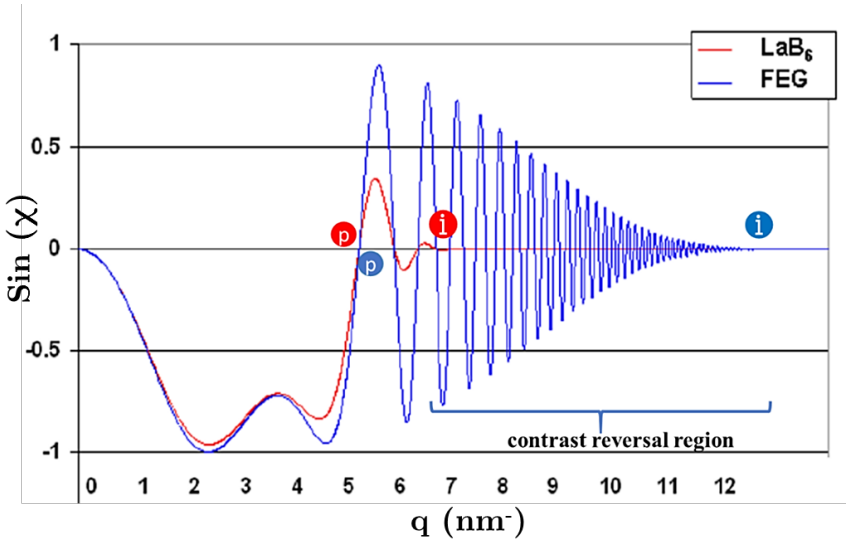

Figure 3.4: Calculated PCTF of a thermionic LaB_6 source (red) and a Schottky FEG source (blue) for 200 kV instruments which have 1 eV and 0.7 eV energy spreads, respectively. Both PCTFs were calculated with C_3= 0.5 mm and C_c= 1 mm. The point resolution (p) and the information limit(i) are also indicated for both highlighting the significant contrast reversals for a FEG source past the point resolution and its extended information limit (adapted by permission from ref [108] © (2012) John Wiley & Sons, Ltd.).

3.4. Aberration Correction

The advent of automation, powerful computers, better mechanical and electronic design of stable lenses has enabled the construction of improved TEM instruments [109]. In parallel there has been considerable research on the hardware correction of spherical aberration, a history of which is outlined in the following references [110,111].

There are two commonly used C_3-correctors, namely those based on extended hexapoles and those based on quadrupoles and octapoles[112,113]. However, only the former was used in the work described and will be discussed further. The hexapole corrector is coupled to the objective lens by round transfer doublet lenses. Transfer doublets ensure that the beam matches all the necessary coma-free nodal planes from the objective lens through to the corrector and from the first hexapole to the last [113] (Figure 3.5). For a rotationally symmetric, optical focal system nodal planes intersect the optic axis orthogonally on nodal points. In Gaussian optics, for a lens immersed in a medium with a uniform refractive index, a ray that intersects the front nodal point will be refracted by the lens into the back nodal point in a manner that retains the ray's angular relationship to the optic axis[114].

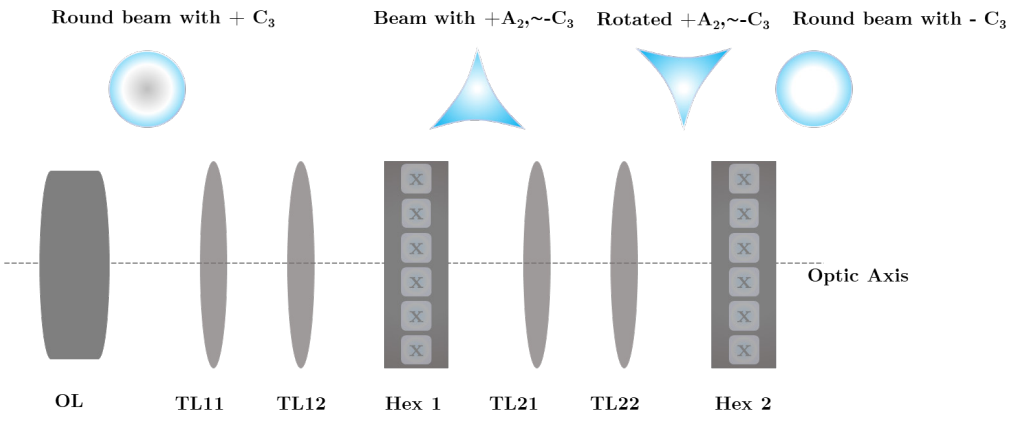

Figure 3.5: A schematic diagram of a hexapole-based aberration corrector with two hexapoles (Hex 1 & 2) linked to each other and to the objective lens (OL) through a pair of transfer doublets (TL*nm*) (adapted from ref [113] © (2011) John Wiley & Sons, Ltd., and ref [112] © (2005) IEEE.

The first hexapole produces a primary three-fold astigmatism (A_2), that is cancelled by the last hexapole [113]. However, the combined effect of the extended

hexapoles is to produce a negative C_3 that compensates for the inherent positive C_3 of the objective lens[112].

Accurate measurement of aberrations is necessary for their correction. They can be measured from tilt induced image shifts[115] or more commonly, from tilt induced changes in A_1 and/or C_1 (the Zemlin tableau approach) measured from power spectra calculated from images of a thin amorphous specimen region[116,117]. These two methods have practical limitations. For example, image shifts are often determined using a cross-correlation function (XCF) which fails to determine shifts when imaging clean crystalline specimens that are displaced by integer multiples of the specimen lattice vectors [105,106]. Furthermore, at high resolution, it is impossible to distinguish image shifts induced by specimen drift from those that are induced by tilting the beam [105,106]. Hence this approach is more commonly applied at low resolution for coarse alignments.

In the Zemlin tableau method, aberration coefficients are calculated for a set of known beam tilts, by least squares fitting of experimental A_1 and C_1 values[118]. Diffractogram measurement has the advantage of not being affected by specimen drift and has been shown to be more accurate[105,106]. Thus, it is commonly used for high resolution applications. However, it requires the presence of amorphous material in the specimen.

Once the aberrations are determined the multipole aberration corrector elements are automatically computer-adjusted to correct for the aberrations

iteratively until a target resolution is attained. In this study the aberrations were iteratively adjusted using tableaus acquired at a magnification of x1M and tilt azimuths ranging from 14 to 40 mrad. The maximum tolerable residual aberration value after correction can be set by limiting the maximum allowable phase shift induced by residual aberrations. During experiments, the phase shift induced by each residual aberration is iteratively minimised based on its contribution to a Fourier space phase plate, which is the sum of all the phase shifts induced by residual aberrations within a given radius. In this study, the phase plate of the corrector typically had a $\frac{\pi}{4}$ phase shift limit at a radius above 25 mrad[118] (Figure 3.6). This was selected as the limit because for a phase object a $\frac{\pi}{4}$ phase shift induced by symmetric aberrations results in a 50% transfer reduction[104]. Typically, the corresponding target resolution in this study was usually set below 1Å. This resolution is enough to resolve the projected distances of almost all anion and cation atomic columns in low order zone axes orientations of 0.5 wt% Pd-SnO_2 nanoparticles.

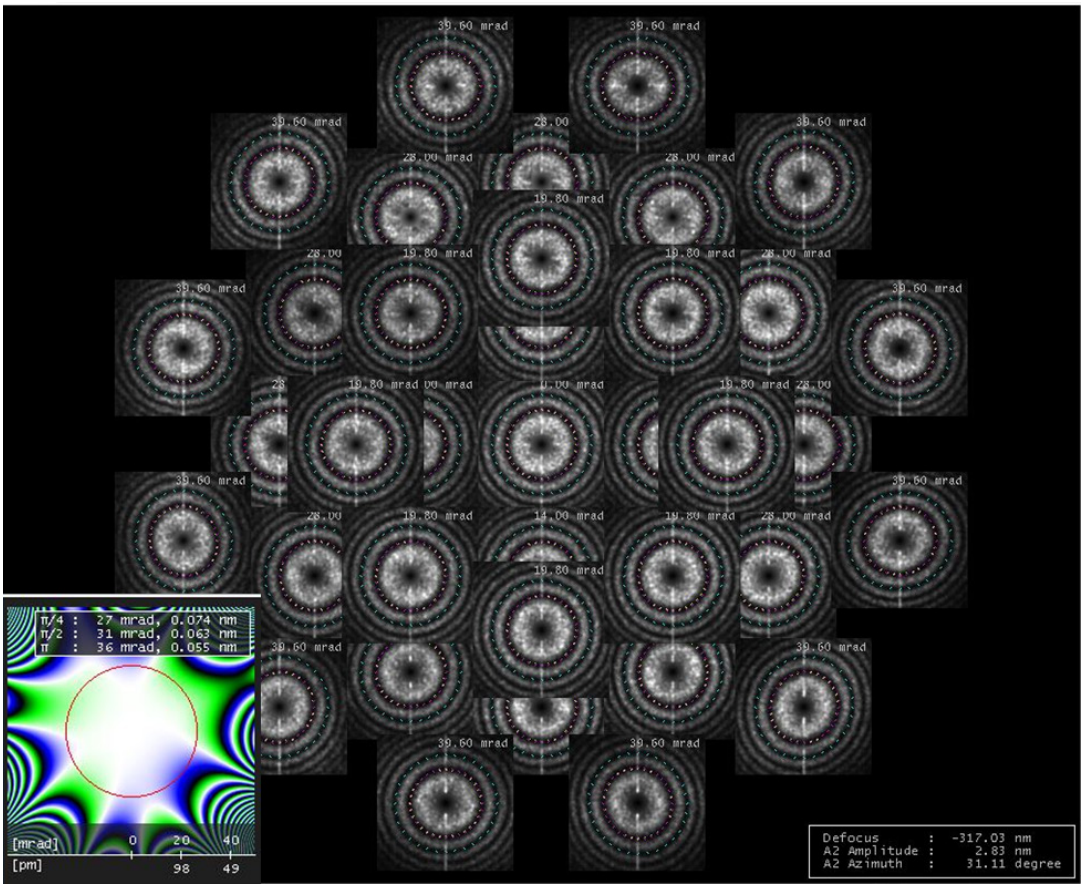

Figure 3.6: An experimental Zemlin tableau acquired using a JEOL aberration corrector with tilt azimuths ranging from 14-40 mrad with an inset of the numerical phase plate showing a $\frac{\pi}{4}$ phase shift limit at a radius of 27 mrad with a corresponding resolution of 0.7 Å.

3.5. Electron detection

Indirect detectors, as used in this study, convert incident primary electrons that impinge on a scintillator into photons which are relayed to the sensor chip via a coupling lens or fibre-optic. Several electron and photon scattering events occur in the scintillator material and the optical coupling such that a single electron detection event generates multiple photons which may be spread across several pixels from the point of impact, resulting in a detector point

spread function (PSF)[119,120]. This detector PSF and its Fourier transform, the modulation transfer function (MTF), damps high spatial frequency information. Two other parameters that determine the performance of a detector are the detective quantum efficiency (DQE) and the noise power spectrum (NPS). These will be discussed in a subsequent section.

Prior to the determination of the detector properties fixed-pattern noise from the fibre-optics coupling in the detector is corrected for by dark correction and gain normalisation[120] (equation 3.10). Dark correction is performed on raw images (I_r) of the knife edge (used for calculating the MTF) and a uniformly illuminated flatfield image (F) (used for calculating the NPS) by subtracting from them an equal number of dark noise images (D). Subsequently, the dark corrected (I_r-D) images are gain normalised by dividing them by the dark corrected flatfield image (F-D) and multiplying them by the mean pixel value of value of the dark corrected flatfield image (c). Typically, a series of an average of 8 or more of F and D images are used to perform this procedure in order to minimise random fluctuations in F [120].

$$I_{DG} = c(I_r - D)/(F-D) \qquad 3.10$$

3.5.1. MTF and NPS calculation

Several deterministic methods have been developed to characterise electron detectors [119]. However, the knife edge method is used in this study (as detailed

in Meyer and Kirkland, 2000) [121]. In this method an inclined straight shadow on the detector is used as a deterministic input that includes all spatial frequencies including those above the Nyquist limit [119] . An inclined pneumatic beam-stopper, with straight sharp edges, situated about 9 cm above the 4kx4k Gatan OneView detector was used to create the shadow on the detector in this study. Individual line profiles along the edge tend to be noisy. Hence, several line profiles were acquired along the edge and averaged to obtain an oversampled line profile to minimise noise effects. The averaged line profile was differentiated to generate a line spread function which is related to the MTF via a Fourier transform [119,120] (Figure 3.7).

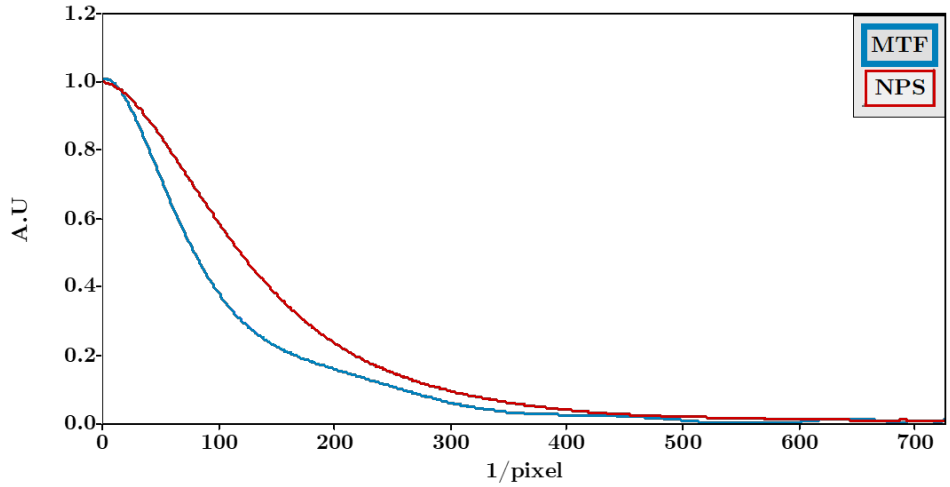

Figure 3.7: The normalised experimental MTF and NPS of a 4kx4k Gatan OneView detector acquired at 300 kV.

Noise transfer is also affected by the detection process. The transfer of noise across different spatial frequencies can be described as the output variance of a series of images, known as the NPS (Figure 3.7) [122]. It is determined from a

series of dark and gain corrected flat field images of a stochastic signal acquired at equal dose and uniform illumination.

The final detector property that is important in describing the detection process is the DQE, which is a measure of the noise added by the detector [123]. It is the square of the signal-to-noise ratio of the input and output signals $(SNR_o/SNR_i)^2$. Experimentally, it is calculated from other measurable detector properties as the quotient of the division of the square of the MTF by the dose normalised NPS.

3.5.2. Magnification calibration

Digital electron detectors are arrays of pixels that discontinuously sample the continuous electron image. Thus, it is essential to know the sampling of the detector at a given imaging magnification, as there is a potential for under- or oversampling the image features. Shannon (1949), among others, showed that for a continuous signal to be accurately discretely represented, it must be sampled at least at twice the frequency of the highest recorded spatial frequency [124].

The physical size of detector pixels is a fixed parameter and only the magnification can be varied. It is thus imperative to accurately know the magnification and its corresponding sampling rate. Magnification calibration in real space is usually performed using a calibration standard with known

periodic features. The sampling, s_i, at the given magnification can be determined by measuring a feature of known size and relating that to the number of pixels over the measured distance.

For example, latex spheres, typically used for low magnification calibrations, have a diameter of about 2.6x10^3 Å. At x200k magnification, for a 4k x 4k pixel detector, the average measured diameter, in pixels, is 3480 (Figure 3.8). Therefore, at x200k magnification the sampling is:

$$s_i = 2.6\text{x}10^3 \text{ Å} / 3480 \text{ pix} = 0.75 \text{ Å /pix}$$

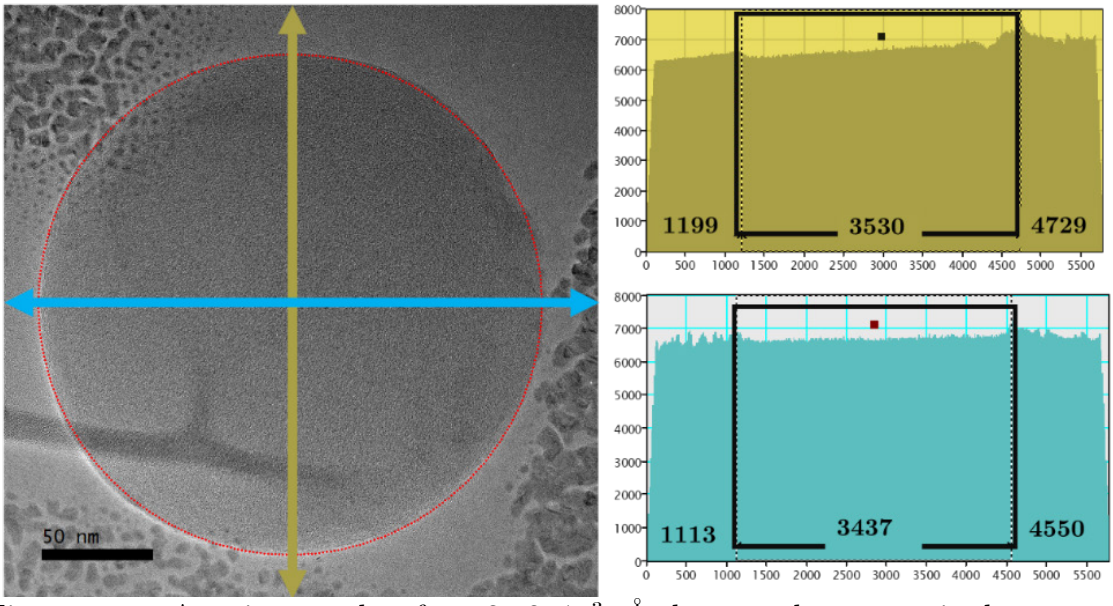

Figure 3.8: A micrograph of a 2.62x10^3 Å latex sphere acquired at a magnification of x200k measuring an average diameter of 3480 pixels as indicated by the corresponding line profiles (blue double arrow line = 3530 pixels and yellow double arrow line = 3437 pixels).

In reciprocal space, the sampling rate can be measured from specific reflections and related to their known real space distance. Equation 3.11 shows that the sampling rate at a specified magnification can be obtained given the total

number of pixels in one dimension (either x or y) of the detector, and the number of pixels in reciprocal space.

$$s_{\mathrm{i}} = (\mathrm{n}_{pix}\, \mathrm{l}_{rs}) / \mathrm{N}_{pix} \qquad 3.11$$

In the expression above, $\mathrm{n_{pix}}$, refers to the number of pixels over the measured reciprocal distance for a specific reflection, l_{rs} , refers to the reflection length in real space and $\mathrm{N_{pix}}$, refers to the number of pixels in one dimension of the detector. As an example, the power spectrum of an image of gold nanoparticles on amorphous germanium acquired at a magnification of x300k, at 300 keV, produces a ring pattern (Figure 3.9).

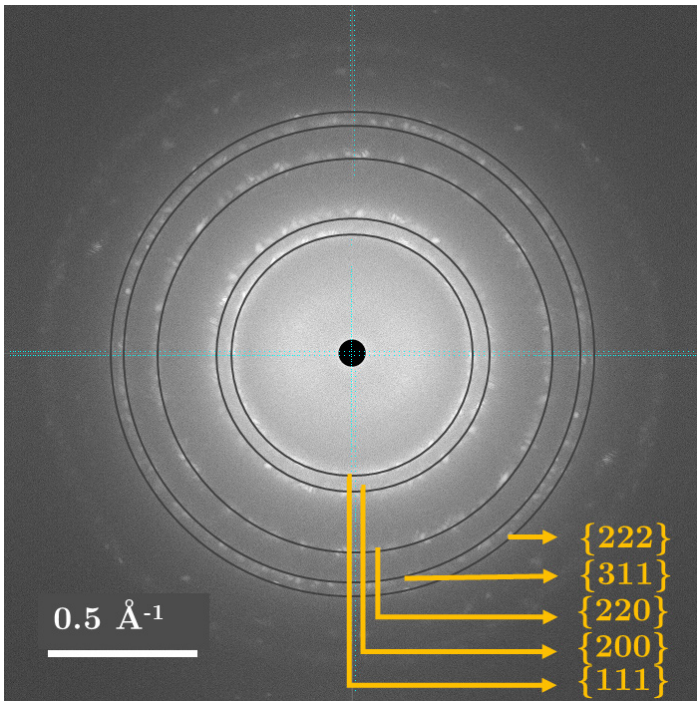

Figure 3.9: Power spectrum of gold nanoparticles acquired at 300 keV at a magnification of x300k showing reflections corresponding to the {111}, {200}, {220}, {311}, and {222} lattice spacings. In real space, these correspond to distances of 2.36 Å, 2.04 Å, 1.44 Å, 1.23 Å and 1.18 Å, respectively.

The {111} reflection corresponds to 2.36 Å in real space and has an average diameter of 1470 pixels on a 4096x4096 pixels imaging device. From equation 3.11 the sampling rate at this magnification is:

$$s_i = ((1470/2)\text{x}2.36\ \text{Å}))/4096 = 0.423\ \text{Å/pixel}$$

The product of the sampling rate with the number of pixels in one dimension of the imaging device gives its field of view (FOV) at the specified magnification. A plot of field of view as a function of magnification gives a magnification calibration curve (Figure 3.10).

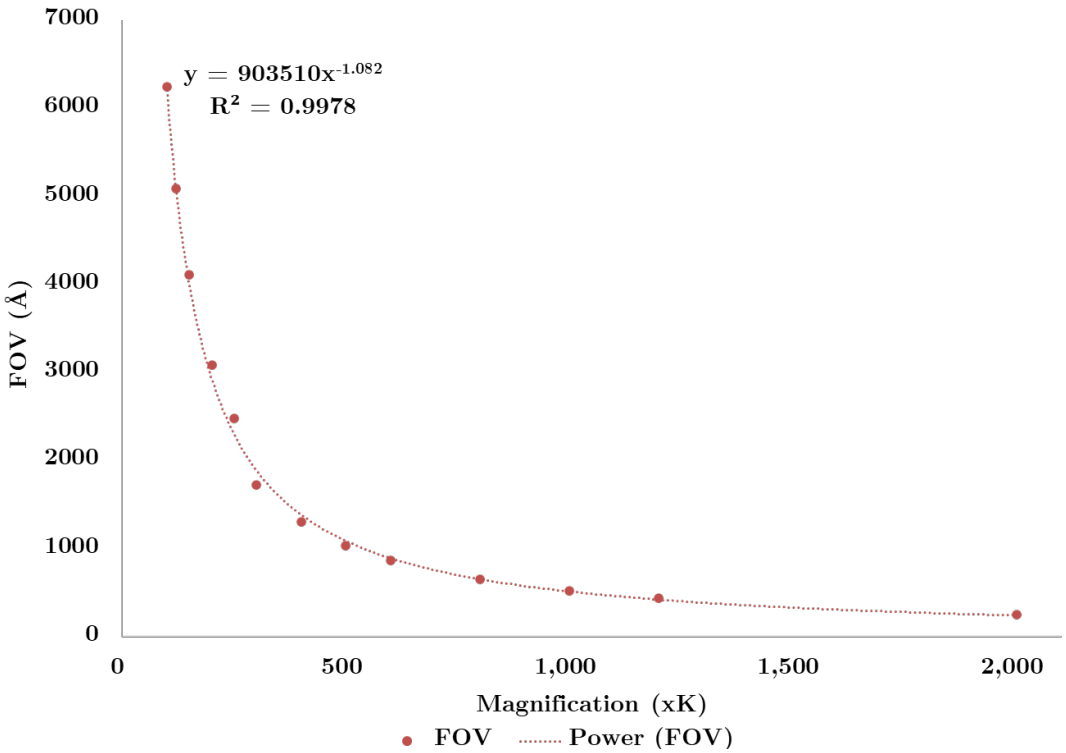

Figure 3.10: A magnification calibration curve for the JEOL ARM 300CF acquired at 300 keV.

Fitting a power law through the calibration data points gives an expression that can be used to extrapolate FOV and for other unmeasured magnification values.

3.5.3. Electron dose measurement

The electron beam can alter the pristine structure of specimens above a critical dose. To derive any quantitative local structural information from images of nanoparticulate specimens beam-induced alterations must be minimised. Thus, it is essential to measure and control the dose to maximise the observed signal while minimising any beam-induced alterations. To quantify the dose, the electron beam current must be accurately measured. Typically, this involves the measurement of an unobstructed beam on a fluorescent viewing screen or using a Faraday cup and the latter provides a more accurate measurement of the beam current.

Within the full well capacity of the detector the response in digital counts is proportional to the number of incident electrons [120]. Their ratio at a given acceleration voltage, exposure time, and beam current gives the gain of the detector in counts/electron:

$$G = c_p / \dot{\imath} t e \qquad 3.12$$

In equation 3.12, c_p is the mean pixel count, $\dot{\imath}$, is the current, t, is the exposure time and e is the elementary charge. At 300 keV the current was measured to be 4.71 nA on the picoammeter. To obtain c_p, a centred and round electron beam was spread to cover the detector screen up to its edges. The exposure time was fixed at 0.4 s and a 150 µm condenser lens aperture was inserted for all the experiments.

The gain under these imaging conditions is 36.3 counts/electron. Knowledge of c_p, G, and s_i ensures that the dose (D) can be calculated after image acquisition using equation 3.13:

$$D = c_p / G s_i^2 \qquad 3.13$$

The dose rate in $e/Å^2s$ is obtained by simply dividing the dose by the exposure time in s.

3.6. Specimen-electron interactions

In a TEM, the specimen will alter the phase and amplitude of the incident electron wave, $\psi_{inc}(r)$. The modulation in the incident plane electron wave can be described using an object function, $\varphi(r)$, such that the wave at the exit of the specimen, $\psi_{ex}(r)$ is equivalent to the object function (equation 3.14).

$$\psi_{ex}(r) = \varphi(r) \qquad 3.14$$

If only the phase of the incident wave is changed, then the *phase object approximation* (POA) is valid:

$$\psi_{ex}(r) = \varphi(r) = e^{-i\sigma\delta(r)} \qquad 3.15$$

In equation 3.15, δ is the projected crystal potential and σ is an interaction constant, $\frac{2\pi me\lambda}{h^2}$, where m, e and λ are the rest mass, charge and the relativistic wavelength of the incident electrons, respectively and h is Planck's constant.

Furthermore, if the specimen is sufficiently thin so that the phase modulation is small $i\sigma\delta(r) << 1$, then the exponential form of the exit wave can be further simplified as the first two terms of a Taylor expansion as shown in equation (equation 3.16)

$$\psi_{ex}(r) \sim 1 + i\sigma\delta(r) \qquad 3.16$$

This defines a *weak phase object* (WPO).

For specimens which are composed of high Z atoms and are relatively thick, dynamical scattering complicates image interpretation [125]. Thus, for thick specimens, a full dynamical treatment of the electron-specimen interaction is required. Several simulation methods that account for dynamical scattering have been developed and one of these will be described in the following section.

3.6.1. Multislice simulations

In this section a brief description of the multislice simulation method which accounts for dynamical scattering effects in thick specimens is given. For a detailed history and mathematical treatment of both the multislice method and its common alternative the Bloch wave method refer to Kirkland (2010) and references therein [125].

The multislice method, was proposed initially by Cowley and Moodie (1957) [126]. It was later expanded to be implemented numerically on a computer by Goodman and Moodie (1974)[127]. The first results were compared to

experimental images by Lynch and O'Keefe (1972) and the introduction of the fast Fourier Transform (FFT) in multislice simulations reduced computation time significantly [128,129].

In the multislice method the specimen is divided into slices of (δz) thickness which are thin enough for the WPO approximation to apply. Each slice is projected onto an infinitely thin plane and then the wave function is transmitted in real space (T(r)) through a thickness, δz and then Fresnel propagated (P(q)) over a distance of Δz - δz [125,130]. This process is repeated for each slice to the desired thickness. Therefore, the amplitude and phase of the exit wavefunction as it propagates through the specimen can be calculated at any thickness (Figure 3.11).

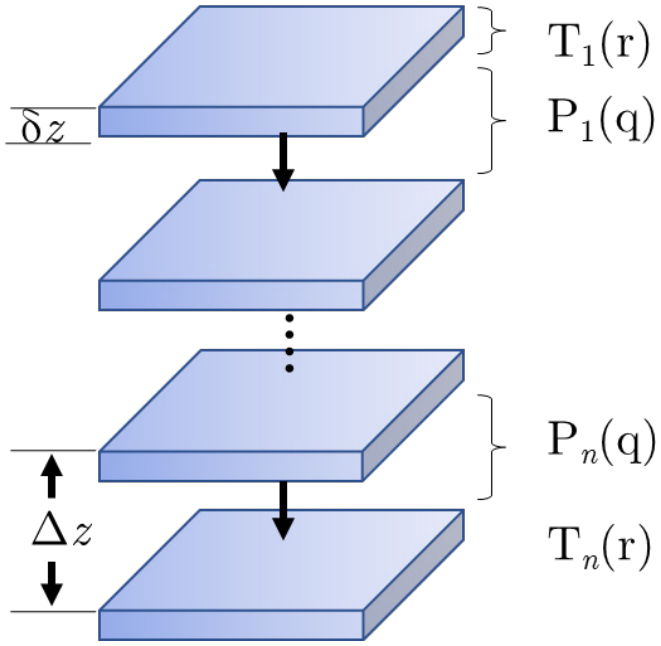

Figure 3.11: A simplified schematic diagram indicating the multislice simulation method (adapted by permission from Springer Nature: Springer US, by ref [131] © (2010).

The success of a multislice simulation depends on the correct specification of instrumental and sample parameters[102]. For simulating AC-HRTEM images the imaging aberrations, partial coherence effects as well as detector properties need to be measured as described in the previous sections with remaining unknown being the specimen structure and thickness.

Typically, a qualitative match between experimental and simulated images is sought by calculating a series of images at different defocus values and thicknesses. However, there remains a contrast reduction by a factor of 2-3 in experimental images compared to simulated ones known as the *Stobbs* factor[132]. The origins of this discrepancy remain an area of active research with no single factor fully accounting for it. Early work to account for the Stobbs factor demonstrated that the mismatch could be largely suppressed by reducing the contribution of inelastically scattered electrons through indirect energy filtering as in off-axis holography[133] or direct zero-loss filtering[134]. Later, Thust et al. (2009) [135], demonstrated that the Stobbs factor can be accounted for by including the correct detector MTF [135]. However, van Dyck (2015) later argued that the MTF alone could not account for the Stobbs factor, partly because image simulations conducted by Thust et al. (2009) did not accurately account for dose rate-dependent thermal motions of atoms[136]. Subsequently, they demonstrated that an accurate description of the dose rate dependent thermal

motion as well as the MTF accounted for a significant portion of the Stobbs factor.

3.7. Exit wave restoration

The phase information in an AC-HRTEM image is lost during the detection process. Hence, numerical post-acquisition restoration frameworks have been developed to retrieve it[137–140]. The objective of these post-acquisition numerical methods is to restore an estimate of the specimen exit wave function given an overdetermined set of differently aberrated images predominantly obtained by focus or in other instances illumination tilt variation [140–143].

There are both linear and non-linear EWR approaches to restore the exit wave of the specimen. Linear reconstruction methods are applicable when the linear imaging model applies. However, in thicker specimens, the imaging process cannot be described without accounting for nonlinear interference effects.

The advantage of non-linear approaches is that they are more generally applicable compared to their linear counterparts when imaging conditions deviate from the linear imaging approximation[104]. However, they are iterative and thus computationally more intensive. In this study, the linear Wiener filter is employed and will form the basis of the following discussion.

In TEM the recorded intensity, I(r), is the square modulus of the electron wave in the image plane, $|\psi_i(r)|^2$. The Fourier transform of the image wave and

specimen exit wave, $\psi_o(q)$, in the objective lens back focal plane, are related through the complex wave transfer function, $\acute{\omega}(q)$, (equation 3.17):

$$\psi_i(q) = \psi_o(q)\acute{\omega}(q) \qquad 3.17$$

where $\acute{\omega}(q) = MTF(q)E_s(q)E_t(q)e^{-i\chi(q)}$

This includes the MTF of the detector, the spatial (E_s) and temporal (E_t) coherence envelopes and the phase shift due to the wave aberration function ($\chi(q)$)[144]. If linear imaging is assumed, the Fourier transform of the intensity variation of the image (the image contrast c(q)), is the sum of the image wave function and its complex conjugate[138]:

$$c(q) = \psi_i(q) + \psi_i^*(-q) \qquad 3.18$$

Substituting equation 3.17 into equation 3.18 the image contrast can be expressed as a function of the object wave function and the wave transfer function (equation 3.19):

$$c(q) = \psi_o(q)\acute{\omega}(q) + \psi_o^*(-q)\acute{\omega}^*(-q) + n(q) \qquad 3.19$$

Where n(q) is the observed experimental noise.

Given a set of image contrast Fourier transforms, c(q), and their individual wave transfer functions, $\acute{\omega}(q)$, in the presence of experimental noise, an estimate of the specimen exit wave ψ'_o can be calculated using the Wiener filter[138,144–146]. The final restoration is the sum of the image transforms with their individual restoration filters, $\boldsymbol{\gamma}_i(q)$ applied as shown in equation 3.20 [145].

$$\psi'_o(q) = \sum_i \boldsymbol{\gamma}_i(q)c_i(q) \qquad 3.20$$

The restoring filter $\gamma_i(q)$ has the following simplified form (equation 3.21):

$$\gamma_i(q) = \frac{\acute{\omega}^*(q)}{|\acute{\omega}(q)|^2 + \frac{P_n}{P_s}} \qquad 3.21$$

Above, P_n/P_s corresponds to the noise-to-signal power ratio, where P_n and P_s are the Fourier transforms of the noise and signal, respectively. In the instance where $P_s >> P_n$, then $\gamma_i(q)$ tends to $1/\acute{\omega}(q)$ and the effect is that any signal component in the image transform is divided by its aberration function. On the contrary when $P_s << P_n$, then $\gamma_i(q)$ tends to zero, effectively suppressing the amplification of noise in the absence of the signal.

It can be advantageous to use more images as the effect of the noise and non-linear image contributions decreases as $\sqrt{n}$, where n is the number of images, assuming Poisson noise[147]. This is particularly relevant for specimens with a high electron dose tolerance although beam sensitive materials may undergo beam-induced alteration.

It must be noted that NCSI is an alternative single shot method routinely used to quantify the structural and chemical properties of oxides[72–74,148]. For a given aberration corrected instrument there is an optimal negative C_3 value that is balanced by an appropriate positive defocus. This imaging configuration results in bright atom contrast in a black background. NCSI imaging enhances the contrast of light atoms because, for a weak phase object, the linear and quadratic terms of the intensity map are summed unlike during conventional positive C_3 negative defocus phase contrast imaging, where they are subtracted

from each other[90]. Additionally, under NCSI conditions the information contained in the micrograph is interpretable up to the information limit of the instrument with minimal delocalisation effects[149], similar to EWR[105]. However, single shot images have the following disadvantages compared to EWR: single shot NCSI images are not free from non-linear imaging contributions, especially at high spatial frequencies, even under optimal imaging conditions, whereas the use of multiple images in EWR suppresses non-linear contributions significantly and enhances the SNR as stated above; the effective contrast transfer of EWR also enhances the transfer of low spatial frequency information compared to that of a single shot NCSI image; furthermore, the retrieval of the complex exit wave allows for numerical correction of residual aberrations *a posteriori* since not all aberrations remain constant in the course of an experimental session[149]. However, it could be argued that single shot imaging generally requires significantly lower doses to visualise light elements in oxides. Nonetheless, if the dose used for NCSI is sufficient to visualise light elements with high SNR. It is equally possible to fractionate that dose across a focal series to restore the exit wave eliminating the limitations of NCSI mentioned above[85]. This can be seen, for example, by comparing quantitative inline holography and NCSI studies on MgO crystals conducted by Chen et al. (2016)[85] and Jia et al. (2014)[148]. Jia used an approximate dose of 100 x 10^3 $e/Å^2$ to achieve single atom sensitivity on their single MgO crystal image, while Chen et al. (2016)

also used a comparable dose of 91 x 10^3 $e/Å^2$ fractionated over a 120 s long focal series to achieve the same sensitivity. Nonetheless, some studies have demonstrated the added benefit of using both techniques to quantify the physico-chemical properties of oxide materials[94,149].

In this thesis, focal series exit wave reconstruction was performed using the FTSR program and is based on the work of Meyer and Kirkland. Full details are given in references[138,144,146] and are not repeated here except to note that the method described employs a linear Wiener filter and makes use of a two-step approach to aberration determination[144]. In this, a phase compensated phase correlation function (PCF_p) is used to determine the registration vectors and relative defocus values between two images on either side of a reference image. An initial restoration of the wave using the above images is used to predict images which are subsequently used to determine the registration vectors and relative defocus values of the other experimental images using a phase correlation function (PCF)[144]. Secondly, assuming a fixed C_3, absolute C_1 and A_1 values for all images in the series are calculated using a phase contrast index function (PCI)[144]. A flow diagram illustrating the essential steps is shown in (Figure 3.12).

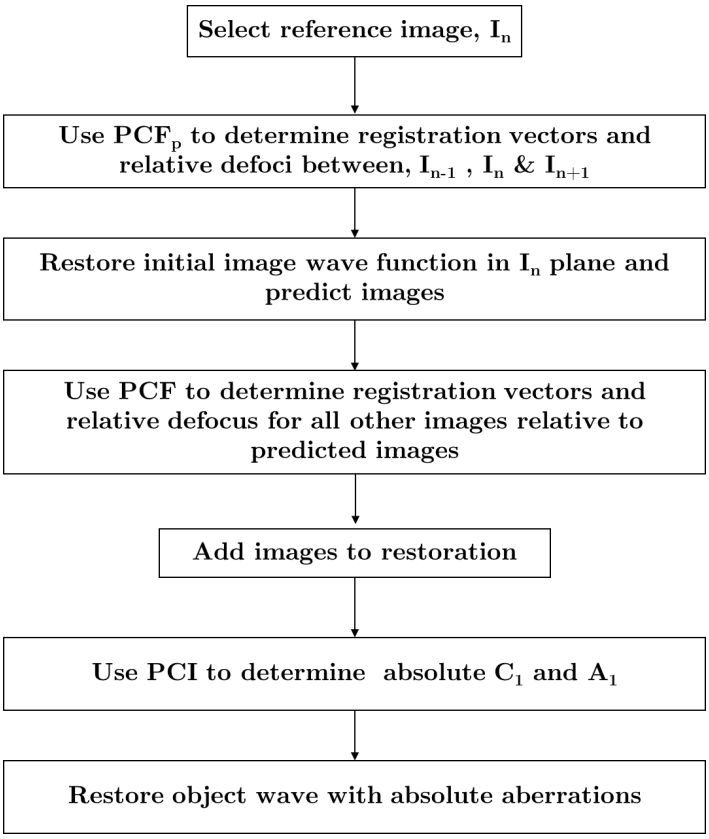

Figure 3.12: A flow diagram showing the essential steps of the focal series exit wave reconstruction method adopted in FTSR (adapted from ref[144] © (2002) with permission from Elsevier).

Note that the default reference plane during EWR is typically the central image of the focal series, from which the preliminary exit wave is calculated. In all cases post-restoration, the wave is restored with respect to this plane. For flat specimens, a single defocus reference plane is sufficient, and it can be numerically propagated to maximise the phase of the atom columns and determine the true exit plane of the specimen. For non-planar specimens, the propagation is typically done to maximise the phase of specific regions. In this study the surface of the nanoparticle was the region of interest and hence the reference plane was propagated until it maximised the phase of surface atoms.

During fully quantitative analysis, such as in 3D inline holography, this propagation is performed for individual atom columns to determine the true exit wave plane of each atom column, enabling the determination of the surface roughness of the nanoparticle [85].

4. Surface chemistry of nominally Pd-doped SnO_2 nanoparticles

4.1. Introduction

As discussed in Chapter 2, to date there is no direct evidence of the surface structure of sub-10 nm SnO_2 nanocatalysts at the atomic scale. This chapter aims to use AC-TEM imaging in conjunction with exit wave restoration (EWR), to characterise the surface atomic structure of 0.5 wt% Pd-SnO_2 nanoparticles. This technique allows imaging of light and heavy elements simultaneously at atomic resolution at the exposed active facets. However, the detectability of the light O atom columns at these surfaces is generally poor and can be corrupted by noise, especially at the low electron doses required to prevent structural damage.

To aid the analysis of the experimental data, a comparison with multislice simulations from a nanoparticle model is made. The calculations include

accurately measured instrument parameters, including the correct signal and noise transfer functions of the detector. Typically, TEM image simulations account only for the signal transfer of the detector via the Modulation Transfer Function (MTF)[148,150–152] because this is said to reduce the contrast mismatch (i.e., the Stobbs factor) between experimental and simulated data [135]. However, Kirkland and Meyer (1998, 2000) demonstrated that the detector noise has a different transfer function from the signal, i.e., the Noise Power Spectrum (NPS) [119,153]. Thus, not only the MTF, but both the MTF and the NPS attenuate information transfer and contribute to the contrast mismatch between experiments and simulations and they must both be included in the simulations. Inclusion of the correct NPS in the calculations is especially important at low dose, as shown for simulations of biological specimens[154,155].

In this study, the simulations serve several purposes. Firstly, they are retrospectively used to determine if the cumulative dose used to acquire the experimental focal series data was sufficient to obtain single O atom sensitivity at the surface. Secondly, the simulations also indicated the minimum cumulative dose in a focal series that is required to visualise single O atoms for all the nanoparticle surfaces observed experimentally. This calculation also provides dose guidelines for EWR experiments, whereby the nanoparticles will not be unintentionally exposed to larger than necessary electron irradiation, while attaining the required O sensitivity. The control of the electron dose in

nanoparticles is in fact essential to prevent and minimise beam-induced transformations that readily occur at the surface where atoms are undercoordinated and have lower binding energies compared to the bulk[156].

Chapter 4 is divided into two main sections: theoretical and experimental methods (4.2) and results (4.3). The first describes the details and methods used for the simulations, the details of the experimental data, and the quantification methods developed to compute the signal-to-noise-fluctuation ratio (SNFR) of the O atoms at the exposed facets as a function of dose and occupancy. In section 4.3 an analysis of the surface terminations exposed at the nanoparticles facets is made by comparison with simulations under the same imaging conditions.

4.2. Theoretical and experimental methods

4.2.1. Sample preparation and imaging

A dry powder of 0.5 wt% nominally Pd-doped SnO_2 nanoparticles was sonicated for 10 minutes in methanol[1]. The supernatant was drop cast using a

[1] A few data on smaller (≈ 2.5 nm) pure SnO_2 nanoparticles were acquired using CFS. However, these data could not be included in the main text for two reasons: (i) loss of contact with collaborator who provided the specimen when the sample ran out meant that the analysis could not be conducted in full; (ii) additionally, the nanoparticles were significantly smaller than those used in this study and thus direct comparison would be hindered by their inherent higher beam sensitivity due to their undercoordination [26,156] (see Figure C.1 and subsequent discussion in Appendix C). This means that the SnO_2 nanoparticles would exhibit more complicated surface chemistry and dynamics.

pipette onto copper grids coated with a holey amorphous carbon film. The grids were then dried in a desiccator for no less than 24 hrs. Subsequently they were plasma-cleaned in a 1:9 O/Ar plasma with a power of 18.83 W for 10 seconds prior to imaging to remove any residual solvent and adsorbed organic matter from the nanoparticle surface as well as prevent any specimen contamination during imaging. The employed plasma power and duration are significantly lower than what is necessary to alter the surface chemistry of ≈ 10 nm nanoparticles. Stuckert et al. (2015), demonstrated using XPS that 4 min O/Ar plasma treatments with plasma powers that range from 10-60 W do not affect the surface composition of SnO_2 nanoparticles relative to their pristine counterparts [157]. Surface reduction occurred at plasma powers greater than 100 W.

4.2.2. Morphological and crystallographic properties

The particles' crystallography and morphology were examined using conventional TEM imaging. The shape of the nanoparticles was found to approximate an ellipse, where the minor and major axes were taken as the width and length of the nanoparticles[86]. The average length (orange) and width (green) of the nanoparticles, along with their standard deviations in parenthesis, was then determined to be 55 (21) Å and 40 (17) Å, respectively, as shown on the particle size histogram (Figure 4.1). Both length and width of

the 141 nanoparticles were measured manually as shown in Figure 4.2 (e). The average aspect ratio of the nanoparticles was found to be 1.41 (0.26).

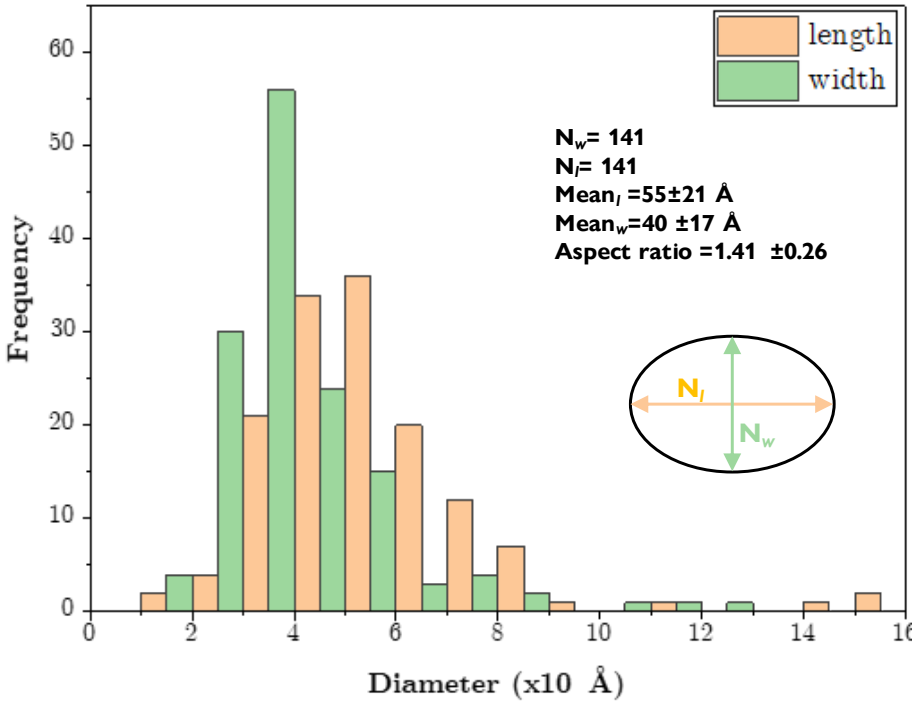

Figure 4.1: Histogram of the length (orange) and width (green) of the 0.5 wt% Pd-SnO_2 nanoparticles. $N_{l/w}$, $Mean_{l/w}$ represent the number of measurements for the length and width, respectively and the measured average length and width of the nanoparticles, respectively.

The orientation and faceting of the nanoparticles were determined primarily by comparing power spectra calculated from images with simulated single crystal diffraction patterns, using the CrystalMaker® program. In Figure 4.2 representative nanoparticle orientations are shown along various low index zone axes, including the [100], [001], [110], [101] and [111] (Figure 4.2 (a-e)). The main crystallographic facets are highlighted with black lines in Figure 4.2 (a-e) and summarised in Table 4.1. These facets have low surface energies according to DFT calculations (see section 4.2.3).

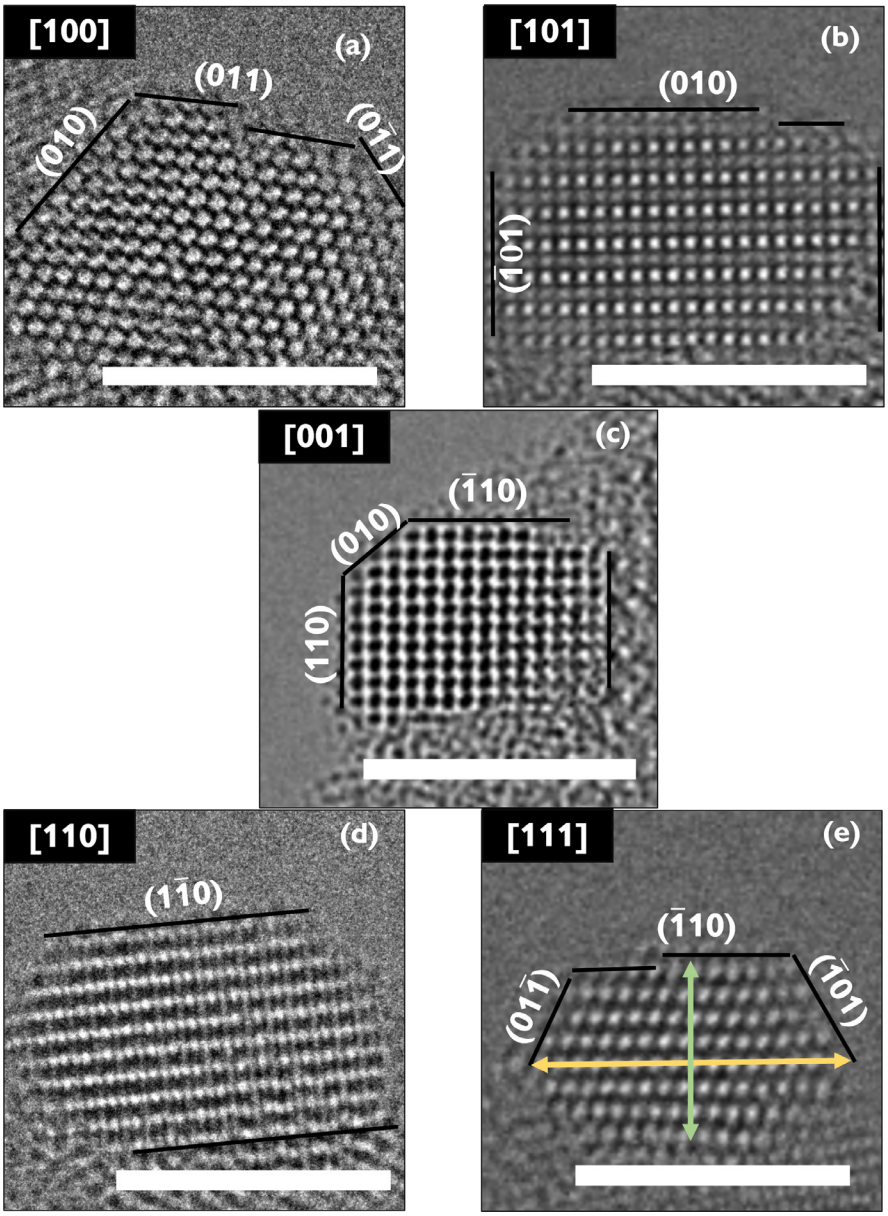

Figure 4.2: Representative 0.5 wt% Pd-SnO_2 nanoparticles samples, oriented along the (a) [100], (b) [001], (c) [110], (d) [101] and (e) [111] projection. In (e), representative measurements for the length (orange) and width (green) are also shown. The scale bar is 50 Å in all cases.

Table 4.1: Experimentally observed crystallographic facets of a 0.5 wt% Pd-SnO_2 nanoparticle sample.

Zone axis	**Facets**
[100]	{100}, {011}
[001]	{110}, {100}
[110]	$\{1\bar{1}0\}$
[101]	{101}, {100}
[111]	$\{\bar{1}10\}$, {011}

The {001} facets are not observed in this study. This is in agreement with theoretical findings which demonstrate that the (001) surface has the highest surface energy making it unlikely to be observed experimentally. Only the {100}, {110} and {101} facets are observed in the experimental data.

4.2.3. Model construction

A representative 3D model of a typical SnO_2 nanoparticle was generated using the average size and morphology determined experimentally in section 4.2.2.

The Visualization for Electronic and Structural Analysis (VESTA ®) program was used to obtain the Wulff construction[158]. The latter is based on the principle that a crystalline object takes the shape which minimises its total surface energy. This equilibrium shape will predominantly expose low energy facets.

In this work, the distance, $d_{hkl,}$ normal to the (*hkl*) facet from the origin is taken as $d_{hkl} = c\gamma_{hkl}$, where γ_{hkl} is the surface energy of the facet (*hkl*)[53]. The theoretically predicted surface energies by Beltran (2008) were used for the

Wulff construction [53,159]. Here, c is a constant, set to be equal to 30 Å, which is half the average length of the experimental nanoparticles.

However, it is noted, as discussed in section 2.2, that to build the model the exact values of the facet surface energies, γ_{hkl}, are not as important as their relative ratios[53]. Thus, despite the differences between theoretical surface energy values that were found in the literature, identical Wulff constructions can be obtained if the relative surface energies are similar [32,50,159].

Examples of the atomic model obtained are shown in projection alongside the experimental data in Figure 4.3. The calculated 3D shape is also consistent with the equilibrium shape of rutile SnO_2 previously observed experimentally and predicted in the literature [160,161].

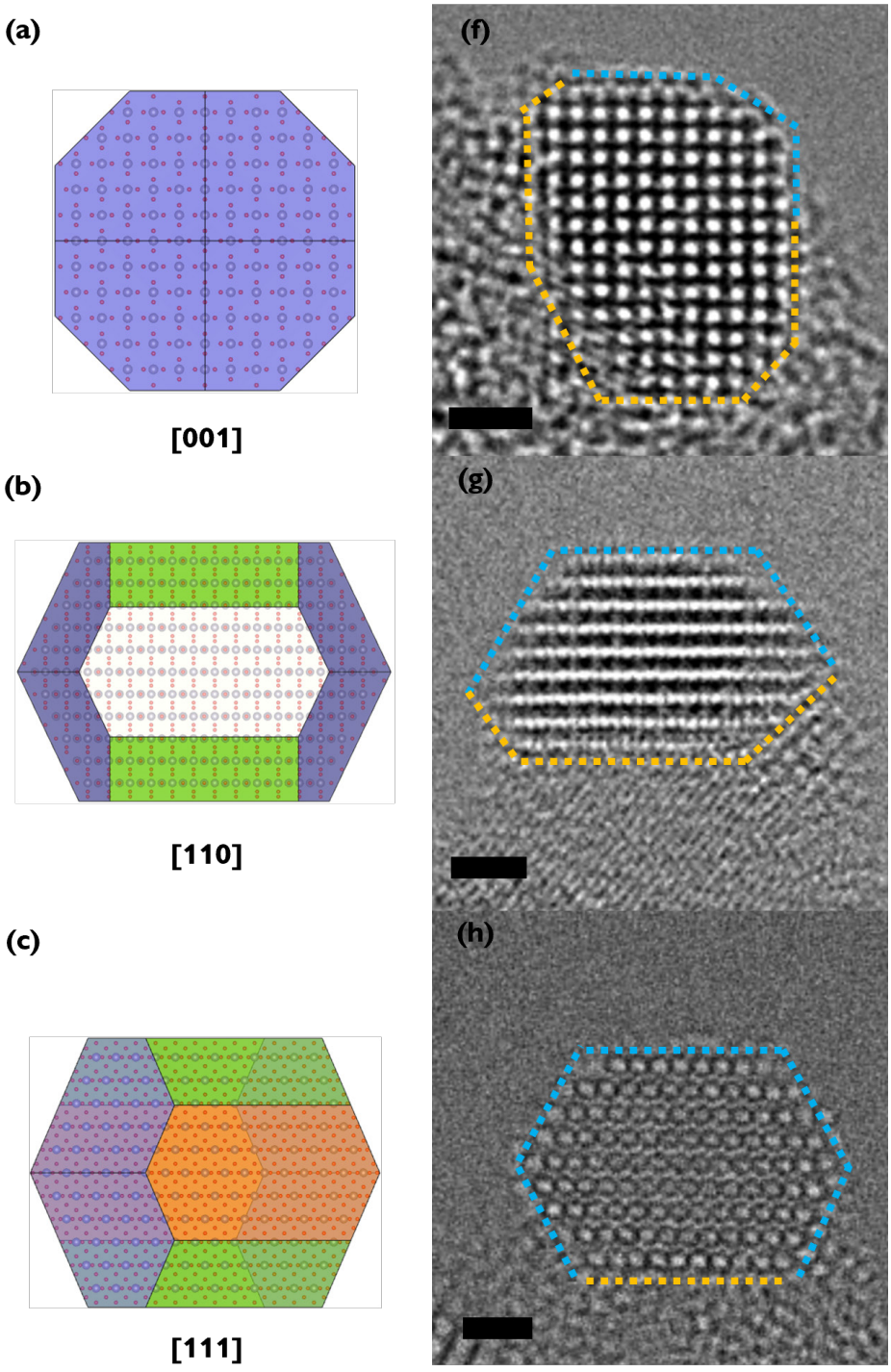

Figure 4.3: *see continuation of image below for full caption.*

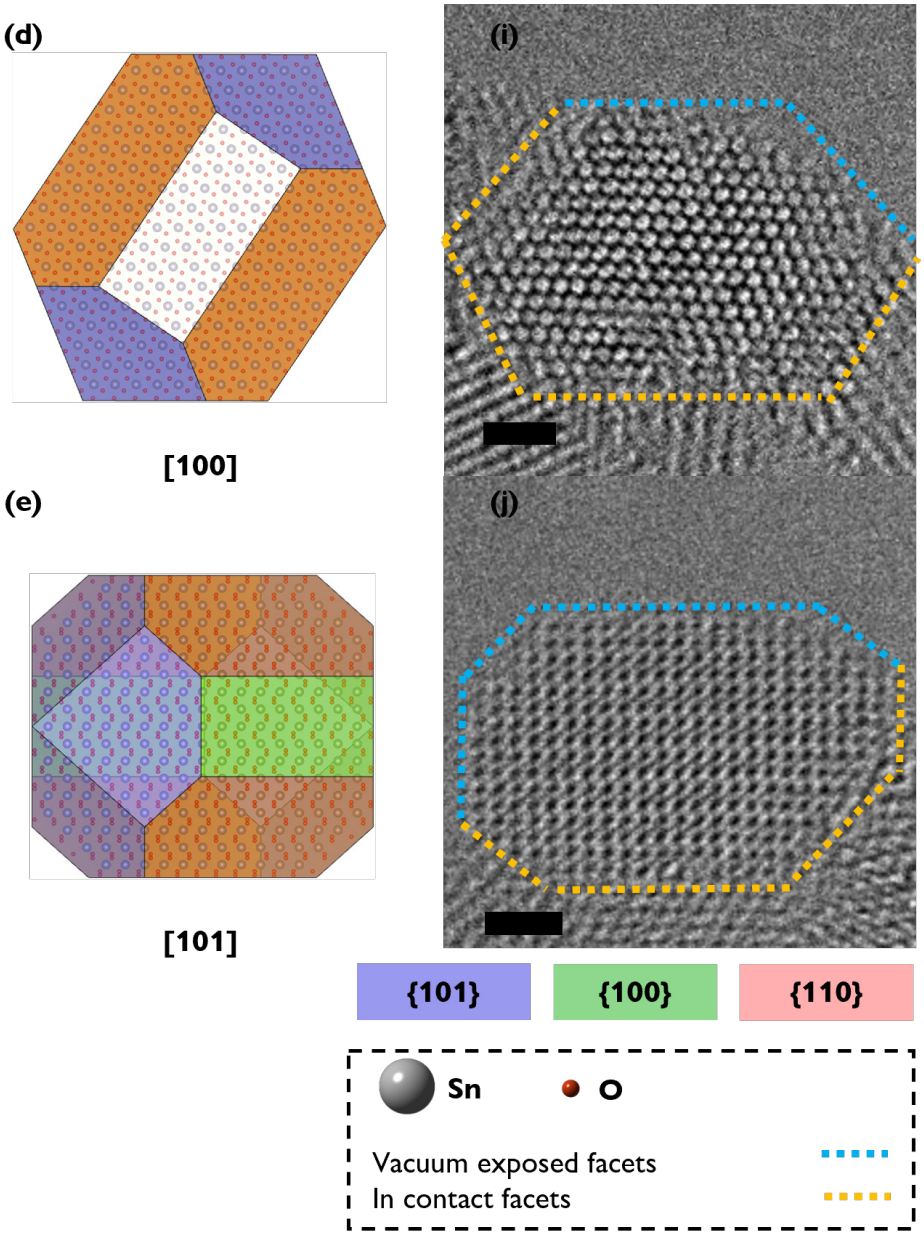

Figure 4.3: (a-e) Projected Wulff models, oriented along several zone axes and corresponding experimental images oriented along the same directions. Facets (f-j) overhanging vacuum are indicated with dashed blue lines, while those in contact with other nanoparticles or the amorphous carbon are indicated with dashed yellow lines. The scale bars correspond to 10 Å in all cases.

The aspect ratio of the model was obtained in a similar manner to that of the experimental nanoparticles. However, not all measured experimental nanoparticles were oriented along a low order zone axis. Thus, to improve the comparability, the aspect ratio of the model nanoparticle was also measured

for off-axis orientations. The off-axis orientations were obtained by rotating the particle from 0° to 180° in the cartesian plane in steps of 30°, first in the x direction, and then in the y direction, for all the experimentally observed projections. The aspect ratio of the model nanoparticle was then measured after every rotation. The average aspect ratio was 1.26(0.16), where the standard deviation is in parenthesis. This value is comparable to the experimentally determined aspect ratio of 1.41(0.26), suggesting that the model accurately represents the experimental ensemble of nanoparticles.

More importantly, a visual comparison between the morphology of the Wulff facets and vacuum exposed facets in Figure 4.3 shows that the model generally matches the experimental morphology. However, regions of the nanoparticles that are in contact with other nanoparticles or sitting on the amorphous carbon substrate (indicated with dashed yellow lines) show a poorer morphological match to the equilibrium model compared to regions of the particles whose facets are exposed in vacuum (shown with blue dashed lines). Hence this study is focused on vacuum exposed facets.

It must be noted that Wulff construction does not account for modifications to the equilibrium shape due to multiparticle interactions or nanoparticle-substrate interactions, all effects that have been shown to influence the relative stability of the facets [54,55]. Modified Wulff construction approaches by Winterbottom (1967) [54] and Marks (1983)[55] are better suited in these cases but

the application of these is beyond the scope of this thesis. A topical review by Marks and Peng (2016) should be consulted for further information[162] on this topic.

The stoichiometric Wulff model of SnO_2 contains 1305 SnO_2 molecules, of which a nominal doping concentration of 0.5 wt% Pd implies that there would be about 7 Pd atoms on the nanoparticle. At low doping concentrations (<1 wt%), Pd atoms are evenly distributed on the surface, and they substitute for surface Sn atoms [26]. This means that 7 of the 16 facets of the nanoparticle will have a single Pd atom.

Finite dose focal series, composed of 30 images, at a dose of 4567 $e/Å^2$ per frame, for pure Sn and doped columns were calculated using MULTEM to assess the detectability of single dopant atoms in Sn atomic columns (see subsequent section for more details on method). The focal series data were calculated using parameters employed in the experiments for the [001] projected nanoparticle (see Table 4.4). In all instances of comparison, the dopant atoms substituted the topmost Sn atom and the projected *z*-distance, column exit plane were identical as shown in step 1 of Figure 4.4. Subsequently, the phase of the restored exit wave (step 2) was quantified using the Atomap programme to locate atoms and refine their positions through a two-step process: (i) the atoms are initially located using centre of mass and their positions are then refined using 2D elliptical Gaussian fitting as shown in

step 3 of Figure 4.4. Afterwards, the integrated phase of the atom columns was determined by integrating over circular Voronoi cells with a diameter of 14 pixels (step 4 in Figure 4.4). The diameter corresponded with the brightest central pixels of the phase for a given atom column. Finally, the integrated phase was divided by the total number of pixels in the integrated area, in this study, 156 pixels, to obtain the mean phase shift per pixel. These values for each dopant are summarised in Table 4.2.

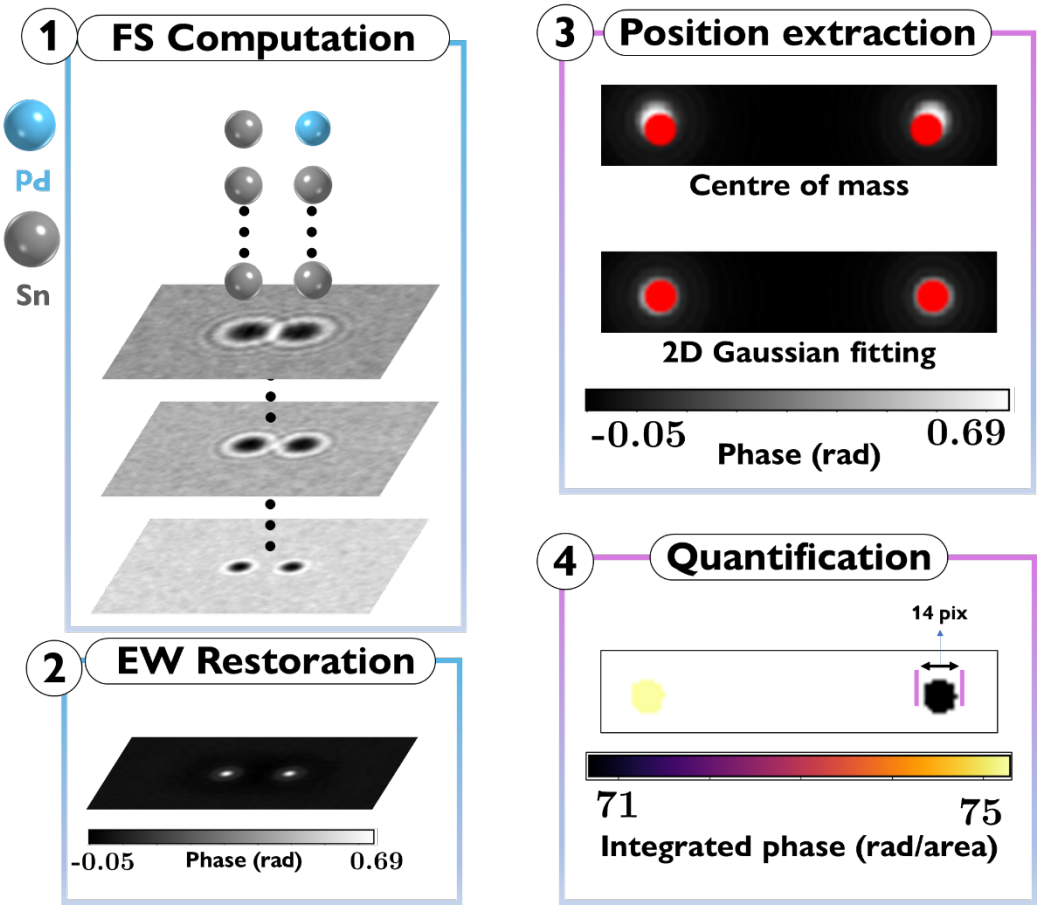

Figure 4.4: A restored phase quantification workflow employed in this study, showing: (1) focal series computation, (2) a restored wave phase, (3) atom position extraction and (4) phase quantification. The grey and blue atoms correspond to Pd and Sn atoms.

Table 4.2: Summary of the mean phase shifts per pixel (in rad/pixel) for pristine and doped Sn atom columns of equal occupancy (8 atoms) oriented in the [001] direction.

Atom	**Pure**	**Doped**	**Phase Difference**
Pd	0.4533	0.4490	0.0043
Ag	0.4560	0.4518	0.0042
Cd	0.4553	0.4512	0.0041
In	0.4600	0.4561	0.0038

Table 4.2 shows that the average phase difference induced by the substitution of a Pd, Ag, Cd and In atom relative to another Sn atom is 0.0043 rad/pixel, 0.0042 rad/pixel, 0.0041 rad/pixel and, 0.0038 rad/pixel, respectively. Such a phase difference can be detected if and only if the standard deviation of the noise (see Figure 4.4) of the restored phase is at least 3 to 5 times smaller than the mean phase difference, based on the Rose Criterion (discussed in section 4.3.2). The standard deviation of the noise in the restored phase at this dose is 0.0033 rad/pix. Hence, based on this criterion, none of the dopant atoms can be detected with great confidence since the phase difference they induce is almost equal to the standard deviation of the noise. Furthermore, it must be noted that the phase shift difference due to the presence of a single Pd atom will also be sensitive to the occupancy of the atom column it is in, its z position with respect to the reference exit plane wave and the spacing between each successive atom in z, as well as the nearest neighbour atoms[163,164,165] (see section

4.3.2 on O detection). Additionally, the error in the phase induced by local residual and parasitic aberrations, specimen mistilt and fluxionality of surface atoms may contribute to introducing a phase difference which could be mistakenly attributed to the presence of dopants in Sn atom columns[85]. Thus, this study is limited to interpreting the Sn/Pd and O atom column phase shifts at the terminating facets, obtained through focal series EWR, rather than determining the exact lattice positions of the Pd atoms on the facets, given the very low nominal doping concentration. Hence, the as-constructed SnO_2 Wulff shape was used as the input model for the multislice simulations in the next section.

4.2.4. Finite electron dose focal series simulations

The multislice method implemented in the MULTEM image simulation software was used to simulate focal series data [126,127,166]. Each noiseless image $I_o(r)$ of the focal series was calculated as the square modulus of the image wave, which is related to the specimen exit wave function through a convolution with the complex wave transfer function in real space (see section 3.7). The latter includes the objective lens aberrations and the partial coherence envelopes. The envelopes were fixed across the simulations (see section 3.2). The C_3 value in the simulations was matched to that measured during hardware aberration correction and the defocus was varied at steps of up to 20 Å as in the experiments. All other aberrations of the objective lens were taken equal to

zero as it is assumed that following hardware aberration-correction the effect of residual aberrations is negligible compared to that of the C_3 and defocus.

As stated previously, the MTF and NPS of the detector were included in the simulations. These determine the transfer of the signal and the noise, respectively. The detector introduces noise due to the stochastic nature of the electron detection (shot noise), in addition to the inherent electronics noise during analogue-to-digital conversion (readout noise) and the noise dependent on the exposure time and temperature (dark current noise) [120]. At the relatively low acquisition times used in this study both readout noise and dark current noise are a few *e*/pix, which is typical for a modern Peltier cooled CMOS detector such as the OneView camera used here. Hence, for the dose regime of interest in this work, only shot noise was included in the simulations as this would be the dominant source of noise.

The conversion of the continuous image plane intensity distribution into a discrete digital image can be described by equation 4.1 [154].

$$I(r) = G\{\mathcal{F}^{-}[\mathcal{F}\ [I_o(r)].MTF(q)] \times \mathcal{F}\ [I_n(r)].NPS(q)]\} \qquad 4.1$$

Here, G is the detector gain (defined in section 3.5.3) and $\mathcal{F}\ [\bullet]$ and $\mathcal{F}^{-}[\bullet]$ refer to forward and inverse Fourier transform operations. $I_n(r)$ is a Poisson distributed noise image, with a mean equal to the expected number of *e*/pix. The first step in 4.1 is to multiply the Fourier transform of the noise free image, $I_o(r)$, in Figure 4.5 (a) by the MTF(q) (see Chapter 3, Figure 3.8). This results

in an image (Figure 4.5 (b)) where information transfer is suppressed for spatial frequencies above q=0.3 $Å^{-1}$ (see the power spectrum in Figure 4.5 (d)). Comparing the signal in the power spectra of the noiseless image and the image damped by the MTF, at low spatial frequencies (q≃0 $Å^{-1}$), where the MTF≃1, the information transfer is identical (Figure 4.6). However, at q=0.38 $Å^{-1}$, corresponding to the (101) reflection, the information transfer is decreased by 10% and rapidly reaches almost total suppression at q=1.9 $Å^{-1}$ for the (505) reflection. As a result, after convolution by the MTF, information transfer is observed up to the (404) Fourier reflection which corresponds to a real space distance of 66.1 pm (marked with an orange circle in Figure 4.5 c and d), below the information limit of the microscope (blue circle in Figure 4.5 (c)).

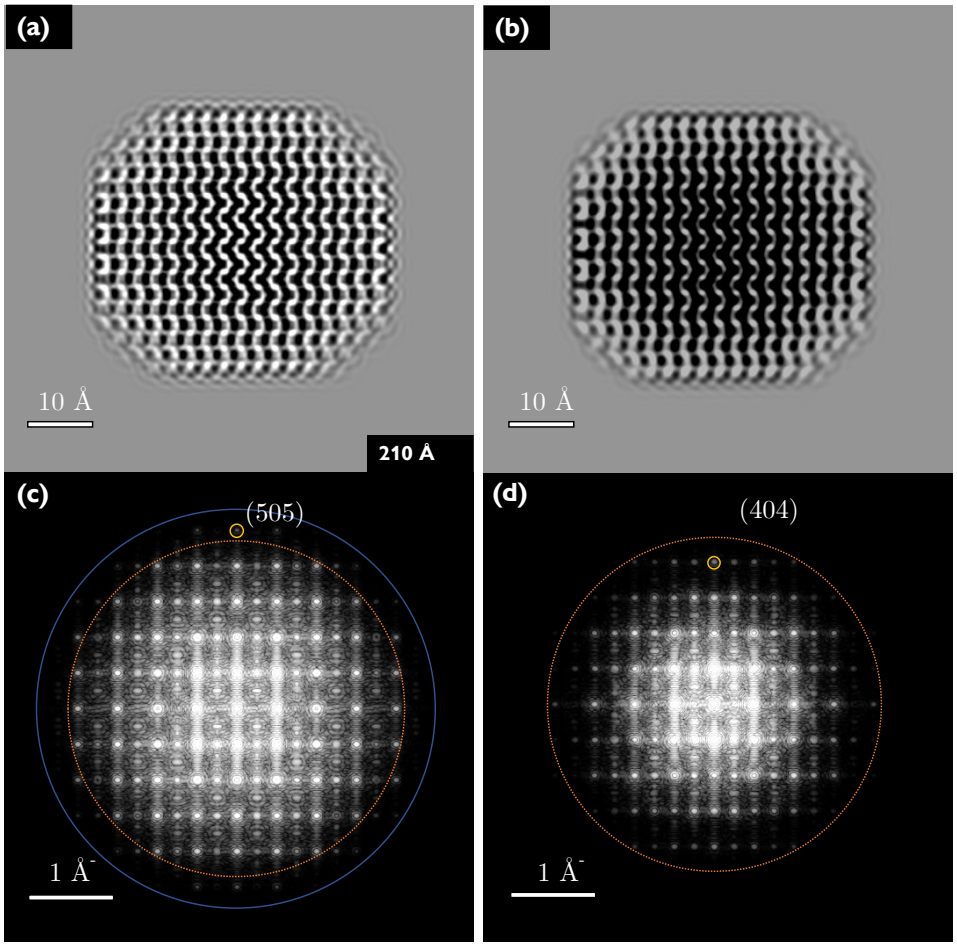

Figure 4.5: Simulated noiseless images before (a) and after (b) MTF convolution for a [101] SnO_2 model nanoparticle, and respective power spectra (c) and (d). In (c) the highest spatial frequency transferred goes up to the (505) Fourier reflection which is close to the information limit of the microscope (blue circle), as opposed to the case where signal is damped by the MTF beyond the (404) Fourier reflection (see (d)).

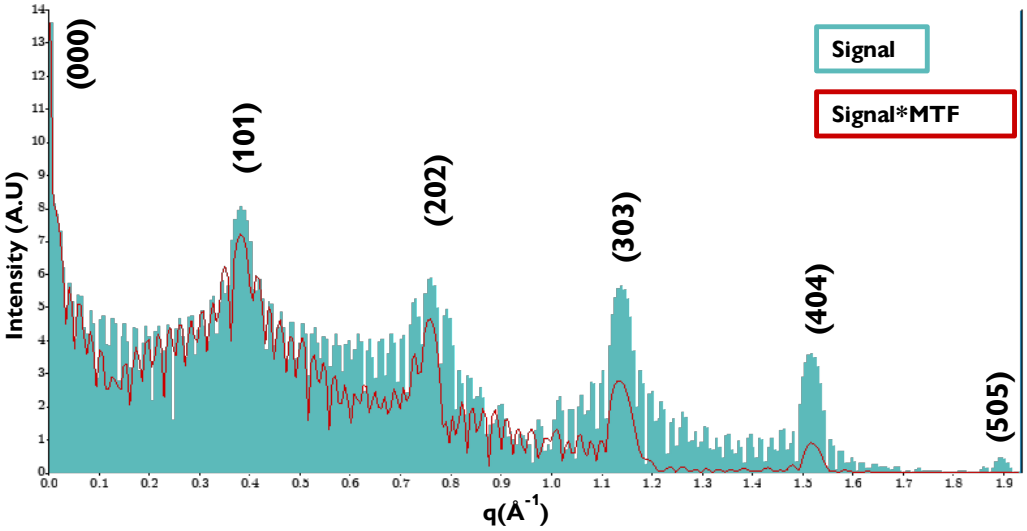

Figure 4.6: Intensity profiles obtained from simulated power spectra before and after MTF convolution, showing the decay of the signal intensity from the (000) to the (505) reflections.

The second step of the simulation in equation 4.1 includes the multiplication of the Fourier spectrum of the noise image by the NPS(q). Here, pure Poisson noise (Figure 4.7 (a)) was assumed as only shot noise is included. The Fourier spectrum in this case has constant power, equivalent to the mean dose (insert in Figure 4.7 (a))[122]. Such noise transfer has no spatial frequency dependence which is not realistic for the electron detection process. Noise transfer must therefore also include convolution by the detector NPS (Figure 4.7 (b)), which introduces a spatial frequency dependency, as shown in the insert in Figure 4.7 (b).

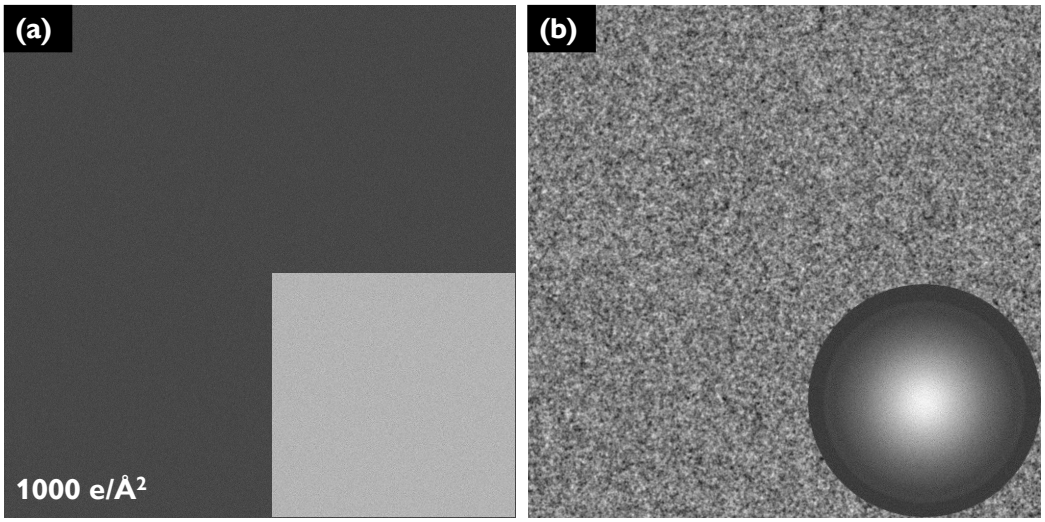

Figure 4.7: 2kx2k images of Poisson noise for an electron dose of 1000 $e/Å^2$ (a) before and (b) after convolution by the NPS. Respective power spectra are shown in the inserts.

The last step in equation 4.1 involves multiplying Figure 4.4 (b) and Figure 4.7 (b) in Fourier space and subsequently multiplying the resultant image by the detector gain in real space. This results in the final image, shown in Figure 4.8 (a). Multiplication by the experimental detector gain, G, converts the output image from e/pix to greyscale in analogue-to-digital units (ADU). Figure 4.8 (a) shows the spatial frequency dependence of both the signal and noise transfer, consistent with the electron detection process.

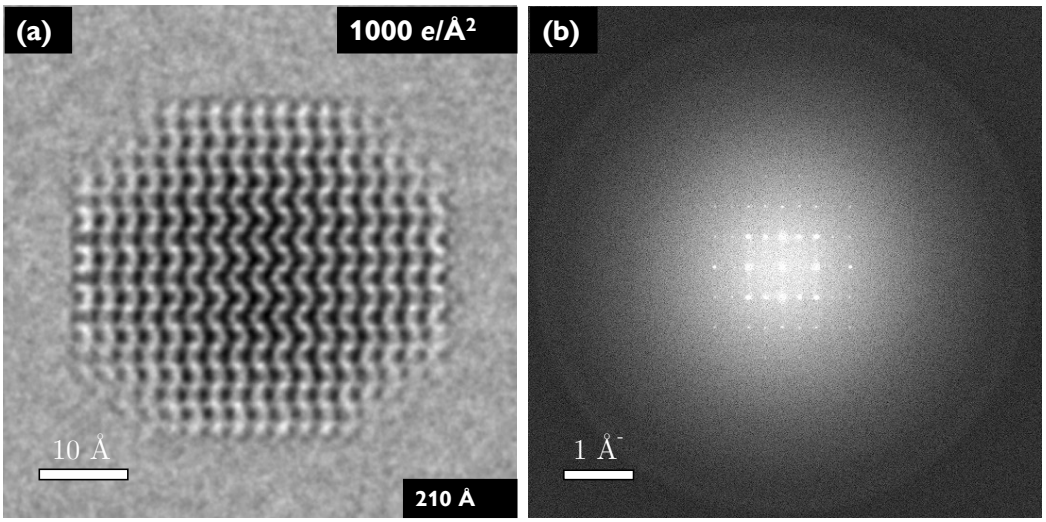

Figure 4.8: (a) Simulated image of a [101] oriented nanoparticle with a 1000 $e/Å^2$ dose and corresponding power spectrum (b) showing spatial frequency dependent transfer of signal and noise.

The results of the approach that I have developed in this section were validated against an alternative simulation method proposed by Vulovic et al. (2013) [154]. The latter involves 4 steps: (i) the multiplication of the Fourier spectrum of the noiseless image, $\mathcal{F}$ [I_o(r)], by $\sqrt{\text{DQE}}$, which is equivalent to the MTF/NPS ratio; (ii) shot noise is added to the inverse Fourier transform of the image obtained in step (i) and; (iii) subsequently the Fourier transform is calculated and multiplied by the NPS(q). Finally, the Fourier transform of the final image is multiplied by the detector gain (iv).

Compared to this method, the approach that I developed in this thesis involves fewer steps. More importantly, it treats the influence of the MTF on the signal and the influence of the NPS on the noise more explicitly. However, the results of the two methods are identical (see Figure 4.11 in subsequent section).

In addition to including the detector response using experimental MTF and NPS in the simulations, to ensure that simulated images have the same counts per pixel as in the experimental images, the data were processed as 32-bit, instead of 8-bit. 8-bit data can be visualised and handled by numerous digital programs unlike images with larger bit-depth which may require specialised programs. However, rescaling images to 8-bit may result in a loss in precision and it exaggerates the noise standard deviation in the restored phases (Appendix A, Figure A.1). Furthermore, it is noted that experimental images also have a bit-depth of 32.

A summary of the pixel counts in simulated and experimental images measured at a few of the finite electron doses used in this work are shown in Table 4.3. The mean pixel counts were measured from 1k x 1k and 512 x 512 pixels vacuum regions, in the experimental and simulated images of the focal series, respectively. A minimum of 9 individual images were used to obtain the average for each mean value. The simulated images have nearly identical mean pixel counts to the experimental data.

Table 4.3: A tabulated summary of experimental and simulated mean pixel counts ($\boldsymbol{\mu}$) obtained in vacuum at various electron doses per frame.

Dose per frame (e/Å^2)	**μ_{sim}(ADU)**	**μ_{exp}(ADU)**
303	75.61	74.23
1029	256.61	265.33
2066	514.74	525.16
3081	768.10	753.62

A typical focal series simulation is shown in Figure 4.9 for a [001] oriented model nanoparticle. The electron dose per frame ranges from 100 $e/Å^2$ to 3000 $e/Å^2$. The SNR increases with dose, consistent to experimental observations. Contrast variations at the atomic column positions are due to changes in defocus (-300 Å, -190 Å and 130 Å from top to bottom row). The exit waves were subsequently restored from this simulated focal series, as described next.

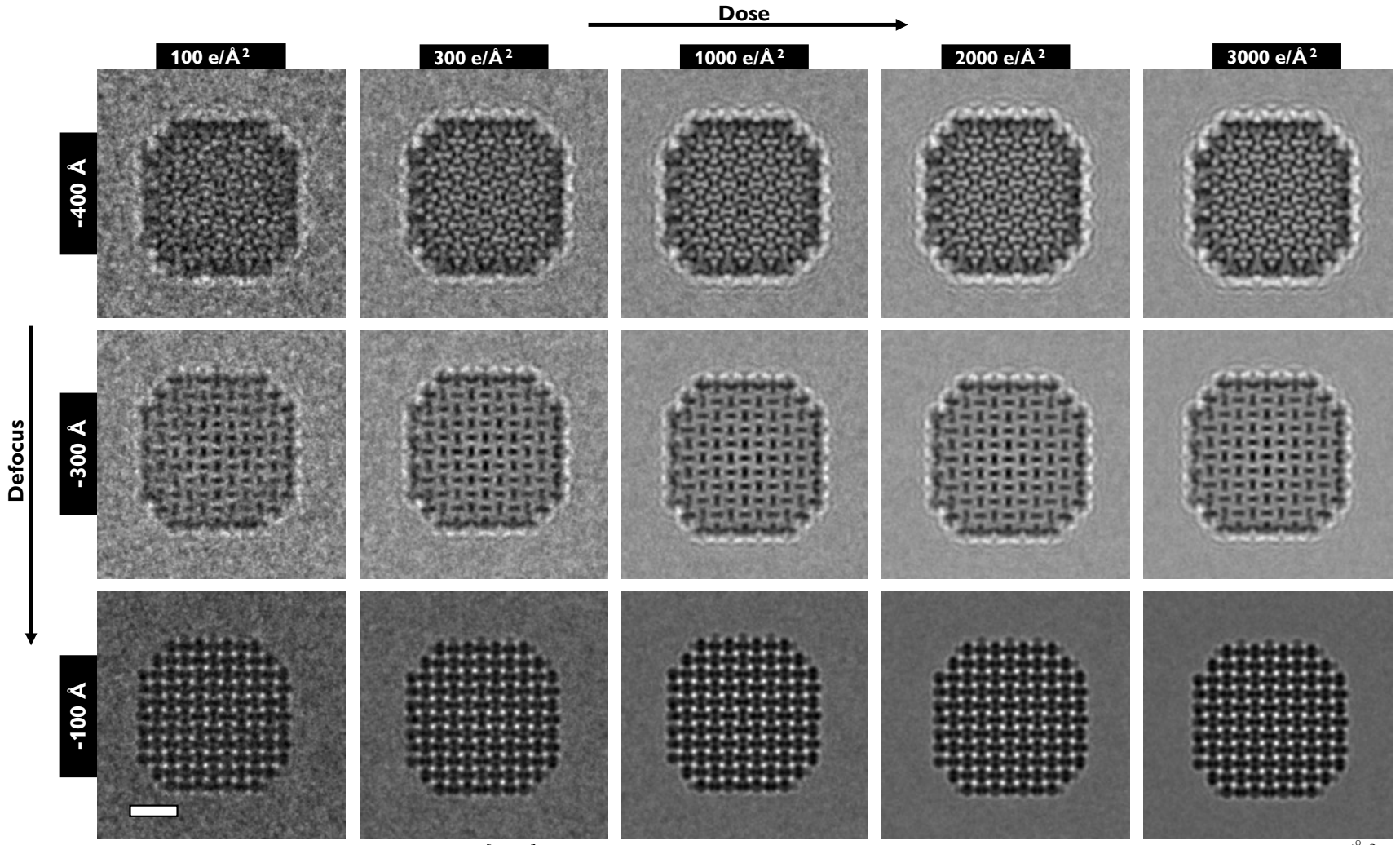

Figure 4.9: Simulated focal series data for a [001] oriented nanoparticle. The electron dose per image ranges from 100 $e/$Å^2 to 3000 $e/$Å^2. From top to bottom, the defocus ranges from -300 Å, -190 Å and 130 Å, respectively. The scale bar is 10 Å.

4.2.5. Focal series exit wave restoration

Experimental focal series data were acquired on a JEOL ARM 300 CF, equipped with both an image and probe C_3-corrector, operating at 300 keV. The images were recorded on a 4k x 4k pixel Gatan OneView detector with an exposure time of 0.4 s/frame and a magnification of 1.2-1.5 Mx, corresponding to a sampling of 0.10-0.083 Å/pix, respectively. A total of 30 images was acquired per focal series with a focal step of up to 20 Å. The focal spread of the instrument was calculated to be 36 Å as discussed in section 3.2.1. A beam divergence value of 0.1 mrad was used in the restorations[104]. These imaging parameters were used as the input parameters for the exit wave restoration of both experimental and simulated data. For the experimental restoration parameters of individual nanoparticles refer to Table 4.5. A summary of the restoration parameters used for the data in this chapter is given in

Table 4.4. As discussed, data analysis was carried out for nanoparticles that had minimal contact with adjacent nanoparticles and were suspended on a thin, amorphous carbon substrate and overhanging the vacuum, as shown in Figure 4.2 as well as in Figure 4.10 below.

An exemplary focal series of the [001] projected nanoparticle is shown in Figure 4.10 (a-c). The total focal range of the series is between -560 Å to -20 Å and, in the figure below, images with defoci of -526 Å, -467 Å, -399 Å, -340 Å, -274

Å, and -235 Å are shown, respectively. The series was acquired with a C_3 value of -1.30 µm and the rest of the other parameters are as summarised in Table 4.4.

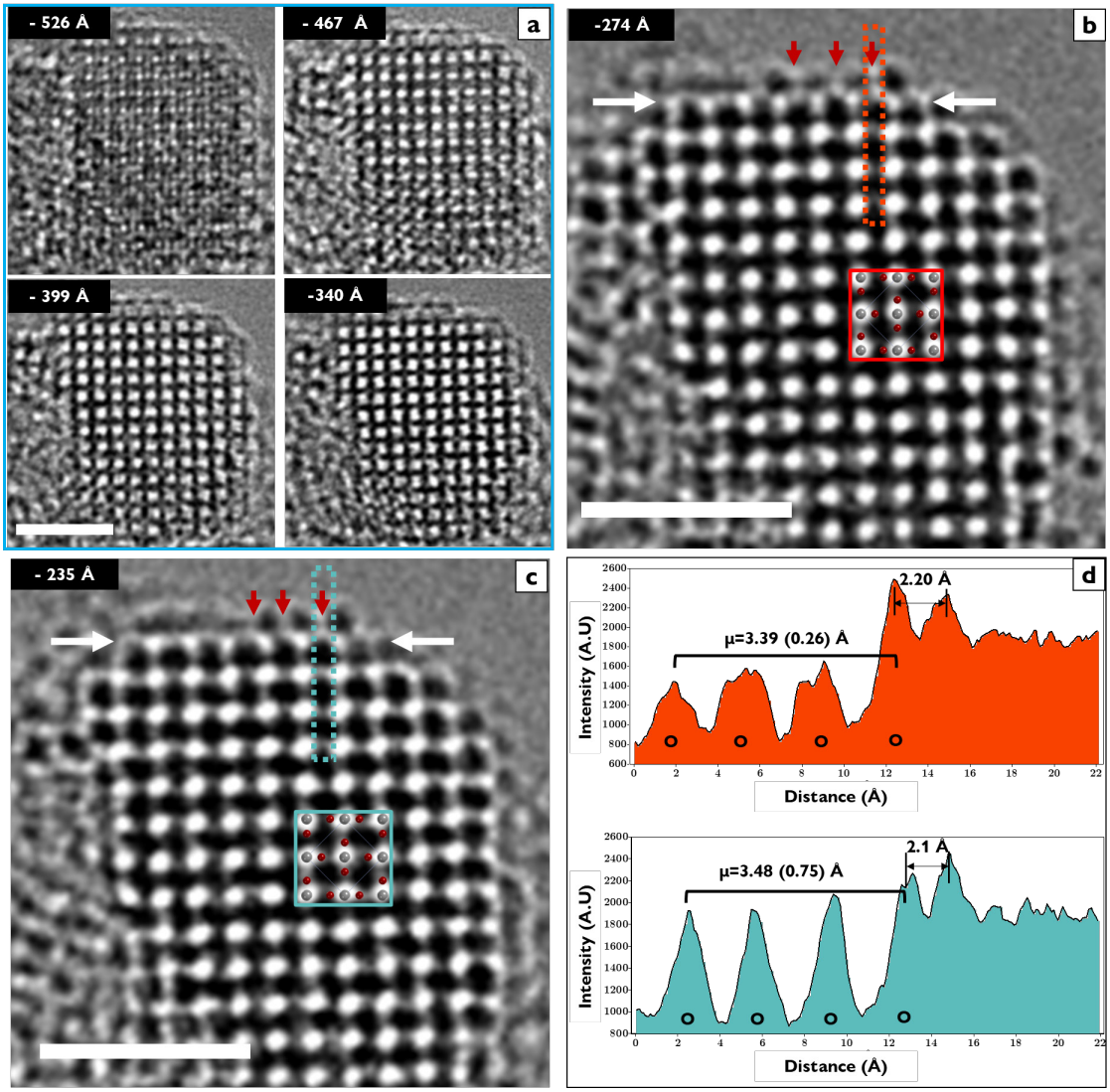

Figure 4.10: Selected images from the focal series of the [001] projected nanoparticle with defoci of (a) -526 Å, -467 Å, -399 Å, and -340 Å, (b) -274 Å, (c) -235 Å. The red arrows in (b) and (c) show the appearance of contrast motif that deviates from the one observed in the bulk of the nanoparticle. An atomic model is overlain in (b) and (c). (d) Orange and blue line profiles acquired with 8-pixel wide integration from dashed ROIs shown in (b) and (c), respectively. The four O atoms in the line profiles acquired in (b) and (c) have average distances of 3.48 (0.75) Å and 3.39 (0.26) Å, respectively. The scale bar is 20 Å.

The second layer of atoms indicated by white arrows in Figure 4.10 (b) and (c) is composed of Sn (bright contrast) and O (light contrast) consistent with what is observed in the bulk. However, contrary to what is observed in the bulk, there is additional atom contrast at about 2.15 Å (see line profiles in Figure 4.10 (d)) above some of the surface O atoms as indicated with red arrows in the figures above. Their distance is shorter than the typical O-O distance of about 3.40 Å measured in the bulk. These observations suggest that the surface was undergoing reconstruction. The reconstructed atoms cannot be O '*interstitials*' ($O_{\mathbf{i}}$) as these are thought to have prohibitively high formation energies [7] and are typically formed under $O_{2(g)}$-rich conditions contrary to the experimental conditions[43]. Thus, these can only be ordered surface Sn interstitials ($Sn_{\mathbf{i}}$) which have been demonstrated by several studies to be stable under low $O_{2(g)}$ conditions[34,37,41,167]. However, despite agreement with these studies in this respect, the resultant model does not correspond to any of the models proposed in the above studies. This may be due to the discrepancy between the stringent requirements for NCSI compared to those employed in this study. These studies, as will be discussed in the subsequent section, demonstrate that the Sn_i are not only coordinated to the bulk through $O_{\mathbf{ip}}$, as observed from Figure 4.10 (b) and (c) but also the $O_{\mathbf{br}}$ and $O_{\mathbf{cus}}$ atoms (see Figure 2.4 and Figure 2.9 for reference).

Furthermore, selected focal series data for the other nanoparticle projections are included in the Appendix A, Figure A.2. However, the dose per frame for all these projections is between 1166 $e/Å^2$ and 1932 $e/Å^2$. These low doses result in low O atom column SNRs at the surface/vacuum interface. As will be shown in section 4.3.2, this dose range is about 10 to 20 times less than the dose required to achieve single O atom sensitivity ($21.8(2.9)x10^3 e/Å^2$). Additionally, the nanoparticle search was conducted at lower doses than those used for acquiring the series and thus they inevitably have notable residual aberrations which were difficult to correct prior to imaging due to the poor SNR. This is best illustrated with the [100] and [101] projected nanoparticles which were found to have A_1 values of -13.4 nm (14 °) and 10.7 nm (-7 °), respectively. Nonetheless, these and other residual aberrations were compensated for during the restoration process and the restored phase matched the atomic models of SnO_2 in the various projections.

Table 4.4: Summary of the exit wave restoration parameters used in this study.

Parameters	**Values**
Primary electron energy (keV)	300
Beam divergence (mrad)	0.1
Focal spread (Å)	36
C_3(µm)	-1.33 - 1.45
Focal step (Å)	20
Acquisition time (s)	0.4
Sampling (Å/pix)	0.083 - 0.10
Dose/frame ($e/Å^2$)	1000 - 5000
Dose rate ($e/Å^2$s)	3000 - 11419

Restoration of the specimen exit wavefunction from simulated and experimental images was performed with the FTSR software (see section 3.5.1) implemented in Gatan Microscopy Suite (GMS) [144,146]. The restoration method in FTSR is based on the linear Wiener filter approach developed by Saxton (1988)[145]. More details about this method can be found in section 3.7.

Figure 4.11 shows the typical phases of a [100] oriented nanoparticle, restored from simulated focal series data in order of increasing electron dose per frame: 100 $e/Å^2$, 300 $e/Å^2$, 1000 $e/Å^2$, 2000 $e/Å^2$ and 3000 $e/Å^2$. The surface region is marked with an orange ROI in the 100 $e/Å^2$ restored phase and it is shown for all the other phases simulated at different doses (Figure 4.11). Qualitatively, the simulated phases show that the noise in the vacuum region surrounding the surface decreases with increasing dose as expected while the contrast of the O atoms (lighter grey) improves. Quantitatively, Figure 4.12 shows a plot of the noise standard deviation as a function of the cumulative dose for several simulated phases.

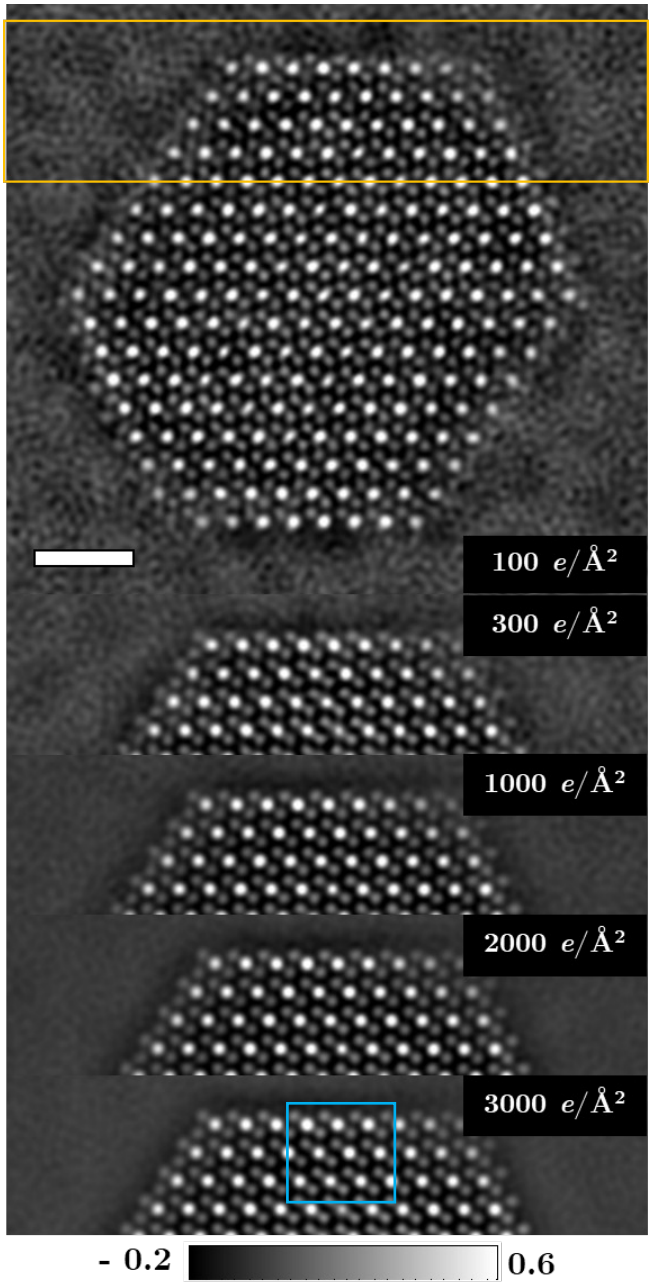

Figure 4.11: Restored phase of a [100] oriented SnO_2 model nanoparticle obtained from a simulated focal series of 30 images with electron doses per frame of 100 $e/Å^2$, 300 $e/Å^2$, 1000 $e/Å^2$, 2000 $e/Å^2$ and 3000 $e/Å^2$. The region marked by the orange box highlights the same areas of the nanoparticle surface. The blue box highlights O atom columns of interest (shown in Figure 4.13). The scale bar is 10 Å.

The standard deviation of the noise was obtained from a 2048 x 512 pixels area

in the vacuum. Noise data from simulated focal series using the Vulovic et al.

(2013)[154] method are also shown to illustrate that the results obtained are identical to the method developed in this thesis (indicated as multiplicative).

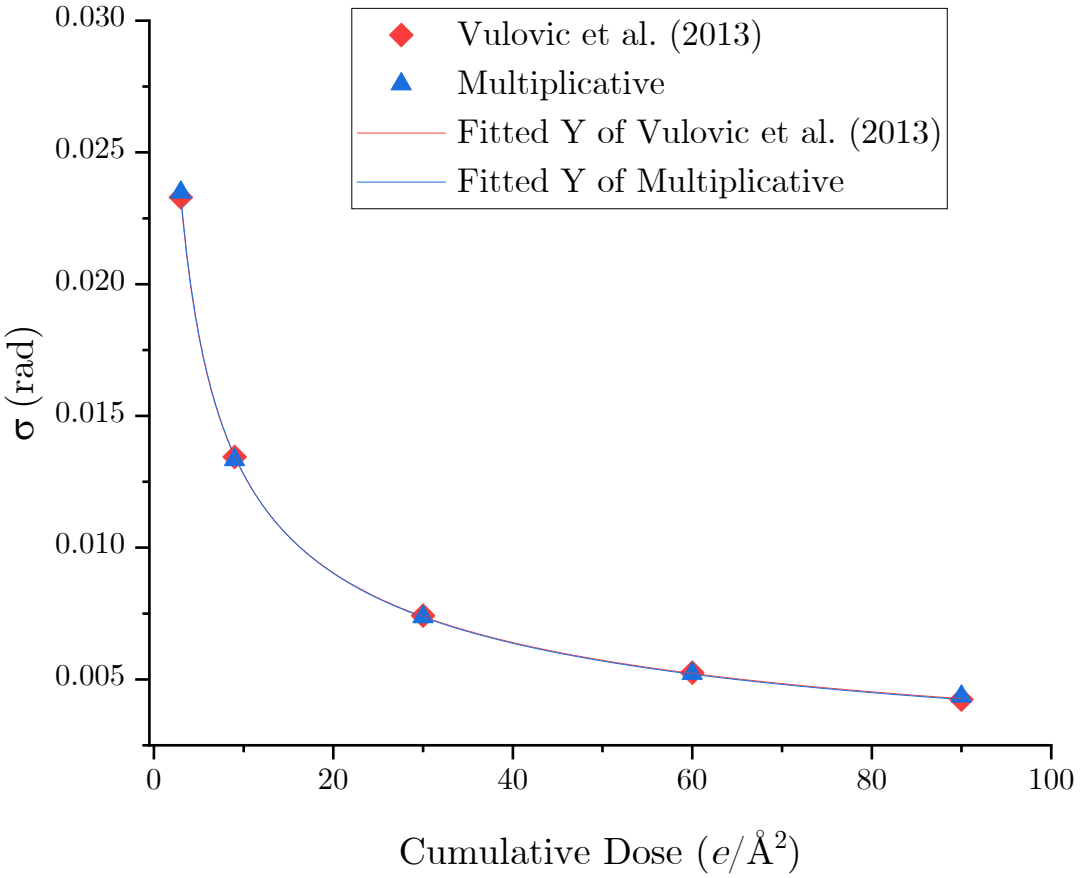

Figure 4.12: Vacuum noise standard deviation measurements as a function of cumulative dose for phases obtained from complex exit waves restored from focal series data calculated using the Multiplicative (thesis approach) and the Vulovic et al. (2013) [154] method.

4.2.6. Quantification of surface O atom SNFR as a function of dose and occupancy

The maximum phase shift of surface O atom columns depends on their occupancy, their z position with respect to the reference exit plane wave and the spacing between each successive atom in z[163]. Furthermore, nearest neighbours can also influence the phase shift[164,165]. Thus, for the same particle,

the phase shift of a single O atom will vary slightly according to the local environment and crystallographic projection. This introduces a level of complexity where atom columns of the same occupancy may have different apparent phase shifts if successive atoms do not have the same interplanar distance in z or have different z positions with respect to the reference exit plane wave.

In this study, using a model nanoparticle eliminates the focus, or z dependence, of the resultant phase shifts because the analysis of comparisons of dose dependent SNFR is made for atom columns having known, equal z and interplanar distance in z, as well as the same mass as a function of cumulative dose per projection. Furthermore, the exit wave of each column of interest was backpropagated to obtain the maximum phase shift. This numerical correction accounts for the difference in z positions with respect to the exit wave restoration plane, ensuring that the phase shift variation for finite dose complex exit wave phases is solely due to the effect of noise[85].

Noise associated with a finite electron dose determines the SNFR in an image. In the case where atoms are subtended by the vacuum, the strength of the phase signal will vary according to the standard deviation of the noise in the vacuum. When the latter is larger than or equal to the first it is difficult to determine when surface atoms are present at the vacuum interface. The

procedure used to quantify the visibility of O atoms at the surface of a nanoparticle is explained next.

The phase shift induced by an atom column is proportional to its atomic number[85]. In the simulated exit wave phase, the maximum phase shift induced by the ith atom column, δ_i, is obtained as the maximum pixel value within a squared region of interest, ROI, (marked with a blue dashed line in Figure 4.13) centred on the atom column of interest. This value, however, is shifted due to the inner potential of the crystal[85] which introduces a negative offset. To correct for this effect, the maximum phase shift, δ_i, is normalised with respect to the '*valley*' or background wave, η_i. This background wave was obtained by averaging 2-4 minima phase values surrounding the atom column of interest (Figure 4.13 (b) & (c)).

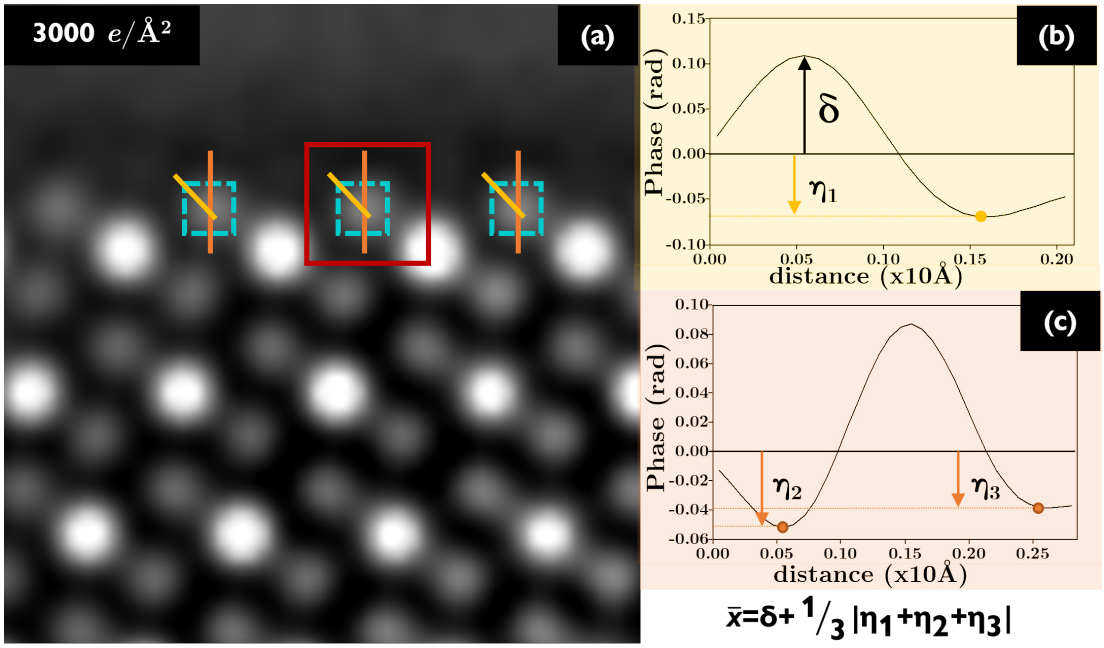

Figure 4.13: (a) A magnified view of the ROI marked in blue in Figure 4.11. Three atom columns (indicated with squares in a dashed blue line) are selected for quantification of the oxygen phase shift at the surface. For each highlighted atom column, the maximum pixel value was taken as the maximum phase value within the marked region. (b) and (c) are line profiles across the atom column from which the average 'valley' wave minimum phase shift values are obtained and used to normalise the maximum phase shift at the atom column.

To minimise the measurement error for the finite dose simulations, the position of the ROI and that of the line profiles for the valley wave, including the sampling points, were positioned with respect to the phase restored at the highest electron dose per frame i.e., 3000 e/Å^2. Care was also taken to avoid taking the valley signal from regions close to neighbouring Sn atom columns. For a given facet, the SNFR of a single O atom column interfacing background vacuum noise was calculated using equation 4.2 below:

$$\text{SNFR} = \frac{1}{\rho_i N}\sum_{i=1}^{N}\left(\frac{\bar{x}_i - \mu}{\sigma_n}\right) \simeq \frac{1}{\rho_i N}\sum_{i=1}^{N}\left(\frac{\bar{x}_i}{\sigma_n}\right) \qquad 4.2$$

Here N is the total number of atom columns used to obtain the average SNFR per facet at a given dose, which was 3 for all facets; $\bar{x}_i = \delta_i + \eta_i$ refers to the total phase shift of the ith O atom column after normalisation with respect to the average valley wave. In addition, μ is the mean vacuum phase value, which is always nearly zero, hence its effect on $\bar{x}_i$ is negligible; σ_n is the standard deviation of the noise in the vacuum and, ρ_i, is the occupancy of the ith column.

4.3. Results

4.3.1. Experimental focal series

Focal series of the nanoparticle model with reduced and stoichiometric surface terminations (shown in section 2.2, see example of various terminations on [001] oriented nanoparticle model in Figure A.3, in Appendix A) were simulated with the experimental parameters in Table 4.5. Additional parameters that were fixed during the experiments and the simulations are listed in

Table 4.4 in section 4.2.5. Most experimental data were acquired at a sampling rate of 0.0083 Å/pix. The detector sampling was fixed at 0.0083 Å/pix for all the simulations. As shown in section 3.5.3, once the detector gain and the pixel sampling are known it is straightforward to calculate the dose per frame.

In the subsequent discussion, the error associated with the measurement of projected distances corresponds to the total error (shown in parentheses after

measurement) obtained after several measurements on multiple phases where the particle retains the feature of interest[†].

Table 4.5: Summary of the cumulative dose, C_3 and detector sampling for the experimental data in this study. The cumulative dose corresponds to that of a 30-image focal series data set and the total cumulative dose at the sample is shown in parenthesis.

Facet$_{zone}$	**C. dose x10^3(eÅ^{-2})**	**C_3(μm)**	**Sampling (Å/pix)**
$(011)_{[100]}$	54 (188)	1.45	0.083
$(110)_{[001]}$	137 (480)	-1.30	0.104
$(1\bar{1}0)_{[110]}$	58 (203)	1.45	0.104
$(\bar{1}01)_{[101]}$	57 (199)	-1.33	0.083
$(100)_{[101]}$	57 (199)	-1.33	0.083
$(\bar{1}10)_{[111]}$	35 (122)	-1.00	0.083

In this study, the cumulative dose of the focal series is defined as the dose per frame multiplied by the number of frames in the focal series. However, the total cumulative dose at the sample is slightly different because the latter includes the dose reaching the specimen during shutter pre-exposure compensation (SPEC). SPEC is generally specified on the detector when imaging specimens that undergo charging. Without SPEC charging specimens, such as those imbedded in plastic, tend to move when first exposed to the electron beam such that they result in blurry images with reduced high spatial resolution information[155]. Thus, to minimise their mobility these are pre-exposed to the

[†] The total error, in parenthesis after measurements, includes both the statistical and systematic errors. The statistical error is represented by the standard deviation while the systematic error is calculated as the error in manual measurement by ± 1 pixel. These are then added in quadrature to produce the total error.

electron beam prior to acquiring images such that they are stable during acquisition (more details given in section 5.2.1).

Thus, in Table 4.5 the total cumulative dose to which the specimen is exposed is given in parenthesis, together with the focal series cumulative dose. For exploring atom visibility, only the focal series cumulative dose (used to generate the observed signal) will be considered. However, for understanding imaging-induced surface transformations the total cumulative dose reaching the specimen will be considered also.

4.3.1.1. {110} facets

A qualitative visual comparison between experimental and simulated phases reported in this section indicates that all {110} facets are non-stoichiometric at the respective experimental doses used. The {110} facets in the [110] and [111] projections are shown in Figure 4.14 and Figure 4.15, respectively. In Figure 4.14 (a), showing the $(1\bar{1}0)_{[110]}$ facet, the yellow arrows indicate regions of contrast suggesting that there are undercoordinated atoms on the surface (see false colour insert in Figure 4.14 (a) and refer to Figure A.7 (a), in Appendix A for the full details).

However, for the most part, other exposed sections of the nanoparticle surface have no apparent bridging O atoms. Below the atomic layer highlighted by the

yellow arrows, in-plane O atoms are present indicated by a periodic phase variation at the surface (white arrows in Figure 4.14 (b)).

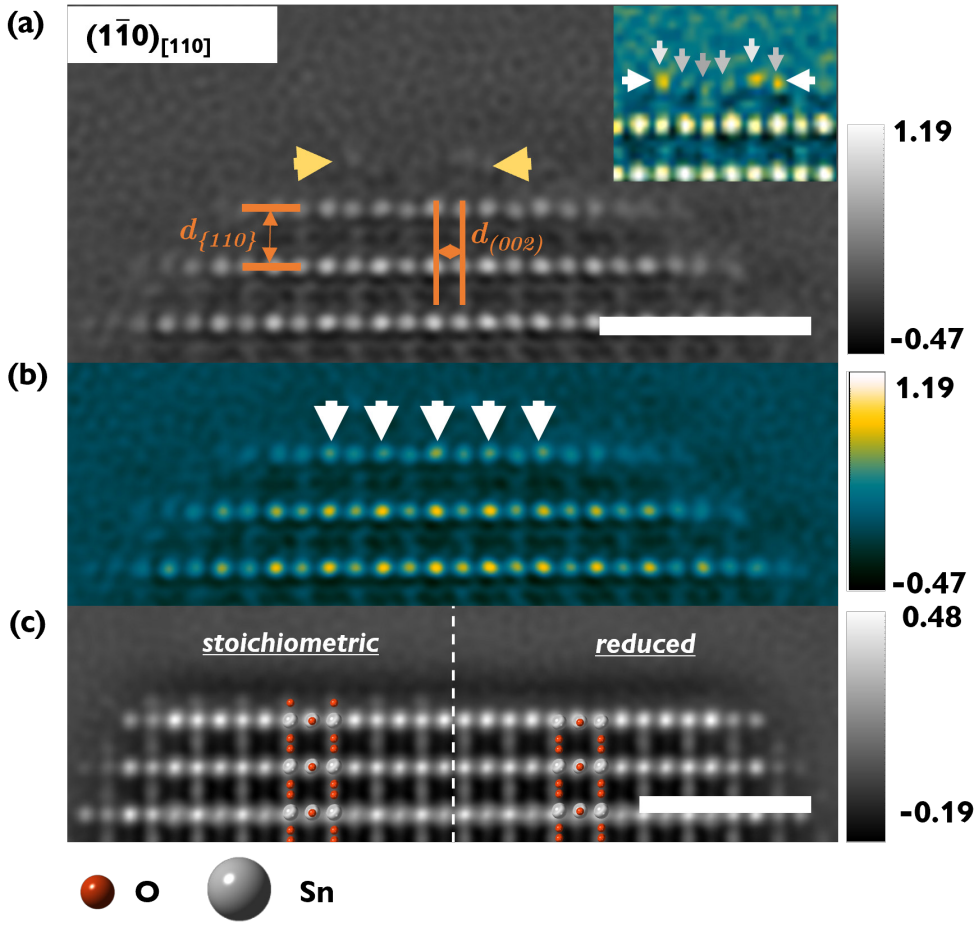

Figure 4.14: (a) Experimental phase of a [110] oriented 0.5 wt% Pd-SnO_2 nanoparticle showing a vacuum exposed stepped (1$\bar{1}$0) surface. Yellow arrows indicate undercoordinated Sn/O surface atoms (see false colour insert in (a)). The interplanar spacings $d_{\{110\}}$ and $d_{\{002\}}$ are also shown. (b) False colourmap of the phase in (a). The white arrows indicate atom columns of mixed Sn and O occupancy. (c) Stoichiometric (left) and reduced (right) reconstructed phases, obtained from the simulated focal series. Atomic model overlays of the stoichiometric (O-terminated) and reduced surfaces are also shown in (c). The scale bar represents 10 Å in all cases.[‡]

This phase variation is indicative of the presence of O because the shift at every other Sn-O atom column on the surface is higher than that of its nearest

[‡] All the phase ranges presented in this chapter are in radians.

neighbours. This motif corresponds to alternating pure Sn atom columns and mixed Sn and O atom columns. The latter have a larger atomic number in projection, resulting in a larger phase shift. This periodic variation is also observed in the bulk of the nanoparticle (see second layer of atoms). Similarly, this variation is also observed in the phase restored from simulated data. Hence, it is concluded that this $(1\bar{1}0)$ facet is reduced with an SnO termination.

Figure 4.15 shows the $(\bar{1}10)$ surface, for a nanoparticle oriented along the [111] axis. Compared to the surface atomic layer (indicated with white arrows in (b)), the atomic layer below has a clear, periodic, and strong phase signal. In the central region, this plane is clearly composed of Sn atoms which are fully coordinated to O atoms, similar to the atomic arrangement observed in the bulk region of the particle in (c). Note that Sn atom columns in the central region of the simulated nanoparticle have reversed contrast compared to thinner edge regions the nanoparticle. The phase switches values due a dynamical mass-thickness effect which causes phase wrapping [168]. This effect occurs rapidly for thick specimen regions composed of high Z atoms [163]. At these regions the phase advance rapidly increases such that it exceeds the modulo 2π phase range [169]. Beyond the modulo 2π phase range, the phase is remapped by the subtraction of integer values of 2π, resulting in the phase wrapping around itself, taking on smaller phase values within the modulo 2π phase range.

At the edges of the experimental nanoparticle, the phase signal is not as sharp because of the vacuum noise, however, the visible atom columns clearly show weaker phase shifts relative to those at the centre of the nanoparticle suggesting that these columns have lower relative occupancy.

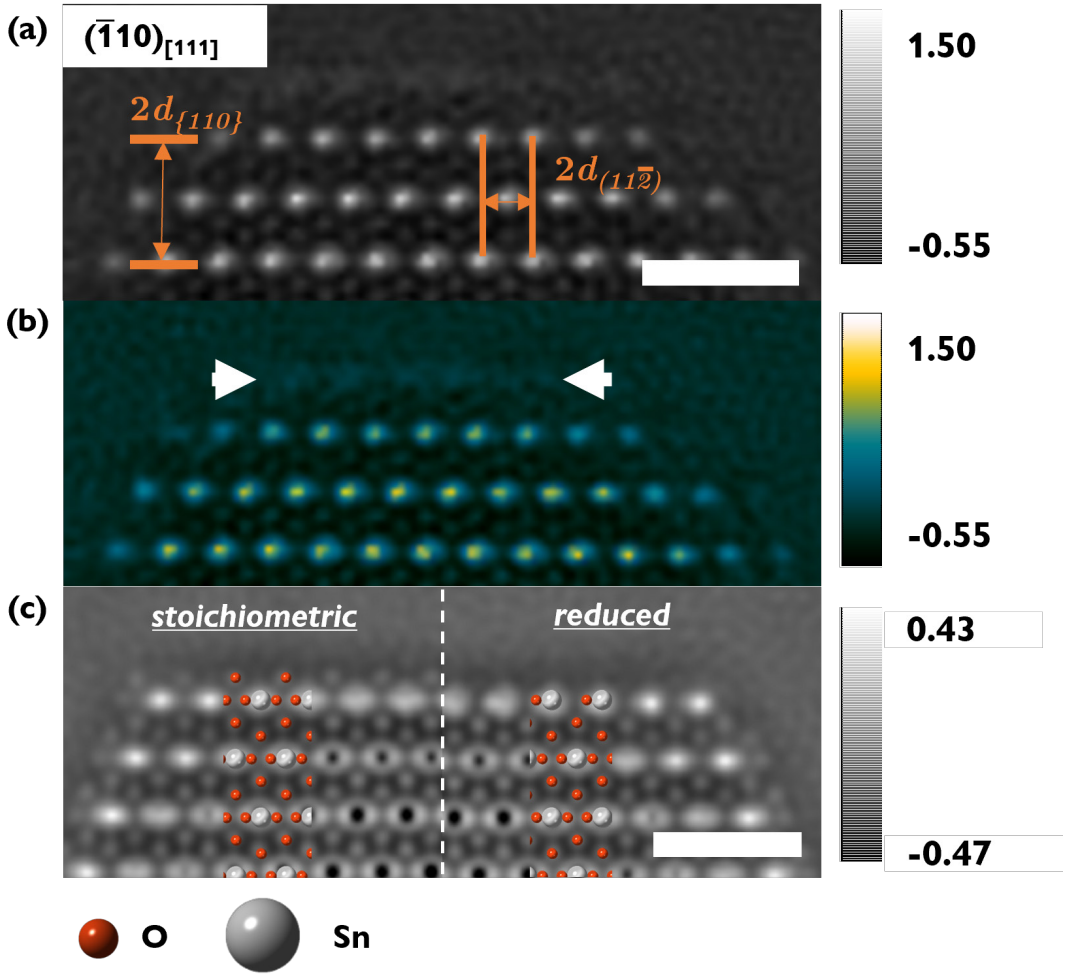

Figure 4.15: (a) Experimental phase of a [111] oriented 0.5 wt% Pd-SnO_2 nanoparticle exposing a stepped $(\bar{1}10)$ surface. The $2d_{\{110\}}$ and $2d_{\{11\bar{2}\}}$ interplanar spacings are also shown. (b) False colourmap of (a) with white arrows showing a possible Sn/O monolayer. (c) Stoichiometric (left) and reduced (right) phase images, obtained from the simulated focal series. Atomic model overlays of stoichiometric (O-terminated) and reduced surfaces are also shown in (c). The scale bars represent 10 Å in all cases.

The diffuse contrast at the surface suggests the presence of a non-periodic atomic layer which is difficult to distinguish from the vacuum noise. This signal

corresponds to the time-average structure composed of low occupancy (possibly monolayer), undercoordinated and mobile Sn/O atoms (see Appendix A, Figure A.8). Carbon atoms may also be present, diffusing from the supporting amorphous carbon. The delocalised nature of this signal is due to the averaging of the weak signal over several structural arrangements induced by thermal and/or electron-induced mobility which occur at time scales shorter than the acquisition time[85].

Beside the visual comparison with simulations, an alternative way to establish the nature of the surface, involving reduced stoichiometry, is to measure the deviation of the surface atoms from their bulk atomic positions. However, in the case of SnO_2, theoretical calculations have shown that relaxation of the {110} facets is similar for reduced and stoichiometric surfaces, resulting in less than a 0.3 Å deviation from the bulk atom positions [3,33]. This was further confirmed experimentally by comparing projected distances between Sn atom columns in the phases of the nanoparticles along the [110] and [111] zone axes. These measurements are summarised in Table 4.6.

Table 4.6: Measured average projected distances for surface and bulk Sn atom columns spacings along the [110] and [111] zone axes.

Facets	**Planes**	**Surface (Å)**	**Bulk (Å)**
$(1\bar{1}0)_{[110]}$	$d_{\{002\}}$	1.6 (0.2)	1.6 (0.1)
	$d_{\{1\bar{1}0\}}$	3.5 (0.1)	3.4 (0.1)
$(\bar{1}10)_{[111]}$	$2d_{\{11\bar{2}\}}$	2.9 (0.1)	3.0 (0.1)
	$2d_{\{110\}}$	6.9 (0.1)	6.9 (0.1)

At the surface, and one monolayer below, the $(110)_{[111]}$ surface shows no significant relaxation compared to the bulk of the crystal. Along the $2d_{\{110\}}$ planes the interplanar distance between the 1st and 3rd SnO layer is 6.9 (0.1) Å which is identical to that in the bulk. In the horizontal direction $2d_{\{11\bar{2}\}}$, the interplanar distance between the Sn atoms for the surface atoms is 2.9 (0.1) Å compared 3.0 (0.1) Å in the bulk. Similarly, the measurements of the $d_{\{1\bar{1}0\}}$ and $d_{\{002\}}$ spacings for the [110] nanoparticle show no significant relaxation at the surface compared to the bulk.

Finally, for both the $(1\bar{1}0)_{[110]}$ and $(\bar{1}10)_{[111]}$ facets the surfaces are composed of small terraces with low occupancy atomic columns which present ambiguities against the vacuum noise. Nonetheless, the exposed sections of the layer below reveal no significant structural rearrangements. Measuring their relaxation relative to the bulk of the nanoparticle shows no significant change; hence, it is concluded that these are likely reduced due to the absence of surface bridging atoms when compared to theory. Hence, they exhibit an SnO termination.

Figure 4.16 shows a $(110)_{[001]}$ surface which is neither stoichiometric (left in Figure 4.16 (c)) nor fully reduced (right in Figure 4.16 (c)). The observed surface has regions terminated by Sn atoms (grey spheres in the figure) which are displaced from their bulk lattice sites by half the projected unit cell lattice parameter, **a**, into surface '*interstitial*' sites. Three atomic models partially consistent with the observed motif have been proposed to date based on purely

theoretical studies[167], DFT combined with *in situ* AC-STEM[37] and LEED/STM studies[34]. Of these studies only Li et al. (2021) provide sufficient evidence to allow for a quantitative comparison of their AC-STEM/DFT-relaxed model to the experimental observations[37]. In contrast, Batzill et al. (2003), postulated a model tentatively based on STM/LEED studies noting that the model was only suggestive due to ambiguities in contrast interpretation of their atomically resolved STM data. However, both Ágoston and Albe (2011) and Merte et al. (2017), computationally tested the validity of the Batzill's model through DFT and found that it had higher surface energy relative to other models under the same computational conditions [65,167]. Hence, further consideration of this model will not be given. Ágoston and Albe (2011), conducted extensive computations of various SnO_2 defects and proposed several models to explain the observed surface reconstructions of SnO_2. However, they do not provide relaxation details of their models and thus these are analysed relative to experimental observations presented herein based on the projected geometric configuration of their atomic models.

It must also be noted that models of SnO_2 surface reconstructions that only involved the removal of single in-plane O atoms on the partially reduced surface without surface Sn_i and relaxation, as shown in section 2.3, were excluded in the analysis [64,70]. Not only would their [001] projected atomic configuration be inconsistent with our observations, but it has been confirmed recently using

DFT that single O_{ip} vacancies have higher formation energies compared to bridging O vacancies [167]. Their formation is also associative, such that two neighbouring O atoms are removed as $O_{2(g)}$ contrary to the previously proposed single O_{ip} based surface reconstructions.

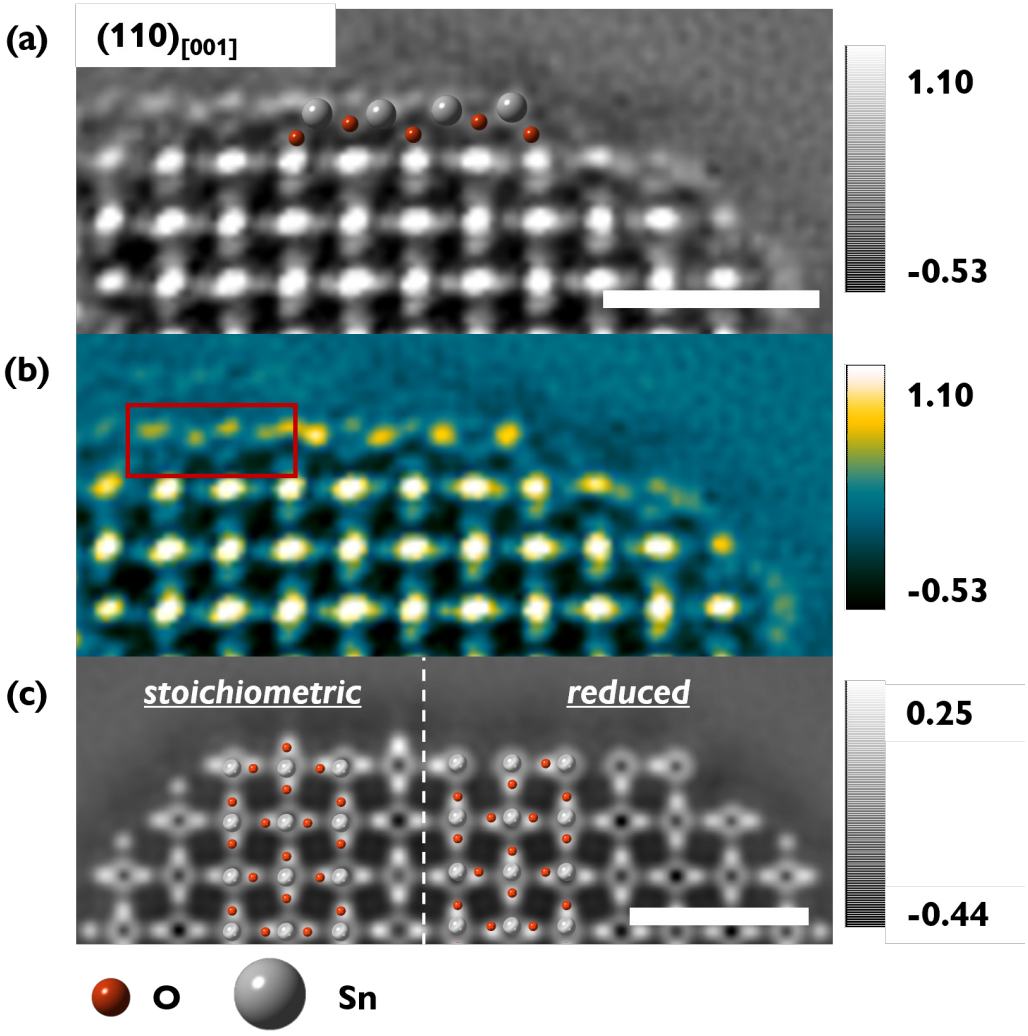

Figure 4.16: (a) Experimentally restored phase of a 0.5 wt% Pd-SnO_2 nanoparticle oriented in a [001] direction exhibiting a surface reconstruction composed of Sn_i atoms. The false colourmap is shown in (b). Contrast in the red ROI in (b) is not fully consistent with the (2x1) motif observed on the right surface. (c) Stoichiometric (left, O-terminated) and fully reduced (right, SnO-terminated) reconstructed phases, obtained from simulated focal series data. Atomic models are overlaid on both terminations in (c). The scale bar is 10 Å in all cases.

Li et al. (2021) propose a surface model of the (2x1) surface reconstruction based on their findings using AC-STEM and DFT[37]. The Sn_i left of the O_{cus} on their model is penta-coordinated to O_{cus} (x2) and O_{ip} (x1) O_{br} (x2) [37] while the one on the right is tri-coordinated to the bulk through O_{cus} (x2) and O_{ip} (x1). The (2x1) surface reconstruction predicted from DFT is thought to be composed of Sn_i tri-coordinated to the bulk through O_{cus} (x2) and O_{ip} (x1) only [167]. Figure 4.17 (b) shows the projected structure of these models in the [001] direction.

In Figure 4.16 ((a) and (b)) the distance between the first (surface) and second (immediately subsurface) atomic layers is 3.0 (0.1) Å, compared to 3.4 (0.1) Å in the bulk. This lattice contraction is similar to the one obtained experimentally and computationally by Merte et al. (2017) for the (4x1) reconstruction (3.0-3.2 Å) and comparable to that of Li et al. (2021), which is formed through the loss of surface bridging and in-plane O atoms [37,65]. Although the value of the surface relaxation measured and predicted by Merte et al. (2017) agrees with the one observed in this study, their predicted surface chemistry differs significantly from the one observed in the experimental reconstruction in Figure 4.16 ((a) and (b)). Merte's model is composed of an overlayer of Sn_3O_3 clusters bonded to the bulk through O_{cus} and O_{br} atoms, and an additional O atom referred to as an 'apex' O atom (for the arrangement of the first atomic plane refer to Figure 2.7 (a), in section 2.2). Significantly,

in the [001] projection, this model has 4 closely spaced Sn atoms in each Sn_3O_3 cluster. These Sn atoms would be clearly visible in the reconstructed phase if present because they would produce a strong phase shift in the [001] projection. Instead, in Figure 4.16 (a) and (b), single Sn atom columns rather than Sn_3O_3 clusters are visible at the surface, in better agreement with the projected models previously proposed by Li et al. (2021) [37] and Ágoston and Albe (2011)[167].

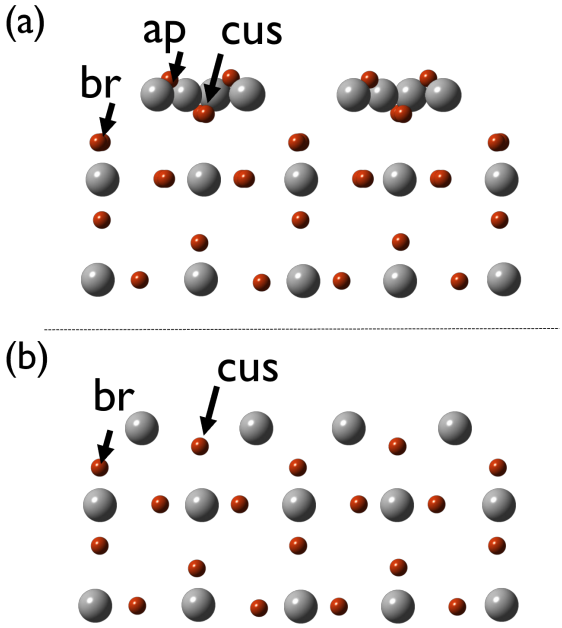

Figure 4.17: Atomic models of the [001] projected (110) (4x1) (a) and (2x1) (b) surface reconstructions. In (a), a Sn_3O_3 overlayer has interstitial Sn atoms (blue spheres) bonded to the bulk through bridging (labelled as br), 'coordinately unsaturated' (labelled as cus) and, 'apex' O (labelled as ap) (red spheres). In (b), Sn_i atoms (grey spheres) are bonded to the bulk through $O_{\mathbf{cus}}$ and $O_{\mathbf{br}}$ atoms. The model in (a) was proposed by Merte et al. (2017) and that in (b) is consistent with that of Li et al. (2021) and Ágoston and Albe (2011). (a) has been adapted with permission from ref [65] © (2017) by the American Physical Society and (b) is adapted from refs [37,167] © (2011) and (2021) with permission from Elsevier and the American Chemical Society, respectively.

It is evident that the agreement between these models and the observed contrast is not exact as there is additional contrast on the left of the

nanoparticle that is not fully consistent with the proposed models (see red ROI in Figure 4.16 (b)). However, this observation is consistent with the predictions and observations made in these studies. These surface reconstructions can co-exist with other surface reconstructions [167] and or other disordered transition states[37]. A detailed analysis will be given in section 4.3.3 where temporal surface dynamics are examined through segmented focal series analysis.

4.3.1.2. {101} facets

Figure 4.18 and Figure 4.19 show experimental phases obtained from nanoparticles oriented along the [100] and [101] zone axes. These particles expose equivalent crystallographic (011) and ($\bar{1}$01) facets in projection. Both facets are terminated with Sn atoms, indicating, by comparison with their simulated counterparts in Figure 4.18 (c) and Figure 4.19 (c), that they are reduced. In the figures open dashed circles show bridging O vacancies. In the [101] oriented particle, the arrows indicate positions where O atoms are observed. Observation of fully reduced {101} facets is consistent with what is expected theoretically and has also been demonstrated experimentally by other methods. Xu et al. (2012) predicted using DFT that under ambient temperature and low $O_{2(g)}$ partial pressure the Sn-terminated reduced surface is energetically favourable[32]. Similarly, using first principle calculations Bergermayer et al. (2004), proposed that the most stable (101) reduced surface is Sn-terminated, at low $O_{2(g)}$ partial pressure or at high temperature[33].

Additionally, using negative C_3-imaging, Lu et al. (2010) demonstrated that SnO_2 nanowires have Sn-terminated facets[170].

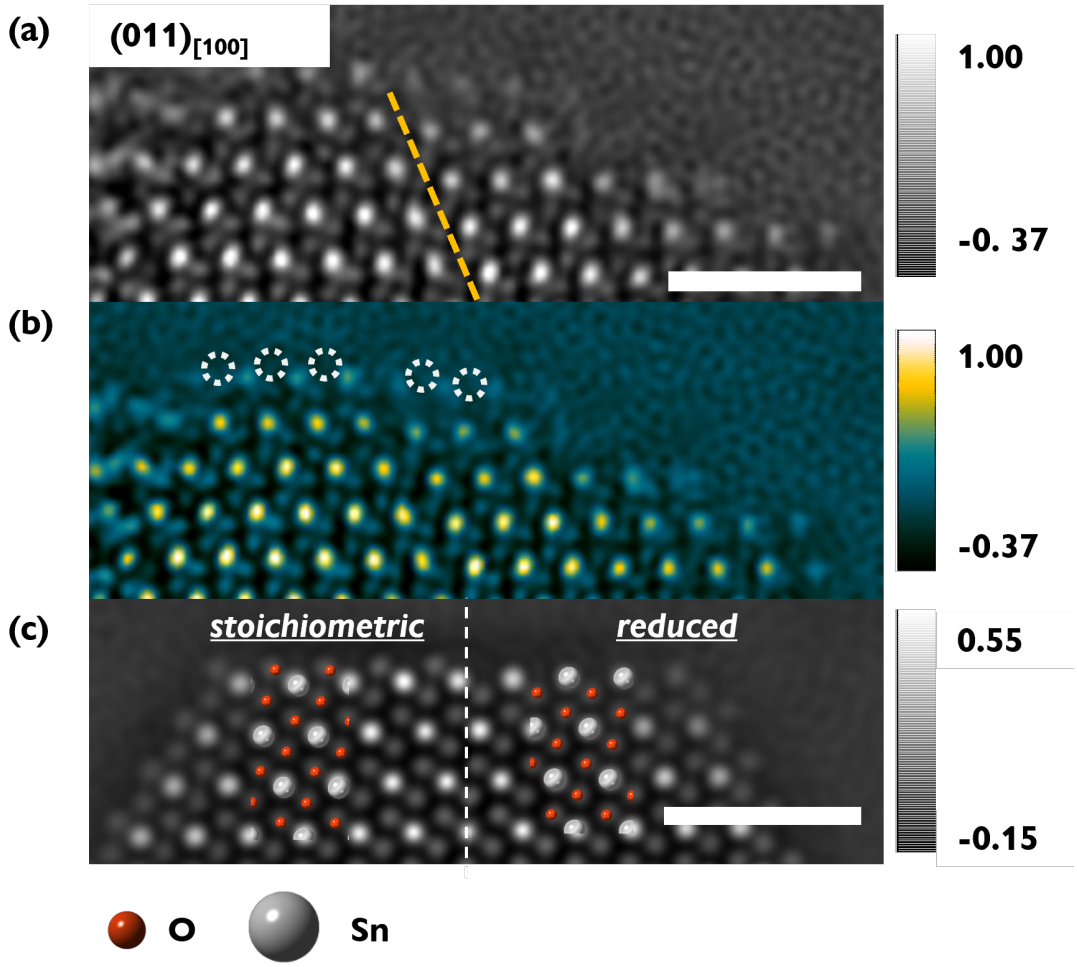

Figure 4.18: (a) Experimental reconstructed phase of a 0.5 wt% Pd-SnO_2 nanoparticle oriented along [100] exposing a stepped (011) facet, and false colourmap image (b). The yellow dashed line indicates a line defect. In (b) the white dashed circles indicate bridging O vacancies. (c) Stoichiometric (left) and reduced (right) reconstructed phases, obtained from simulated focal series. Atomic model overlays of the stoichiometric (O-terminated) and reduced (Sn-terminated) surfaces are also shown in (c). The scale bars represent 10 Å in all cases.

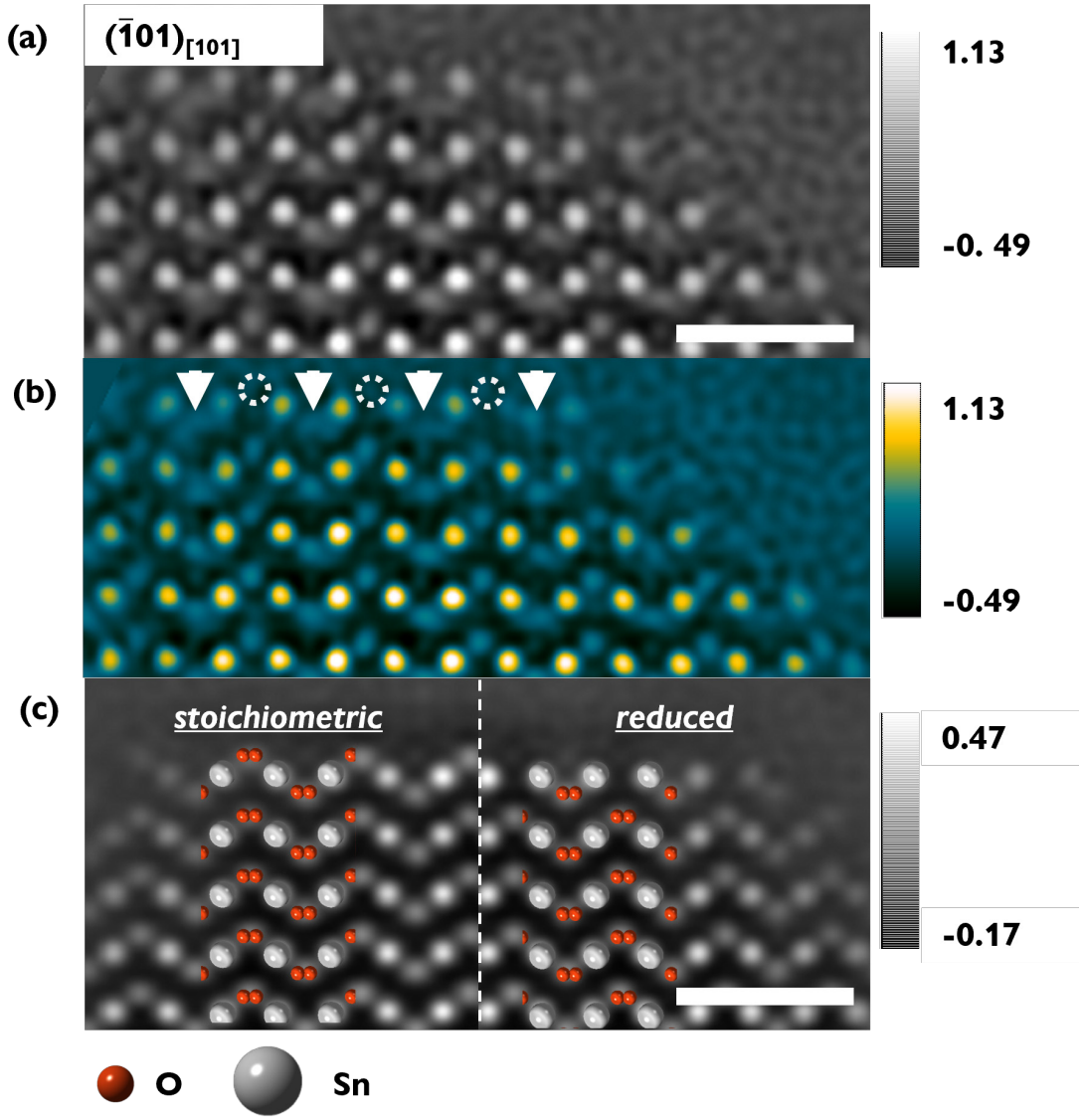

Figure 4.19: (a) Experimental reconstructed phase of a 0.5 wt% Pd-SnO_2 nanoparticle oriented along [101] exposing a Sn-terminated stepped ($\bar{1}01$) facet and its (b) false colourmap. The dashed white circles and arrows in (b) show bridging O vacancy positions and three-fold coordinated O atoms, respectively. (c) Stoichiometric (left) and reduced (right) reconstructed phases, obtained from simulated focal series. Atomic model overlays of the stoichiometric (O-terminated) and reduced (Sn-terminated) surfaces are also shown in (c). The scale bars represent 10 Å in all cases.

4.3.1.3. {010} facets

Figure 4.20 shows a (010) facet along the [101] zone axis of a 0.5 wt% Pd-SnO_2 nanoparticle. The contrast indicates that this facet is fully reduced as no

bridging O atoms are visible by visual comparison with the simulations. In the left region of the nanoparticle however, there are O atoms (shown with yellow arrows) overlaid by a diffuse layer of atoms as was observed on the $((\bar{1}10)_{[111]}$ facet (Figure 4.15) indicated with white arrows. Following a similar argument to Figure 4.14, these atoms may correspond to undercoordinated low occupancy Sn and C atoms (see insert in Figure 4.20 (a) and refer to Appendix A, Figure A.11 ((a) and (b) for full details). The fact that a fully reduced surface is observed is consistent with theoretical findings showing that this surface is Sn-terminated at low $O_{2(g)}$ partial pressures[29].

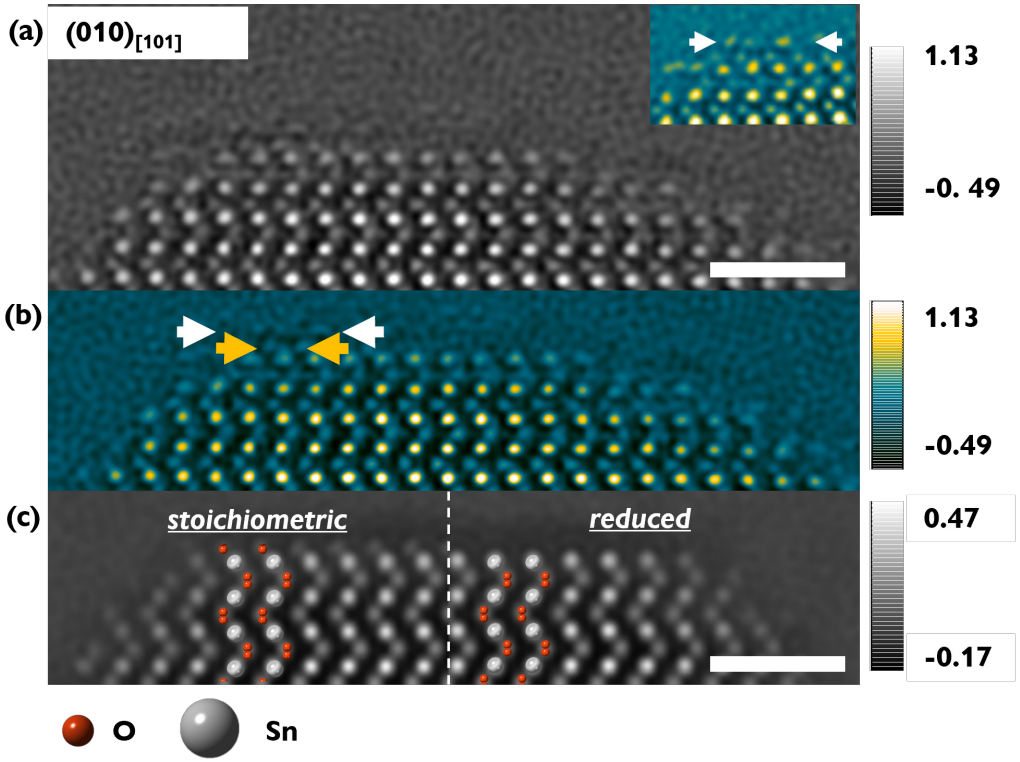

Figure 4.20: (a) Experimental reconstructed phase of a 0.5 wt% Pd-SnO_2 nanoparticle oriented along [101] exposing a reduced stepped (010) facet and its false colourmap (b). In (b), in the upper left region of the nanoparticle, a diffuse layer of Sn atoms is shown indicated by white arrows, while oxygen surface atoms are indicated by yellow arrows. (c) Simulated phases of O-terminated (stoichiometric) and Sn-terminated (reduced) surfaces and corresponding atomic model overlays. The scale bars represent 10 Å in all cases.

EWR shows that the (010) and {101} facets are present in a reduced form for sub-10 nm nanoparticles. The analysis also indicates, by a qualitative visual comparison with the simulations, that these are Sn-terminated. These findings agree well with theoretical studies by DFT, and STM/LEED investigations on reduced SnO_2 bulk single crystals. According to the latter, non-stoichiometric SnO units cover the bulk following the loss of bridging O atoms. Charge compensation is re-established by the reduction of Sn^{4+} to Sn^{2+} without further surface reconstruction[38]. Thus, the termination observed for the surface of the

nanoparticles does not differ from that of the reduced bulk crystal surface, observed under low $O_{2(g)}$ partial pressures. However, for the (110) facet (observed on a [001] oriented nanoparticle), a surface reconstruction was observed for the first time. This reconstruction is in close agreement with several models in literature[37,167]. A summary of the surface terminations is given in Table 4.7.

Table 4.7: Facets observed in this study for 0.5 wt% Pd-SnO_2 nanoparticles along with their terminations. A comparison with DFT and STM/LEED surfaces reported in the literature is also shown. The Sn_i atoms are related to (110) surface reconstructions.

Facets	**Projections**	**Terminations**		
		Experiment	**DFT**	**STM/LEED**
{010}	[101]	Sn	Sn[29]	Sn[29]
{101}	[101], [100]	Sn	Sn [29]	Sn [29]
{110}	[001],[110],[111]	Sn_i /SnO	Sn_i[37,65,167]/in-plane SnO[3,33]	Sn_i[34]/in-plane SnO[3,70]

4.3.2. Single O atom sensitivity study: simulated focal series

It has been demonstrated that SnO_2 surfaces are reduced and Sn-terminated. Relative to Sn, O atom columns produce a weaker phase shift which may be corrupted or masked by dose-dependent noise at the vacuum-facet interface. In this section, I examine using simulations whether the cumulative doses used in this study for the focal series acquisition are sufficient for single O atom

sensitivity. These simulations account for the correct transfer of both the signal and noise of the detector by including the experimental MTF and NPS as described in section 3.5.1. Secondly, I examine the lower bound limits for the cumulative dose of the focal series before the loss of single O atom sensitivity. Finite dose focal series were simulated for all experimentally observed projections of the SnO_2 model. The complex exit waves were then restored, and the phases of the stoichiometrically terminated facets were quantified. Specifically, the O atom columns with a maximum occupancy and 2 of their nearest neighbours were quantified for all facets of the SnO_2 model nanoparticle[4]. The quantification measures the average phase shift per single O atom, and its standard deviation, as demonstrated in section 4.2.6 (see Figure 4.13, for an example on the $(011)^{6}_{[100]}$ facet).

Subsequently, the SNFR values were calculated using equation 4.2, as shown in Table 4.8. At a focal series cumulative dose range of 35-137x10^3 $e/Å^2$, the SNFR values for all projected facets are between 4.3 to 11.5, hence higher than SNFR = 3 as required by the Rose criterion for single atom sensitivity (see later for details)[171]. This also indicates that the cumulative dose employed in the experiments lies within the range of doses where single atom sensitivity is

[4]Herein, the hkl indices in parenthesis, (), and square brackets, [], show the facet plane, and the projection of the nanoparticle, respectively. The superscript between these two indices indicates the maximum occupancy of the surface O atom columns for that given projection i.e., $(hkl)^{n}_{[hkl]}$ (also see Table 4.8)

maintained. This finding also suggests that if there were single O atoms present on the facets of the nanoparticles, their signal in the reconstructed phase would be sufficient for visibility above the background noise. This further indicates that, when no O signal was detected in the experimental images, the surfaces are effectively Sn-terminated.

Table 4.8: A summary of the signal-to-noise fluctuation ratios (**SNFR**) at the vacuum/nanoparticle surface interface for different nanoparticles projections and cumulative doses in the simulated focal series.

Facet$^{\mathbf{occ}}_{\mathbf{zone}}$	**Cumulative dose x10$^{\mathbf{3}}$(eÅ^{-2})**	**SNFR**
$(011)^{6}_{[100]}$	54	5.0 (0.18)
$(110)^{13}_{[001]}$	137	11.5 (0.07)
$(1\bar{1}0)^{3}_{[110]}$	58	7.3 (1.13)
$(\bar{1}01)^{10}_{[101]}$	57	4.7 (0.10)
$(100)^{3}_{[101]}$	57	5.4 (0.27)
$(\bar{1}10)^{4}_{[111]}$	35	4.26 (0.26)

In general, nanoparticle surfaces are comprised of undercoordinated atoms which have lower binding energies compared to their bulk counterparts. This makes them susceptible to electron beam damage which may alter the termination during electron imaging. It is, therefore, worth exploring what the minimum cumulative dose necessary to achieve O single atom sensitivity is, O being the lightest element in the material which is the most susceptible to damage. This is important as it guarantees that the nanoparticles are not unnecessarily exposed to damaging radiation during recording of the focal series, while it also ensures light atom sensitivity.

Noiseless focal series damped by the MTF were simulated for all experimentally observed projections of the SnO_2 model. Their exit waves were restored, and their phases quantified, as described in section 4.2.6**,** to establish a ground truth from which deviations of the O phase shift of a single atom are solely attributable to finite dose noise. The expected phase shift for a single O atom is shown in Figure 4.21 (a) for different crystal projections and atomic facets (dashed lines). The value obtained for the $(110)^{13}_{[001]}$ and $(1\bar{1}0)^{3}_{[110]}$ surfaces is significantly larger than that obtained for the remaining facets at all doses. This can be explained by the proximity of the O columns to heavy Sn atom columns and their overlap (see Figure A.4, in Appendix A). To quantify the effect of column overlap, a comparison between the O phase in the SnO_2 crystal lattice and the O sub-lattice alone was made (model shown in Figure A.4, of appendix A). From this calculation it was found that the average O phase shift in the former is 0.039 rad (red dashed line (shown in Figure 4.21 (a)) compared to 0.033 rad (red solid line) in the latter for the $(110)^{13}_{[001]}$ case, and 0.040 rad (green dashed line) compared to 0.029 rad (green solid line) in the $(1\bar{1}0)^{3}_{[110]}$ case. These values are comparable to the average O phase shift from all the other projections 0.030 (0.002) rad. This indicates that the average phase shift of a single O atom column is a result of the complex interplay between atomic number in projection, focus and height, and it includes influences of

neighbouring atom columns which varies according to the separating distance [164,165].

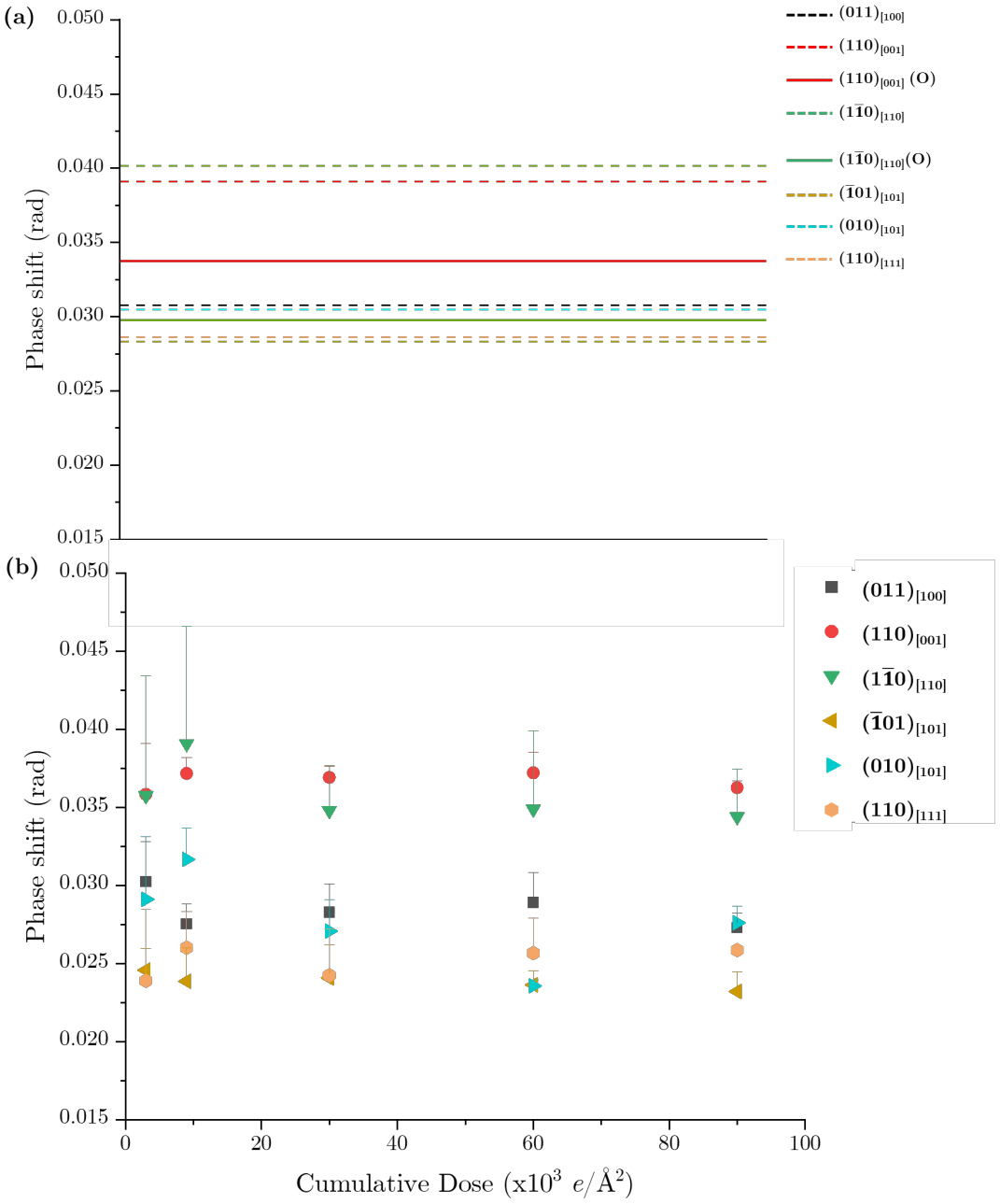

Figure 4.21: (a) Plots of the average phase shifts from single O atoms obtained from noiseless focal series data damped by the MTF (dashed lines), for different facets in projection of a SnO_2 model nanoparticle. For the $(110)^{13}_{[001]}$ and $(1\bar{1}0)^{3}_{[110]}$ facets, the phase shifts of single O atoms from the O sub-lattice only are also shown as solid lines. (b) Data points showing the phase shifts obtained for a single O atom at finite doses. The colour of the data points corresponds to the same projection in the infinite dose calculations. To aid visibility only the positive error bars of the data points are shown.

Finite dose focal series, with doses ranging from 100 $e/Å^2$ to 3000 $e/Å^2$ per frame, were also simulated and the exit wave was restored. The phase shift of a single O atom was again quantified for a given projection as above. The results are plotted in Figure 4.21 (b) and are shown as data points with colours identical to the noiseless case. The standard deviation was used as the error bars on the plots. In Figure 4.21 (b), all projections have slightly varying O phase shifts and associated errors, following the trend observed for infinite dose phase shifts in Figure 4.21 (a).

For all cases the effect of the finite dose noise is to damp the expected phase shift. This is especially true at low dose, where fewer electrons reach the detector plane; the wave signal in this case is poorly sampled and is consequently corrupted by the detector noise. As expected, the error in the phase for a single projection decreases as a function of cumulative dose. The standard deviation of the noise also decreases with cumulative doses, meaning that the influence of the noise on the signal is lower. Similarly, the errors induced by noise decrease with increasing occupancy for different projections of the same surface. For example, atom columns with lower occupancy, such as the ones present at the $(1\bar{1}0)^3_{[110]}$ facets, will generate a small overall phase shift and thus, for a given cumulative dose, noise contributions become significant relative to the signal than for higher occupancy columns, e.g. $(110)^{13}_{[001]}$, especially at lower cumulative doses. This indicates that for

quantitative purposes[85] the accuracy of atom counting for light atoms at the surface will increase with occupancy and dose.

Figure 4.22 shows the variation of SNFR values calculated using equation 4.2 for a single O atom as a function of cumulative dose for differently projected atom columns on stoichiometrically terminated facets. The error bars in this figure were calculated as the standard deviation of the phase of a single O atom as obtained in Figure 4.21. The black dashed horizontal lines signify the range of the SNFR ≥ 3 which is the minimum required for single atom visibility according to the Rose criterion[171].

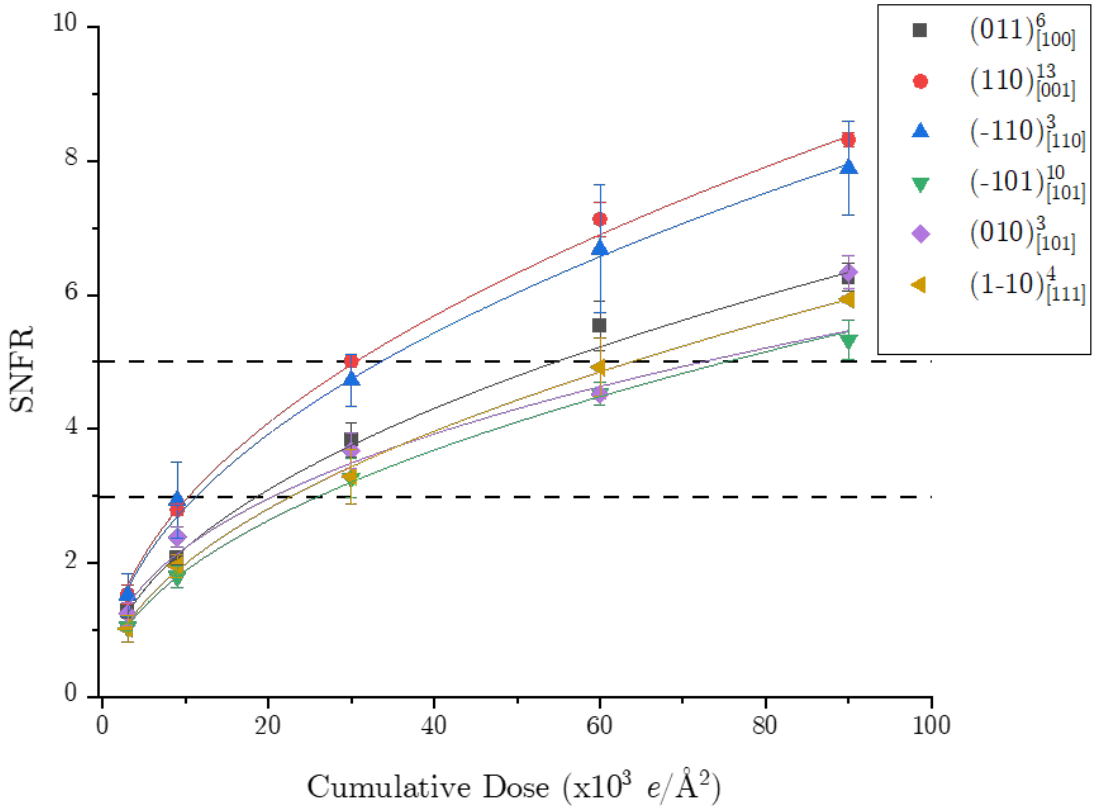

Figure 4.22: SNFR for a single O atom as a function of cumulative dose for the facets of interest in the respective zone axis. The black dashed horizontal lines signify the range of the minimum SNFR values greater than 3 required for single atom visibility.

As expected from the infinite dose calculation, the relative SNFR values obtained for single O atoms in the $(1\bar{1}0)^{3}_{[110]}$ and $(110)^{13}_{[001]}$ facets are larger than those obtained for all other projections because of the overlap with Sn atom columns. When the O signal is not strongly influenced by the overlap with Sn, an average minimum cumulative dose of 21.8 (2.9) x 10^3 $e/Å^2$ is sufficient to achieve single O atom sensitivity (the dose range was obtained by interpolating the data points in Figure 4.22 with power law functions (see Table A.1, in Appendix A)). This also confirms that the cumulative doses employed in this study to acquire the focal series data are sufficient to attain single O atom sensitivity with the detector used. It also means that, in principle, if single O atoms were present at the surface of the specimen, they would generate a signal above the detection noise. In the next section, I evaluate if the range of doses used in the experiments induces irreversible damage at the surface.

4.3.3. Surface dynamics

For the analysis of the surface dynamics all the experimental focal series were segmented into three parts and the waves restored separately from each part in order to compare the surface structure with that obtained from the restoration of the full focal series. The surface dynamics are qualitatively examined to determine if any significant changes occur in the bulk and at the surface of the nanoparticles with beam exposure. Secondly, the critical cumulative dose at which surface changes become significant is determined.

This is the point where exposure to the beam alters the surface significantly beyond the termination observed at the start of the focal series.

Surface transformation of the specimen can be examined provided that the surface changes happen within the time resolution used in the experiment. In the case where the transformation is faster than the time resolution (400 ms in this study), then the surface features will not have any periodicity, but instead will appear diffuse[172]. The rate at which surface transformations occur depends on the mechanism type as well as the activation energy threshold, i.e., the activation energy of surface diffusion[156]. Structural transformations can be induced by the electron beam and/or thermal effects. Surface changes induced by the electron beam can be driven either by radiolysis (inelastic electron-electron interactions) and/or knock-on damage (elastic electron-nucleus interactions)[173]. The objective of this section is to assess whether a change on the specimen surface occurs during electron beam exposure, independent of the dominant mechanism of damage. Determining the type of damage is beyond the scope of this work.

Focus will be given to the (110) surface reconstruction, shown again in Figure 4.23, since its structure deviates from what has been observed in the literature, as discussed in section 4.3.1.

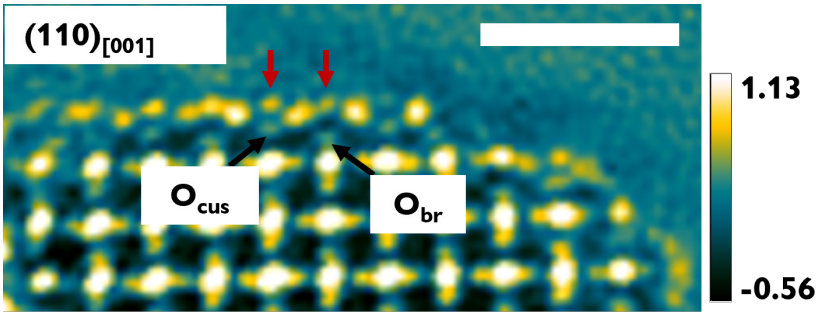

Figure 4.23: False colourmap reconstructed phase of the $(110)_{[001]}$ surface as in Figure 4.16. The red arrows indicate contrast above bridging O (O_{br}) and on-top O (O_{cus}) atom columns, contrary to reports in the literature[31,156]. The scale bar is 10 Å.

In Figure 4.24, the phase restored using the first (a), second (b) and, last (c) 10 images of the 30-image focal series are shown along with the corresponding log moduli of the Fourier transforms (d-f) of the complex exit waves. The likely differences in information transfer were quantified by plotting the effective contrast transfer functions (ECTF) for each 10-image member restoration[138]. The ECTF calculation accounts for the spatial (E_s) and temporal (E_t) coherence envelopes and the phase shift due to the wave aberration function ($\chi(q)$) for each image[144]. The defocus values used were derived from the FTSR predicted values (see section 3.7). No gaps are observed on the ECTFs for all the restorations (see appendix A, Figure A.5 and Figure A.6). Therefore, the contrast variation of the exit wave phases in Figure 4.24 is not due to differences in their information transfer but to actual specimen changes. In addition, none of the relevant spatial frequencies have been suppressed as shown through the superimposed reciprocal distances of all Sn-Sn, O-O and O-Sn in the projected unit cell (Figure A.5 and Figure A.6 in appendix A).

At the start of the series (Figure 4.24 (a)) the surface termination was largely composed of Sn_i and Sn_b atoms and some $O_{\mathbf{cus}}$ (x2) atoms (yellow dashed circles). This is contrary to the structure observed in the phase restored using all 30 images where O atoms are not clearly distinguishable from the noise (Figure 4.23). It is possible that additional terminating $O_{\mathbf{cus}}$ atom columns may have been present at the start of the focal series acquisition but were removed during subsequent acquisition. Thus, the phase shift associated with these columns may progressively cancel out with vacuum noise as more images without the $O_{\mathbf{cus}}$ atoms are added to the restoration. In Figure 4.24 (a), the surface also has Sn atoms in bulk lattice positions (grey arrows, Sn_b) as well as at interstices (orange arrows, Sn_i). It is assumed that the contrast at the interstices can only be due to the presence of Sn_i, as these have been predicted to have lower formation energies at low $O_{2(g)}$ partial pressures compared to that of O interstitials, which have prohibitively high formation energies [7] and typically require $O_{2(g)}$ rich conditions to form[43], contrary to the experimental conditions used here. In addition, the atoms at the interstices are thought to be Sn atoms because their phase shifts are visually comparable to those of the Sn atoms in the bulk Sn positions. Sn_b at the edges of the nanoparticle have lower phase shifts compared to those at the centre of the nanoparticle. Despite their low phase shifts, these cannot be attributable to O antisite defects as they

are theoretically predicted to have prohibitively high formation energies under all pressure and temperature conditions[7].

In Figure 4.24 (a) the interlayer distance between the second atomic plane with Sn_i and Sn_b on the surface is 2.8 (0.1) Å and 3.4 (0.1) Å, respectively. The interlayer distance of Sn_b is consistent with that measured in the bulk of the nanoparticle (3.4 (0.1) Å), validating that these atoms are indeed Sn_b. Here the bulk of the nanoparticle is defined as a minimum of 3 atomic planes away from the surface in all <110> directions. To date, the only theoretically predicted model to possess a surface composed of Sn_i and Sn_b is the (4x2) reconstruction predicted by Ágoston and Albe (2011)[167]. Their proposed model is thought to be a structure with a small stability range that is composed of superimposed sequences of Sn_2O_2 strands with partially reduced (loss of $O_{\mathbf{br}}$ only) sections in the [001] direction. In this model all the Sn_b in the partially reduced sections are coordinated to surface $O_{\mathbf{ip}}$ atoms. The Sn_i atoms in the Sn_2O_2 strands relax into the interstitial positions[167] which is consistent with the observed motif in the [001] direction, in this study.

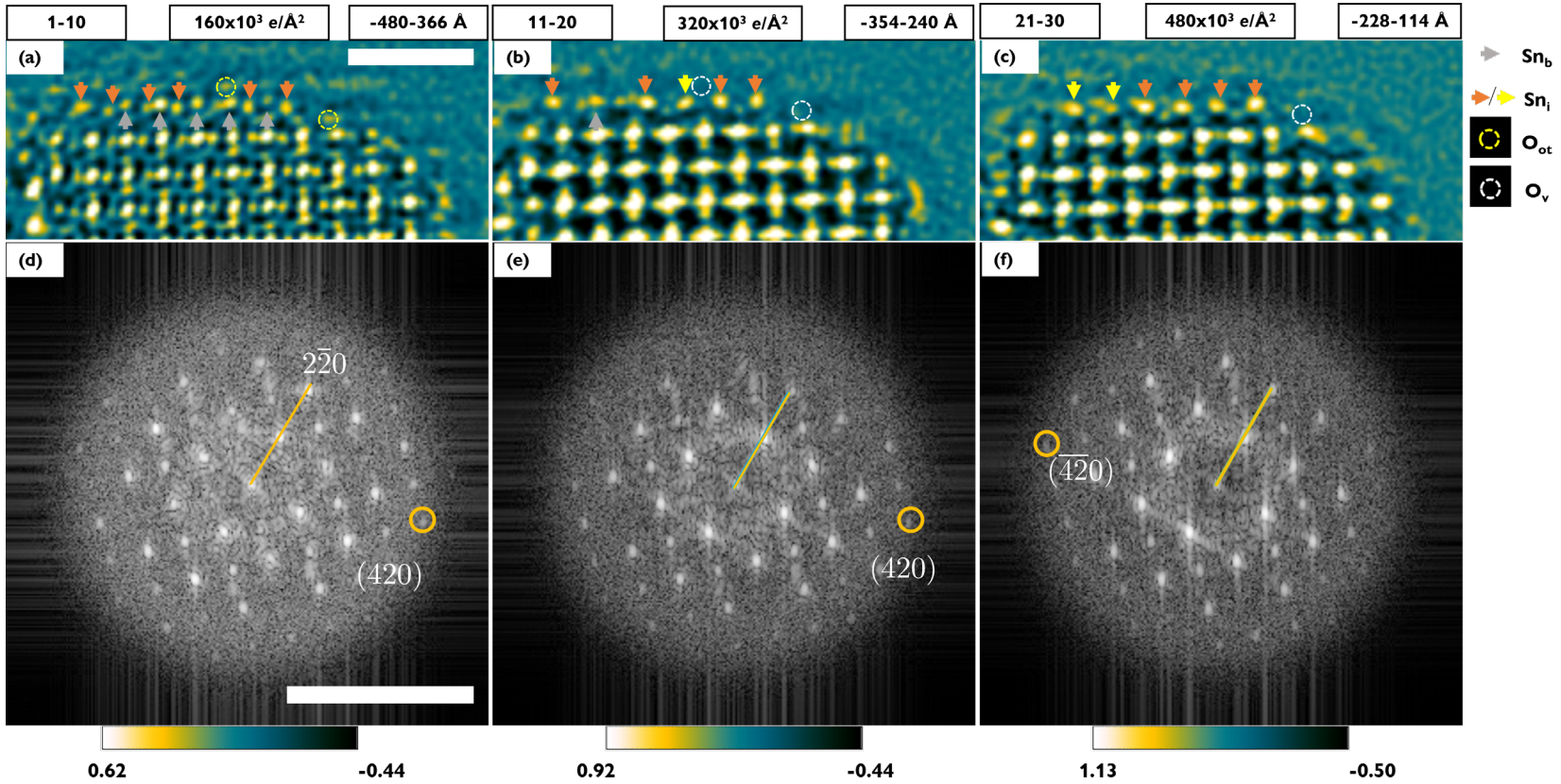

Figure 4.24: Phases of a [001] oriented nanoparticle restored using the first (a), second (b), and third (c) third of the 30-image focal series. The cumulative dose at a given point in time is shown as well as Sn atoms in bulk lattice positions (grey), interstitial positions (yellow/ orange arrows) as well as O atoms (yellow dashed circles) and their vacancies (white dashed circles) that progressively appear compared to the previous phase. Each restoration had a cumulative dose of 45.7x10^3 $e/$Å^2(O SNFR = 6). Below each phase is the log modulus of the Fourier transform of the restored complex exit wave. These indicate that the nanoparticle did not rotate but underwent some slight tilting with time as seen in the asymmetry of the Fourier components (d-f).

With time, the surface loses more Sn_b and begins to resemble the (110) (2x1) surface reconstructions proposed by Ágoston and Albe (2011) and Li et al. (2021), as shown in section 4.3.1.1. Comparing Figure 4.24 (a) and Figure 4.24 (b), there are four less Sn_b atom columns in (b), an additional Sn_i column as well as two $O_{\mathbf{cus}}$ vacancies (indicated with dashed white circles). The additional Sn_i atom presumably comes from the partially reduced sections of the (4x2) reconstruction. This suggests that some Sn_b atoms migrate to and relax into interstitial positions to compensate for the charge imbalance induced by the loss of $O_{\mathbf{ip}}$ atoms[34]. Kiliç and Zunger (2002), have proposed that there is a mutual attraction of Sn_i and O_v, making this Frenkel defect pair much more stable under low $O_{2(g)}$ partial pressure conditions[7]. More significantly, their study demonstrated that the presence of Sn_i significantly lowers the formation of O_v. Evidently, the Sn_i atom columns are more stable to thermal/electron irradiation effects than Sn_b, as the number of Sn_i atoms gradually increases during imaging to the end of the focal series acquisition as seen in Figure 4.24 (c).

As already discussed, Li et al. (2021) performed *in situ* AC-STEM on {110} facets of micron sized cuboctahedra of SnO_2[37]. Their study primarily focused on the formation and characterisation of the high temperature (>1073 K) (1x2) surface reconstruction of SnO_2. Their DFT-relaxed and validated (2x1) model for the 'metastable' intermediate reconstruction leading to the formation of the

high temperature (1x2) model from an initially bulk terminated surface was generated from HAADF image analysis. The projected contrast of the surface reconstruction is consistent with that of the (2x1) reconstruction proposed by Ágoston and Albe (2011) as discussed in section 4.3.1. Li et al. (2021), however, provide strong evidence for their proposed model by validating the thermal stability of their proposed (2x1) surface reconstruction using DFT calculations. Their proposed model with a glide plane along which alternating Sn_i units are coordinated to the bulk through O atoms creating a zig-zag surface pattern is geometrically consistent with both the theoretical calculations by Liu et al. (2022)[41] (as derived from Ágoston and Albe (2011)) as well as the STM observations by Sinner-Hettenbach (2001)[69].

The interplanar distances measured in the bulk, from the reconstructed layer to the bulk and between Sn_i atoms on the overlayer are consistent with the measurements obtained in Figure 4.24 ((b) and (c)) and are summarised in Table 4.9. Based on the current evidence it can be concluded that the (4x2) surface reconstruction progressively forms a (2x1) surface reconstruction under the employed imaging conditions.

Table 4.9: Comparison between the interatomic distances measured from bulk and surface atomic planes for the (2x1) surface reconstruction observed in this study and that of Li et al. (2021)[37].

Author	**Sn_i - bulk (Å)**	**Sn_i – Sn_i (Å)**
Li et al. (2021)	3.1 (0.2)	3.5 (0.3)
This study	2.9 (0.2)	3.5 (0.2)

It will be shown in the next chapter that in TEM-based techniques the observed surface reconstructions are also electron dose/dose rate dependent. Previous work on *in situ* AC-STEM studies have alluded to the importance of the role of the electron beam in the reconstruction pathway. Yuan et al. (2017), suggested that a previously unobserved intermediate structure of the (001) surface leading to the formation of the (1x4) reconstruction on TiO_2 formed through electron beam stimulation[93].

No bulk damage was detected on the nanoparticle despite it being exposed to a large total dose of 479 x 10^3 $e/Å^2$ at a dose rate of 11 419 $e/Å^2s$. The log moduli of the Fourier transforms show no loss of crystallinity and exhibit identical maximum intensity in the {420} reflections at a real space distance of 1.05 Å. There are also no additional reflections which might signify a phase change with time. However, visible asymmetry can be observed in the distribution of the reflections when comparing the log moduli of the Fourier transforms, indicating that the nanoparticle was tilting about the [001] axis during imaging. The nanoparticle did not undergo any measurable rotation in

the plane perpendicular to the imaging direction. This is evidenced by the unchanged relative position of the yellow line placed from the (000) to the $(2\bar{2}0)$ reflections in (d) compared to the green (e) and blue ones (f), respectively. Nonetheless, the nanoparticle shows a distortion of the O sublattice which characteristically occurs when there are Sn^{2+} ions in the bulk of SnO_2[174] suggesting that the nanoparticle is undergoing bulk reduction under these imaging conditions.

All the other focal series obtained for the remaining projections in this study were similarly divided into three segments and analysed (see Figures A.7-11 in Appendix A). Comparing the structure obtained from the first 10 images shown in Figures A.7-11 (a) of the focal series with the final restoration (Figures A.7-11 (c)) it was found that the surface terminations of the full series do not generally change with beam exposure. The damage is limited to the loss of individual Sn atoms, presumably accompanied by the creation of O_v, which is usually observed on all facets as shown with white dashed circles in Figures A.7-11 ((b) and (c)). This loss is typically confined to undercoordinated step edges i.e., on the $(1\bar{1}0)_{[110]}$, $(\bar{1}01)_{[101]}$ and, $(\bar{1}10)_{[111]}$ facets or on a few unit-cell wide surface atomic terraces such as that observed on the $(010)_{[101]}$ facet.

A comparison of the log moduli of the Fourier transform of the complex exit waves of the nanoparticles with time demonstrates that they undergo no loss of crystallinity or phase change. They do, however, indicate some mis-tilt. The

[110], [111] and, [101] oriented nanoparticles also exhibit slight particle rotation (≈≤2°) orthogonally to the beam direction. These findings suggest that the nanoparticles are indeed reduced and exhibit no surface reconstructions as shown in section 4.3.1 despite exposing them to relatively high total cumulative doses. The $(010)_{[101]}$ facet has a critical cumulative dose (d) which is between $132\text{x}10^3$ $e/\text{Å}^2$ ≤d ≤ $198\text{x}10^3$ $e/\text{Å}^2$ at the employed dose rate. The surface chemistry changes from being purely Sn-terminated to exhibiting a mixed O- and Sn-termination above a total cumulative dose of $198\text{x}10^3$ $e/\text{Å}^2$ (Figure A.11 (c)).

Additionally, the $(110)_{[001]}$ has a critical cumulative dose below $160\text{x}10^3$ $e/\text{Å}^2$ at the employed dose rate. Beyond this point the surface only exhibits an Sn-terminated surface. However, all the other facets do not exhibit any surface chemistry change indicating that they have higher critical cumulative doses than the total cumulative doses employed in this study.

Other additional surface properties such as exposed undercoordinated Sn atoms on step-edges in addition to those observed on facet terraces and local surface strain[175,176] (grey arrows in Figure A.7 (a)) as well as planar defects[177] (Figure A.9) have been shown to enhance selectivity and activity of SnO_2-based nanomaterials in CO_2RR.

4.4. Conclusions

The local surface structure of sub-10 nm 0.5 wt% Pd-SnO_2 nanoparticles was characterised at atomic resolution using aberration-corrected focal series EWR. Its low energy facets were studied for the first time for this specific nanoparticle size range. The data demonstrated that the {010} and {101} facets are largely Sn-terminated, confirming findings from previously reported DFT and STM/LEED studies. These facets were also shown to be robust against significant electron-induced surface termination alteration under the imaging conditions. The {110} surfaces of the [110] and [111] projected nanoparticles was shown to be reduced with an SnO termination. Contrary to the other facets, the [001] oriented (110) surface exhibited dynamic surface transformation. The nanoparticle surface transforms from a (4x2) projected structure to a (2x1) reconstruction that is identical to that proposed in theoretical and more recently experimental literature[37,167]. Additionally, it was also shown retrospectively, using multislice simulations that include relevant detector parameters, that single O atom sensitivity was attainable under the chosen imaging conditions.

5. Surface chemistry of beam-induced surface reconstructions on {110} facets

5.1. Introduction

The previous chapter demonstrated that there is general agreement between the termination chemistry of nanoparticle facets observed with conventional focal series (CFS) exit wave reconstruction (EWR) and that calculated theoretically for SnO_2 under low $O_{2(g)}$ partial pressure and under the reducing influence of the electron beam (as in the electron microscope) [33,38]. Under these conditions, the {100} and {101} facets were shown to be reduced and more stable than their stoichiometric counterparts. The (110) facet is more dynamic, undergoing surface rearrangements with increasing cumulative dose, eventually transforming this surface into the (2x1) surface reconstruction. This surface

rearrangement involves the ordering of Sn_i in agreement with the corresponding model proposed by Li et al. (2021)[37]. Using CFS, this reconstruction was observed at atomic resolution on sub-10 nm nanoparticles for the first time.

During surface reconstruction, atoms undergo several dynamic processes that include bond breakage/formation, fluxionality (dynamic reordering of local atomic arrangement), and atom diffusion. Bond-related processes typically occur at picosecond (ps) to femtosecond (fs) temporal resolution and cannot be observed through conventional AC-TEM imaging[178]. Dynamical TEM has the necessary temporal resolution to observe the above processes, however, it has poor spatial resolution primarily limited by space-charge effects[179,180].

In TEM, the loss of surface anions in inorganic nanoparticles gives rise to fluxionality in the cation sublattice which has been observed at atomic resolution[79,181] or computed[182] in the millisecond (ms) and ps temporal resolutions, respectively. For surface cations in low coordination sites, such as step-edges, fluxionality may progress to atom diffusion under the influence of the electron beam and/or thermal effects due to their low binding energies to the bulk lattice[156]. Diffusion may lead to metastable local atomic reconfigurations which can be observed within the s-µs temporal resolution regime at atomic resolution [79,181,183].

With the recent advent of direct electron detectors and fast electrostatic deflectors dynamic processes such as fluxionality and diffusion have been

successfully observed in the TEM with millisecond (ms) to microsecond (µs) temporal resolutions and with high spatial resolution[79,181,183–185]. These studies have been typically conducted through the analyses of AC-TEM time series data. In this work, the temporal resolution of CFS is improved by recording images in continuous readout mode (video mode) albeit on an integrating CMOS detector. This approach, termed fast focal series (FFS), enables a temporal resolution of ca. 10 ms (per frame) and sub-nm spatial resolution to capture dynamic events[186].

Using the FFS method, this chapter examines the dynamics of the surface reconstruction of the {110} facets, projected in the [001] direction at various dose rates (≈1000 – 11000 $e/Å^2s$) and increasing cumulative doses (up to ≈ 500 x 10^3 $e/Å^2$). The surface reconstructions observed on the (110) facet of the [001] projected nanoparticle in the previous chapter will be compared to those attained through FFS at lower dose rates but at comparable cumulative doses.

This chapter also examines possible sources of poor temporal resolution in CFS (section 5.2.1). The image processing and calibration details of the FFS acquisition method are given in section 5.2.2, and the FFS restoration procedure is discussed briefly in section 5.2.3. The exit waves restored from the FFS and used to examine the influence of the dose rate and the cumulative dose on the surface reconstructions are shown in section 5.3.1. In addition, the observed reconstructions and surface transformations are compared to several

proposed computational models, including low energy and metastable surface reconstructions.

5.2. Experimental methods

5.2.1. Effects of overhead time on dose and temporal resolution

Figure 5.1 compares the workflows for the FS scripts employed in this study: CFS1 saves the focal series into a stack, and FFS records the image while changing the OL focus in parallel. The main difference between these image acquisition methods is that the OneView camera operates in *single-shot* mode during a CFS, or in continuous *in-situ* (movie) mode during an FFS. Furthermore, in the CFS approach, the change of the OL defocus happens in series with the image recording, while during FFS the focus change is applied in parallel to the recording. In the workflow schematics, steps that require manual user input are indicated with blue borders. Both approaches include setting the pre-acquisition parameters, starting the image acquisition command, and stopping the image recording (FFS only).

Before image acquisition, the required user-defined parameters are the exposure time per frame (t_e), the camera binning (a binning of 1 corresponds to the full camera resolution 4kx4k pixels), the number of steps/focal planes (n_x), the focal

change step size (Δd) and the OL settling time (t_s) post-OL focus change (refer to Figure B.1, in Appendix B for the exact DM code). The OL settling time is specified to allow for the stabilisation of the objective lens with every focus change. Once the pre-acquisition parameters are set, the processes in the *for loops* are automatically executed by the script.

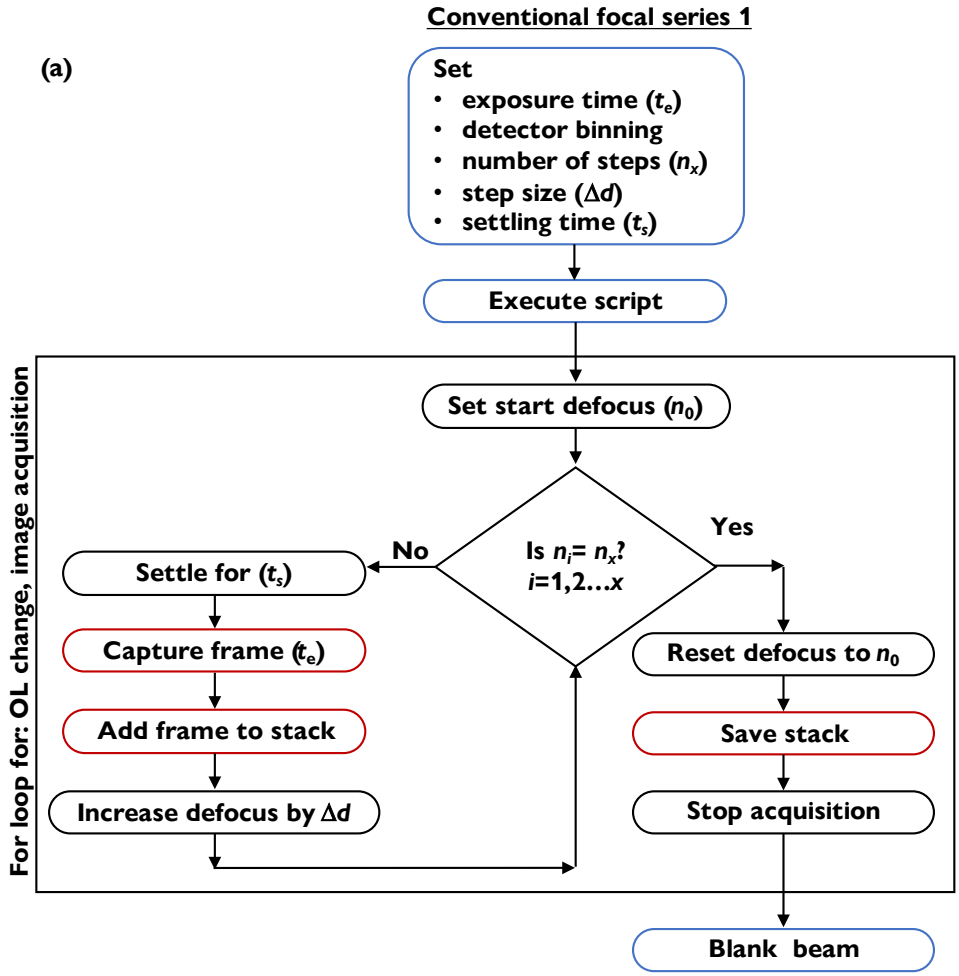

Figure 5.1: see the continuation of the image below for the full caption.

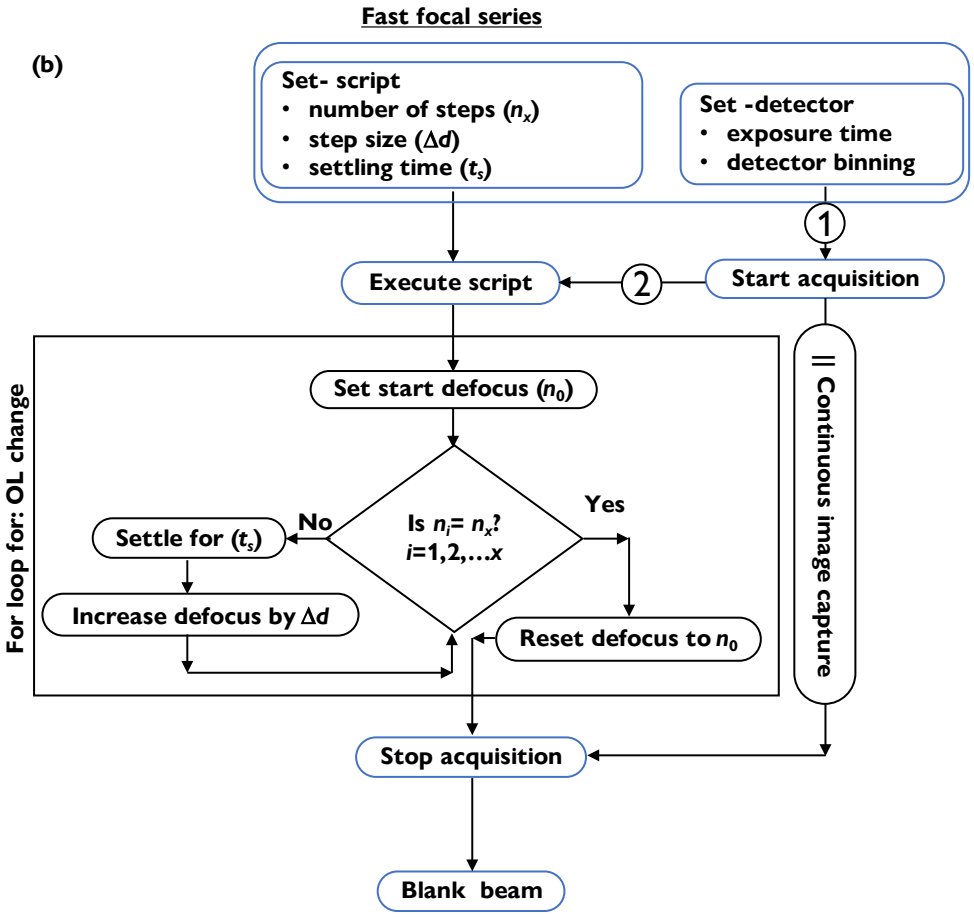

Figure 5.1: Full schematic workflows of (a) CFS1, and (b) FFS scripts. For all scripts, the processes that take place in the main *for loops* are automated and script driven whereas steps that require manual input are blue-bordered. However, the *for loop* indicating the automatic acquisition (continuous image capture) of images in a FFS is directly performed by the detector and not script driven. Refer to the main text for further details on pre-image acquisition parameters.

For the CFS, there is an overhead time (O_t) whose source was examined systematically as a function of all user-defined parameters. For an exposure time per frame of 0.4 s (as used in Chapter 4), the detector binning, the focus step size, and the OL settling time were varied, and their influence on the overhead time quantified. The overhead time, O_t is calculated according to equation 5.1:

$$O_t = t_t - n_x(t_e + t_s) \qquad 5.1$$

where t_t, refers to the actual total time it takes to acquire the CFS. To obtain the overhead per focal plane O_{tp}, O_t was divided by the total number of focal planes. Experimentally, t_t is obtained as the time difference between the first and last image of the focal series. Under the imaging conditions employed in Chapter 4, its average value was 125 (4)** s and subtracting the sum of all t_e and t_s per focal series gave an O_t of 83 (4) s. The value of 2.8 (0.1) s for the O_{tp} is obtained by dividing the overhead time by $n_x = 30$.

For the CFS script, it was observed that varying the step size per focal plane by 3, 9, and 20 OL bits had no effect on the overhead times, nor did it affect the total time for focal series acquisition (see Figure 5.2 (a-c)). However, changing the detector binning to 2 (2kx2k) and 4 (1kx1k) reduced the overhead time per focal plane marginally, by 0.1 s and 0.3 s, respectively, compared to a binning of 1 (4kx4k). This indicates that a small fraction of the overhead time is related to the size of the data recorded by the camera. Additionally, reducing the settling time to 0.5 s and 0.1 s was found not to affect the overhead time, but it did reduce the total acquisition time by 15% and 25%, respectively. Here the percentage was calculated relative to the total time of 1 s OL settling time. For a fixed exposure time, only changing the detector binning directly

** For time measurements the number in parenthesis is the standard deviation.

reduces the overhead time. All the other parameters do not have any influence on the overhead time. However, a 25% temporal resolution improvement can be achieved by changing the OL settling time from 1 s to 0.1 s.

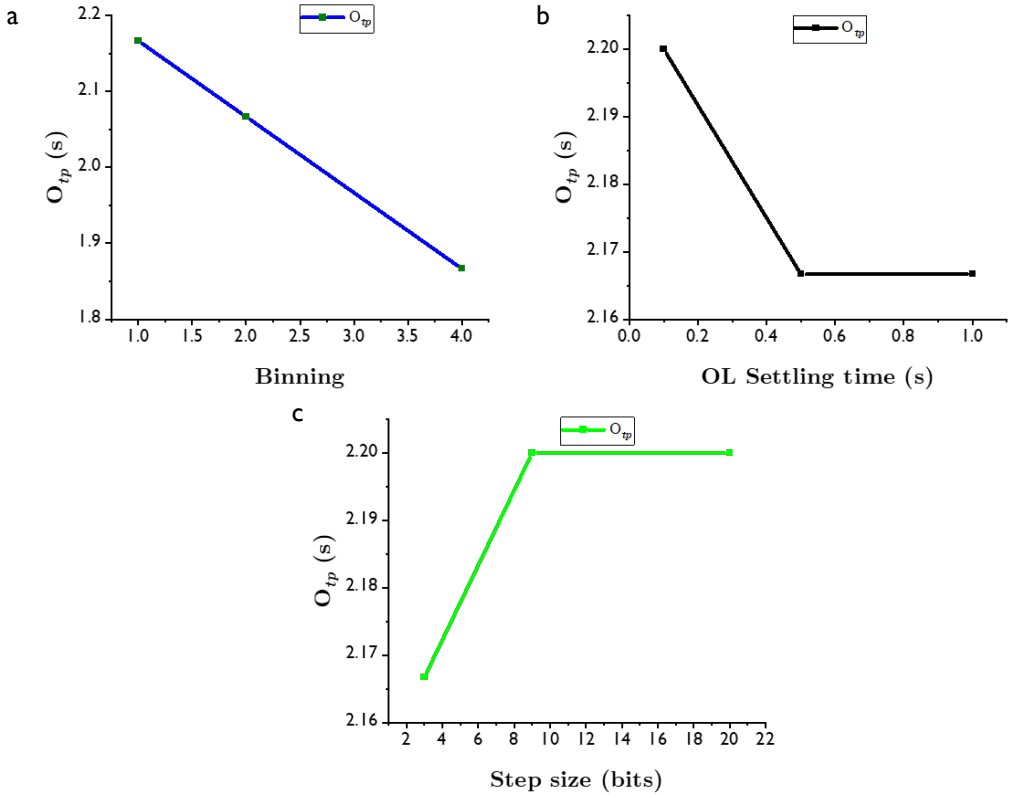

Figure 5.2: (a) Variation of the O_{tp} as a function of binning, (b) OL settling time and (c) step size during CFS.

Further examination of the metadata for the CFS data revealed that there was an additional default parameter, referred to as the specimen pre-exposure compensation (SPEC) value (see section 4.3.1 for more details). This parameter is constant and for the data presented in Chapter 4, it was set to values between 0.5-1.0 s by default.

The OneView automatically triggers the Gun deflector when it is processing images. This beam blanking prevents unnecessary electron exposure to the

specimen and the detector during this time. The frequency and the duration of the beam deflection were examined during CFS acquisition by monitoring the voltage of the deflector, using a digital oscilloscope. This enables quantification of the dose reaching the specimen.

Figure 5.3 shows voltage curves as a function of experimental parameters during a CFS and the SPEC. Blanking corresponds to a voltage of 5 V, and exposure corresponds to a voltage of 0 V. The units for the settling time and the SPEC are in seconds, while the focal step is in bits. The exposure time was fixed at 0.4 s for all experiments, while the OL settling time (1.0 s) and the SPEC (0 s) were kept constant under all experiments, except when their effect was being studied. Changing the focal step had no effect on either the exposure or blanking time. However, binning had a marginal influence on both the exposure and the blanking time. The OL settling time only affected the blanking time and not the exposure time, while the SPEC had a marginal effect on the blanking time but a notable effect on the exposure time. To minimise unnecessary beam exposure, the SPEC can be set to 0 and the binning can be optimised depending on the spatial frequency of interest in the experiments.

At a binning of 1, setting the SPEC and the OL settling time to 0 s would still result in approximately a 1.5 s gap between every image acquisition, due to software gain normalisation and dark correction. Thus, for a 30-image focal series imaged at 0.4 s acquisition time, this would translate to a temporal

resolution of a minute per restored wave. However, since in the experiments in Chapter 4, the SPEC and the OL settling time were 1 s each, the temporal resolution of those experiments is halved i.e., it takes 2 minutes to acquire focal series. Moreover, binning the detector by 4, with a SPEC and OL settling time of 0 s would result in a restored wave with a temporal resolution of 51 s. Evidently, for an integrating detector the temporal resolution of the restored waves from a CFS will be limited by the detector post-acquisition processing times.

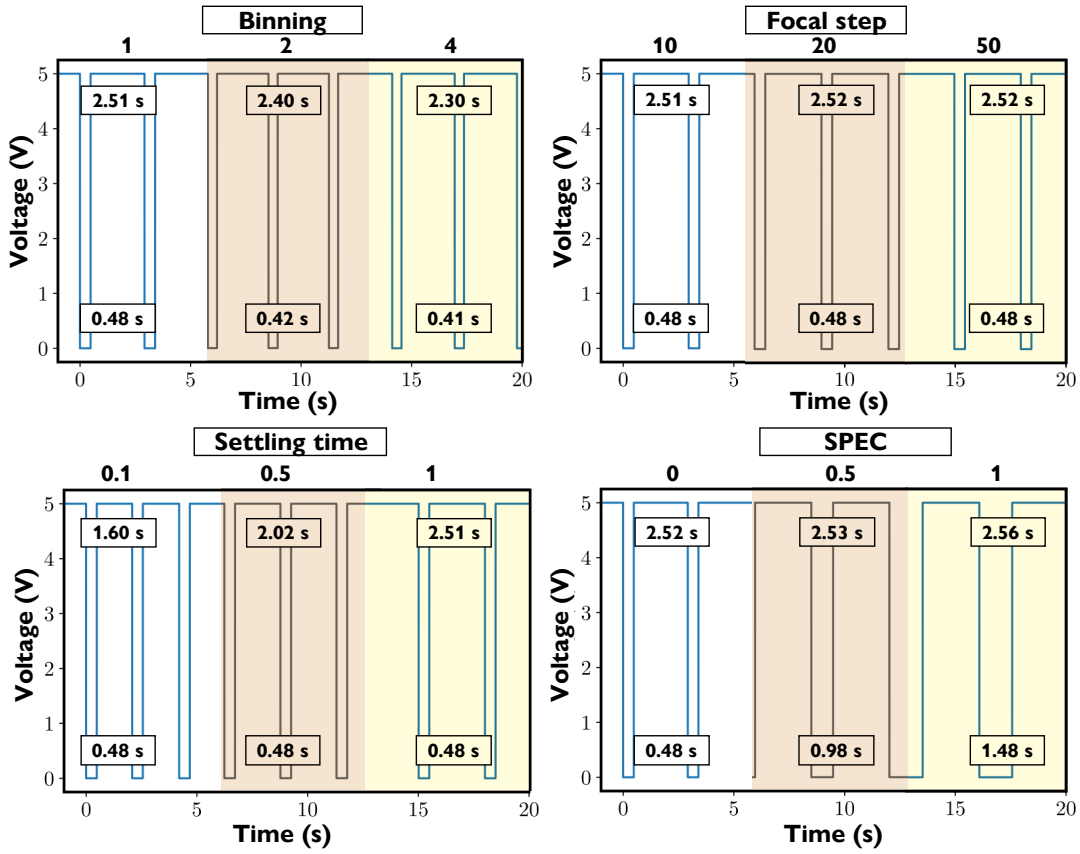

Figure 5.3: The influence of varying binning, focal step, OL settling time and SPEC on the blanking (top value) and exposure (bottom value) times during CFS.

The alternative FFS method circumvents the temporal resolution limitations due to detector post-acquisition processing times by imaging in continuous readout mode (*in-situ* mode). This method allows for the parallel acquisition of the images and the OL change (see FFS script workflow in Figure 5.1). In an FFS, the *for loop* only sets the number of focal planes/steps and the OL focus change. This reduces the overhead time down to 0.1 s per focal plane (measurement method detailed in the next section) and improves the temporal resolution of the restored waves to a quarter compared to data in section 4.3.1.

5.2.2. Post-acquisition image processing and calibrations

In the FFS experiments of this chapter, the objective lens (OL) reference defocus (n_0) is known and set between 200-500 Å. The initial (n_i) and final (n_f) defoci of the series are determined for every data set (see Figure 5.4 (a) and Figure 5.5), given that image acquisition and OL change are executed in parallel, not simultaneously (imaging is initiated before executing the OL change defocus script). After calibrating the OL focus step size in Angstroms per bit, n_i and n_f are calculated according to equations 5.2 and 5.3, respectively:

$$n_i = n_0 - 0.5 n_x \Delta d \qquad 5.2$$

$$n_f = n_i + n_x \Delta d \qquad 5.3$$

where Δd and n_x are the OL focus step size in bits and the total number of focal steps, respectively. The former was set to 3 bits/step and the latter was

typically between 30-40 steps. The total number of images per focal plane depended on the OL settling and the acquisition times, which were set to be 1 s and 0.04 s/frame, respectively. To determine n_i, Δd must be calibrated accurately. Once n_i is known, n_f can be extrapolated as a function of the defocus step size and the total number of steps set during FFS acquisition (see Figure 5.4 (a)).

3.1.1.1 Defocus step (Δd) calibration

To calibrate Δd a focal series movie was acquired on amorphous carbon. This movie was analysed using a GPU-accelerated CTF-fitting program called Gctf which estimates the OL defocus of each micrograph of the movie [187]. To determine the defocus value of each image Gctf maximises the cross-correlation coefficient (XCC) between simulated CTFs and the log amplitude spectrum†† (LAS) calculated from the experimental micrographs through a 1-dimensional (1D) search and 2-dimensional (2D) refinement ('1S2R') strategy. A 1D circularly averaged CTF is calculated from the LAS obtained from each experimental micrograph. Subsequently, this is numerically compared to a simulated 1D CTF and matched with the one having the highest XCC. This result is then used to seed a further 2D refinement of the defocus and astigmatism values. For further details on the program refer to Zhang (2016)

†† $\mathbf{LAS} = \log\sqrt{\mathbf{Re}^2 + \mathbf{Im}^2}$

[187]. The calibration of Δd was obtained using a high dose focal series movie of an amorphous carbon support acquired at 2 frames per second (fps) with an OL settling time of 2 s. On average 4 images were acquired per step. The number of steps, OL reference defocus and the focal step were set to 15, ≈3000 Å and 60 bits, correspondingly.

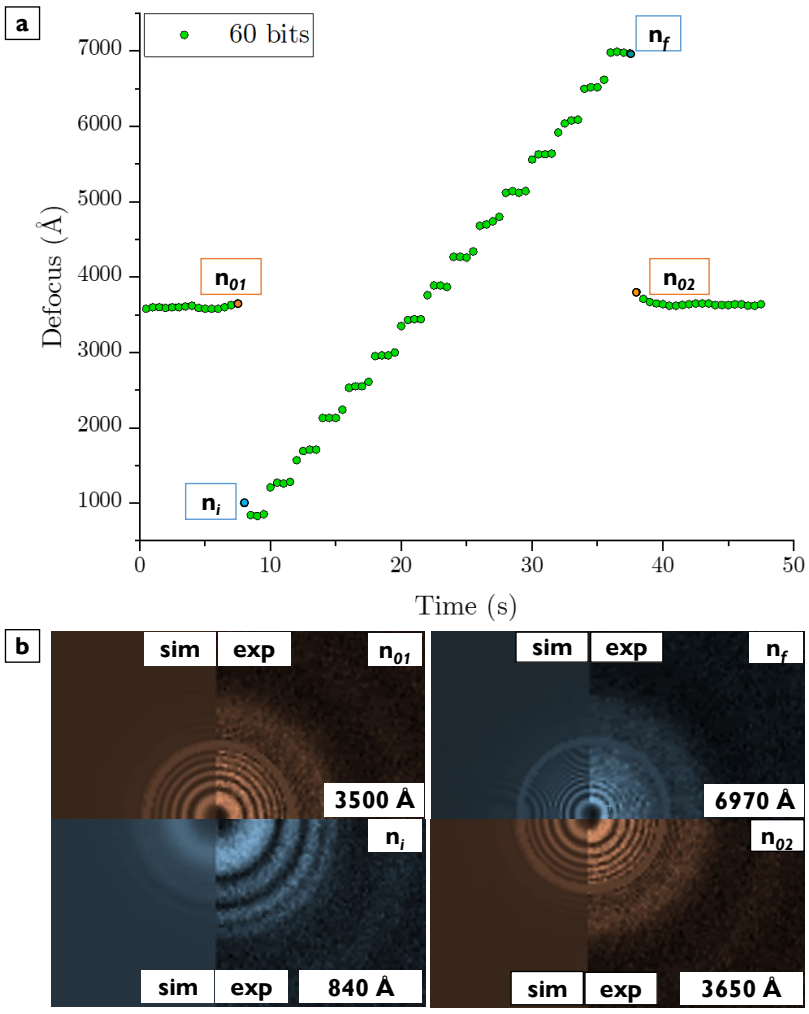

Figure 5.4: (a) A stepwise calibration defocus profile of a FFS acquired on amorphous carbon. The points labelled as n_i and n_f correspond to the first and last images of the FFS. Each step size is 60 bits and 4 images per step were acquired during OL settling at a frame rate of 2 fps. The last and first images of the pre- and post-focal series defocus plateaus are labelled as n_{01} and n_{02}, respectively. (b) A comparison between simulated CTFs from the Gctf software and LAS calculated from experimental micrographs for the points labelled in (a).

Typically, a large starting defocus, and a high dose, ensure that there are sufficient, sharp Thon rings in the LAS of the experimental micrographs for a better CTF fitting accuracy. The acquired DM3 micrographs of the focal series were then sorted and converted to a file format compatible with Gctf, namely MRC format, on the Diamond Light Source Linux computer cluster. Once in the appropriate format for Gctf, the pixel size, acceleration voltage, C_3, and the approximate initial and final defoci were specified in Gctf, for the simulation of the CTF. The resultant defocus profile plot is shown in Figure 5.4 (a).

Figure 5.4 (b) shows a good fit between the refined 2D simulated and experimental LAS of amorphous carbon along with their respective calculated defocus values. In Figure 5.4 the images labelled n_{01} and n_{02} correspond to the last and first image of the pre- and post-focal series defocus plateaus, respectively. While n_i and n_f correspond to the first and last images of the focal series, respectively.

From the defocus profile plot, it is straightforward to determine the defocus per step and the defocus/bit (Figure 5.4 (a)). Per focal plane, the defocus value is the average of the defoci of all the images recorded on that plane. This average defocus value per focal plane is subtracted from its subsequent neighbouring average to attain the focal difference between steps (height of each step). Averaging all the differences, gives an average defocus step value

of 439 (34) Å for the calibration series. Dividing this value by the height in bits (60 bits here) gives a defocus/bit of 7.3 (0.6) Å.

The accuracy of the defocus calibration using the Gctf software was verified against the results obtained using an alternative calibration by hardware correction. Here, a CFS with a known focal step in bits is acquired on an amorphous substrate while the defocus value is measured using the JEOL COSMO aberration corrector software. Using this method, the average defocus/bit was found to be 7.1‡‡ Å/bit, that matches the value determined by the fitting in Gctf.

A defocus/bit of 7 Å/bit was then used to calibrate focal steps for all the FFS experiments. This calibration on amorphous carbon is particularly important as the experimental data for the nanoparticles are generally acquired at lower starting defocus values (200-500 Å) and at high magnification. This leads to images whose LAS have few Thon rings and strong crystalline reflections which would reduce the accuracy of the calculated defocus values using the Gctf software. This is especially true because the program computes the initial defocus value by circularly averaging the LAS of the experimental micrographs[187].

‡‡ Calibrated value.

For the nanoparticles, real space images, instead of log FTs, were used to determine the start and end of the focal series. As shown in Figure 5.5[§§], for an FFS of a nanoparticle a sharp contrast change occurs before and after the start and end of the defocus ramp. This contrast change is used for the manual identification of the initial defocus n_i (first image of the focal series) and final defocus n_f (last image of the focal series) images.

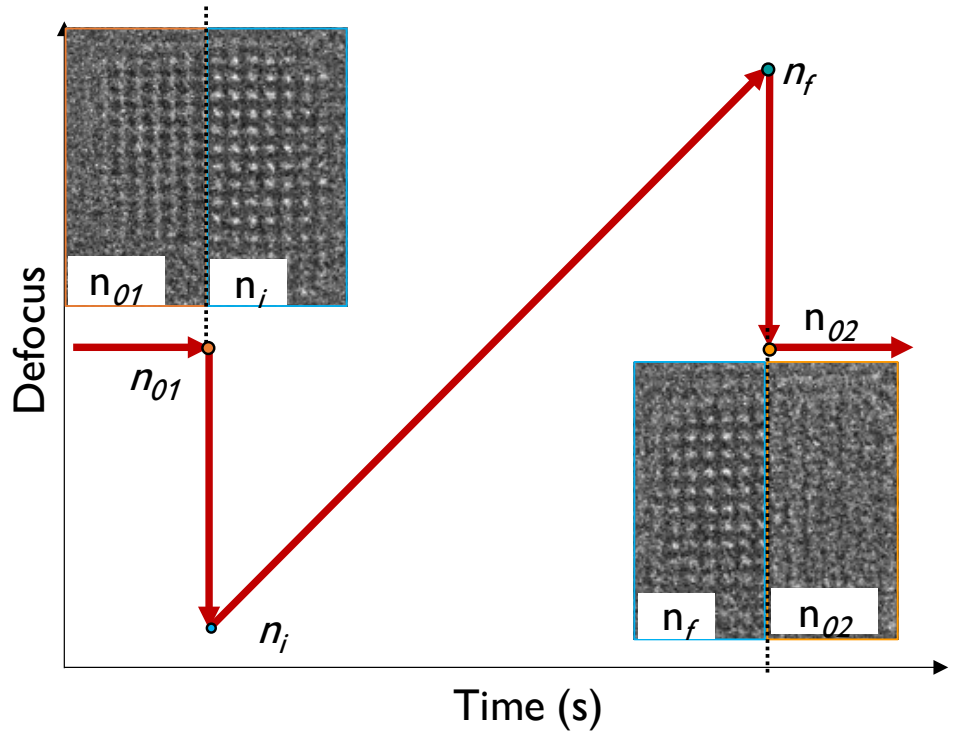

Figure 5.5: A schematic diagram of an FFS defocus profile plot indicating sharp contrast changes between the last image of the pre-focal series plateau (n_{01}) and the first image of the focal series (n_i) as well as that between the image at the end of the focal series (n_f) and the first image of the post-focal series plateau (n_{02}). The latter were used to determine the beginning and end of the focal series.

[§§] The difference in contrast between n_{01} and n_{02} is likely due to objective lens hysteresis induced by the large defocus change from n_f to n_{02}.

Once the time differences between n_i and n_f are known they can be used to calculate the difference between the expected FFS acquisition time and the actual experimental time, i.e., the overhead time. The expected time difference between n_f and n_i, for a 30-focal plane FFS acquired at an exposure time of 0.04 s per frame (25 frames per second) with an OL settling time of a second is 30 s. However, it was found that there is typically an additional 0.1 s per focal plane such that 2 more images per plane are acquired. Therefore, the total overhead for the FFS is 2.85 (0.53) s. As discussed in section 5.2.1, the temporal resolution of the FFS restored waves is a quarter that of the CFS restored waves in Chapter 4.

Although the FFS method improves the temporal resolution by allowing images to be recorded independently of the OL change, stacking of images must be performed manually post-focal series acquisition. The manual assessment of the starting and end points of the FFS data stack is also a drawback of this method. Additionally, data handling and transfer is more difficult for a FFS because each dataset is composed of approximately 1000 images. In the next section, subsequent procedures for restoring exit waves from FFS data are detailed.

5.2.3. Exit wave restoration

As discussed in section 4.2.6, the quality of the restored complex exit wave depends on the SNR of the images used in the focal series, which in turn is

dose dependent. This is because images dominated by noise reduce the accuracy of aberration estimations and result in poor image registration. The advantage of acquiring FFS data is that images recorded on the same focal plane can be summed up without registration to boost the average SNR per focal plane. The total number of images that can be summed per focal plane depends on the OL settling time and the frame rate, as well as the overhead time. In this study, images were acquired at 25 fps (0.04s/frame) with an OL settling time of 1 s and an overhead delay of 0.1 s. This implies that up to ≈27 images (Figure 5.6 (c)) can be summed per focal plane without the need for image alignment, unlike for multiple images acquired at slower rates (0.5 – 1.0 s/ frame) [188]. This in turn boosts the SNR of the summed image by $\sqrt{n}$ compared to the case of a single image (Figure 5.6 (a)), where n is the number of images.

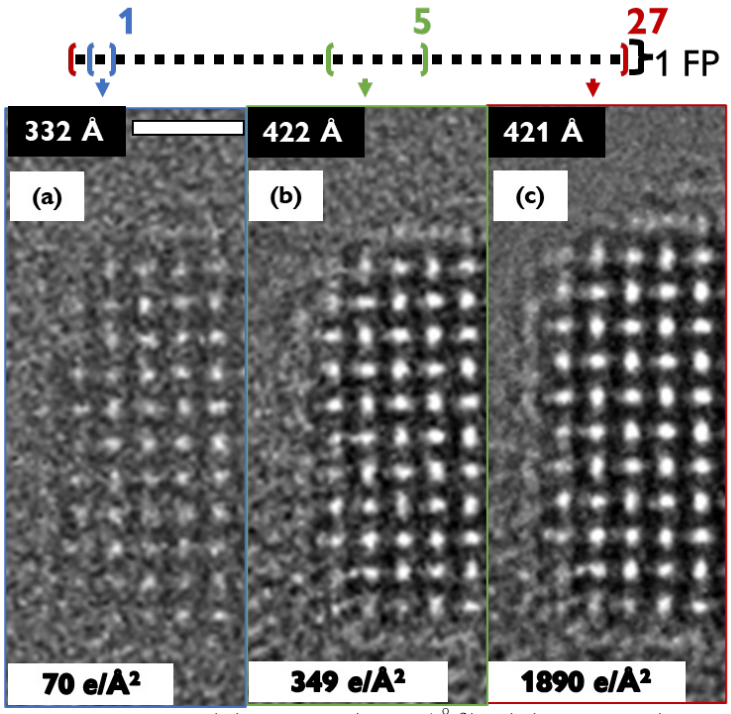

Figure 5.6: Comparison of (a) single (70 $e/Å^2$), (b) 5-sum (349 $e/Å^2$), and 27-sum images (1890 $e/Å^2$) obtained from the 7th focal plane of the focal series whose transition points are shown in Figure 5.5. The defocus in a single image was approximated based on the expected defocus calculated using equation 5.1. The defocus values of (b) and (c) were obtained from values estimated by FTSR. The dotted line at the top of this figure represents a focal plane with the dots representing individual images. The brackets show the number of images that were summed to produce the respective images. The scale bar corresponds to 10 Å.

In principle, it is reasonable to assume that summing the maximum number of images per focal plane is the most advantageous option to increase the SNR, for the detector used. However, care must be taken as nanoparticulate specimens may rotate, tilt and drift by a few pixels in x and y and experience focal drift in z during image acquisition at each focal plane. This drifting may result in the accumulation of small registration errors which may blur high-resolution information and/or dampen the phase of the restored exit wave[188]

which may subsequently reduce the accuracy of atom counts for quantitative exit wave analysis[85,188].

In this study, the reconstructed phase, particularly from low occupancy surface atoms, is nonetheless improved by summing all the 27 images per focal plane, despite the small registration errors that may accumulate in this process. This is clearly demonstrated in Figure B.2 in Appendix B. Images of the summed (top) and individual frames per focal plane are shown at various defoci for the nanoparticles imaged using dose rates of 1746 $e/Å^2s$ (a-c) and 1150 $e/Å^2s$ (d-f) (see Figure 5.8 ((a) & (d) for exemplary restored phases). After summing the images at each focal plane, the restoration process of the FFS data is identical to that used for CFS. Table 5.1 reports the general restoration parameters used in this study.

Table 5.1: Summarised parameters used for restoring complex exit waves from FFS data.

Parameters	**Values**
Primary electron energy (keV)	300
Beam divergence (mrad)	0.1
Focal spread (Å)	36
C_3(µm)	-4.94 – 0.44
Focal step (Å)	21
Starting defocus (Å)	200-500
Acquisition time (s)	0.04
Sampling (Å/pix)	0.166
Dose/frame ($e/Å^2$)	49 - 271
Dose rate ($e/Å^2s$)	1150 - 6948

As for a CFS, exit wave restoration from an FFS relies on the PCI/PCF method (section 3.7) for the estimation of the aberrations. The advantage of the latter is that it does not require the presence of an amorphous area in the image like traditional methods including Gctf[144]. By fitting the defoci determined by the PCI/PCF, the defocus change per step is found to be 23.0 (0.4) Å (see Figure B.3 in Appendix B). Dividing this value by the number of bits per step applied, 3, confirms that the value of a bit is 7.7 (0.1) Å, comparable with the calibration value obtained using the amorphous carbon in section 3.1.1.1. This further validates the accuracy of the defoci estimated by the restoration which were obtained in the absence of amorphous material.

5.2.4. Electron dose properties

In the previous chapter, it was shown that the (110) facet of a [001] projected nanoparticle underwent several surface atomic reconfigurations leading to the formation of the (2x1) surface reconstruction, identical to the one proposed in the literature[37]. To investigate the effect of cumulative dose and dose rate on the formation of this surface structure, multiple FFS data were acquired under the same experimental conditions for several nanoparticles.

To ensure that the data are comparable, nanoparticles with similar widths and lengths were used for the analysis. The average values were 47 (5) Å and 40 (5) Å, respectively. This narrow size range was chosen to limit the influence of

different surface-to-bulk ratios when comparing nanoparticles. This ratio depends on the size of the nanoparticles, and it decreases with increasing size[26]. Surface atoms tend to be undercoordinated and thus have lower binding energies relative to their bulk counterparts[156]. Thus, smaller nanoparticles with a higher density of undercoordinated surface atoms will be more sensitive to beam-induced excitations which may lead to more complex structural transformation pathways compared to larger nanoparticles with a comparatively lower density of undercoordinated surface atoms.

Additionally, the OL settling time per focal step was fixed at 1 s. This ensured that the total dose of the series is comparable to that employed in a CFS within reasonable experimental and data processing times. Here, the total dose corresponds to the cumulative dose the nanoparticle is exposed to at the end of consecutive FFS acquisitions. As shown in section 4.3.2, the cumulative dose required for the detection of a single O atom with the OneView detector is approximately 20 x 10^3 $e/Å^2$. To attain this minimum dose using FFS, the OL settling time could be reduced to 0.4 s, such that at 0.04 s/frame only 10 images per focal plane are acquired and summed. However, under these experimental conditions, about 27 FFS data sets, instead of 7, would have to be acquired to attain a total dose of 543 x 10^3 $e/Å^2$, comparable to that of the CFS data in Chapter 4 ((as shown in Table 5.2 for the second nanoparticle). These would

also have had to be processed, significantly increasing the experimental and post-acquisition processing times per nanoparticle.

In all FFS experiments, the cumulative dose used to generate the signal referred to as the focal series dose, and dose rate were kept constant during FFS image acquisition. The total dose was gradually increased by recording multiple FFS data sets on the same nanoparticle under the same imaging conditions.

For the first FFS acquisition (FS_1), the cumulative dose (CD_1) includes the dose used to image the nanoparticle prior to the start of the focal series up to the last image of the focal series (red defocus pathway in Figure 5.7 (a)), and it excludes the exposure post-focal series acquisition (blue defocus pathway in Figure 5.7 (a)).

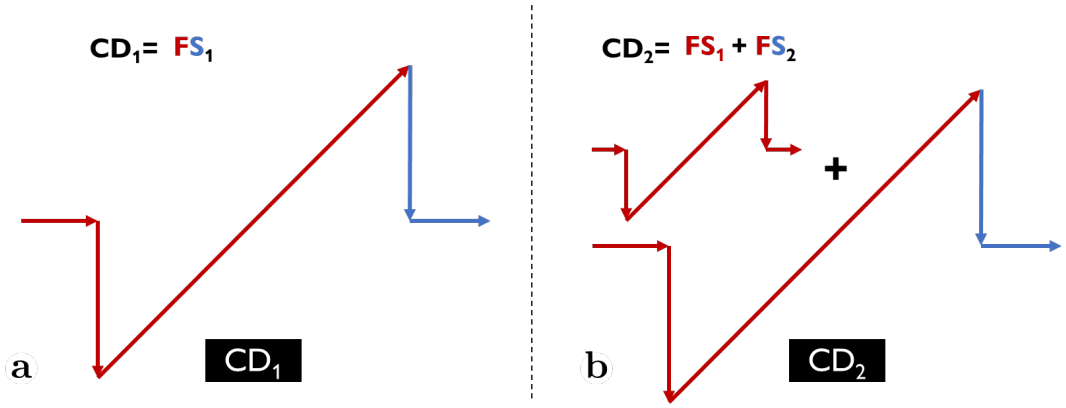

Figure 5.7: A schematic diagram showing images included in the cumulative dose (CD) calculation for the (a) first and (b) second focal series for a given nanoparticle. The red defocus pathways show the number of images added in the cumulative dose calculation while the blue defocus pathways show the images that are excluded.

However, the cumulative dose (CD_2) of the subsequent FFS dataset (FS_2), includes the total dose of the previous FFS data (CD_1), shown as the red

defocus pathway, but it excludes the post-focal series exposure of FS_2 (blue defocus pathway), as shown in Figure 5.7 (b).

Table 5.2 below lists the average focal series dose and dose rates for one FFS acquisition for the first two nanoparticles. The total dose from consecutive series is also shown, as well as the total number of focal series (No. FS) acquired on each nanoparticle. The third nanoparticle in Table 5.2 corresponds to the nanoparticle reported in the previous chapter in Figure 4.15. The focal series of this nanoparticle was acquired using CFS and hence the total number of FS datasets is 1. This dataset is included in this chapter to compare the surface transformation obtained with that of similarly sized nanoparticles imaged using FFS at lower dose rates and comparable cumulative doses.

Table 5.2: Dose parameters for the nanoparticles examined in this thesis. In order the dose parameters shown are the cumulative focal series dose (FSD), dose rate (DR), the number of consecutive focal series (No. FS) and the total dose (TD) at the end of the FFS and CFS acquisition. Here, the third dataset corresponds to the CFS data while the first and second are FFS.

Nanoparticle	**FSD (e/Å^2)**	**DR**	**No. FS**	**TD (x10^3 e/Å^2)**
Figure 5.8 (a-c)	37 513	1 150	12	548
Figure 5.8 (d-f)	57 164	1 746	7	543
Figure 5.8 (g-i)	137 023	11 419	1	480

5.3. Results and discussion

The surface reconstructions observed from the FFS experiments are analysed along the [001] projection and compared against experimental data obtained from alternative techniques and theoretical models proposed to date[28,31,49,55]. The comparison is largely qualitative, because most theoretical studies in literature do not provide the coordinates of their DFT-relaxed atomic models[34,56].

5.3.1. Dose rate and cumulative dose dependence

In this section, the effect of the dose rate and cumulative dose on the stability of the surface terminations of {110} facets as well as their subsequent reconstruction mechanisms is studied. Figure 5.8 (i-h) shows restored phases of three nanoparticles which were acquired at increasing dose rates of 1150 $e/Å^2s$, 1746 $e/Å^2s$ and 11 419 $e/Å^2s$ (top to bottom). The cumulative dose increases from an average of approximately 160 000 $e/Å^2$ (section 5.3.1.1), 300 000 $e/Å^2$ (section 5.3.1.2) to 500 000 $e/Å^2$ (section 5.3.1.3) (left to right). The data will be discussed with respect to their average cumulative dose and up to a cumulative dose below the next average cumulative dose. The restored phases of the first two nanoparticles in Figure 5.8 (a-c) and Figure 5.8 (d-f) were restored from FFS. On the third row, Figure 5.8 (g-i) shows phases that are reported in Figure 4.23 (a-c) in the previous chapter.

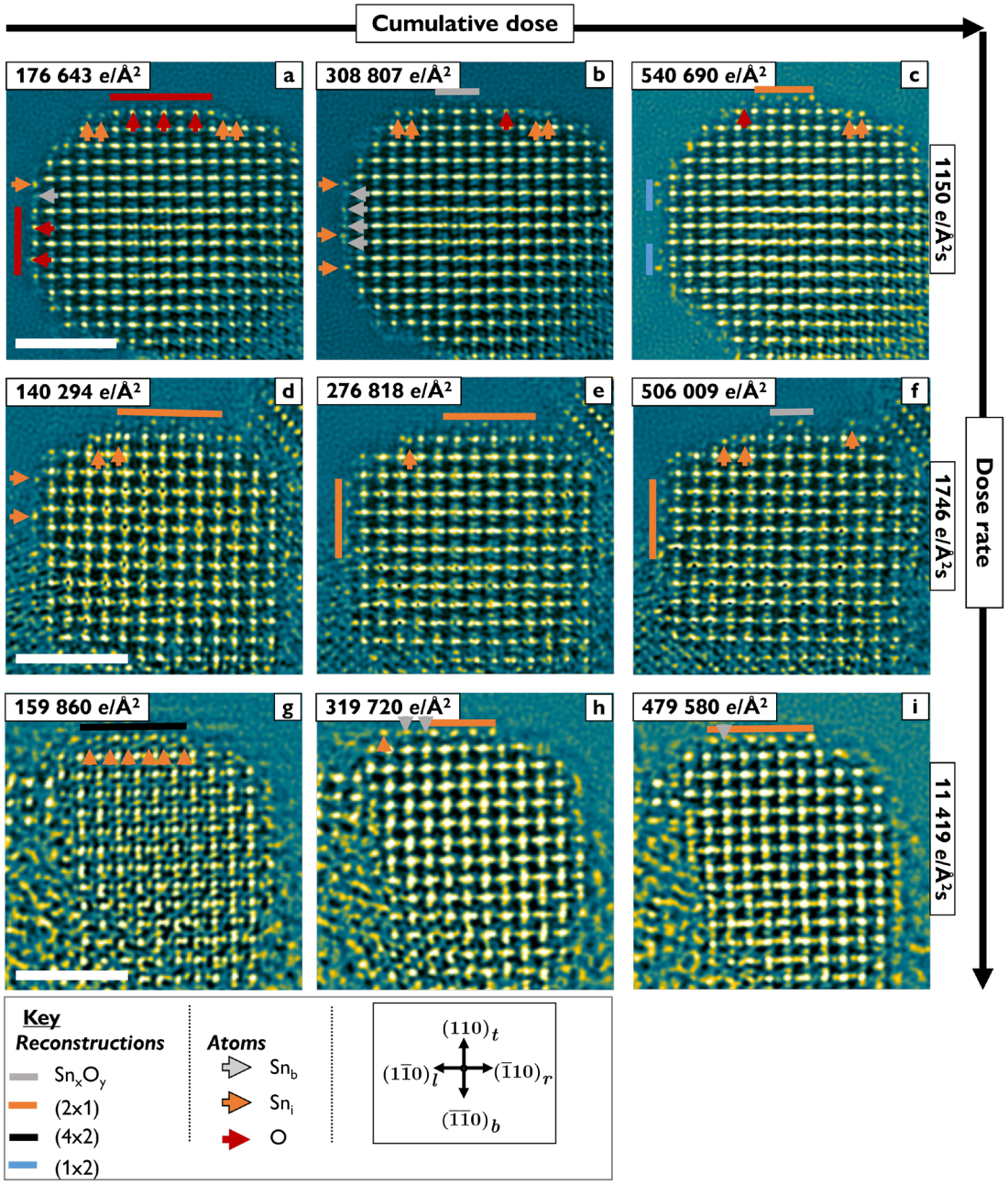

Figure 5.8: (a-i) Restored phases of ≈4 nm-sized nanoparticles, acquired at increasing dose rate (down column) and cumulative dose (left to right). The red, black, orange, and blue lines represent facets with stoichiometric, (4x2), (2x1) and (1x2) surface reconstructions, respectively. The grey lines show isolated strands of Sn_xO_y units. The grey, orange, and red arrows show Sn_b, Sn_i and O surface atoms in that order. The scale bar represents 20 Å.

For tetragonal SnO_2, facets belonging to the {110} family are non-unique.

Hence, to simplify the discussion of the facets, a reference coordinate has been

added as shown in the key of Figure 5.8. The top, bottom, left and right facets will hence be referred to as the $(110)_{t}$, $(\bar{1}\bar{1}0)_{b}$, $(1\bar{1}0)_{l}$ and $(\bar{1}10)_{r}$ facets, respectively. The red, orange, and grey bars shown on the facets exposed to vacuum indicate the stoichiometric termination, the projected (2x1) reconstruction, and isolated or periodically arranged protrusive interstitial Sn atoms, respectively. Individual O atoms and Sn atoms in their bulk or interstitial atomic positions are shown using red, grey, and orange arrows.

5.3.1.1. Cumulative dose: 160 000 e/Å²

In Figure 5.8 (a), (d) and (g)), it is clear that the (110) surface terminations show a strong dependence on the dose rate. For the nanoparticle observed at the lowest dose rate (Figure 5.8 (a)), both the $(110)_{t}$ and $(1\bar{1}0)_{l}$ facets adjacent to the vacuum exhibit an O terminated surface. These are O bridging atoms based on their coordination geometry and their low phase shift with respect to that of surface Sn atoms. This shows that the surface is stoichiometric. These O sites cannot be mistaken for antisite Sn atoms because the latter are unstable relative to other intrinsic defects of SnO_2 under $O_{2(g)}$-poor conditions, as predicted by theory[7]. Furthermore, the average projected distance between these O atoms was measured on multiple restored phases where the nanoparticle retained a stoichiometric termination, and it was found to be 6.8 (0.2) Å. This value is consistent with that of 6.7 Å, as predicted by theory [189].

The line profiles were acquired on the region marked with an orange dashed 8-pixel wide integration line in Figure 5.9 (a) and Figure 5.10 (a).

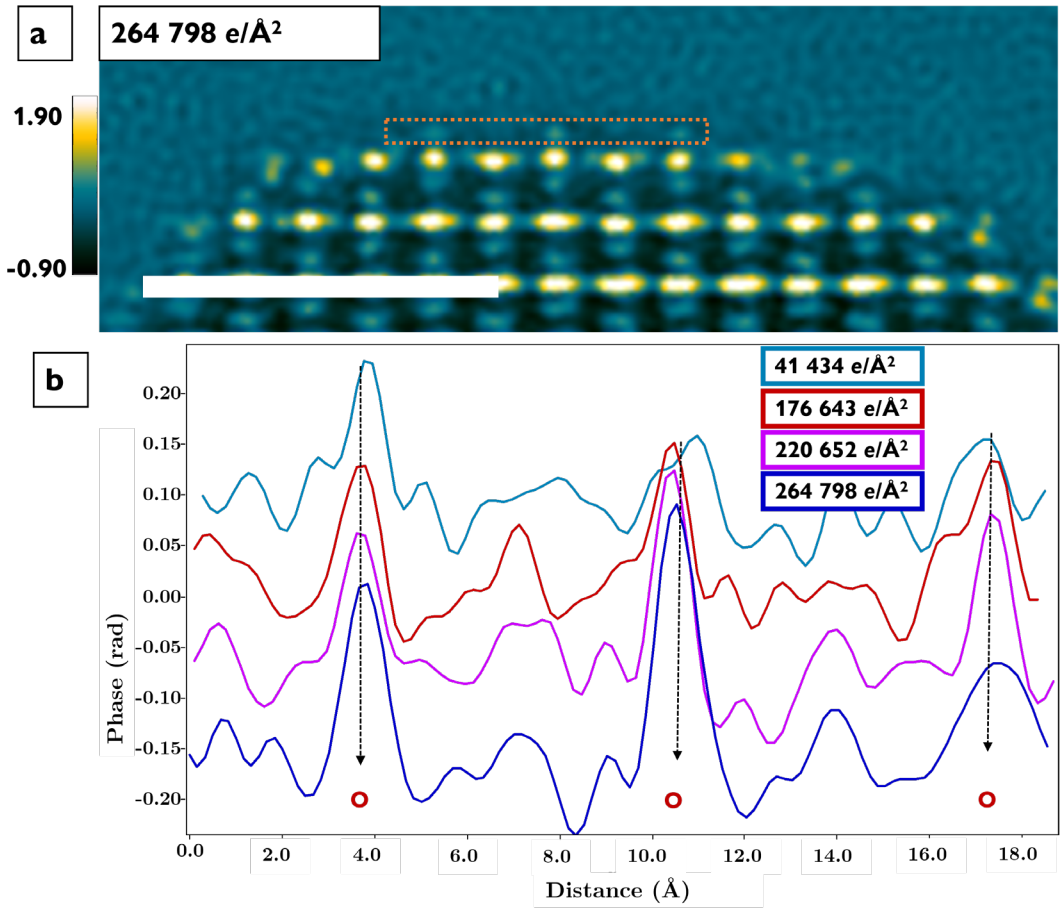

Figure 5.9: (a) Phase of the stoichiometrically terminated $(110)_t$ facet, at a cumulative dose of 264 798 $e/Å^2$, for the nanoparticle shown in Figure 5.8 (a-c). (b) Line profiles acquired from its surface at increasing cumulative doses. The phase shifts induced by O atoms are shown with black dashed arrows. The integration width of the line profiles was 8 pixels (orange box with dashed lines). The scale bar corresponds to 20 Å.

The stoichiometric terminations remain stable from a cumulative dose of 41 434 $e/Å^2$ up to a cumulative dose of 264 798 $e/Å^2$ and 220 652 $e/Å^2$ for both the $(110)_t$ and $(1\bar{1}0)_l$ facets, respectively (phases not shown here). Line profiles taken from the corresponding restored phases at these cumulative doses are shown in Figure 5.9 (b) and Figure 5.10 (b), respectively.

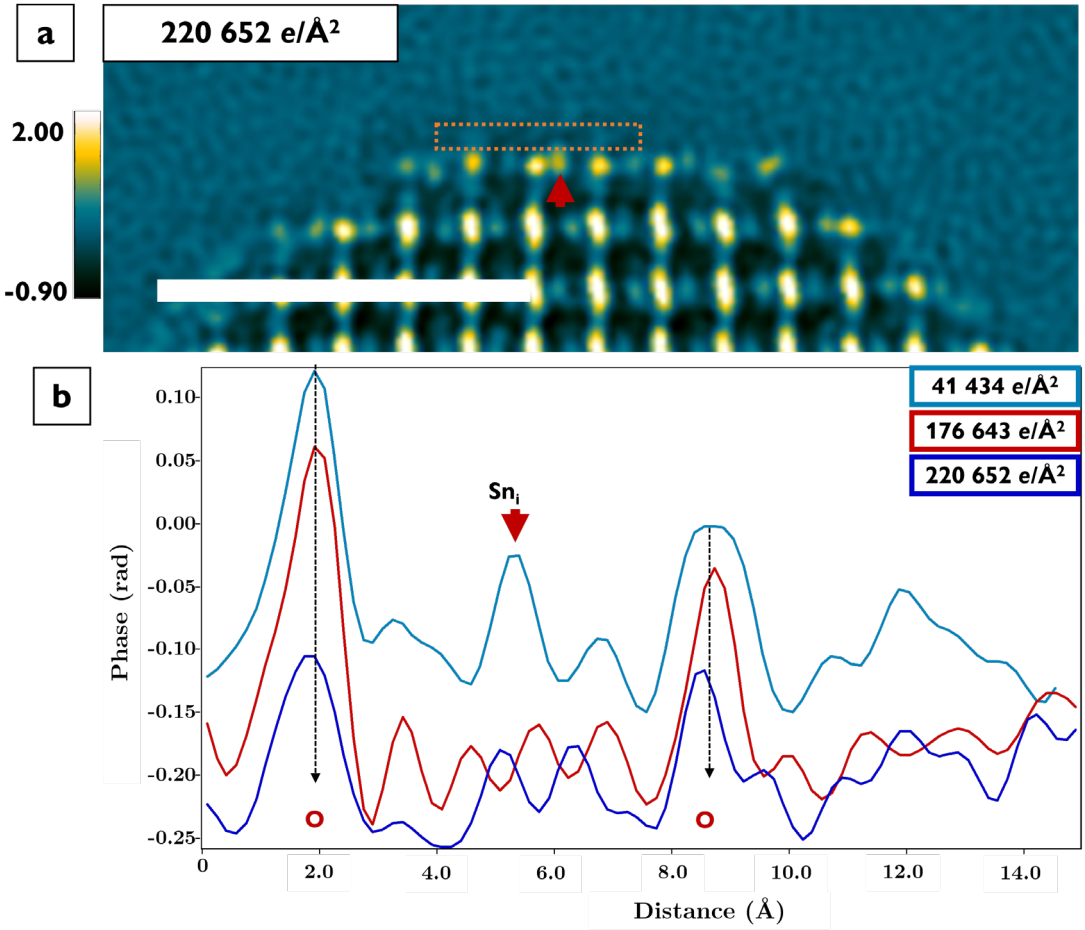

Figure 5.10: (a) Phase of the stoichiometrically terminated $(1\bar{1}0)_t$ facet, at a cumulative dose of 220 652 e/Å^2, for the nanoparticle shown in Figure 5.8 (a-c) and (b) line profiles acquired from its surface at increasing cumulative dose. The phase shifts induced by O atoms is shown with black dashed arrows and that of the Sn_i atom column by a red arrow. The integration width of the line profiles was 8 pixels (orange box with dashed lines). The scale bar corresponds to 20 Å.

At a higher dose rate of 1746 e/Å^{2}s, the $(110)_t$ surface shows a termination composed of Sn_i atom columns (Figure 5.8 (d)). On average, the distance between the surface layer and the atom plane below is comparable to that reported by Li et al. (2021) for the (2x1) reconstruction, using HAADF imaging [37]. Similarly, the average distance between the Sn_i atoms at the surface is also comparable to the one reported in this study. The agreement is observed for

all the nanoparticles in Figure 5.8 where the {110} facets possessed an atomic configuration consistent with the (2x1) surface reconstruction, as summarised in Table 5.3. It is worth noting that unlike the HAADF images, the phase of the exit wave reveals the position of both O and Sn_i atoms on the {110} facets unambiguously.

Table 5.3: Comparison of interatomic distances for surface atomic planes and bulk, obtained for the (2x1) surface reconstruction on the nanoparticles in Figure 5.8 and the results reported by Li et al. (2021)[37].

	Sn_i - bulk (Å)	**Sn_i – Sn_i (Å)**
Li et al. (2021)	3.1 (0.2)	3.5 (0.3)
Figure 5.8 (a-c)	2.8 (0.2)	3.4 (0.3)
Figure 5.8 (d-f)	2.6 (0.3)	3.5 (0.2)
Figure 5.8 (g-i)	2.9 (0.2)	3.5 (0.2)

At the highest dose rate of 11 419 $e/Å^2s$, the $(110)_t$ surface exhibits a complex surface structure composed of Sn_i and Sn_b. As explained in section 4.3.3 of Chapter 4, this motif corresponds to a (4x2) reconstruction, as proposed by Ágoston and Albe (2011) using DFT calculations[56].

5.3.1.2. Cumulative dose: 300 000 e/Å2

Figure 5.8 ((b), (e) and (h)) shows the facets at an average cumulative dose of approximately 300 000 $e/Å^2$. At this cumulative dose the $(110)_t$ facets of the first (Figure 5.8 (b)) and last (Figure 5.8 (h)) nanoparticle exhibit significant transformation relative to their initial terminations at 160 000 $e/Å^2$, while that

of the second nanoparticle (Figure 5.8 (e)) retains its (2x1) surface reconstruction.

The $(110)_{\boldsymbol{t}}$ facet of the nanoparticle shown in Figure 5.8 (b) is composed of a combination of the stoichiometric surface (see O atom shown with red arrow) with another structure composed of two Sn_i atoms centred on an unsaturated O atom ($O_{\mathbf{cus}}$) and bound to two $O_{\mathbf{br}}$ that previously formed part of the stoichiometric termination.

Figure 5.11 (a) shows that this termination remains stable from a cumulative dose of 308 807 $e/Å^2$ to 398 568 $e/Å^2$, where the number of the Sn_i atoms in projection increases with increasing cumulative dose, as described in detail later in this chapter. This is observed through the phase line profiles acquired on the Sn_i atom columns within this cumulative dose range shown in Figure 5.11 (b). Line profiles at the surface where the $O_{\mathbf{br}}$ atom was located were also analysed as shown in the inserts in Figure 5.11 (a).

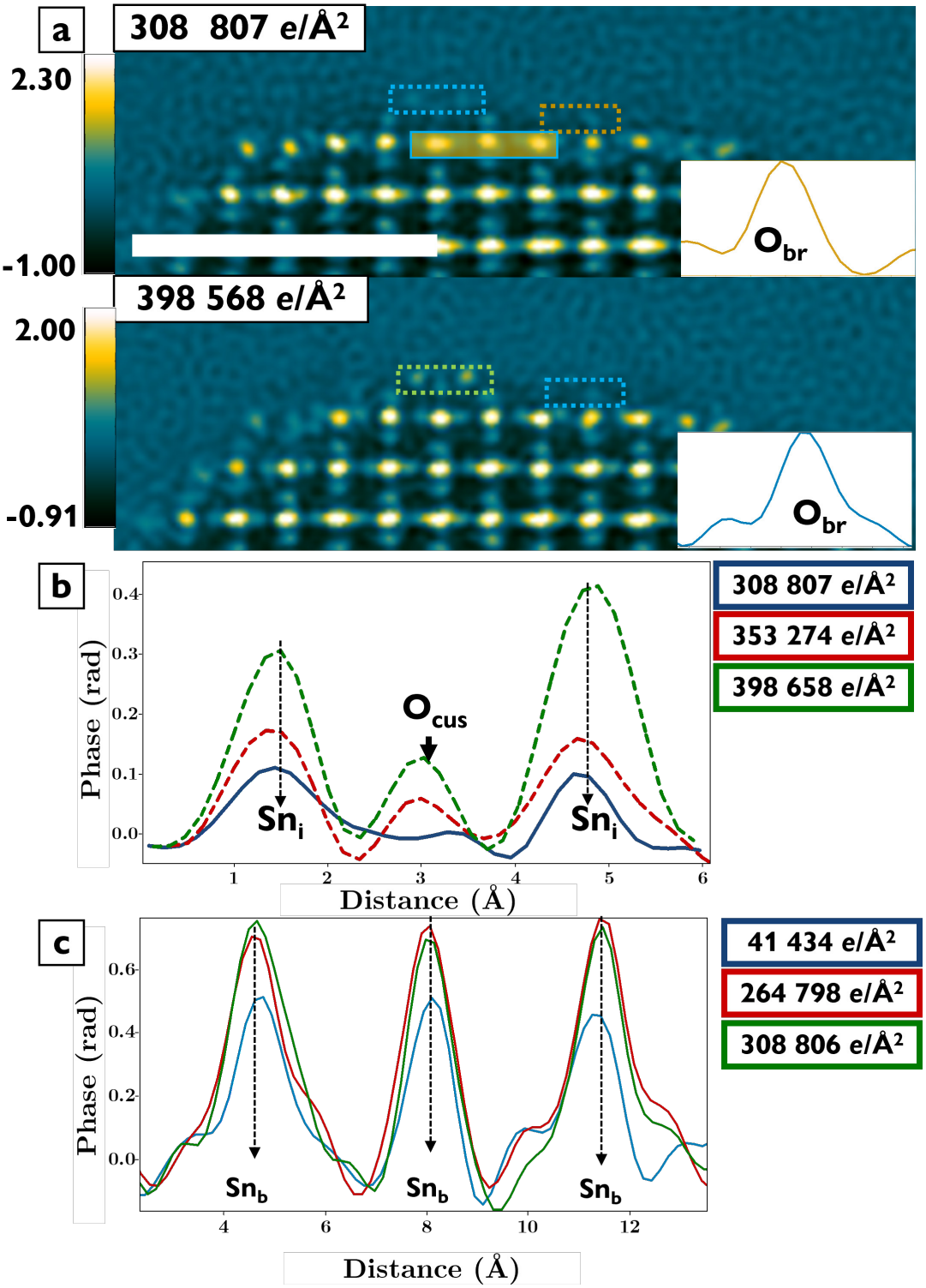

Figure 5.11: (a) Phases of the $(110)_t$ facet of the nanoparticle shown in Figure 5.8 (a-c) at cumulative doses of 308 807 $e/Å^2$ and 398 568 $e/Å^2$. Line profiles (8-pixels wide) are shown as insets in (a) for O atoms, while traces in (b) indicate pairs of Sn_i atoms coordinated to O_{cus}. (c) Line profiles acquired in the yellow ROI in (a) showing the stability of the facet with increasing cumulative dose. The scale bar corresponds to 20 Å.

The Sn_xO_y motif observed here is similar to the Sn_2O_2 strands, proposed by Ágoston and Albe (2011) in a DFT study. In their model, the Sn_i are considered bound to 2 O_{cus} and 2 O_{br} atoms. In addition, they postulate that Sn_2O_2 strands may constitute building blocks for most (110) reconstructions, under reducing conditions [56]. Assuming this to be the case, the data shown here are consistent with the reconstructions observed on the $(110)_t$ facet, as discussed later in detail. When the cumulative dose exceeds 398 658 $e/Å^2$, the surface changes from a Sn_2O_2/stoichiometric termination to one that is composed of two Sn_2O_2 units, coalescing to form a (2x1) surface reconstruction, as seen in Figure 5.12 (a) for a cumulative dose of 450 102 $e/Å^2$. By comparing line profiles from the region marked with a blue dashed box in Figure 5.12 (a), it is evident that, due to its initial low occupancy, the newer Sn_2O_2 unit produces a lower average maximum phase shift (0.085 rad) than its nearest neighbour (0.31 rad). Subsequently, with the increment of dose, the average maximum phase increases by a factor of 3.6 to 0.31 rad, as seen for a cumulative dose of 540 690 $e/Å^2$. Additionally, the initial Sn_2O_2 unit experiences a decrease of a factor of 0.4, down to an average maximum phase shift of 0.185 rad. This result is consistent with the (2x1) facet growing through the progressive coalescing of Sn_2O_2 units.

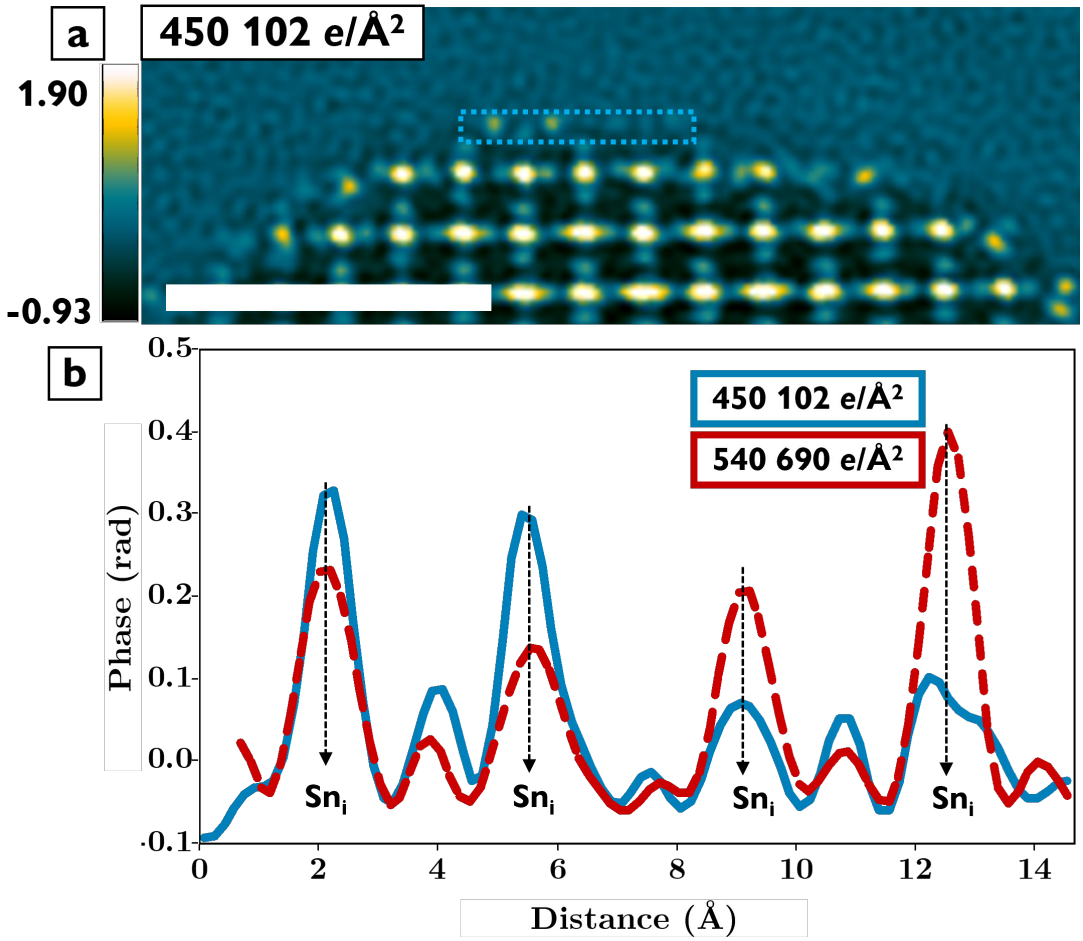

Figure 5.12: (a) Phase of the $(110)_t$ facet of the nanoparticle shown in Figure 5.8 (a-c) at a cumulative dose of 450 102 $e/Å^2$. (b) 8 pixel wide line profiles obtained from the region shown in (a) at a cumulative dose of 450 102 $e/Å^2$ (blue) and 540 690 $e/Å^2$ (red), respectively. The scale bar represents 20 Å.

The additional surface atoms that form the (2x1) motif may be sourced from the bulk or surface lattice sites. It is known that surface atoms at low coordination sites have a low activation energy for surface diffusion as they are weakly bound to the bulk[156]. For isolated nanoparticles, the electron beam is likely to promote surface diffusion of Sn and O atoms. However, in the case of clustered nanoparticles it is also possible for the atoms to be sourced indirectly through the surface diffusion from nearby nanoparticles. Additionally, Agoston

and Albe (2011), demonstrated through DFT that the diffusion of Sn_i atoms in the [110] and [001] direction has a very low energetic cost (≈0.07 eV) [56]. This may partly explain why the initial Sn_2O_2 unit experiences a reduction in relative occupancy to the later Sn_2O_2 unit. In fact, O isotopic exchange studies show that appreciable bulk diffusion of O atoms on pristine, and Pd-doped, nanoparticles (with a diameter comparable to this study of 30-60 Å) requires heating to temperatures above 573 K and 773 K, respectively[26]. Given that the experiments were conducted at room temperature, it is unlikely therefore that O atoms diffuse from the bulk in the FFS experiments.

In comparison to the $(110)_t$ facet shown in Figure 5.8 (b), the $(1\bar{1}0)_l$ facet is terminated by a terrace composed of Sn_b and O atom columns as well as one Sn_i atom column (see red arrow in Figure 5.13 (a) and (b)). Additionally, at either end of the terrace there are isolated Sn_i coordinated to the bulk through $\mathbf{O_{ip}}$ and $\mathbf{O_{br}}$ atoms. The phase shift of these atom columns is notably lower than at a cumulative dose of 176 643 $e/Å^2$ shown in Figure 5.8 (a). In fact, these progressively decrease, indicating lower site occupancy with respect to the initial structure, as measured using line profiles (Figure 5.13 (b)). The latter were taken from the orange dashed line profile, in Figure 5.13 (a), of the 3 central Sn_b atoms of the facet (indicated with black dashed arrows in Figure 5.13 (b)). These indicate that the surface undergoes Sn_b loss with an increase in the cumulative dose. In comparison, the line profiles acquired on three

central Sn atom columns of the second atomic layer of $(110)_t$ shown in Figure 5.13 (c) indicates that this facet increases in occupancy from its initial state and then remains relatively static above a cumulative dose of 264 798 $e/Å^2$. For reference, these line profiles were acquired on the yellow ROI shown in Figure 5.11 (a).

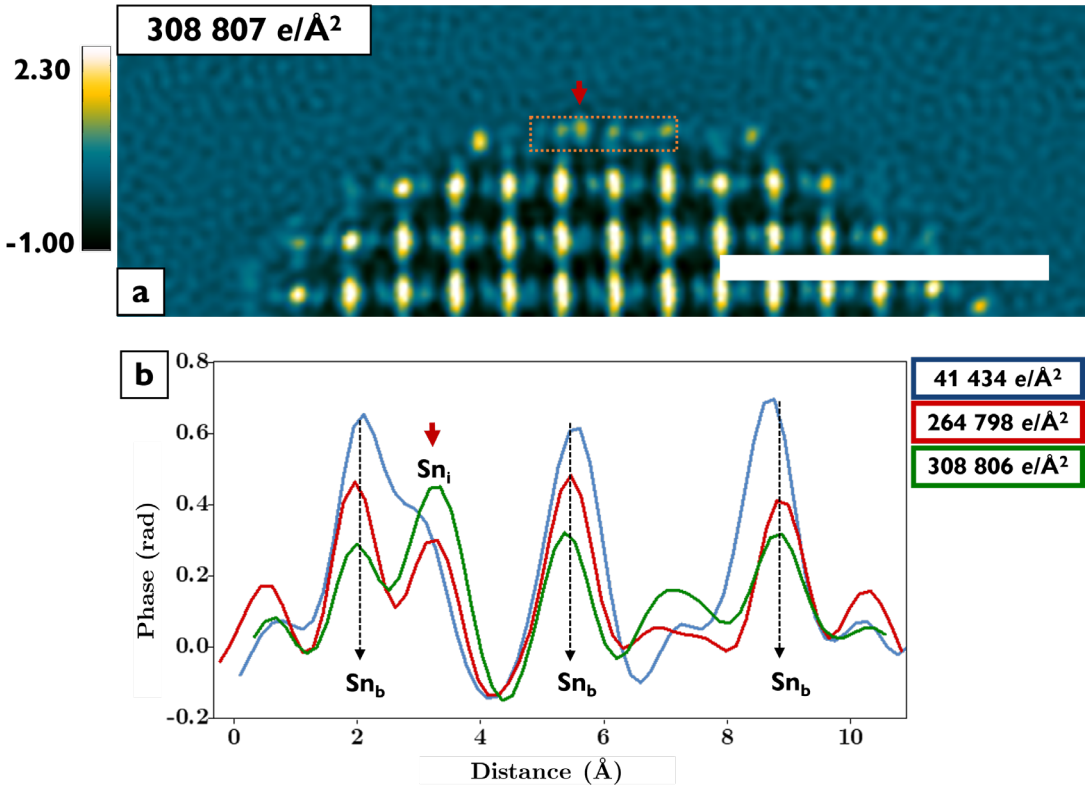

Figure 5.13: (a) Phase of the $(1\bar{1}0)_t$ facet at a cumulative dose of 308 807 $e/Å^2$. (b) Line profiles were acquired from the ROI in dashed orange borders indicate a relative Sn_b atom loss and Sn_i gain (red arrow) from a cumulative dose of 41 343 $e/Å^2$ to 308 807 $e/Å^2$. The scale bar in (a) corresponds to a length of 20 Å.

The low occupancy terrace converted into an asymmetric (2x1) surface reconstruction which was found to be stable from a cumulative dose of 353 274 $e/Å^2$ to 498 150 $e/Å^2$, as shown in Figure B.4, in Appendix B. This asymmetry has been observed before for the (1x2) reported by Li et al. (2021) as will be

discussed further below[37]. Similarly, through non-contact atomic force microscopy (NC-AFM) surface reconstructions of other rutile systems such as TiO_2 have also been shown to exhibit symmetric and asymmetric surface reconstructions with the same periodicity and atomic arrangement[190,191]. For example, the (1x2) surface reconstruction of the {110} surfaces of TiO_2 has been shown to be composed of Ti_2O_3 added rows that have pairs of Ti interstitials (Ti_i) of different distances relative to the nearest bulk layer such that they formed different surface domains[191]. The coordination environment of the surface interstitial cations to the bulk is similar for the Sn_2O_2 and Ti_2O_3 units. However, the Ti_2O_3 units are further coordinated to O atoms i.e., O-terminated unlike the Sn-terminated Sn_2O_2 units. Homogeneous asymmetric domains are composed of the same Ti_i of the pairs of Ti_i being higher than the other. On the other hand, heterogeneous asymmetric domains have both Ti_i pairs changing heights relative to the bulk. The origin of the asymmetry remains to be investigated.

The third nanoparticle, at this cumulative dose, using the highest dose rate has a $(110)_t$ facet largely composed of a (2x1) surface reconstruction (Figure 5.8 (h)). However, a motif resembling that of the (4x2) reconstruction on the leftmost part of the surface is also observed. This indicates a progressive transformation from the (4x2) into the (2x1) surface reconstruction as discussed in Chapter 4.

5.3.1.3. Cumulative dose: 500 000 $e/Å^2$

At a cumulative dose of about 500 x 10^3 $e/Å^2$, the $(110)_t$ facets mostly exhibit a (2x1) surface reconstruction, as shown by the phases in Figure 5.8 (c - i). However, at the lowest dose rate of 1150 $e/Å^2s$ (Figure 5.8 (c)), the $(1\bar{1}0)_t$ facet exhibits an asymmetric termination. Here, the surface is composed of Sn_2O_2[56]/Sn_2O[37] units, separated by a distance of 14.0 Å and the average distance between the Sn_i pairs is 3.7 Å. These distances are consistent with the projected motif of a (1x2) surface reconstruction observed by Li et al. (2021). In their study, they annealed micron-sized cuboctahedra of SnO_2 and used both atomically resolved *in situ* AC-(S)TEM and DFT calculations to analyse the {110} facets[37]. The surface observed in Li's work is composed of pairs of Sn_i atoms that have equal distances relative to the nearest bulk atomic layer. However, some local asymmetry, identical to the one observed in this study is also present. In addition, of the pair of surface Sn_i atoms, the Sn_i atom column closer to the bulk exhibits lower occupancy compared to its higher counterpart as observed also in this study. These similarities justify the conclusion that the observed motif in Figure 5.8 (c) is consistent with the (1x2) surface reconstruction of SnO_2. As an alternative to this (1x2) motif, Ágoston and Albe (2011) proposed a model composed of Sn_i, on one side of the $O_{\mathbf{cus}}$, coordinated to the bulk through $O_{\mathbf{cus}}$ and $O_{\mathbf{ip}}$. Nonetheless, theoretical calculations in their study predicted that the model is unstable, making it unlikely to be observed

experimentally. This conclusion was also independently verified theoretically by Li et al. (2021).

Figure 5.8 (i) indicates that at a cumulative dose of 479 x 10^3 $e/Å^2$, the $(110)_t$ facet has a (2x1) surface reconstruction, as discussed in Chapter 4, section 4.3.3. However, what is also evident is that the O sublattice exhibits distortion. Typically, such distortion is associated with the presence of dopant mediated Sn^{2+} ions in the SnO_2 matrix[174]. In the context of this study, it may also suggest that the nanoparticle at high dose rates undergoes electron beam mediated bulk reduction of Sn^{4+} to Sn^{2+}, as also observed for other oxide systems, such as CeO_2 [77].

At a dose rate of 1746 $e/Å^2s$ (Figure 5.8 (f)), the $(110)_t$ has a surface termination composed of Sn_2O_2 units and isolated Sn_i coordinated to the bulk through $O_{\mathbf{br}}$ and $O_{\mathbf{cus}}$. The exposed step-edge of the Sn atomic plane below this surface has an atomic configuration composed of Sn_b and Sn_i atoms. Figure 5.14 (a) shows Sn_i line profiles from the phase of the $(110)_t$ facet of the nanoparticle, at a fixed dose rate of 1746 $e/Å^2s$, and increasing cumulative dose. It is clear that the facet shows a (2x1) surface reconstruction up to a cumulative dose of 425 840 $e/Å^2$. However, the surface is also observed to revert to a surface termination composed of Sn_2O_2 units and isolated Sn_i (i.e., at cumulative doses of 210 862 $e/Å^2$ and 506 009 $e/Å^2$). In general, {110} facets of the nanoparticles consistently exhibited the (2x1) surface reconstruction

when imaged at dose rates between ≈ 2000 and 7000 $e/Å^2s$ and cumulative doses up to 500 x 10^3 $e/Å^2$ (see Figure B.5 of Appendix B). This result is also obtained quantitatively by measuring interatomic distances for all the nanoparticles in Figure B.5 (Table B.1, in Appendix B) which are consistent with the measurements obtained on the (2x1) reconstruction observed by Li et al. (2021).

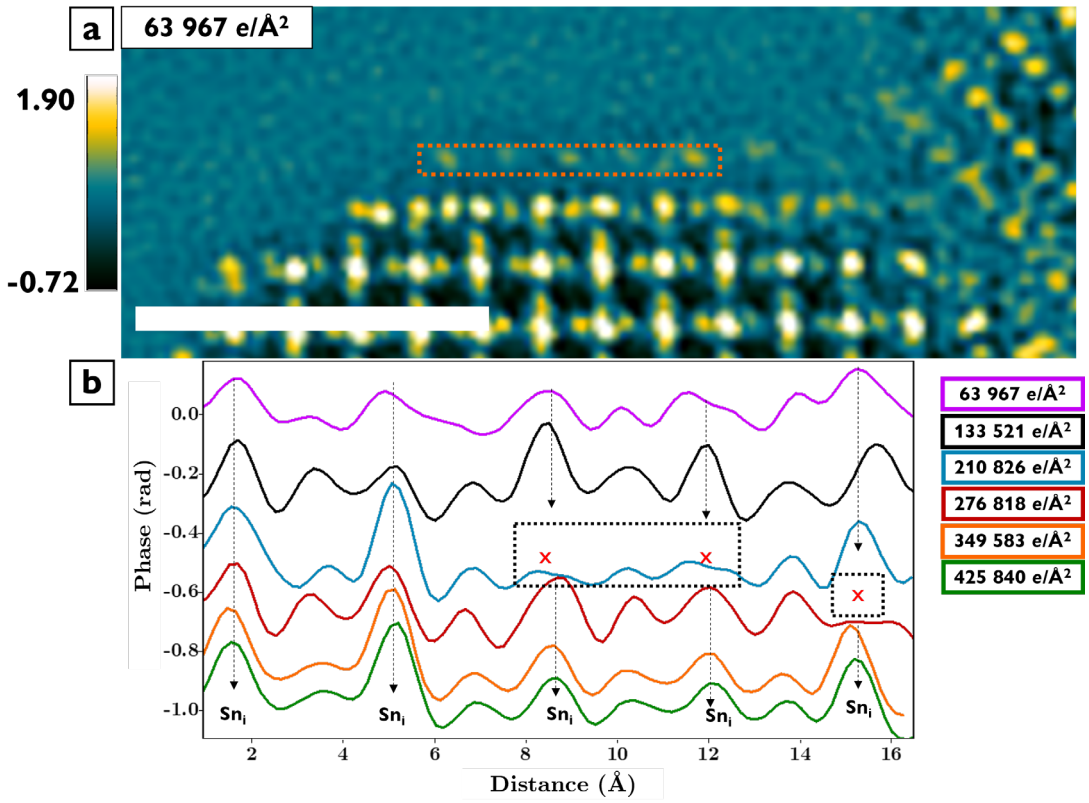

Figure 5.14: (a) Phase of the $(110)_t$ facet shown in Figure 5.8 (i) at a cumulative dose of 63 967 $e/Å^2$. The region where line profiles were acquired is shown by the orange dashed ROI. (b) Line profiles of the reconstructed surface layer shown at increasing cumulative doses. The dashed black arrows indicate phase shifts by Sn_i atoms from the overlayer. Areas without Sn_i atoms are shown with red crosses. The scale bar corresponds to 20 Å.

A graphical summary of the reconstruction pathways observed in this study as a function of dose rate and cumulative dose is shown in Figure 5.15 where,

several clear reconstruction pathways are identified (also refer to Table 5.4, below).

At a dose rate of 1150 $e/Å^2s$, two surface reconstruction pathways are observed depending on the extent to which the surface is defective. For the relatively beam resistant $(110)_t$ facet with a lower defect density relative to the $(1\bar{1}0)_l$, the stoichiometric termination gradually converts into the (2x1) termination through the coalescing of Sn_2O_2 units as the cumulative dose increases. The pathway is consistent with DFT calculations which compared the formation energy of single and clustered defects that can form on the (110) facet of SnO_2[56]. In this theoretical study, it was demonstrated that the most stable surface defect under reducing conditions is the Sn_2O_2 unit (see Figure 2.6 in section 2.3 and Figure B.6, in Appendix B for more details). Relative to the stoichiometric surface, the Sn_2O_2 units have lower surface energy at $\Delta\mu_O <$ -1.91 eV. At $\Delta\mu_O =$ -1.91 eV, the stoichiometric surface is predicted to be in equilibrium with isolated Sn_2O_2 units. For $\Delta\mu_O >$ -1.91 eV, the stoichiometric termination is the most stable (note that the $\Delta\mu_O$ is 0 eV under O-rich conditions, and -3.0 eV under O-poor conditions). This is consistent with the observed O reduction following the increase of the cumulative dose from 308 807 $e/Å^2$ to 398 658 $e/Å^2$ where the $(110)_t$ facet is transformed from being purely stoichiometric to a mixed Sn_2O_2/stoichiometric surface.

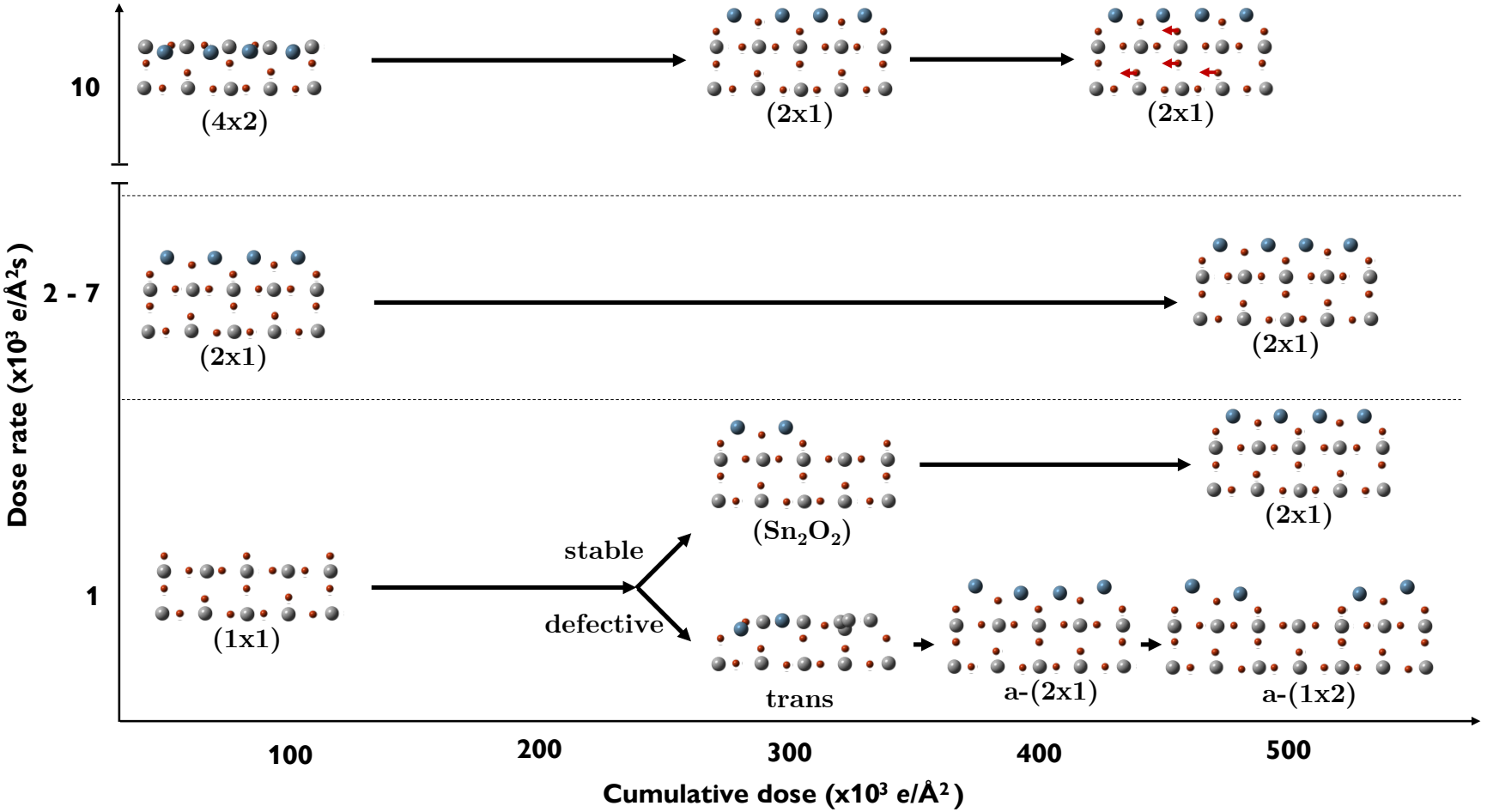

Figure 5.15: Graphical summary of the experimentally observed surface reconstruction pathways for 0.5 wt% Pd-doped SnO_2 nanoparticles as a function of electron dose.

Table 5.4:A summary of the stability of the observed surface reconstructions as a function of cumulative dose and dose rate.

	Cumulative dose (e/Å²)										
Dose rate (e/Å²)	0-50 k	50 k-100 k	100 k-150 k	150 k – 200 k	200 k - 250 k	250 k - 300 k	300 k – 350 k	350 k – 400 k	400 k - 450 k	450 k - 500 k	500 k - 550 k
1150	stoichiometric						Sn_2O_2/stoichiometric		(2x1)		
	stoichiometric					Trans		asym (2x1)		asym (1x2)	
1750	(2x1)				Sn_2O_2/Sn_i		(2x1)			Sn_2O_2/Sn_i	
2-7000	(2x1)										
11 419	(4x2)			(4x2)->(2x1) trans				(2x1) + O-sublattice distortion			

Theoretically, under more negative O chemical potentials (- 2.68 eV<$\Delta\mu_O$<-1.91 eV) the Sn_2O_2 units may coalesce to subsequently form (2x2) (-2.19 eV<$\Delta\mu_O$<-2.06 eV) and (2x1) (-2.38 eV<$\Delta\mu_O$<-2.19 eV) surface reconstructions in that order[167]. However, in this study, the (2x2) surface reconstruction is not observed, and the surface converts directly into the (2x1) surface reconstruction which is observed from a cumulative dose of 450 102 $e/Å^2$ and greater. This is possibly due to the small surface energy difference (0.0017 eV/$Å^2$) between the (2x2) reconstruction and the Sn_2O_2 units.

However, it has also been shown that the pathway is not purely dose dependent but also depends on the degree of defect density on the surface. Low coordination sites are expected to be more susceptible to electron beam and thermal excitations relative to their bulk counterparts. Hence, the $(1\bar{1}0)_l$, facet although imaged under identical conditions to the $(110)_t$ facet, undergoes a more complex surface reconstruction pathway. This behaviour is proposed to be related to the initial defect density.

The atoms on this surface are observed to gradually become undercoordinated with increasing cumulative dose, forming low occupancy terraces, alongside isolated Sn_i atoms. The facet subsequently forms asymmetric (2x1) and (1x2) surface reconstructions. Although observed under different experimental conditions, this reconstruction pathway is consistent with that observed in STM for oxidised {110} facets [167]. From these studies, it is known that surfaces

that are oxidised transform into a (1x1) surface reconstruction, and subsequently into a (1x2) reconstruction with thermal annealing [30,34,167]. In this study, the (1x1) surface reconstruction is not directly observed, similar to the observations by Li et al. (2021), where the surface is observed *in situ* using AC-(S)TEM[37]. In the latter, the sequence of periodic reconstructions from the bulk termination to the (2x1) reconstruction, and finally to the (1x2) surface, is identical to the one obtained in this study on the facet. However, in this work these transformations are observed on much smaller nanoparticles without the need for thermal annealing, in contrast to the study by Li et al. (2021)[37].

In the [001] projection, the model proposed by Li et al. (2021) agrees with the observations made in this study as shown through the overlaid atomic model on the [001] projected nanoparticle phase, restored from a FFS acquired at dose rate of 6946 $e/Å^2s$ and at a cumulative dose of 513 671 $e/Å^2$ shown in Figure 5.16 (a). This surface corresponds to the yellow ROI marked in Figure B.5 (h), in Appendix B. In addition, a [110] oriented nanoparticle imaged under similar FFS conditions (average dose rate of 5450 $e/Å^2s$ at a cumulative dose of 593 041 $e/Å^2$) as the nanoparticle in Figure 5.16 (a) was seen to possess a surface reconstruction. The Sn_i atoms in the reconstruction have an average distance of 2.7 (0.1) Å from the second atomic plane comparable to the value of 2.8 (0.2) Å measured for the (2x1) surface reconstruction shown in Figure 5.16 (a).

Moreover, the average distance between Sn_i atoms is 3.0 (0.2) Å which is consistent with 3.20 Å measured from the atomic model of Li et al. (2021). In the [110] projection, the Sn_i atoms have two sites that they can occupy, namely above pure Sn or above mixed Sn-O atom columns. These sites are referred to as the interstitial-vertical (*iv*) and the interstitial-horizontal (*ih*) sites[92]. It is evident from the model that the Sn_i are in *ih* sites. This evidence supports the conclusion that the observed reconstruction in the [110] direction is a (2x1) type. Qualitative comparison between the experimental data (Figure 5.16 ((a) and (b)) and that of phases restored from simulated focal series under the same imaging conditions (Figure 5.13 (c) and (d)), shows correspondence between the two. Focal series using models of both projections of the (2x1) surface reconstruction with thicknesses of 10 Å were simulated and subsequently restored with the same parameters as their experimental counterparts. Furthermore, consistent with these observations, the (2x1) surface identified by Li et al. (2021), also progressively converts into a (1x2) surface reconstruction. The conversion of the stoichiometric surface to the (2x1) and then (1x2) surface reconstruction is therefore consistent with theoretical and experimental observations.

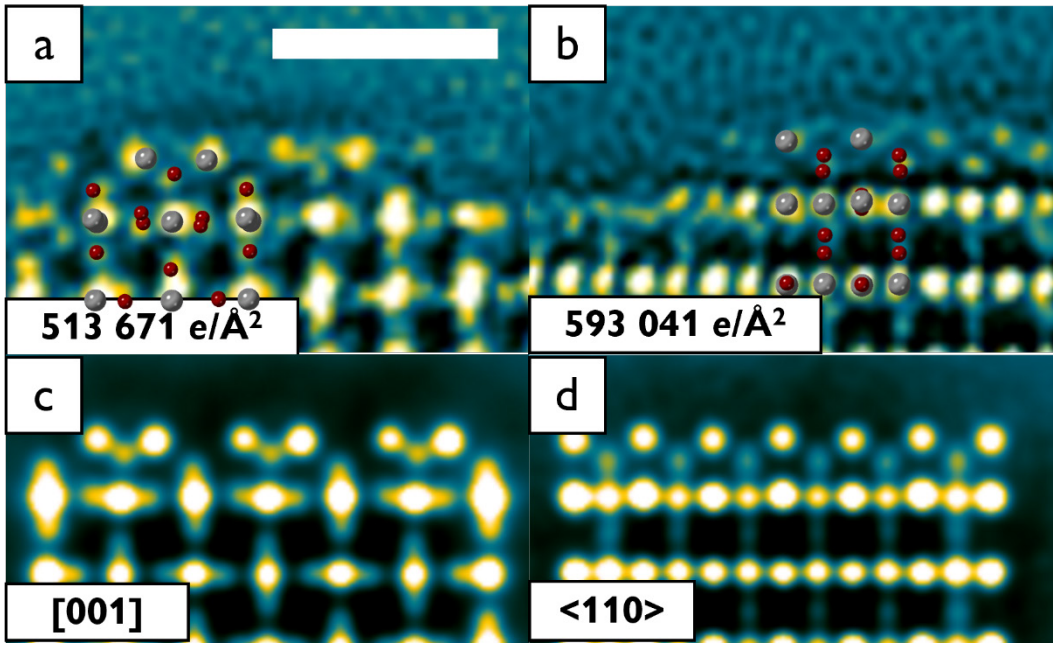

Figure 5.16: Magnified ROI shown on the surface of the [001] nanoparticle from Figure B.5 (h) and (b) that of a nanoparticle projected in a [110] direction acquired under comparable dose conditions. The nanoparticle was acquired with a dose rate of 5450 $e/Å^2s$. The grey and red atoms in the atomic model overlays represent Sn and O atoms, respectively. In (c) and (d) phases restored from simulated focal series of ≈10 Å thick atomic models of the (2x1) reconstruction model proposed by Li et al. (2021) [31] in the [001] and [110] projections are shown. The scale bar represents 10 Å.

At dose rates greater than 1150 $e/Å^2s$, all the examined facets show a (2x1) surface reconstruction at the lowest cumulative dose. At 1746 $e/Å^2s$ the (2x1) surface reconstruction occasionally converts to a facet composed of Sn_2O_2 units with increasing cumulative dose. Beyond this dose rate, the (2x1) reconstruction remained the most stable surface termination.

However, at the highest dose rate of 11 419 $e/Å^2s$ used for the CFS, the (4x2) surface reconstruction is observed alongside the (2x1) surface reconstruction. Little experimental evidence exists in literature for the (4x2) surface reconstruction. This motif has only been reported by de Frésart et al. (1981)

using LEED[64], and agrees well with the theoretical model proposed by Ágoston and Albe (2011)[167]. Despite the subsequent stability of the (2x1) surface reconstruction at this dose rate, bulk Sn atoms undergo reduction from Sn^{4+} to Sn^{2+} as evidenced by the distorted O sublattice [174].

At dose rates of about 1000 $e/Å^2s$, the stoichiometric surface is shown to be stable. However, it is also shown, here for the first time, that the reconstruction pathways of the {110} facets may be constructive or destructive, depending on the defect density of the facet. Here, constructive means the formation of reconstructions through the accumulation of atoms while destructive means reconstruction occurs through the loss of atoms. For the beam resistant facet, the stoichiometric facet converts to the (2x1) surface reconstruction at the highest cumulative dose. While that of the beam sensitive stoichiometric facet converted to the (1x2) surface reconstruction. Above a dose rate of 1000 $e/Å^2s$, the (2x1) surface reconstruction is the most stable surface reconstruction. Furthermore, at dose rates above 10 000 $e/Å^2s$ the nanoparticle undergoes bulk reduction. It is important to note that once the (1x2) surface reconstruction is formed STM/LEED studies and atomically resolved in situ AC-(S)TEM data show that it remains stable at room temperature, further indicating that it is indeed a low energy reconstruction of the (110) facet[37,69].

5.1. Conclusions

The dose dependence of (110) surface reconstructions on sub-10 nm 0.5 wt% Pd-SnO_2 nanoparticles is shown for the first time through an alternative image acquisition strategy for phase retrieval using focal series. It is shown that the stoichiometric surface is stable at lower dose rates ($\approx$ 1000 $e/Å^2s$) with increasing cumulative dose and it converts to known surface reconstructions of {110} SnO_2 facets through different mechanisms. On the more defective surface, the reconstruction proceeds through the loss of surface atoms, while on the less defective surface the reconstruction forms through the addition of more atoms. The reconstruction sequences are shown to be largely in agreement with those from STM/LEED and DFT studies. Further increase in the dose rate results in the formation of the (2x1) surface reconstruction. However, at dose rates above 10 000 $e/Å^2s$ reduction of the bulk of the nanoparticle is observed through the distortion of the O sublattice. Imaging in another projection reveals close agreement with the model previously proposed based on HAADF images and DFT calculations.

6. Conclusions and Recommendations

6.1. Conclusions

6.1.1. Surface chemistry of nominally Pd-doped SnO_2 nanoparticles

- Crystallographic and morphological analysis revealed that the facets observed experimentally corresponded to those theoretically predicted to have low surface energies: {100}, {110} and {101} [32,167].
- Similarly, it was revealed that vacuum projected facets of the experimental nanoparticles showed good morphological agreement with a Wulff constructed model, suggesting that nominal low concentration doping with Pd does not affect the relative surface energies of SnO_2 facets significantly: {110}<{101}<{100}[167].

- A method to increase the comparability of experimental and finite dose simulated focal series EWR was developed. The simulation approach demonstrated that the focal series cumulative dose used were all sufficient to achieve single O atom sensitivity at the vacuum/surface interface according to the Rose criterion i.e., all SNR>3.
- Simulations were used to compare the termination chemistry of the experiments with the stoichiometric and reduced terminations predicted to be stable theoretically. It was confirmed that for sub-10 nm nanoparticles the {100} and {101} facets of the nominally doped 0.5 wt% Pd-doped SnO_2 nanoparticles are largely Sn-terminated with a SnO overlayer. These findings validated theoretical predictions which have demonstrated that these reduced surfaces have low surface energies under low $O_{2(g)}$ partial pressures [32,33,38].
- The [110] and [111] projected nanoparticles were shown to have reduced {110} surfaces with an SnO termination when compared with theory. However, the reduced [001] projected (110) facet agreed with neither the stoichiometric nor non-stoichiometric surface terminations predicted by theory. Instead, it exhibited bulk O sublattice distortion and a surface motif comparable to the recently atomically resolved (2x1)-type surface reconstruction[37,41].

- Quantitative analysis of electron beam-induced surface dynamics was explored by segmenting 30-member focal series of the nanoparticles into 3 10-member focal series, which were shown to not have any information transfer gap through ECTF plots. Each segment was restored independently, and the transformations were assessed.
- This analysis revealed that {100} and {101} facets were stable under the electron beam and at the low $O_{2(g)}$ partial pressure in the microscope, also confirming DFT calculations and consistent with data from bulk single crystals[33,38]. These facets did not undergo reconstructions nor was their initial surface termination chemistry altered significantly with increasing cumulative dose.
- In contrast, the [001] projected (110) facet underwent significant surface transformations which progressively led to the formation of a full (2x1) surface reconstruction on this facet. This facet is terminated by Sn_i atoms which also compensate for O loss through a change in oxidation state from 4+ to 2+[167]. These findings are also consistent with experimental and theoretical findings that suggest that the {110} facets tend to undergo complex surface reconstructions with reduction[34,167].

6.1.2. Surface chemistry of beam-induced surface reconstructions on {110} facets

- In this chapter the sources of longer overhead times during CFS were quantified and an alternative, approach, termed FFS, was developed. Detailed workflows were developed, and all the necessary dose and defocus step per bit calibrations were measured. The overhead time per focal plane, O_{tp}, for the new approach was found to be 0.1 s compared to 2.8 s for CFS. Compared to the imaging conditions employed in Chapter 4, this resulted in the improvement of the temporal resolution of an exit wave restored from a 30-member focal series from 125 s to 32.85 s.
- Subsequently, multiple FFS per nanoparticle were acquired at various dose rates up to a cumulative dose comparable to that employed in Chapter 4 ($\approx$ 500 x 10^3 $e/Å^2$) to study the dose rate dependence of the observed surface reconstruction pathways.
- The initial surface chemistry and subsequent reconstructions on {110} facets were shown to be sensitive to the dose rate. Facets imaged at the lowest dose rate ($\approx$1100 $e/Å^2s$) initially exhibited a stoichiometric termination. However, their reconstruction pathways differed depending on the sensitivity of the facet to the electron beam.

- The facet that was very sensitive to the electron beam lost surface atoms to form an asymmetric (2x1) surface reconstruction which subsequently transformed into an asymmetric (1x2) surface reconstruction, consistent with theoretical calculations and experiments on SnO_2 cuboctahedra[37]. On the other hand, the beam-resistant facet formed a (2x1) surface reconstruction through the coalescing of Sn_2O_2 units, which has been shown to be a plausible reconstruction pathway using DFT calculations [167].
- For dose rates greater than 1800 $e/Å^2s$ and up to 7000 $e/Å^2s$ the {110} facets had a (2x1) surface reconstruction which remained stable up to the highest cumulative dose. This indicated that under these conditions, the (2x1) surface reconstruction has the least surface energy [41].
- At a dose rate of >10 000 $e/Å^2s$ a more complex reconstruction pathway was observed. This pathway involved the transformation of a (4x2) surface reconstruction into a (2x1) reconstruction. Moreover, the nanoparticle was observed to exhibit distortion in the O sublattice a factor attributed to the reduction of Sn atoms in the bulk of the nanoparticle[174].

6.2. Recommendations and Future Work

This thesis demonstrates the surface chemistry of sub-10 nm nominally Pd-doped SnO_2 nanoparticles at atomic resolution for the first time. Comparison with theoretical predictions shows good agreement with the observations in this study for all observed facets. The facets were shown to be Sn-terminated for the {100} and {101} facets, with Sn in their bulk positions. These facets, as predicted in theory and demonstrated experimentally, do not undergo progressive reconstruction beyond the initial loss of $O_{\mathbf{br}}$.

In contrast, {110} facets underwent complex surface reconstructions whose pathways are dependent on the dose rate and cumulative dose employed. The surface Sn atoms are mainly in interstitial positions on most reconstructions (excluding the (4x2) reconstruction where both bulk and interstitial Sn atoms are observed).

More experiments can be conducted to further understand the effect of Pd doping, the distribution of the dopants, elucidating the 3D nature of the nanoparticles as well as determining the active sites on pristine and reconstructed {110} surfaces under various experimental conditions. It must be noted that not all the experiments proposed below can be conducted on the instrument used in this study either due to the need of specialised equipment additions or complete instrument reconfiguration. For example, ptychography

was not enabled at the time of this study and aloof EELS can only be conducted on instruments with monochromators[192]. Additionally, environmental TEM experiments require specialised holders or differentially pumped microscopes that allow gases in the specimen chamber while keeping high pressures in the source and detector regions[193].

- Electron energy loss spectroscopy (EELS)

It has been demonstrated, on large crystals, that core loss EELS can be used to differentiate various forms of tin oxide i.e., SnO, SnO_2 and an intermediate state containing both phases[194]. In particular, the M_5 edge of SnO_2 is shifted to higher energies by 3.5 eV compared to those of the intermediate and SnO phases. Experimentally, this implies that undercoordinated surface Sn2+ atoms can be detected and differentiated from the bulk Sn4+ atoms. However, the dose required to generate the signal would be too high for performing EELS on the surface characteristics of sub-10 nm nanoparticles without damaging them or inducing surface modification.

Alternatively, a non-destructive phonon and vibrational spectroscopic aloof mode of low-loss EELS can be conducted. In this mode, the electron probe is placed several nanometres away (called the impact parameter) from the specimen to eliminate knock-on and significantly reduce radiolytic damage[192]. It has been shown in the case of guanine that the EELS spectrum features have similarities to those observed in FTIR data[195]. Suggesting that it may be

possible, at higher Pd doping concentrations, to determine characteristic vibrational modes measured using FTIR, due to terminal Sn-O[196] (526 cm^{-1} (65.2 meV)) and O-Pd[197] (580 cm^{-1} (71.9 meV), 650 cm^{-1} (81.0 meV)) stretching vibrations. However, this technique is applicable on instruments equipped with monochromators which reduce the energy spread of the electron beam for a cold-FEG from 300 meV to about 15 meV (at 200 keV)[192].

- Environmental TEM (ETEM)

Most of the analysis of SnO_2 materials have been conducted under high vacuum conditions in AC-(S)TEM and for all the facets there has been consistency between experimental findings and theory[33,34,37,39,41,167,170]. Although such studies are insightful, it may be better to examine the physico-chemical properties of the pristine and reconstructed facets on catalytically-relevant nanoparticles and the processes that take place on them under various gaseous/experimental conditions such as in $O_{2(g)}$. This may enable a direct link between structure-function properties under operating conditions as has been successfully elucidated for oxides such as TiO_2 [94,95,198] and CeO_2 [199].

Canhui et al. (2012) and Agoston et al. (2011), demonstrated that all SnO_2 facets at room temperature and under $O_{2(g)}$ are predominantly bulk terminated [167]. This suggests that in an ETEM, provided that the rate of O atom surface loss is less than the rate of O replacement due to the presence of $O_{2(g)}$ in the microscope, then the facets would be bulk terminated. This observation would

be consistent with the observations of Bugnet et al. (2017) for CeO_2 nanocubes [199].

Furthermore, under controlled, low dose rate conditions, increasing the temperature, in the presence of $O_{2(g)}$, results in the formation of temperature-driven surface reconstructions, in keeping with STM studies as has been observed with TiO_2 nanoparticles by Ek et al. (2018)[94] and single crystal lamellae by Yuan et al. (2020)[198]. In the case of SnO_2, this will mean that the metastable reconstructions such as the (4x1) surface reconstruction will not be observed. Since, it is primarily observed when the surface has been sputtered and annealed[29].

Additionally, Yuan et al. (2016), used ETEM to study the surface of TiO_2 nanocrystals with annealing[95]. They determined the various metastable and low energy surface reconstructions that lead to the (1x4) reconstruction under $O_{2(g)}$. They found that the $O_{2(g)}$ prolonged the stability of the surface reconstructions compared to high vacuum conditions and inert gases. Suggesting that $O_{2(g)}$ at high temperatures protects against the beam-induced O loss on surface reconstructions. Additionally, Yuan et al. (2020), determined that interstitial Ti4c (four-fold coordinated Ti atoms) on the (1x4) surface reconstruction were the active sites in water-gas shift reaction. Their experiments, conducted in an ETEM, showed that the (1x4) reconstruction in an oxygen atmosphere remained stable. While in the presence of water

molecules, twin protrusions were observed which disappeared in the absence of water vapour. Such an experiment can be conducted for various reconstructions of SnO_2 to extract similar information on active sites as well as the adsorption configuration of adsorbates under realistic reaction conditions.

- 3D inline holography

The 3D atom distribution on nanoparticles can be elucidated with single atom sensitivity from restored phases using inline holography[85]. This can be achieved through focal series exit wave reconstruction data acquired at low dose rates as successfully demonstrated by Chen et al. (2016) [85]. Alternatively, more dose efficient phase retrieval techniques such as ptychography can be used for the same purposes[200]. The advantage of using ptychography is that the data can be acquired simultaneously with HAADF data [201–203]. The HAADF data can be utilised to determine the 3D atom distribution of the cation sublattice as has been successfully implemented using statistical parameter estimation theory[81,204]. Then the ptychographic phase can be used to determine the 3D atom distribution of the anion sublattice using the inline holography scheme as demonstrated by Chen et al. (2016) and explicitly examined by Liberti et al. (2019, 2021a, 2021b) [201–203] and Mostaed et al. (2022)[205]. Combining these two approaches enables the use of HAADF data to rescale ptychographic data, especially for heavy atom columns, where phase wrapping can make heavy atom columns appear to have lower occupancy. Additionally, clarity on the

degree of non-stoichiometry in nanoparticles based on the counts of both Sn and O atoms can be attained as well as nanoparticle shape and surface roughness.

Appendix A

4.2 Theoretical and experimental methods

4.2.4 Finite electron dose focal series simulations

Figure A.1 shows a plot of vacuum noise standard deviations of phases restored using simulated focal series data. This image demonstrates how rescaling images to 8-bit increases the noise standard deviation. The rescaled images have a ≈2-times the vacuum noise standard deviation of the 32-bit phases at all doses.

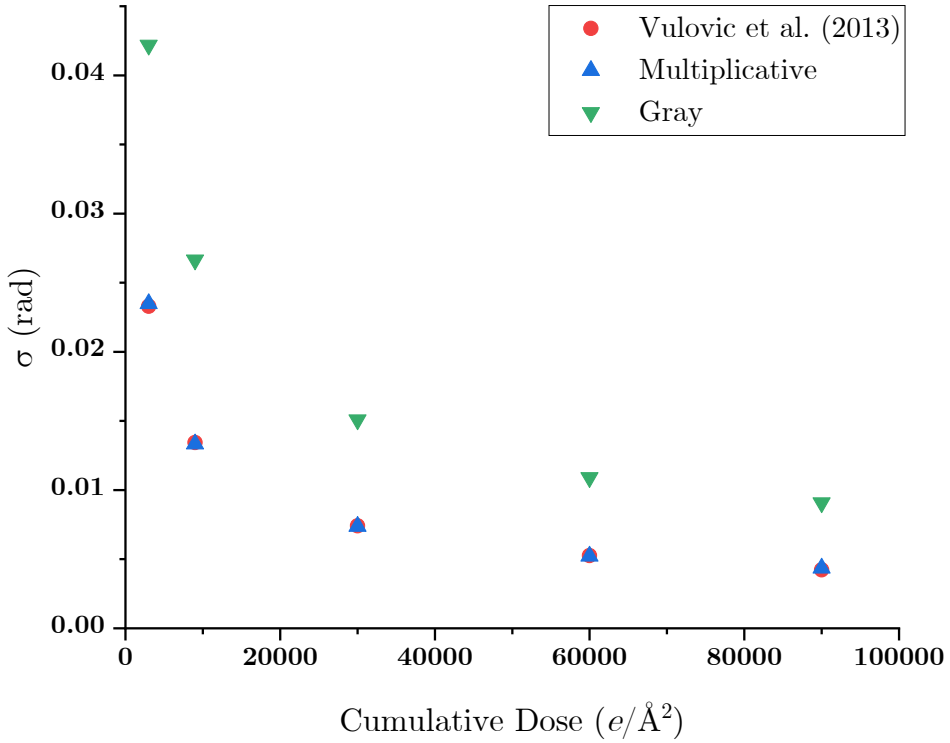

Figure A.1: Vacuum noise standard deviations from phases restored using experimental and simulated focal series saved as 32-bit (Multiplicative) and 8-bit (Gray) as a function of cumulative dose.

4.2.5 Focal series exit wave restoration

Figure A.2 shows selected focal series data for the [110], [111], [100] and [101] projected nanoparticles. These nanoparticles were acquired at low doses per frame and thus their surface chemistry cannot be unambiguously determined due to the poor SNR at the vacuum surface interface. Additionally, given that these data were searched for at lower doses than during the acquisition, they inevitably have residual aberrations.

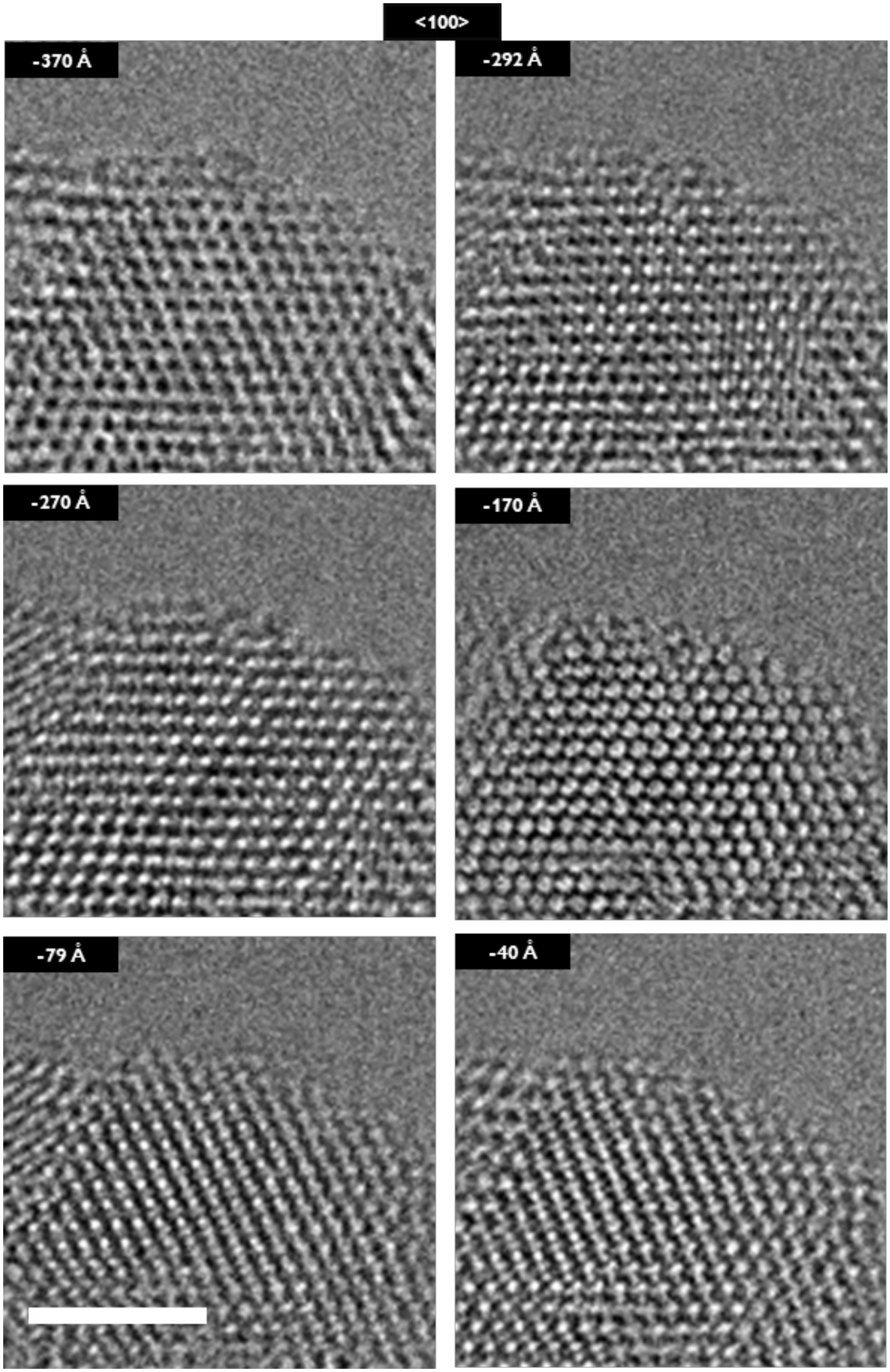

Figure A.2: *see continuation of image below for full caption.*

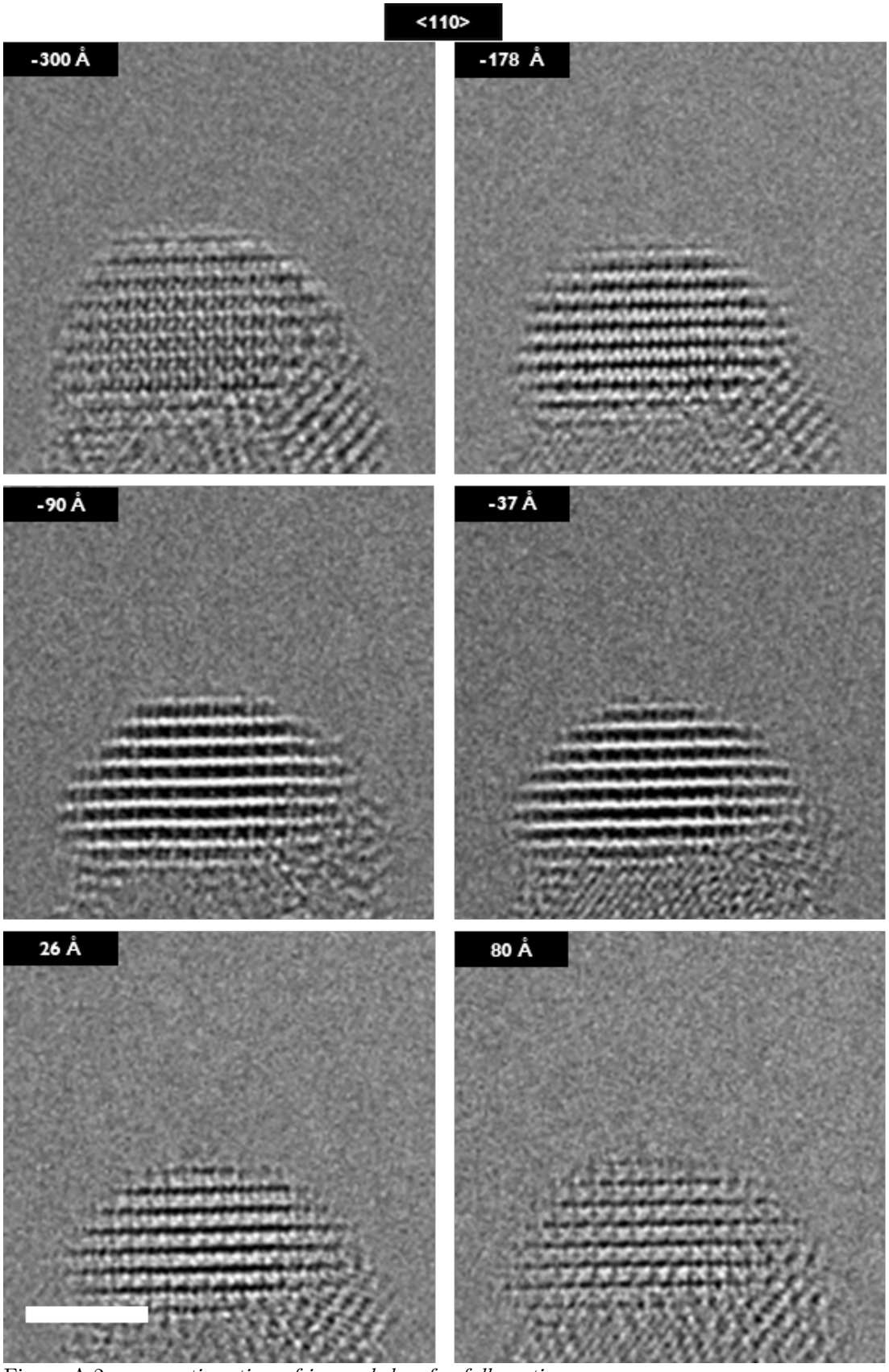

Figure A.2: *see continuation of image below for full caption.*

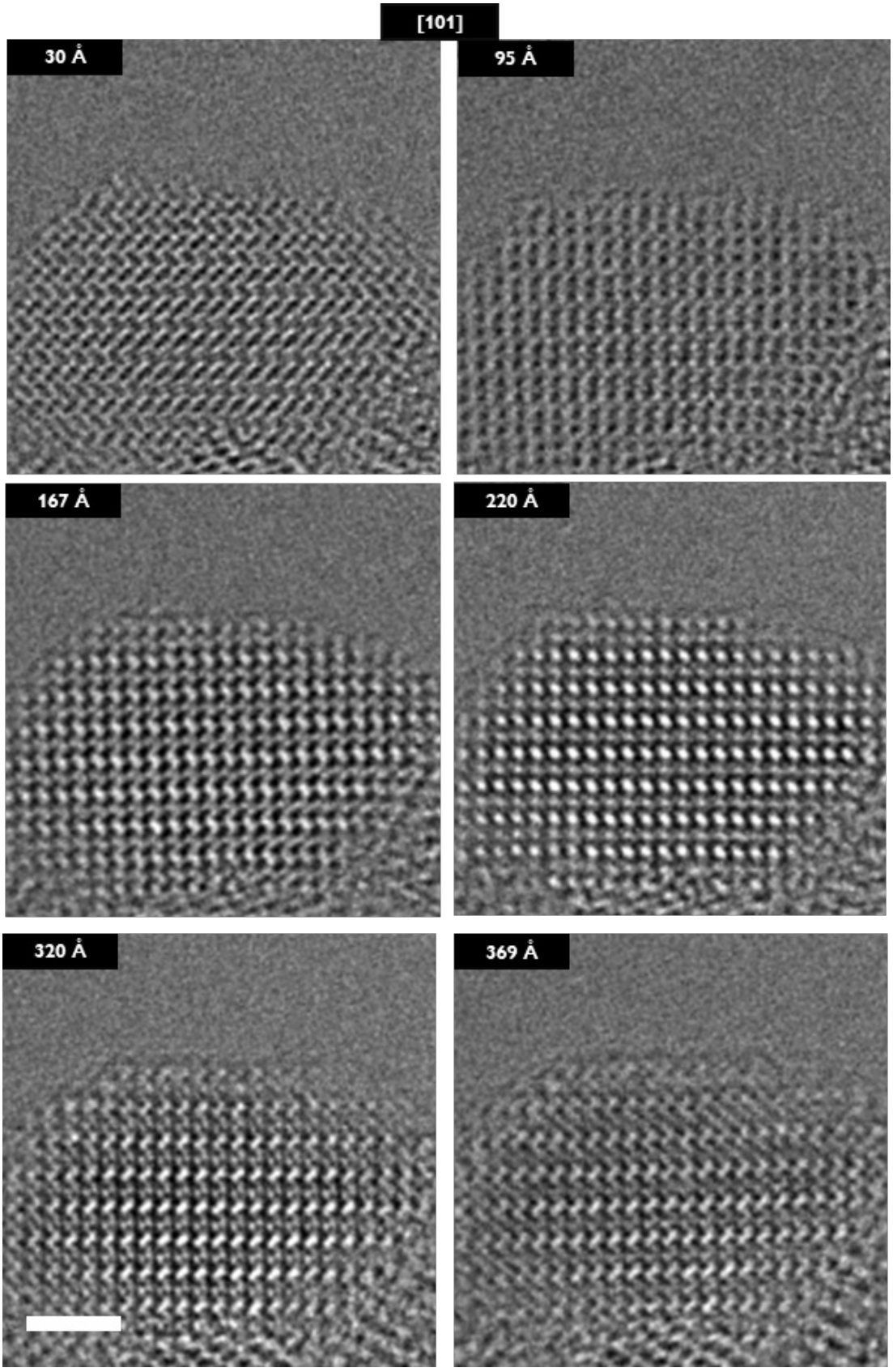

Figure A.2: *see continuation of image below for full caption.*

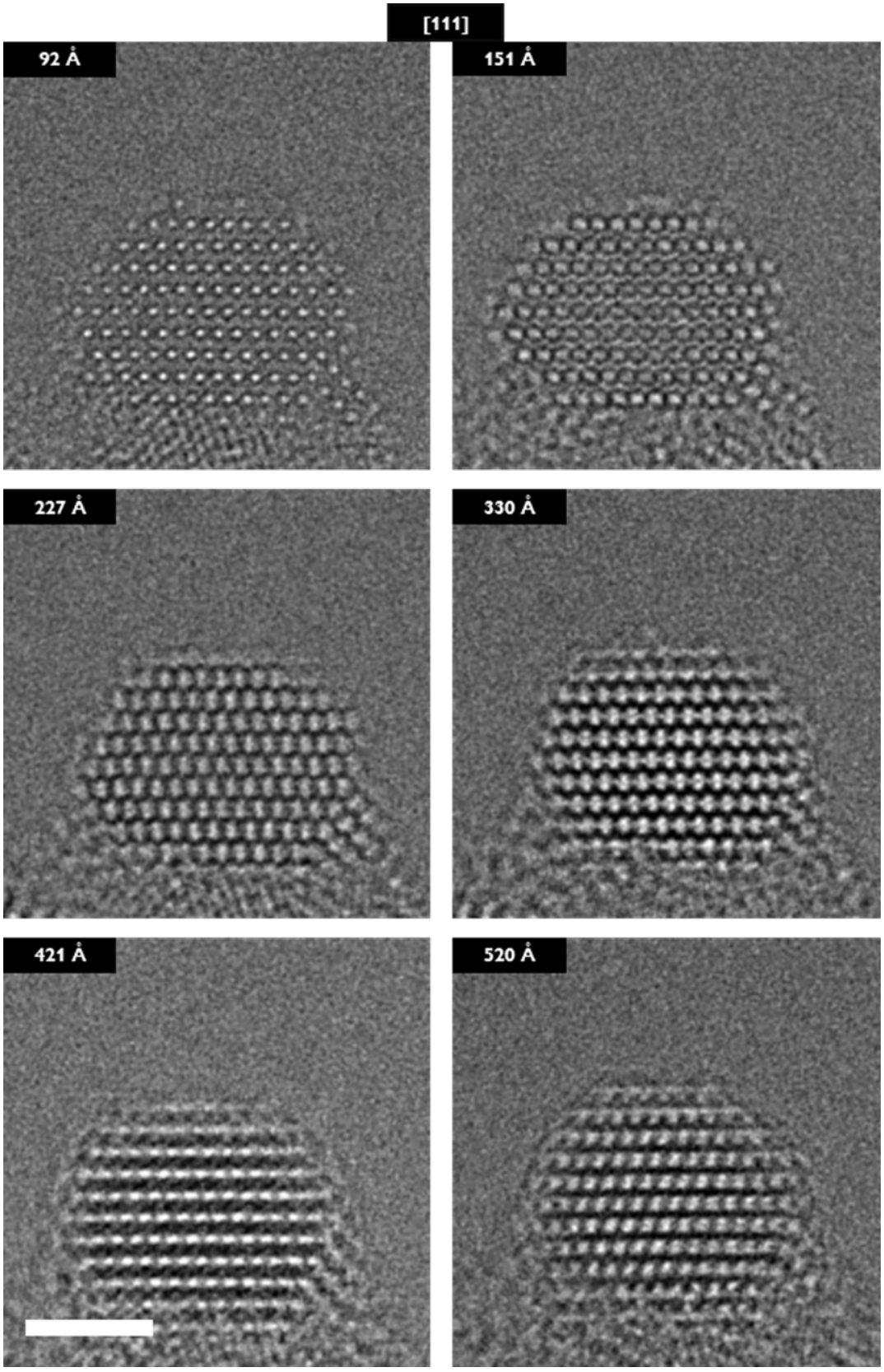

Figure A.2: Selected examples of focal series data acquired for the [100], [110], [101] and [111] oriented nanoparticles. The defoci of the selected images are shown and the scale bars on all the series correspond to 20 Å.

For example, based on EWR computations, the [100] and [101] focal series data had A_1 values of -13.4 nm (14 °) and 10.7 nm (-7 °), respectively. Nonetheless these and other residual parasitic aberrations were compensated for during the restoration process such that there was clear correspondence between the phase and the atomic model of SnO_2 in these projections (see Figure 4.18 – 4.20 in the main text).

4.3 Results

4.3.1 Experimental focal series

Surface terminations of the unrelaxed Wulff model were generated by deleting atoms in projection to match the projected atomic arrangement based on theoretical findings[29,34]. An example of the surface terminations of the {110} facets possessing various surface terminations is shown in Figure A.3.

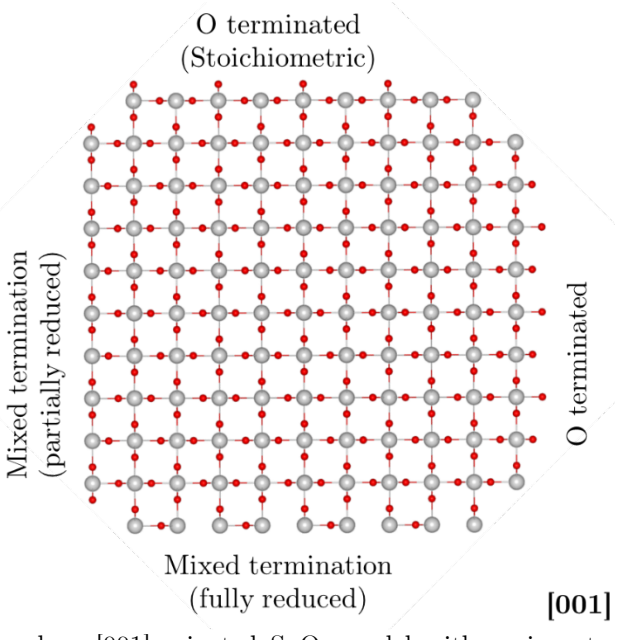

Figure A.3: An exemplary [001] oriented SnO_2 model with various termination chemistries based on theoretical and experimental findings [105,106].

4.3.2 Single O atom sensitivity study: simulated focal series

Figure A.4 shows phases restored from simulated noiseless MTF-damped focal series of the SnO_2 lattices (left) and O sublattices (right) of the [001] (top) and [110] (bottom) projected Wulff models. Quantifying the phase shifts of surface O atom columns from the SnO_2 lattice and O sublattices shows that the large phase shifts induced by these atoms can be accounted for by their overlap with nearest neighbour Sn atom columns (see inserts in Figure A.4) as was shown in Figure 20 (a).

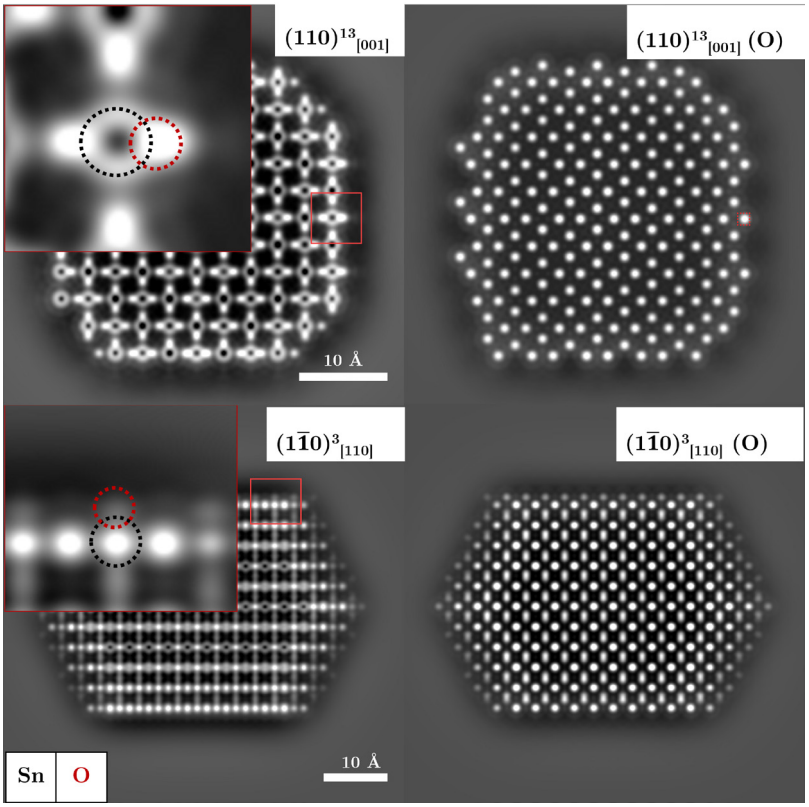

Figure A.4: Simulated noiseless phase images from a [001] (top left and right) and [110] (bottom left and right) SnO_2 model nanoparticle. The phases on the left were restored using an SnO_2 model while those on the left were restored from the O sublattice of the same model. The O columns with maximum occupancy are highlighted with a red box for the stoichiometric surface. The insert is an enlarged version of the red box indicating the position of overlapping Sn and O atom columns, in black and red dashed circles respectively.

Table A.1 summarises the fitting parameters used for plotting the dose-dependent SNFR plot shown in Figure 20 in the main text. The SNFR values scale by a factor of $\sim \mathbf{A}\sqrt{dose}$, where **A** is close to 1.

Table A.1: A summary of the fitted parameters of the power law functions, SNFR=Ax^c, fitted to SNFR data with the values in parenthesis being the standard errors of the fitted parameters.

Facet	**A**	**c**	**R^2**
$(011)^6_{\|100\|}$	0.74 (0.05)	0.48 (0.02)	0.998
$(110)^{13}_{\|001\|}$	0.98(0.04)	0.46(0.01)	0.999
$(1\bar{1}0)^3_{\|110\|}$	0.96(0.20)	0.47(0.06)	0.997
$(\bar{1}01)^{10}_{\|101\|}$	0.62(0.04)	0.48(0.02)	0.999
$(010)^3_{\|101\|}$	0.87(0.09)	0.41(0.03)	0.964
$(\bar{1}10)^4_{\|111\|}$	0.63(0.09)	0.50 (0.03)	0.999

4.3.3 Surface dynamics

Figure A.5 and Figure A.6 shows the effective contrast transfer functions (ECTF) of the individual complex exit waves obtained using segments of 10-member series for each nanoparticle projection. The vertical lines in the plots represent the spectral density of each projection. The ECTF was calculated using PCF/PCI derived defocus values for each 10-image focal series. As discussed in the main text, these plots demonstrate that all the restored waves contain identical information and none of the relevant spatial frequencies are dampened or lost within the explored defocus ranges. Therefore, the contrast variation is attributed to actual specimen changes.

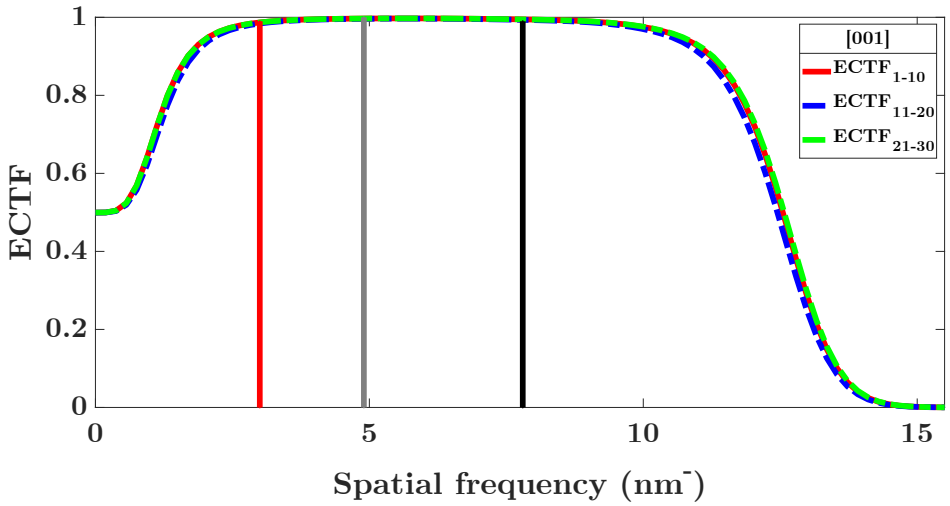

Figure A.5: The ECTF of the restorations of the nanoparticle oriented in the [001] direction. The black, grey and red lines indicate reciprocal distances between O-O atoms, Sn-Sn atoms and O-Sn atoms in the projected unit cell.

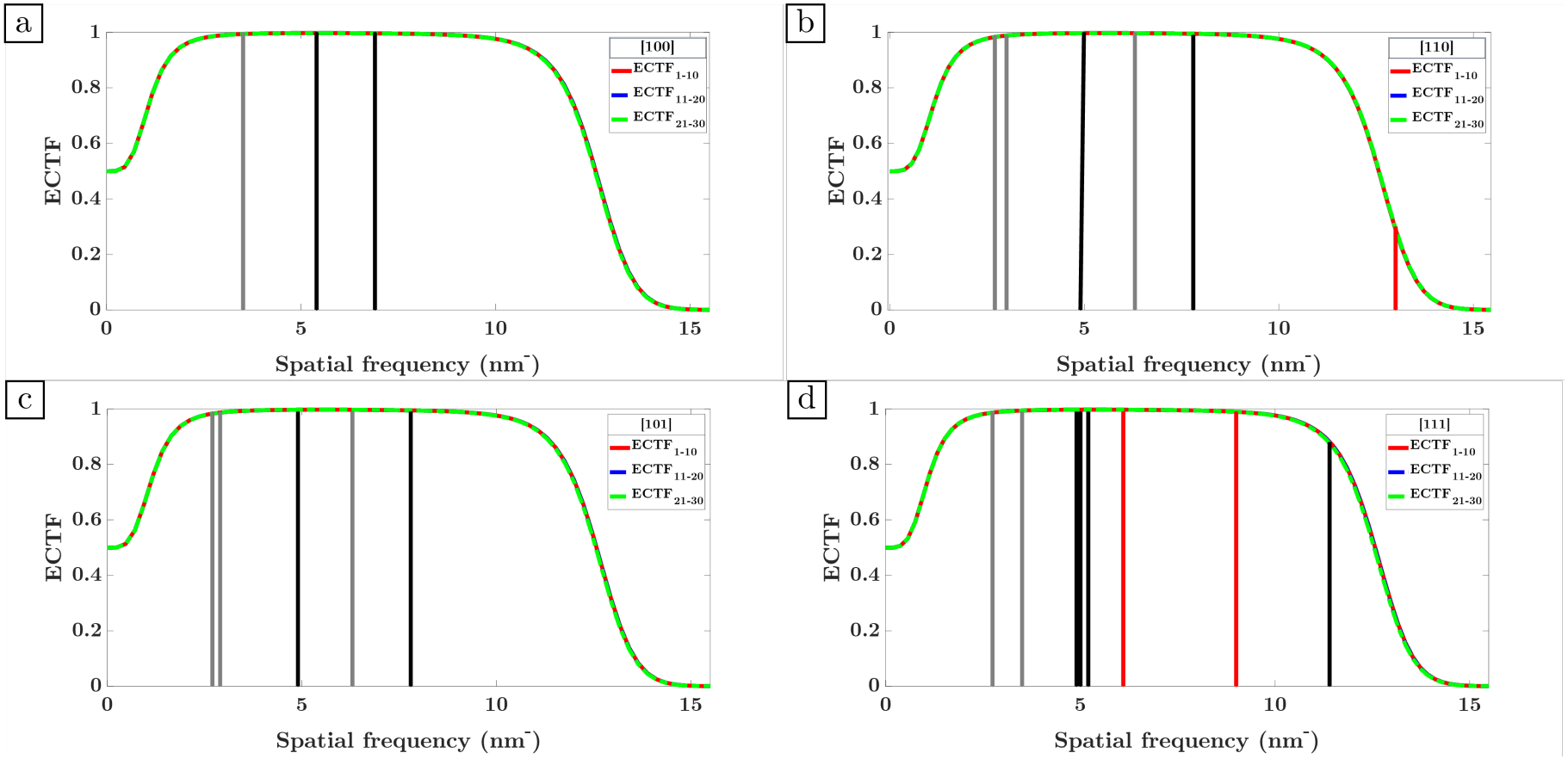

Figure A.6: The ECTF of the restorations of the nanoparticles oriented in the (a)[100], (b) [110], (c) [101] and (d) [111] directions. The black, grey, and red lines indicate reciprocal distances between O-O atoms, Sn-Sn atoms, and O-Sn atoms.

Figures A.7-11 (a-c) show the phases of experimental nanoparticles restored using the first, second and last 10 images of the full 30-member focal series. For all projections, the first (a) 10-image phase is assumed to be most representative of the nanoparticle prior to beam/thermal induced transformation. The second (b) and third (c) show the subsequent visual bulk and surface transformation of the nanoparticle with time. For each phase restored using the 10-member focal series images, the corresponding log moduli of the FFTs of the complex exit waves (d-f) are used as an indirect means to assess any bulk phase transformation. The bulk phase transformations can either be observed through the fading of Fourier components, signifying amorphisation or through the introduction of additional Fourier components indicating phase change [206]. Additionally, nanoparticle rotation and partial mistilt can be observed through the rotation of the nanodiffractograms and the asymmetric distribution of their Fourier components, respectively.

For all the nanoparticles, in general, the surface chemistry obtained using the first 10-member focal series is identical to that obtained using the full 30-member focal series i.e., all the surfaces remain largely Sn-terminated. Additionally, interpolating from Figure 4.21, all the 10-member focal series restored phases should have single O atom SNFR values close to 3.0, except for the [111] oriented nanoparticle which has a predicted SNFR value of 2.2.

In theory this implies that single O atoms should be detectable above the noise for all the other projections according to the Rose criterion.

Atom loss at the step edges and small terraces is evident with time for the [110], [111] and, [101] oriented nanoparticles (b, c). The visible damage is limited to the loss of a few atom columns (shown with white dashed circles in all figures) without the change of the surface chemistry for most of the nanoparticles. The exception is the $(010)_{[101]}$ facet which exhibits mixed O and Sn-terminated regions after the loss of surface Sn atoms post-beam exposure at a total cumulative dose of 194×10^3 e/Å^2 (see red arrows in Figure A.11 (c)). Also, in the surface termination of the [100] oriented nanoparticle remains largely Sn-terminated despite visible surface atom redistribution at the surface across the planar defect (shown with dashed red line). Evidently, the surfaces of the nanoparticles are beam resistant as exposure to high electron doses and the subsequent surface transformation, generally, do not change the findings made in Chapter 4 using the full focal series. Other additional surface properties such as exposed undercoordinated Sn atoms on step-edges in addition to those observed on facet terraces (Figure A.7) and local surface strain[175,176] (grey arrows in Figure A.7 (a)) as well as planar defects[177] (Figure A.9) have been shown to enhance selectivity and activity of SnO_2-based nanomaterials in CO_2 electroreduction reaction (CO_2RR).

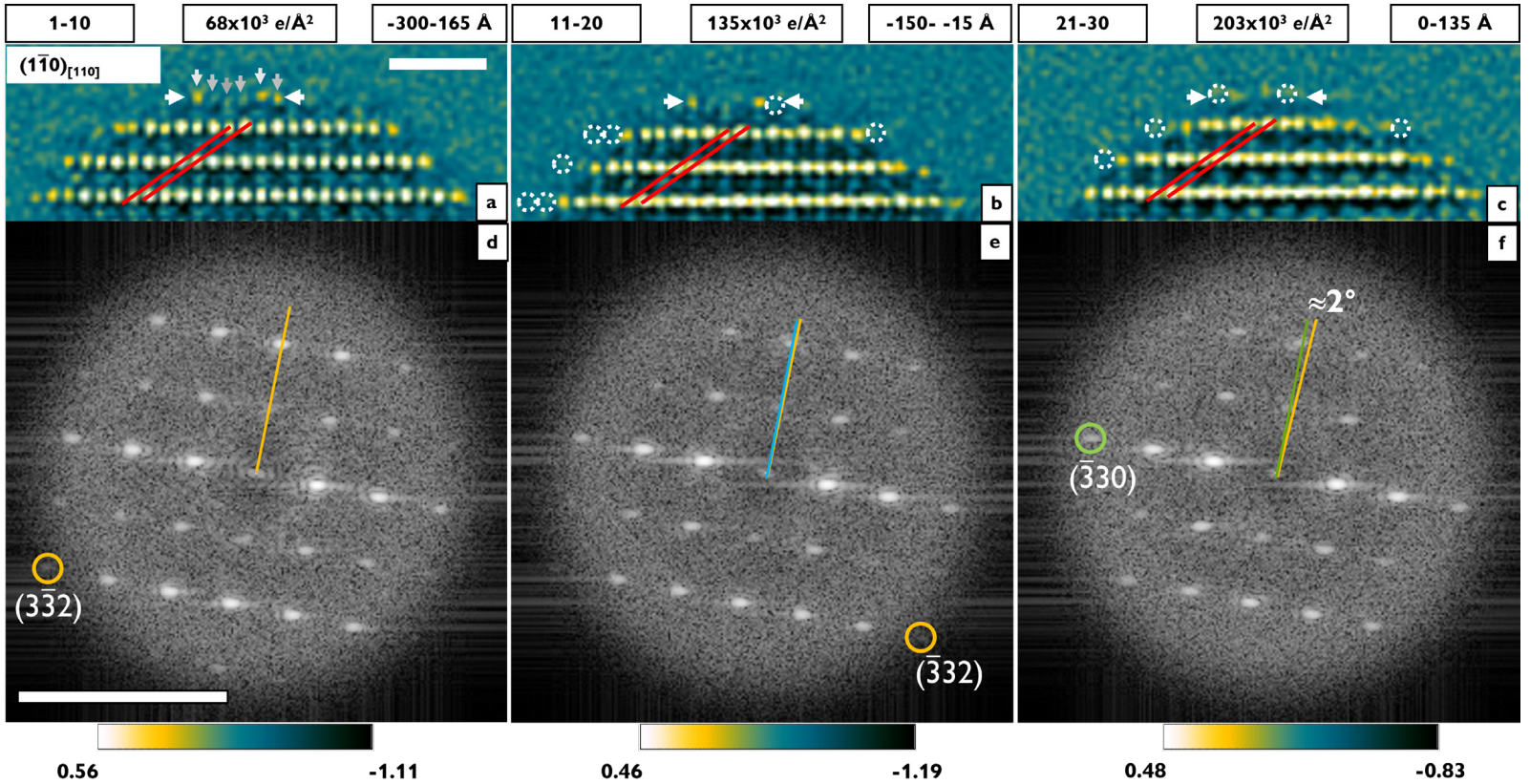

Figure A.7: Phases of the $(1\bar{1}0)_{[110]}$ facets restored using the first (a), second (b), and third (c) third of the 30-member focal series. The total dose at a given point in time is shown as well as Sn vacancies (shown with white dashed circles) that progressively appear compared to the previous phase. Each restoration had a focal series cumulative dose of 1.93x10^3 e/Å^2 (O SNFR= 3.81). The arrows show atoms on the upper layer that were not clear on the phase restored using the full focal series. (c-e) Below each phase is the log modulus of the FFT of the complex exit wave it was restored from. These indicate that the nanoparticle underwent some slight tilting with time as seen in the asymmetry of the Fourier components. Additionally and the nanoparticle also underwent rotation of up to ≈2° clockwise relative to the first nanodiffractogram. Although, the {332} reflections are not present in (f), they correspond to the interplanar spacings indicated with red lines which are visible on all phases. This effect maybe induced by particle tilting.

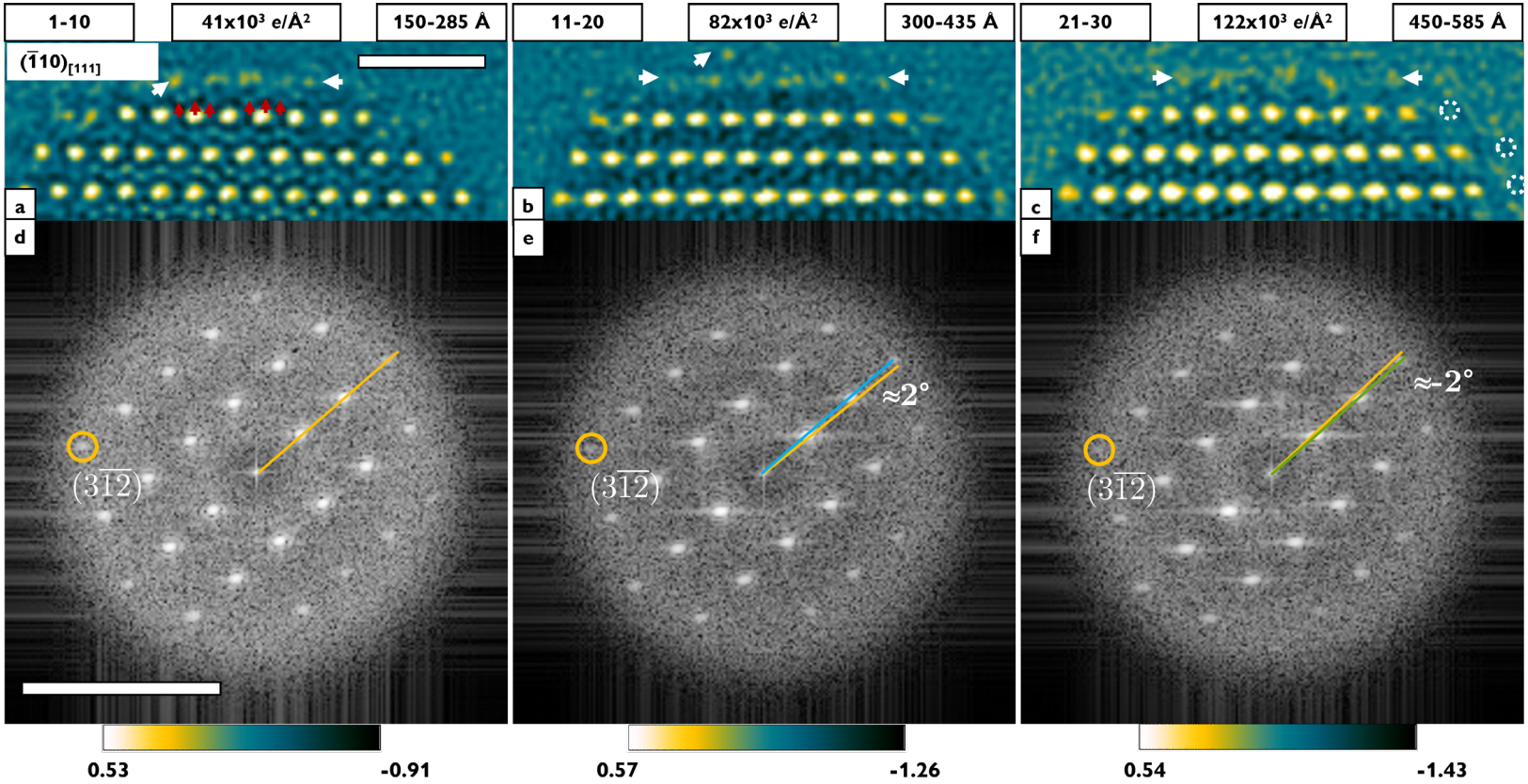

Figure A.8: Phases of the $(110)_{[111]}$ facets restored using the first (a), second (b), and third (c) third of the 30-member focal series. The total dose at a given point in time is shown as well as Sn vacancies (shown with dahsed circles) that progressively appear compared to the previous phase. The contrast of the upper atoms which was not visible on the phase restored using the full 30-member focal series is also shown with white arrows and the red arrows show the exposed O atom columns in the second atomic layer. Each restoration had a focal series cumulative dose of $11.7\text{x}10^3$ $e/\text{Å}^2$ (O SNFR= 2.2). (c-e) Below each phase is the log modulus of the FFT of the complex exit wave it was restored from. The asymmetry of the Fourier components shows that the nanoparticle mis-tilted and also under went rotation firstly 2° clockwise (d) and then 2° anticlockwise (e) relative to its initial position (d).

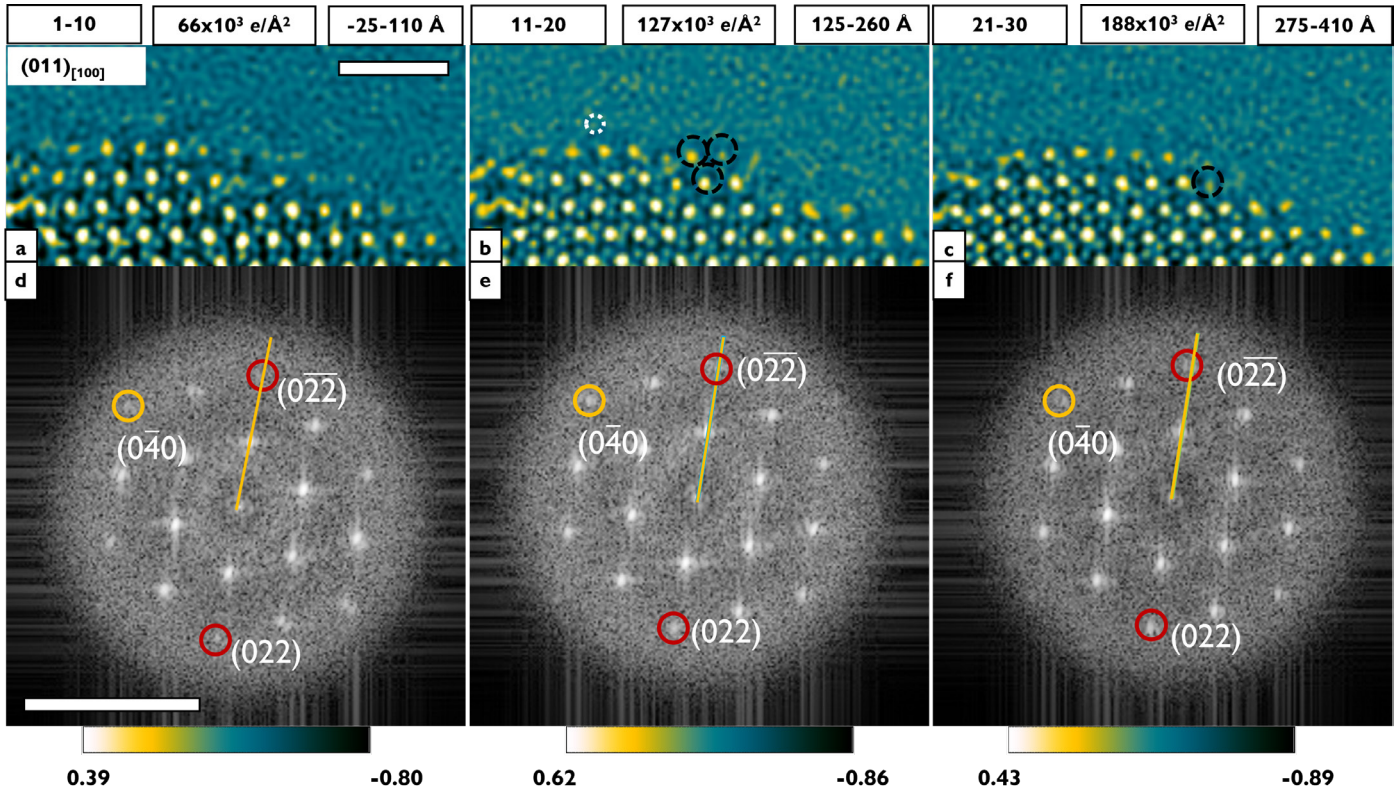

Figure A.9: Phases of the $(011)_{[100]}$ facets restored using the first (a), second (b), and third (c) third of the 30-member focal series. The total dose at a given point in time is shown as well as Sn vacancies (shown with white dashed circles) that progressively appear compared to the previous phase and additional Sn atoms relative to the previous phase are also shown using black dashed circles. The surface was undergoing atom redistribution. Additionally, a planar defect (red dashed line) that progressively ameliorates is shown also. Each restoration had a focal series cumulative dose of $18.0\text{x}10^3$ $e/\text{Å}^2$ (O SNFR$\approx$ 3.0) (c-e) Below each phase is the log modulus of the FFT of the complex exit wave it was restored from. The nanoparticle also progressively reoriented to be fully on axis in time as the asymmetry of the Fourier components was reduced i.e., introduction of the $(0\bar{2}\bar{2})$ Fourier reflection and the simultaneous intensification of this reflection and its Friedel pair, the (022) reflection. The nanoparticle did not undergo measurable rotation, however.

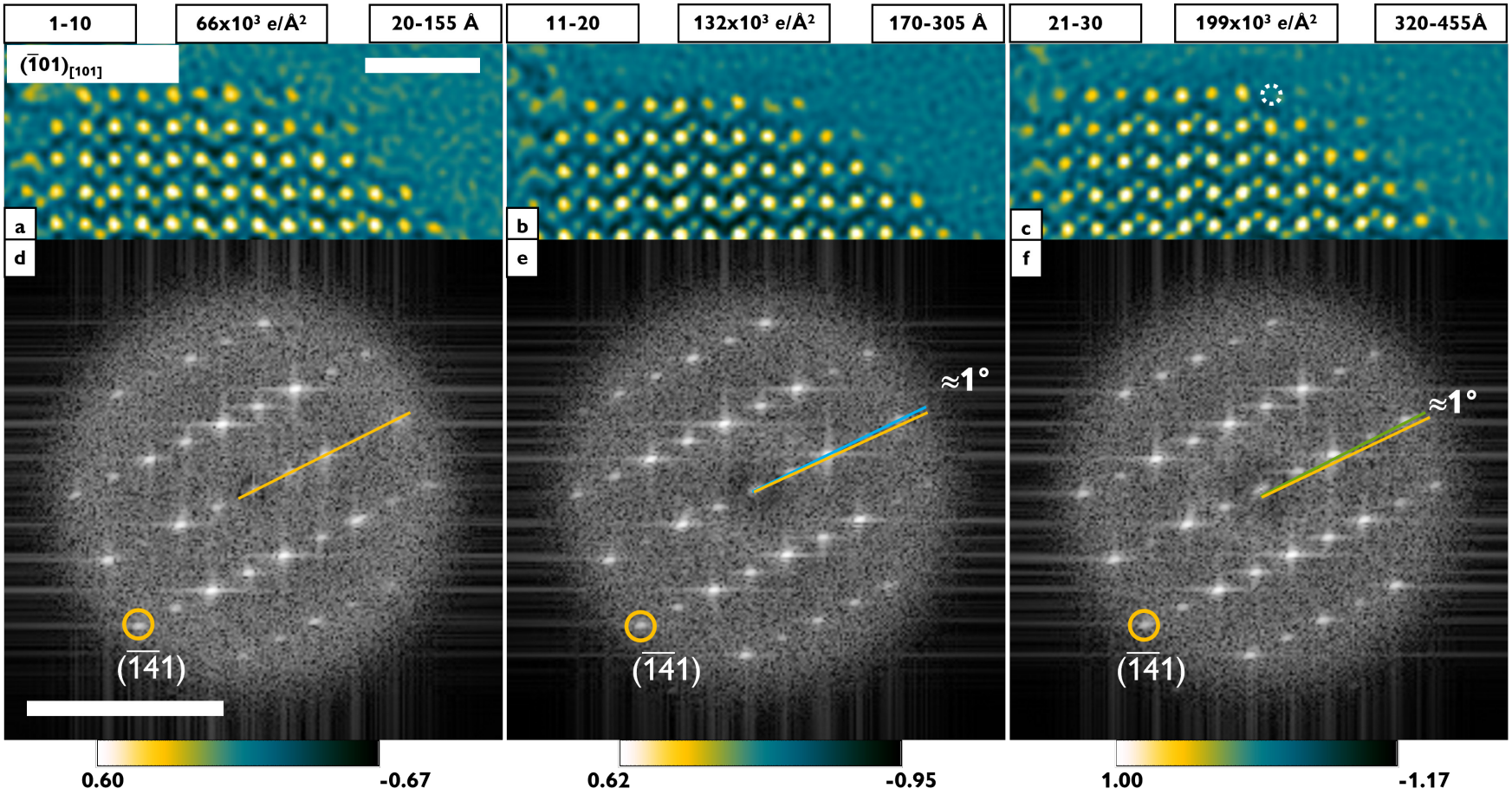

Figure A.10: Phases of the $(\bar{1}01)_{[101]}$ facets restored using the first (a), second (b), and third (c) third of the 30-member focal series. The total dose at a given point in time is shown as well as Sn vacancies (shown with dahsed circles) that progressively appear compared to the previous phase. Each restoration had a focal series cumulative dose of 18.9x10^3 e/Å^2 (O SNFR= 2.6) (c-e) Below each phase is the log modulus of the FFT of the complex exit wave it was restored from. These indicate that the nanoparticle did not experience significant mistilting about the zone axis but it did rotate slightly by ≈1° from (d) and remained in that orientation to the end of the focal series (e).

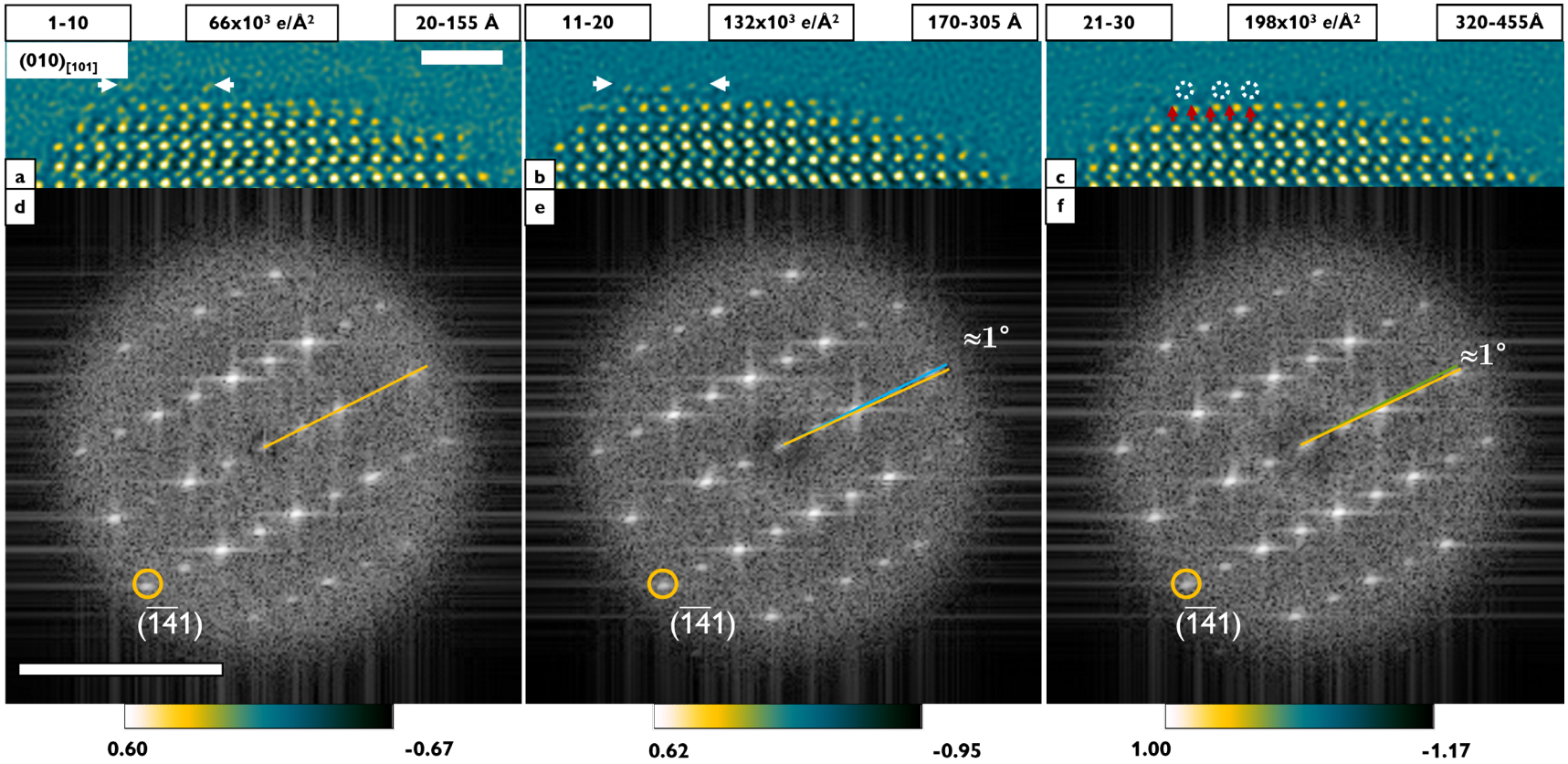

Figure A.11: Phases of the $(010)_{[101]}$ facets restored using the first (a), second (b), and third (c) third of the 30-member focal series. The total dose at a given point in time is shown as well as Sn vacancies (shown with white dashed circles) that progressively appear compared to the previous phase. Additionally, the last phase shows mixed surface termination i.e., O (red arrows in (c)) and Sn post beam-exposure. Each restoration had a focal series cumulative dose of $18.9\text{x}10^3$ $e/\text{Å}^2$ (O SNFR ≈ 3.0) (c-e) Below each phase is the log modulus of the FFT of the complex exit wave it was restored from. These indicate that the nanoparticle did not experience significant mis-tilting about the zone axis, but it did rotate slightly by $\approx 1^\circ$ from (d) and remained in that orientation to the end of the focal series (e).

Moreover, comparing the nanodiffractograms of the nanoparticles with time indicates that they were partially mis-tilted as the relative intensity of the Fourier components changes slightly with time. However, for most nanoparticles the maximum transferred spatial frequency is identical with no additional Fourier components introduced as time progresses, indicating that the nanoparticles were not experiencing any detectable beam-induced damage or phase change in the bulk also. Additional particle rotation perpendicular to the imaging direction can be seen through the slight rotation of $\leq 2^{\circ}$ of the nanodiffractograms (Figure A.7 (f) and A.8 (e, f)).

Appendix B

5.2 Experimental methods

5.2.1 Effects of overhead time on dose and temporal resolution

Figure B.1 shows the scripts used during FFS and CFS. The first script indicates the pre-acquisition parameters and the loop for changing the OL focus as well as the OL settling time for FFS. Similarly, the CFS script also shows the pre-acquisition parameters, instructions to write calibrations and the *for loop* for several processes which include creating the stack and copying calibrations and applying the OL settling time.

FFS OL change script

```
number nImages  = 60;
number focal_step    = 3;          // X bit
number focal_settle_delay_s = 1;
// Get the current focal value
number focus_start = EMGetFocus();
// string starttime = datestamp();
number i = 0;
for(i = 0; i < nImages; i++)
{
//Set focus
       EMSetFocus((i+1)*focal_step + focus_start nImages*focal_step/2);
// Delay for settling
              Sleep(focal_settle_delay_s);
}
EMSetFocus(focus_start);
Sleep(focal_settle_delay_s);
```

Figure B.1: *See below for full image caption.*

CFS script

```
//set binning
number exposure_s     = 0.4;
number nImages        = 30;
number focal_step     = 3;          // bit
number focal_settle_delay_s = 1;
taggroup tag;
Image frame,final_frame;
// Get the current focal value
number focus_start = EMGetFocus();
string starttime = datestamp();
// Create the data container
Image out := Realimage("Through focus series", 4, image_width, image_height,
nImages);
ShowImage(out);
// Write some calibrations
out.ImageSetDimensionScale(2, focal_step);
out.ImageSetDimensionUnitString(2, "focal step");
//start focus series
number i = 0;
for(i = 0; i < nImages; i++)
{OpenAndSetProgressWindow("Acquire focal series", " - frame " + (i+1) + "/" +
nImages, "");
       //Set focus
       EMSetFocus((i+1)*focal_step + focus_start - nImages*focal_step/2);
// Delay for settling
       Sleep(focal_settle_delay_s);
       // Acquire image & inset it into stack
       frame     :=     SSCGainNormalizedBinnedAcquire(exposure_s,     binning,
ccd_height/binning/2  -  image_height/2,  ccd_width/binning/2  -  image_width/2,
ccd_height/binning/2 + image_height/2, ccd_width/binning/2 + image_width/2);
       tag=ImageGetTagGroup( out );
       TagGroupReplaceTagsWithCopy(tag, ImageGetTagGroup( frame ));
       out[0, 0, i, image_width, image_height, i+1] = frame;
       // Update image
       out.UpdateImage();
       out.ImageGetImageDisplay(0).ImageDisplaySetDisplayedLayers(i, i);
```

Figure B.1: *See below for full image caption.*

CFS script

```
        // Copy some calibrations
        if(i == 0)
        {number j;
        for(j = 0; j <= 1; j++)
                {out.ImageSetDimensionScale(j,
frame.ImageGetDimensionScale(j));
                out.ImageSetDimensionUnitString(j,
frame.ImageGetDimensionUnitString(j));}}
                ImageSetDescriptionText(out, "Start : "+starttime + "\n" + "End
: " + Datestamp() + "\n" + focal_step + "bit \n" +  exposure_s+ "sec \n");
                        if(ShiftDown()==1&&OptionDown()==1)
                        {i=nImages;}}
//End focal series
EMSetFocus(focus_start);
        Sleep(focal_settle_delay_s);
final_frame     :=     SSCGainNormalizedBinnedAcquire(exposure_s,     binning,
ccd_height/binning/2 - image_height/2, ccd_width/binning/2 - image_width/2,
ccd_height/binning/2 + image_height/2, ccd_width/binning/2 + image_width/2);
saveAsGatan(final_frame, "finalimage")
OpenAndSetProgressWindow("", "", "");
out.ImageGetImageDisplay(0).ImageDisplaySetDisplayedLayers(0, 0);
```

Figure B.1: Scripts for executing the fast (FFS) and conventional (CFS) focal series.

5.2.3 Exit wave restoration

Figure B.2 shows individual (bottom) and summed (top) frames per focal plane at various defoci for FFS acquired at dose rates of 1746 $e/Å^2s$ (a-c) and 1150 $e/Å^2s$ (d-f).

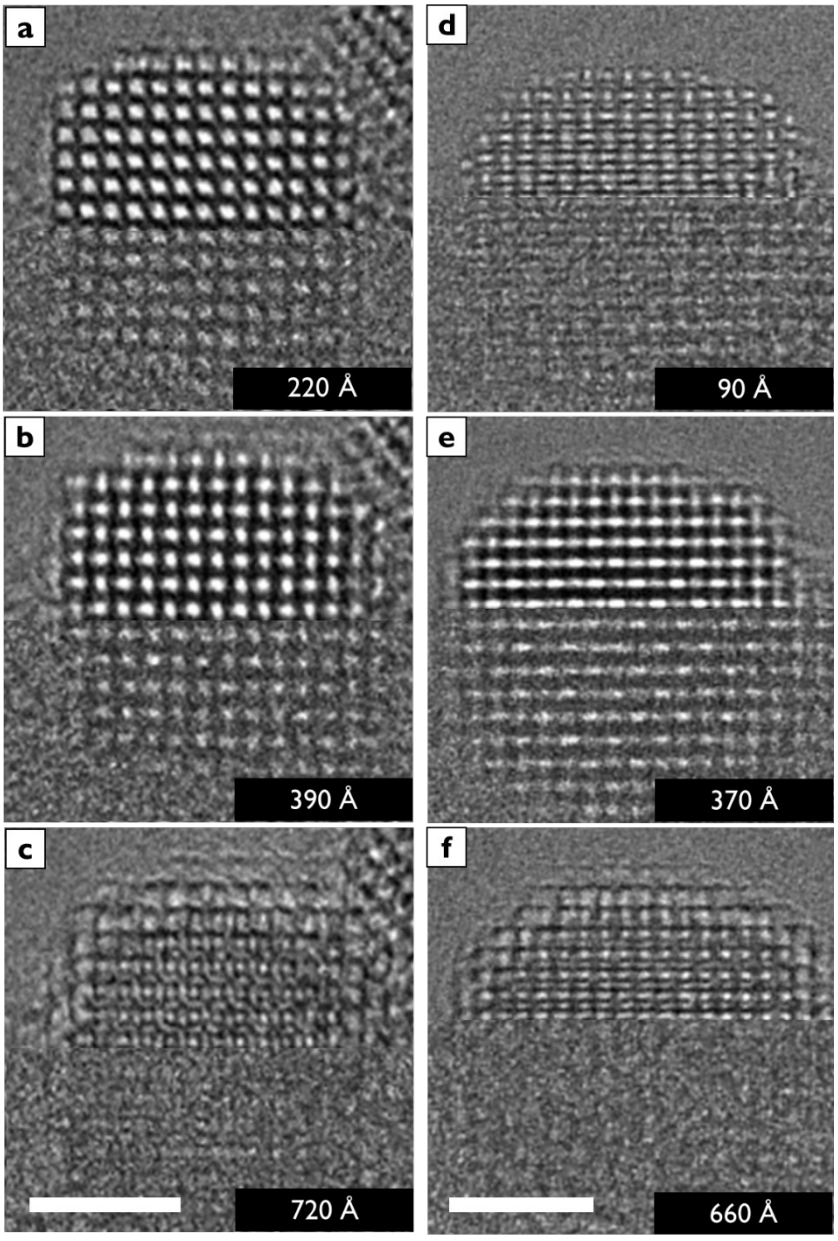

Figure B.2: A subset of focal series data, at the shown defoci, obtained using dose rates of 1746 $e/Å^2s$ (a-c) and 1150 $e/Å^2s$ (d-f), respectively. The top and bottom of each image shows the summed and individual frames per focal plane. The scale bar is 20 Å. The C_3 values of the data were -4.94 µm and 0.44 µm, respectively. Refer to the main text for all the other parameters.

Figure B.3 shows a linear curve fitted onto the defocus values predicted by FTSR using the PCI/PCF method for the FFS dataset used to restore the phase shown in Figure 5.8 (d). Each data point corresponds to a single focal plane. The value of ~7.7Å for a bit was obtained by dividing the gradient by the number of bits per focal step, 3 bits.

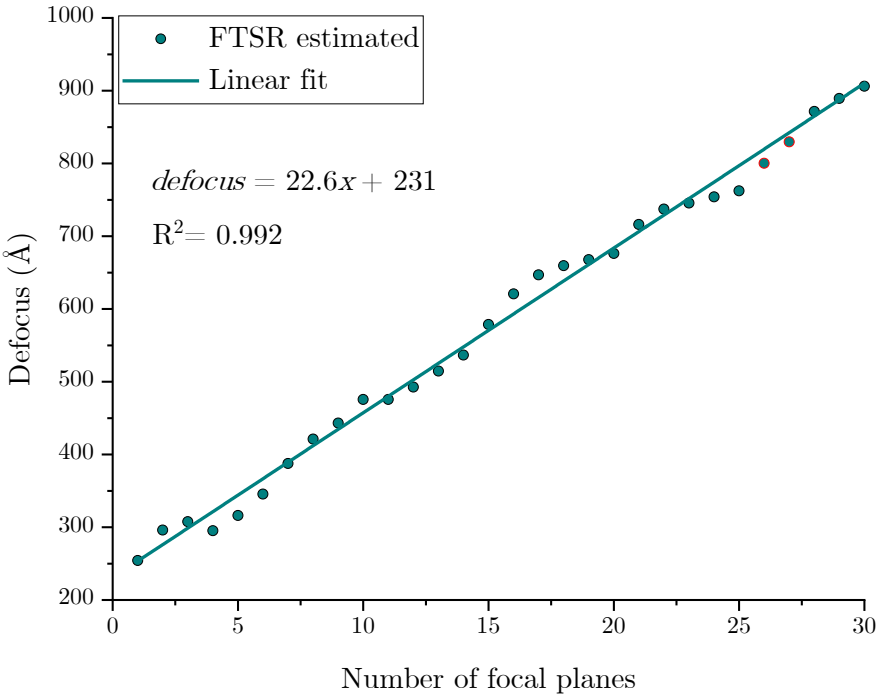

Figure B.3: Linear fit to FTSR estimated defocus values for the focal series used to restore the phase shown in Figure 5.8 (d).

5.3 Results and discussion

5.3.1.2 Cumulative dose: 300 000 e/Å²

Figure B.4, shows the asymmetric (2x1) surface reconstruction on the $(1\bar{1}0)_l$ facet of the nanoparticle shown in Figure 5.8 (a-c). The surface is composed of Sn_i atoms with different heights relative to the second atomic plane. The blue and orange arrows indicate the pairs of Sn_i atoms that are furthest and closest to the second atomic plane, respectively.

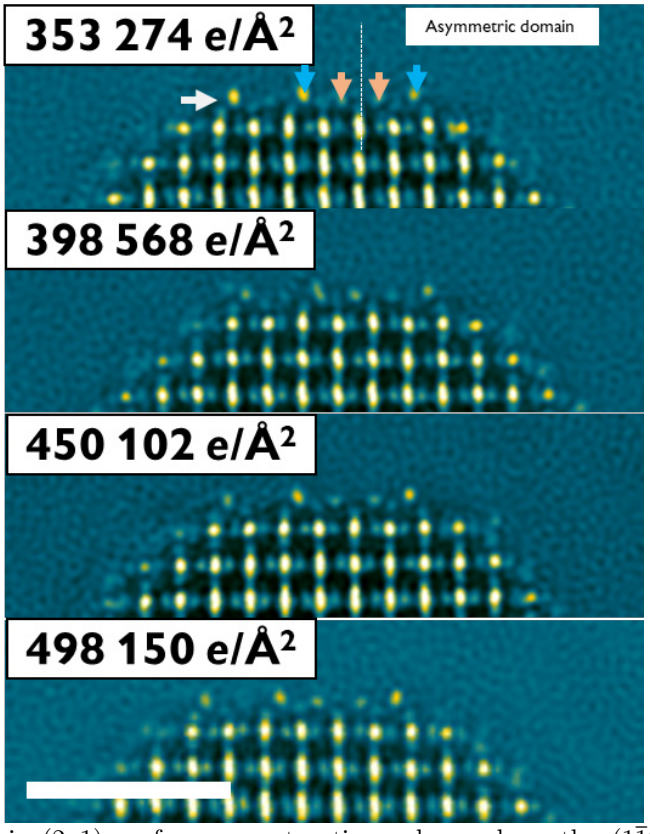

Figure B.4: Asymmetric (2x1) surface reconstructions observed on the $(1\bar{1}0)_l$ facet of the nanoparticle shown in Figure 5.8 (a-c) at cumulative doses of 353 274 $e/Å^2$ to 498 150 $e/Å^2$. The white dashed line indicates the mirror plane on which two rows of Sn_2O_2 units reflect each other. The blue and orange arrows show the pairs of high and low Sn_i atoms with respect to the bulk, correspondingly. The white arrow shows an isolated Sn_i atom column.

The atoms form a heterogeneous asymmetric domain with a mirror plane between the two Sn_2O_2 rows. This reconstruction remains stable from a cumulative dose of 353 274 $e/Å^2$ to 498 150 $e/Å^2$. This asymmetry has also been observed on (1x2) (110) TiO_2[191] and (1x2) {110} SnO_2[37] surface reconstructions, respectively and its origin remains an area of research interest.

Nanoparticles images at dose rates between 2820 $e/Å^2s$ and 6946 $e/Å^2s$ are shown in Figure B.5 (a-h). Under these imaging conditions the (2x1) surface reconstruction has the smallest surface energy. The nanoparticles initially possess the (2x1) surface reconstruction and retain it up to cumulative doses up to 500 000 $e/Å^2$. The interatomic distances between Sn_i-bulk and Sn_i-Sn_i atoms, shown in Table B.1, are comparable to those measured by Li et al. (2021) for the (2x1) surface reconstruction.

5.3.1.3 Cumulative dose: 500 000 e/Å²

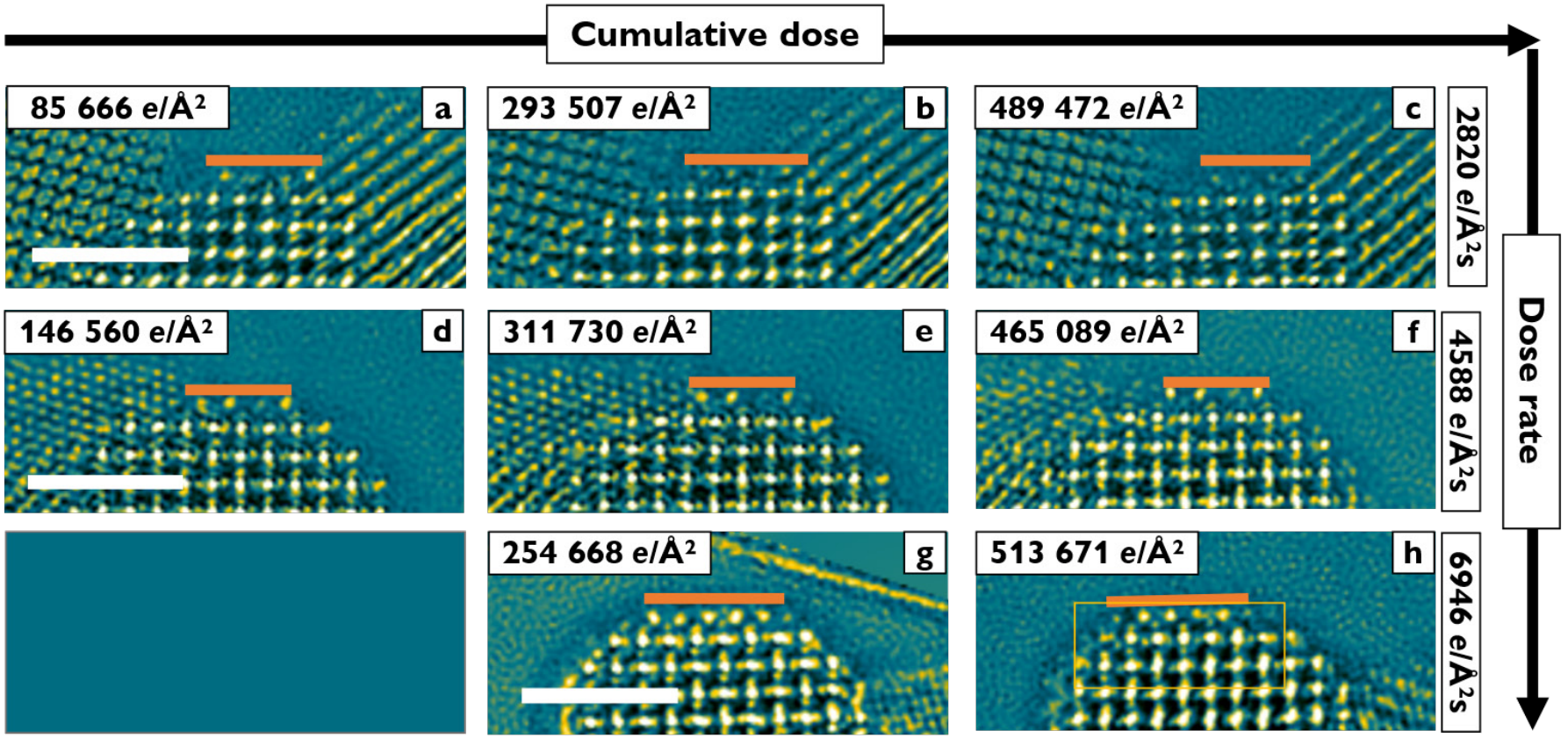

Figure B.5: A matrix of 4 nm-sized nanoparticles, acquired at increasing dose rates between 2820 $e/Å^2s$ and 6946 $e/Å^2s$ and at cumulative doses up to about 500 x 10^3 $e/Å^2$. The orange lines represent the (2x1) surface reconstruction. The scale bar represents 20 Å.

Table A.1: A comparison between the interatomic distances measured from bulk and surface atomic planes for the (2x1) surface reconstruction observed on the nanoparticles presented in Figure B.5 and that of Li et al. (2021)[37].

Particle	Sn_i **- bulk (Å)**	Sn_i – Sn_i **(Å)**
Li et al. (2021)	3.1 (0.2)	3.5 (0.3)
Figure.5 (a-c)	2.8 (0.2)	3.5 (0.3)
Figure B.5 (d-f)	3.0 (0.2)	3.5 (0.5)
Figure B.5 (g,h)	2.8 (0.3)	3.4 (0.3)

Figure B.6, shows the surface energies of the surface reconstructions theoretically predicted by Agoston and Albe to have low surface energies as a function of $\Delta\mu_O$[56]. The basic building block is the Sn_2O_2 unit for all the reconstructions at $\Delta\mu_O <$ -1.91 eV. Their order of stability as a function of $\Delta\mu_O$ is as follows: Stoichiometric→Sn_2O_2 strands → (2x2)→ (2x1). This trend is consistent with the observations made on the $(110)_t$ facet in Figure 5.8 (a), Figure 5.11 (a) and Figure 5.12 (a), respectively. Although, the (2x2) surface reconstruction is not observed in this study, similar to the observations by Li et al. (2021)[37]. A tabulated summary of the graphical summary of dose vs stability range shown in Figure 5.15 is given in Table B.2 and it shows that the (2x1) surface reconstruction has the lowest surface energy under the imaging conditions.

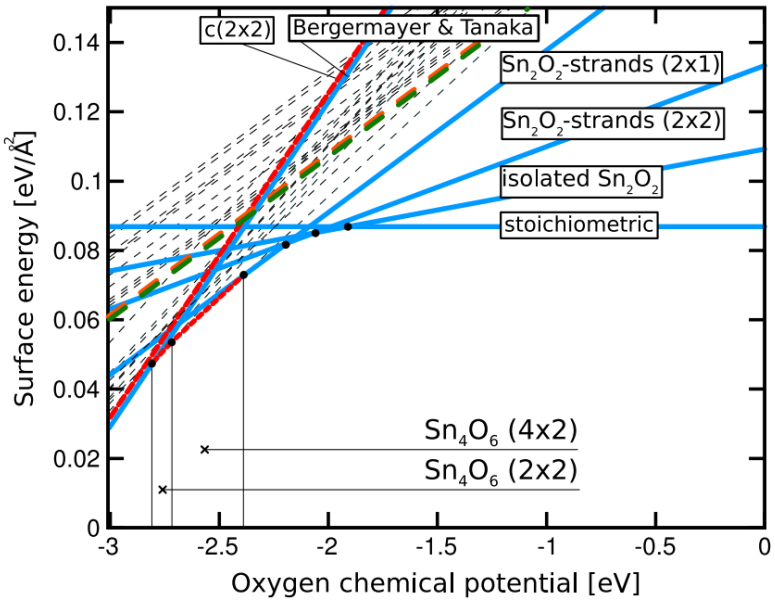

Figure B.6: Surface energies of various surface reconstructions as a function of $\Delta\mu_O$. The red dotted lines indicate surface reconstructions related to the high temperature (1x2) surface reconstruction. The Sn_2O_2-strands (2x1) and (2x2) reconstructions are related to the high temperature disordered (1x1) surface reconstruction. Adopted from ref[56] © (2011) with permission from Elsevier.

Appendix C

Figure C.1 shows a [001] projected SnO_2 nanoparticle acquired at a dose rate of 6522 $e/Å^2s$. It was acquired with a focal step, sampling rate and C_3 values of 2.1 Å, -1.49 µm and 0.083 Å, in that order similar to those used for acquiring data presented in Chapter 5.

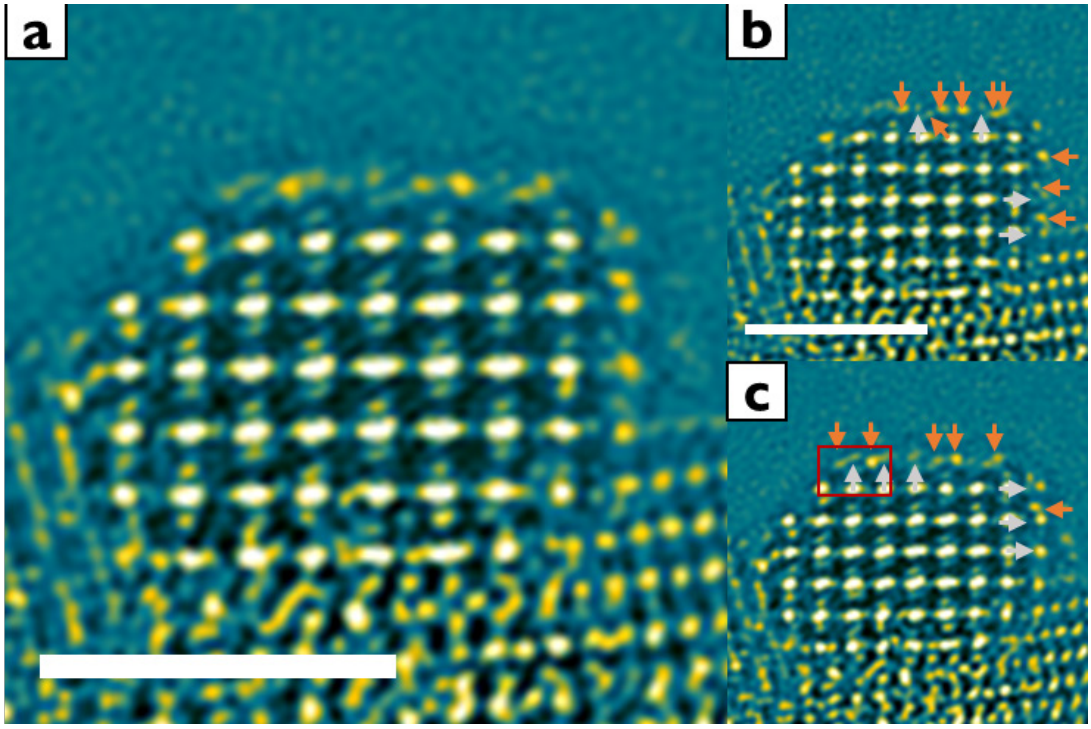

Figure C.1: (a) a SnO_2 nanoparticle phase restored using a 20-member focal series with a defocus range of -100 Å to 320 Å. The focal step, sampling rate and C_3 values were 2.1 Å, -1.49 µm and 0.083 Å, in that order. (b) and (c) show the phases restored from the first and second half of the focal series used to restore (a) to reveal the temporal dynamics of the surface. The red ROI in (c) indicates a section resembling a (4x2) surface reconstruction. The orange and grey arrows show the presence of Sn_i and Sn_b atoms, respectively. The focal series was acquired at a dose rate of 6522 $e/Å^2s$ with a dose per frame of 1304 $e/Å^2$. The scalebars correspond to 20 Å.

The cumulative dose including the effect of SPEC is 156 x $10^3 e/Å^2$. At this dose rate the Pd-SnO_2 nanoparticles largely exhibit (2x1) surface reconstructions up to a cumulative dose of 500 x $10^3 e/Å^2$ (see Figure B.5 in

general and Figure B.5(d) specifically as the cumulative doses are comparable). However, the smaller SnO_2 nanoparticle has a complex surface chemistry composed of Sn_i and Sn_b with some regions, shown in the red ROI in Figure C.1 (c), resembling the (4x2) surface reconstruction proposed by Agoston et al. (2011)[167]. The (4x2) surface reconstruction for larger Pd-doped nanoparticles is observed at almost twice the dose rate (Figure 5.8 (g)). This shows the electron beam sensitivity of the smaller SnO_2 nanoparticle. Additionally, it also demonstrates that the surface chemistry of smaller nanoparticles is more complex in that Sn_i, Sn_b atoms and a (4x2) reconstruction can be found on the same facet under the same experimental conditions. Lin et al. (2014) made similar observations on nanoscopic CeO_2 cuboids. They found that various atomic configurations can form locally ordered structures at nanoscale that result in an overall lower surface energy configuration [49].

Glossary

Abbreviation	***Definition***
1S2R	1-Dimensional Search & 2-Dimensional Refinement
ADU	Analogue-to-Digital Units
AFM	Atomic Force Microscopy
BF	Bright Field
BFP	Back Focal Plane
C_3	Third Order Spherical Aberration
XCC	Cross Correlation Coefficient
CFS	Conventional Focal Series
CMOS	Complementary Metal Oxide Semiconductor
CO_2RR	Carbon Dioxide Reduction Reaction
CTEM	Conventional Transmission Electron Microscopy
CTF	Contrast Transfer Function
DFT	Density Functional Theory
DM	Digital Micrograph®
DQE	Detector Quantum Efficiency
ECTF	Effective Contrast Transfer Function
EWR	Exit Wave Restoration
FEG	Field Emission Gun
FFS	Fast Focal Series
FSD	Focal Series Dose
FTSR	Focal Tilt Series Restoration
GMS	Gatan Microscopy Suite®
HAADF	High Angle Annular Dark Field
HRTEM	High Resolution Transmission Electron Microscopy
LAS	Log Amplitude Spectrum
LEED	Low Energy Electron Diffraction
LEIS	Low Energy Ion Spectroscopy
MRC	Medical Research Council Format
MTF	Modulation Transfer Function

NC-AFM	Near Contact Atomic Force Microscopy
NCSI	Negative Spherical Aberration Coefficient Imaging
NPS	Noise Power Spectrum
OL	Objective Lens
PCF	Phase Correlation Function
PCI	Phase Correlation Index
PCTF	Phase Contrast Transfer Function
POA	Phase Object Approximation
PSF	Point Spread Function
SNFR	Signal To Noise Fluctuation Ratio
SNR	Signal To Noise Ratio
SPEC	Specimen Pre-Shutter Exposure Compensation
SPM	Scanning Probe Microscopy
STEM	Scanning Transmission Electron Microscopy
STM	Scanning Tunnelling Microscopy
TEM	Transmission Electron Microscopy
UHV	Ultra-High Vacuum
VESTA	Visualization For Electronic and STructural Analysis™
WPO	Weak Phase Object
XCF	Cross Correlation Function

References

1. Moreno, M. S. *et al.* 'Probing electronic structure of stoichiometric and defective SnO_2'. *Physical Review B* **95**, 1–7 (2017).

2. Maestre, D. *et al.* 'Study of the defects in sintered SnO_2 by high-resolution transmission electron microscopy and cathodoluminescence'. *European Journal of Inorganic Chemistry* 1544–1548 (2007).

3. Manassidis, I. *et al.* 'The structure of the stoichiometric and reduced SnO_2 (110) surface'. *Surface Science* **339**, 258–271 (1995).

4. Sarmah, S. & Kumar, A. 'Optical properties of SnO_2 nanoparticles'. *Indian Journal of Physics* **84**, 1211–1221 (2010).

5. Li, Y. *et al.* 'Realizing a SnO_2-based ultraviolet light-emitting diode via breaking the dipole-forbidden rule'. *NPG Asia Materials* **4**, e30–e30 (2012).

6. Diéguez, A. *et al.* 'The complete Raman spectrum of nanometric SnO_2 particles'. *Journal of Applied Physics* **90**, 1550–1557 (2001).

7. Kılıç, Ç. & Zunger, A. 'Origins of Coexistence of Conductivity and Transparency in SnO_2'. *Physical Review Letters* **88**, 1–4 (2002).

8. Lee, H. *et al.* 'Improved Efficiency of Inverted Organic Light-Emitting Diodes Using Tin Dioxide Nanoparticles as an Electron Injection Layer'. *ACS Applied Materials & Interfaces* **5**, 1977–1981 (2013).

9. D'Arienzo, M. *et al.* 'New Insights into the SnO_2 Sensing Mechanism Based on the Properties of Shape Controlled Tin Oxide Nanoparticles'. *Chemistry of Materials* **25**, 3675–3686 (2013).

10. Yeom, E. J. *et al.* 'Controllable synthesis of single crystalline Sn-based oxides and their application in perovskite solar cells'. *Journal of Materials Chemistry A* **5**, 79–86 (2017).

11. Etacheri, V. *et al.* 'Ordered network of interconnected SnO_2 nanoparticles for excellent lithium-ion storage'. *Advanced Energy Materials* **5**, 2–9 (2015).

12. Gong, J. *et al.* 'Selective Electro-reduction of Carbon Dioxide over SnO_2-nanodot Catalysts'. *ChemSusChem* (2020).

13. Daiyan, R. *et al.* 'Highly Selective Reduction of CO_2 to Formate at Low Overpotentials Achieved by a Mesoporous Tin Oxide Electrocatalyst'. *ACS Sustainable Chemistry & Engineering* **6**, 1670–1679 (2018).

14. He, Y. *et al.* 'Pore-structure-directed CO_2 electroreduction to formate on SnO_2 /C catalysts'. *Journal of Materials Chemistry A* **7**, 18428–18433 (2019).

15. Jiang, L. *et al.* 'Size-Controllable Synthesis of Monodispersed SnO_2 Nanoparticles and Application in Electrocatalysts'. *The Journal of Physical Chemistry B* **109**, 8774–8778 (2005).

16. Wang, X. *et al.* 'Controlled synthesis and enhanced catalytic and gas-sensing properties of tin dioxide nanoparticles with exposed high-energy facets'. *Chemistry - A European Journal* **18**, 2283–2289 (2012).

17. Han, X. *et al.* 'Synthesis of tin dioxide octahedral nanoparticles with exposed high-energy {221} facets and enhanced gas-sensing properties'. *Angewandte Chemie - International Edition* **48**, 9180–9183 (2009).

18. Nandan, B. *et al.* 'Effect of Pd ion doping in the band gap of SnO_2 nanoparticles: structural and optical studies'. *Journal of Nanoparticle Research* **15**, 1999 (2013).

19. Zeng, W. *et al.* 'Hydrogen sensing and mechanism of M-doped SnO_2 (M = Cr3+, Cu2+ and Pd2+) nanocomposite'. *Sensors and Actuators B: Chemical* **160**, 455–462 (2011).

20. Tangirala, V. *et al.* 'A Study of the CO Sensing Responses of Cu-, Pt- and Pd-Activated SnO_2 Sensors: Effect of Precipitation Agents, Dopants and Doping Methods'. *Sensors* **17**, 1–24 (2017).

21. Bechthold, P. *et al.* 'DFT study of CO adsorption on Pd-SnO_2 (110) surfaces'. *Applied Surface Science* **347**, 291–298 (2015).

22. Germán, E. *et al.* 'A DFT study of H_2 adsorption on Pdn/SnO_2 (110) surfaces (n = 1−10)'. *European Physical Journal B* **92**, (2019).

23. Robina, A. *et al.* 'Electronic structure and bonding of small Pd clusters on stoichiometric and reduced SnO_2(110) surfaces'. *Vacuum* **106**, 86–93 (2014).

24. Mäki-Jaskari, M. A. & Rantala, T. T. 'Density functional study of Pd adsorbates at SnO_2(1 1 0) surfaces'. *Surface Science* **537**, 168–178 (2003).

25. Xue, Y. B. & Tang, Z. A. 'Density functional study of the interaction of CO with undoped and Pd doped SnO_2(1 1 0) surface'. *Sensors and Actuators, B: Chemical* **138**, 108–112 (2009).

26. Gaskov, A. *et al.* 'Tin oxide nanomaterials: Active centers and gas sensor properties'. in '*Tin Oxide Materials*' 163–218 (Elsevier, 2020).

27. Liu, G. *et al.* 'Black reduced porous SnO_2 nanosheets for CO_2 electroreduction with high formate selectivity and low overpotential'. *Applied Catalysis B: Environmental* **260**, 118134 (2020).

28. Deng, W. *et al.* 'Crucial Role of Surface Hydroxyls on the Activity and Stability in Electrochemical CO_2 Reduction'. *Journal of the American Chemical Society* **141**, 2911–2915 (2019).

29. Batzill, M. & Diebold, U. 'The surface and materials science of tin oxide'. *Progress in Surface Science* **79**, 47–154 (2005).

30. Batzill, M. 'Surface science studies of gas sensing materials: SnO_2'. *Sensors* **6**, 1345–1366 (2006).

31. Das, S. & Jayaraman, V. 'SnO_2: A comprehensive review on structures and gas sensors'. *Progress in Materials Science* **66**, 112–255 (2014).

32. Xu, C. *et al.* 'Environment-dependent surface structures and stabilities of SnO_2 from the first principles'. *Journal of Applied Physics* **111**, 1–10 (2012).

33. Bergermayer, W. & Tanaka, I. 'Reduced SnO_2 surfaces by first-principles calculations'. *Applied Physics Letters* **84**, 909–911 (2004).

34. Batzill, M. *et al.* 'Surface morphologies of SnO_2 (110)'. *Surface Science* **529**, 295–311 (2003).

35. De Frésart, E. *et al.* 'Influence of the surface reconstruction on the work function and surface conductance of (110)SnO_2'. *Applications of Surface Science* **11–12**, 637–651 (1982).

36. Shen, G. L. *et al.* 'Correlation between the surface conductivity and structure of SnO_2 (110)'. *Journal of Physics: Condensed Matter* **3**, S291–S296 (1991).

37. Li, G. *et al.* 'In Situ Resolving the Atomic Reconstruction of SnO_2 (110) Surface'. *Nano Letters* **21**, 7309–7316 (2021).

38. Batzill, M. *et al.* 'Gas-phase-dependent properties of SnO_2 (110), (100), and (101) single-crystal surfaces: Structure, composition, and electronic properties'. *Physical Review B* **72**, 1–20 (2005).

39. Liu, S. *et al.* 'Atomic Structure and Properties of SnO_2 (100) and (101) Surfaces and (301) Steps in the (100) Surface'. *The Journal of Physical Chemistry C* **124**, 27631–27636 (2020).

40. Lu, N. *et al.* 'Surface Structure of Zigzag SnO_2 Nanobelts'. *The Journal of Physical Chemistry Letters* **1**, 1468–1471 (2010).

41. Liu, S. *et al.* 'Nematic-type Structure of the SnO_2 (110) Surface at Room Temperature'. *ChemPhysChem* **23**, (2022).

42. Suito, K. *et al.* 'High pressure synthesis of orthorhombic SnO_2'. *Materials Research Bulletin* **10**, 677–680 (1975).

43. Godinho, K. G. *et al.* 'Energetic and Electronic Structure Analysis of Intrinsic Defects in SnO_2'. *The Journal of Physical Chemistry C* **113**, 439–448 (2009).

44. Han, R. & Yan, Y. 'Electronic structure and magnetic properties of oxygen deficient low-index surfaces of SnO_2'. *Surface Science* **649**, 112–119 (2016).

45. Bonu, V. *et al.* 'Invoking forbidden modes in SnO_2 nanoparticles using tip enhanced Raman spectroscopy'. *Journal of Raman Spectroscopy* **46**, 1037–1040 (2015).

46. Venkataramana, B. *et al.* 'Intrinsic high magnetism in SnO_2 quantum dots'. in '*Solid State Physics: Proceedings of the 58th DAE Solid State Physics Symposium 2013*' (editors Murli, C., Bhattacharyya, D. & Gadkari, S. C.) 490–492 (American Institute of Physics, 2014).

47. Chetri, P. & Choudhury, A. 'Investigation of optical properties of SnO_2 nanoparticles'. *Physica E: Low-Dimensional Systems and Nanostructures* **47**, 257–263 (2013).

48. Marikutsa, A. V. *et al.* 'Active sites on the surface of nanocrystalline semiconductor oxides ZnO and SnO_2 and gas sensitivity'. *Russian Chemical Bulletin* **66**, 1728–1764 (2017).

49. Lin, Y. *et al.* 'Imaging the Atomic Surface Structures of CeO_2 Nanoparticles'. *Nano Letters* **14**, 191–196 (2014).

50. Oviedo, J. & Gillan, M. J. 'Energetics and structure of stoichiometric SnO_2 surfaces studied by first-principles calculations'. *Surface Science* **463**, 93–101 (2000).

51. Oviedo, J. & Gillan, M. J. 'Reconstructions of strongly reduced SnO_2 (110) studied by first-principles methods'. *Surface Science* **513**, 26–36 (2002).

52. Beltrán, A. *et al.* 'Thermodynamic argument about SnO_2 nanoribbon growth'. *Applied Physics Letters* **83**, 635–637 (2003).

53. Barmparis, G. D. *et al.* 'Nanoparticle shapes by using Wulff constructions and first-principles calculations'. *Beilstein Journal of Nanotechnology* **6**, 361–368 (2015).

54. Winterbottom, W. L. 'Equilibrium shape of a small particle in contact with a foreign substrate'. *Acta Metallurgica* **15**, 303–310 (1967).

55. Marks, L. D. 'Modified Wulff constructions for twinned particles'. *Journal of Crystal Growth* **61**, 556–566 (1983).

56. Ágoston, P. & Albe, K. 'Disordered reconstructions of the reduced SnO_2 (110) surface'. *Surface Science* **605**, 714–722 (2011).

57. Tasker, P. W. 'The stability of ionic crystal surfaces'. *Journal of Physics C: Solid State Physics* **12**, 4977–4984 (1979).

58. Küfner, S. *et al.* 'Energetics and approximate quasiparticle electronic structure of low-index surfaces of SnO_2'. *Physical Review B* **86**, 075320 (2012).

59. Epifani, M. *et al.* 'Synthesis and Gas-Sensing Properties of Pd-Doped SnO_2 Nanocrystals. A Case Study of a General Methodology for Doping Metal Oxide Nanocrystals'. *Crystal Growth & Design* **8**, 1774–1778 (2008).

60. Zhu, S. *et al.* 'Mechanism study on extraordinary room-temperature CO sensing capabilities of Pd-SnO_2 composite nanoceramics'. *Sensors and Actuators, B: Chemical* **285**, 49–55 (2019).

61. Frolov, D. D. *et al.* 'Oxygen exchange on nanocrystalline tin dioxide modified by palladium'. *Journal of Solid State Chemistry* **186**, 1–8 (2012).

62. Batzill, M. *et al.* 'Surface oxygen chemistry of a gas-sensing material: SnO_2 (101)'. *Europhysics Letters (EPL)* **65**, 61–67 (2004).

63. Batzill, M. *et al.* 'Tuning surface properties of SnO_2 (1 0 1) by reduction'. *Journal of Physics and Chemistry of Solids* **67**, 1923–1929 (2006).

64. de Frésart, E. *et al.* 'Surface reconstructions of the SnO_2 (110) face'. *Solid State Communications* **37**, 13–17 (1981).

65. Merte, L. R. *et al.* 'Structure of the SnO_2 (110)-(4×1) Surface'. *Physical Review Letters* **119**, 096102 (2017).

66. Pang, C. L. *et al.* 'Structures of the 4 × 1 and 1 × 2 reconstructions of SnO_2 (110)'. *Physical Review B* **62**, R7775–R7778 (2000).

67. Cox, D. F. *et al.* 'Surface reconstructions of oxygen deficient SnO_2(110)'. *Surface Science* **224**, 121–142 (1989).

68. Cox, D. F. *et al.* 'Oxygen vacancies and defect electronic states on the SnO_2 (110)-1x1 surface'. *Physical Review B* **38**, 2072–2083 (1988).

69. Sinner-Hettenbach, M. *et al.* 'Oxygen-deficient SnO_2 (110): A STM, LEED and XPS study'. *Surface Science* **477**, 50–58 (2001).

70. Jones, F. H. *et al.* 'The surface structure of $SnO_2(110)(4 \times 1)$ revealed by scanning tunneling microscopy'. *Surface Science* **376**, 367–373 (1997).

71. Bai, X. *et al.* 'Exclusive Formation of Formic Acid from CO_2 Electroreduction by a Tunable Pd-Sn Alloy'. *Angewandte Chemie - International Edition* **56**, 12219–12223 (2017).

72. Jia, C. L. *et al.* 'Atomic-Resolution Imaging of Oxygen in Perovskite Ceramics'. *Science* **299**, 870–873 (2003).

73. Jia, C. L. & Urban, K. W. 'Atomic-Resolution Measurement of Oxygen Concentration in Oxide Materials'. *Science* **303**, 2001–2004 (2004).

74. Jia, C. L. *et al.* 'Atomic-Scale Analysis of the Oxygen Configuration at a $SrTiO_3$ Dislocation Core'. *Physical Review Letters* **95**, 1–4 (2005).

75. Bhatta, U. M. *et al.* 'Cationic Surface Reconstructions on Cerium Oxide Nanocrystals: An Aberration-Corrected HRTEM Study'. *ACS Nano* **6**, 421–430 (2012).

76. Möbus, G. *et al.* 'Dynamics of polar surfaces on ceria nanoparticles observed in situ with single-atom resolution'. *Advanced Functional Materials* **21**, 1971–1976 (2011).

77. Haigh, S. J. *et al.* 'Imaging the Active Surfaces of Cerium Dioxide Nanoparticles'. *ChemPhysChem* **12**, 2397–2399 (2011).

78. Johnston-Peck, A. C. *et al.* 'Dose-rate-dependent damage of cerium dioxide in the scanning transmission electron microscope'. *Ultramicroscopy* **170**, 1–9 (2016).

79. Lawrence, E. L. *et al.* 'Atomic Scale Characterization of Fluxional Cation Behavior on Nanoparticle Surfaces: Probing Oxygen Vacancy Creation/Annihilation at Surface Sites'. *ACS Nano* **15**, 2624–2634 (2021).

80. Manzorro, R. *et al.* 'Quantifying fluxional behavior in catalytic CeO_2 nanoparticles: toward thermodynamic insight into the stability of surface atomic structures'. *Microscopy and Microanalysis* **27**, 3070–3071 (2021).

81. De Backer, A. *et al.* 'Atom counting in HAADF STEM using a statistical model-based approach: Methodology, possibilities, and inherent limitations'. *Ultramicroscopy* **134**, 23–33 (2013).

82. De Wael, A. *et al.* 'Hybrid statistics-simulations based method for atom-counting from ADF STEM images'. *Ultramicroscopy* **177**, 69–77 (2017).

83. De Backer, A. *et al.* 'StatSTEM: An efficient approach for accurate and precise model-based quantification of atomic resolution

electron microscopy images'. *Ultramicroscopy* **171**, 104–116 (2016).

84. Van Aert, S. *et al.* 'Procedure to count atoms with trustworthy single-atom sensitivity'. *Physical Review B* **87**, 064107 (2013).

85. Chen, F.-R. *et al.* 'In-line three-dimensional holography of nanocrystalline objects at atomic resolution'. *Nature Communications* **7**, 10603 (2016).

86. Stroppa, D. G. *et al.* 'Unveiling the Chemical and Morphological Features of Sb–SnO_2 Nanocrystals by the Combined Use of High-Resolution Transmission Electron Microscopy and ab Initio Surface Energy Calculations'. *Journal of the American Chemical Society* **131**, 14544–14548 (2009).

87. Stroppa, D. G. *et al.* 'Dopant Segregation Analysis on Sb:SnO_2 Nanocrystals'. *Chemistry - A European Journal* **17**, 11515–11519 (2011).

88. Jin, Z. *et al.* 'Tin Oxide Crystals Exposed by Low-Energy {110} Facets for Enhanced Electrochemical Heavy Metal Ions Sensing: X-ray Absorption Fine Structure Experimental Combined with Density-Functional Theory Evidence'. *Analytical Chemistry* **89**, 2613–2621 (2017).

89. Xi, G. & Ye, J. 'Ultrathin SnO_2 Nanorods: Template- and Surfactant-Free Solution Phase Synthesis, Growth Mechanism, Optical, Gas-Sensing, and Surface Adsorption Properties'. *Inorganic Chemistry* **49**, 2302–2309 (2010).

90. Jia, C.-L. *et al.* 'High-Resolution Transmission Electron Microscopy Using Negative Spherical Aberration'. *Microscopy and Microanalysis* **10**, 174–184 (2004).

91. Urban, K. W. *et al.* 'Negative spherical aberration ultrahigh-resolution imaging in corrected transmission electron microscopy'. *Philosophical Transactions of the Royal Society A: Mathematical, Physical and Engineering Sciences* **367**, 3735–3753 (2009).

92. Shibata, N. *et al.* 'Direct Imaging of Reconstructed Atoms on TiO_2 (110) Surfaces'. *Science* **322**, 570–573 (2008).

93. Yuan, W. *et al.* 'In Situ STEM Determination of the Atomic Structure and Reconstruction Mechanism of the TiO_2 (001) (1 × 4) Surface'. *Chemistry of Materials* **29**, 3189–3194 (2017).

94. Ek, M. *et al.* 'Step edge structures on the anatase TiO_2 (001) surface studied by atomic-resolution TEM and STM'. *Faraday Discussions* **208**, 325–338 (2018).

95. Yuan, W. *et al.* 'Real-Time Observation of Reconstruction Dynamics on TiO_2 (001) Surface under Oxygen via an

Environmental Transmission Electron Microscope'. *Nano Letters* **16**, 132–137 (2016).

96. Feynman, R. P. 'There's plenty of room at the bottom'. *Engineering and Science* **23**, 22–36 (1960).

97. Freitag, B. & Kisielowski, C. 'Determining resolution in the transmission electron microscope: object-defined resolution below 0.5Å'. *EMC 2008 14th European Microscopy Congress 1–5 September 2008, Aachen, Germany* **1**, 21–22.

98. Kisielowski, C. *et al.* 'Detection of Single Atoms and Buried Defects in Three Dimensions by Aberration-Corrected Electron Microscope with 0.5-Å Information Limit'. *Microscopy and Microanalysis* **14**, 469–477 (2017).

99. Erni, R. *et al.* 'Atomic-Resolution Imaging with a Sub-50-pm Electron Probe'. *Physical Review Letters* **102**, 096101 (2009).

100. Tuggle, D. W. & Swanson, L. W. 'Emission characteristics of the ZrO/W thermal field electron source'. *Journal of Vacuum Science & Technology B: Microelectronics and Nanometer Structures* **3**, 220–223 (1985).

101. Scheu, C. & Kaplan, W. D. 'Introduction to Scanning Electron Microscopy'. in '*In-Situ Electron Microscopy*' (editors Dehm, G.,

Howe, J. M. & Zweck, J.) 1–37 (Wiley-VCH Verlag GmbH & Co. KGaA, 2012).

102. Williams, D. B. & Carter, C. B. '*Transmission Electron Microscopy*'. '*Springer*' (Springer US, 2009).

103. Morishita, H. *et al.* 'Brightness evaluation of pulsed electron gun using negative electron affinity photocathode developed for time-resolved measurement using scanning electron microscope'. *Ultramicroscopy* **230**, 113386 (2021).

104. Haigh, S. J. & Kirkland, A. I. 'High Resolution Exit wave Restoration'. in '*Modeling Nanoscale Imaging in Electron Microscopy. Nanostructure Science and Technology*' (editors Vogt, T., Dahmen, W. & Binev, P.) 41–72 (Springer, 2012).

105. Kirkland, A. I. *et al.* 'Atomic Resolution Transmission Electron Microscopy'. in '*Springer Handbook of Microscopy, Springer Handbooks*' (editors Hawkes, P. W. & Spence, J. C. H.) 1–45 (Springer, 2019).

106. Haigh, S. J. & Kirkland, A. I. 'Aberration-Corrected Imaging in CTEM'. in '*Aberration-Corrected Analytical Transmission Electron Microscopy*' (editor Brydson, R.) 241–261 (John Wiley & Sons, Ltd, 2011).

107. Scherzer, O. 'The Theoretical Resolution Limit of the Electron Microscope'. *Journal of Applied Physics* **20**, 20–29 (1949).

108. Kirkland, A. & Young, N. 'high-resolution electron microscopy Advances in high-resolution transmission electron microscopy for materials science'. *Microscopy and Microanalysis* 19–24 (2012).

109. Batson, P. E. *et al.* 'Sub-Ångstrom resolution using aberration corrected electron optics'. *Nature* **418**, 617–620 (2002).

110. Hawkes, P. W. 'The correction of electron lens aberrations'. *Ultramicroscopy* **156**, A1–A64 (2015).

111. Rose, H. H. 'Historical aspects of aberration correction'. *Journal of Electron Microscopy* **58**, 77–85 (2009).

112. Rose, H. & Wan, W. 'Aberration correction in electron microscopy'. in '*Proceedings of 2005 Particle Accelerator Conference*' 44–48 (IEEE, 2005).

113. Bleloch, A. & Ramasse, Q. 'Lens Aberrations: Diagnosis and Correction'. in '*Aberration-Corrected Analytical Transmission Electron Microscopy*' (editor Brydson, R.) 55–87 (John Wiley & Sons, Ltd, 2011).

114. Greivenkamp, J. E. '*Field Guide to Geometrical Optics*'. '*SPIE Field Guides*' (SPIE, 2004).

115. Saxton, W. O. 'Simple prescriptions for estimating three-fold astigmatism'. *Ultramicroscopy* **58**, 239–243 (1995).

116. Zemlin, F. *et al.* 'Coma-free alignment of high resolution electron microscopes with the aid of optical diffractograms'. *Ultramicroscopy* **3**, 49–60 (1978).

117. Zemlin, F. 'A practical procedure for alignment of a high resolution electron microscope'. *Ultramicroscopy* **4**, 241–245 (1979).

118. Uhlemann, S. & Haider, M. 'Residual wave aberrations in the first spherical aberration corrected transmission electron microscope'. *Ultramicroscopy* **72**, 109–119 (1998).

119. Meyer, R. R. & Kirkland, A. I. 'Characterisation of the signal and noise transfer of CCD cameras for electron detection'. *Microscopy Research and Technique* **49**, 269–280 (2000).

120. Fan, G. Y. & Ellisman, M. H. 'Digital imaging in transmission electron microscopy'. *Journal of Microscopy* **200**, 1–13 (2000).

121. Meyer, R. R. *et al.* 'Experimental characterisation of CCD cameras for HREM at 300kV'. *Ultramicroscopy* **85**, 9–13 (2000).

122. Clough, R. & Kirkland, A. I. 'Direct Digital Electron Detectors'. in '*Advances in Imaging and Electron Physics*' vol. 198 1–42 (Academic Press Inc., 2016).

123. Craven, A. 'Details of STEM'. in '*Aberration-Corrected Analytical Transmission Electron Microscopy*' (editor Brydson, R.) 111–161 (John Wiley & Sons, Ltd, 2011).

124. Shannon, C. E. 'Communication in the Presence of Noise'. *Proceedings of the IRE* **37**, 10–21 (1949).

125. Kirkland, E. J. '*Advanced Computing in Electron Microscopy*'. '*Advanced Computing in Electron Microscopy: Second Edition*' (Springer US, 2010).

126. Cowley, J. M. & Moodie, A. F. 'The scattering of electrons by atoms and crystals. I. A new theoretical approach'. *Acta Crystallographica* **10**, 609–619 (1957).

127. Goodman, P. & Moodie, A. F. 'Numerical evaluations of N -beam wave functions in electron scattering by the multi-slice method'. *Acta Crystallographica Section A* **30**, 280–290 (1974).

128. Lynch, D. F. & O'Keefe, M. A. 'n -Beam lattice images. II. Methods of calculation'. *Acta Crystallographica Section A* **28**, 536–548 (1972).

129. Allpress, J. G. *et al.* 'n -Beam lattice images. I. Experimental and computed images from $W_4Nb_{26}O_{77}$'. *Acta Crystallographica Section A* **28**, 528–536 (1972).

130. Kirkland, E. J. 'Image Simulation in Transmission Electron Microscopy'. *Simulation* 1–14 (2006).

131. Haigh, S. J. & Kirkland, A. I. 'Finding phase information in the darkness'. *Journal of Physics: Conference Series* **241**, 012013 (2010).

132. Hÿtch, M. J. & Stobbs, W. M. 'Quantitative comparison of high resolution TEM images with image simulations'. *Ultramicroscopy* **53**, 191–203 (1994).

133. Lehmann, M. & Lichte, H. 'Is there a Stobbs-Factor in Off-axis Electron Holography?' *Microscopy and Microanalysis* **9**, 46–47 (2003).

134. Du, K. *et al.* 'Quantitative comparison of image contrast and pattern between experimental and simulated high-resolution transmission electron micrographs'. *Ultramicroscopy* **107**, 281–292 (2007).

135. Thust, A. 'High-Resolution Transmission Electron Microscopy on an Absolute Contrast Scale'. *Physical Review Letters* **102**, 220801 (2009).

136. Van Dyck, D. *et al.* 'Do you believe that atoms stay in place when you observe them in HREM?' *Micron* **68**, 158–163 (2015).

137. Gerchberg, R. W. & Saxton, W. O. 'A Practical Algorithm for the Determination of Phase from Image and Diffraction Plane Pictures'. *Optik* **35**, 1–6 (1972).

138. Kirkland, A. I. & Meyer, R. R. '"Indirect" High-Resolution Transmission Electron Microscopy: Aberration Measurement and Wavefunction Reconstruction'. *Microscopy and Microanalysis* **10**, 401–413 (2004).

139. Op de Beeck, M. *et al.* 'Wave function reconstruction in HRTEM: the parabola method'. *Ultramicroscopy* **64**, 167–183 (1996).

140. Thust, A. *et al.* 'Focal-series reconstruction in HRTEM: simulation studies on non-periodic objects'. *Ultramicroscopy* **64**, 211–230 (1996).

141. Kirkland, A. I. *et al.* 'Super-resolution by aperture synthesis: tilt series reconstruction in CTEM'. *Ultramicroscopy* **57**, 355–374 (1995).

142. Kirkland, A. I. *et al.* 'Multiple beam tilt microscopy for super resolved imaging'. *Journal of Electron Microscopy* **46**, 11–22 (1997).

143. Coene, W. M. J. *et al.* 'Maximum-likelihood method for focus-variation image reconstruction in high resolution transmission electron microscopy'. *Ultramicroscopy* **64**, 109–135 (1996).

144. Meyer, R. R. *et al.* 'A new method for the determination of the wave aberration function for high resolution TEM 1. Measurement of the symmetric aberrations'. *Ultramicroscopy* **92**, 89–109 (2002).

145. Saxton, W. O. 'Accurate atom positions from focal and tilted beam series of high resolution electron micrographs'. in '*Image and Signal processing in Electron Microscopy; Scanning Microscopy Supplement 2*' 213–224 (Scanning Microscopy International, 1988).

146. Meyer, R. R. *et al.* 'A new method for the determination of the wave aberration function for high-resolution TEM 2. Measurement of the antisymmetric aberrations'. *Ultramicroscopy* **99**, 115–123 (2004).

147. Saxton, W. O. 'What is the focus variation method? Is it new? Is it direct?' *Ultramicroscopy* **55**, 171–181 (1994).

148. Jia, C. L. *et al.* 'Determination of the 3D shape of a nanoscale crystal with atomic resolution from a single image'. *Nature Materials* **13**, 1044–1049 (2014).

149. Tillmann, K. *et al.* 'Spherical Aberration Correction in Tandem with Exit-Plane Wave Function Reconstruction: Interlocking Tools for the Atomic Scale Imaging of Lattice Defects in GaAs'. *Microscopy and Microanalysis* **10**, 185–198 (2004).

150. Krause, F. F. *et al.* 'Comparison of intensity and absolute contrast of simulated and experimental high-resolution transmission electron microscopy images for different multislice simulation methods'. *Ultramicroscopy* **134**, 94–101 (2013).

151. Ophus, C. & Ewalds, T. 'Guidelines for quantitative reconstruction of complex exit waves in HRTEM'. *Ultramicroscopy* **113**, 88–95 (2012).

152. Lee, Z. *et al.* 'Electron dose dependence of signal-to-noise ratio, atom contrast and resolution in transmission electron microscope images'. *Ultramicroscopy* **145**, 3–12 (2014).

153. Meyer, R. R. & Kirkland, A. I. 'The effects of electron and photon scattering on signal and noise transfer properties of scintillators in CCD cameras used for electron detection'. *Ultramicroscopy* **75**, 23–33 (1998).

154. Vulović, M. *et al.* 'Image formation modeling in cryo-electron microscopy'. *Journal of Structural Biology* **183**, 19–32 (2013).

155. Rullgård, H. *et al.* 'Simulation of transmission electron microscope images of biological specimens'. *Journal of Microscopy* **243**, 234–256 (2011).

156. Egerton, R. F. 'Beam-Induced Motion of Adatoms in the Transmission Electron Microscope'. *Microscopy and Microanalysis* **19**, 479–486 (2013).

157. Stuckert, E. P. & Fisher, E. R. 'Ar/O_2 and H_2O plasma surface modification of SnO_2 nanomaterials to increase surface oxidation'. *Sensors and Actuators, B: Chemical* **208**, 379–388 (2015).

158. Momma, K. & Izumi, F. 'VESTA 3 for three-dimensional visualization of crystal, volumetric and morphology data'. *J. Appl. Cryst* **44**, 1272–1276 (2011).

159. Beltrán, A. *et al.* 'Density Functional Theory Study on the Structural and Electronic Properties of Low Index Rutile Surfaces for TiO_2 /SnO_2 /TiO_2 and SnO_2 /TiO_2 /SnO_2 Composite Systems †'. *The Journal of Physical Chemistry A* **112**, 8943–8952 (2008).

160. Hines, R. I. *et al.* 'Oxidation catalysts: a comparative simulation study of the lattice, defect and surface structure of the stannates $ASnO_3$(A = Ca, Sr and Ba) and SnO_2'. *Journal of the Chemical Society, Faraday Transactions* **92**, 2057 (1996).

161. Stroppa, D. G. *et al.* 'Assessment of a nanocrystal 3-D morphology by the analysis of single HAADF-HRSTEM images'. *Nanoscale Research Letters* **8**, 475 (2013).

162. Marks, L. D. & Peng, L. 'Nanoparticle shape, thermodynamics and kinetics'. *Journal of Physics: Condensed Matter* **28**, 053001 (2016).

163. Van Aert, S. *et al.* 'Electron channelling based crystallography'. *Ultramicroscopy* **107**, 551–558 (2007).

164. Wang, A. *et al.* 'A method to determine the local surface profile from reconstructed exit waves'. *Ultramicroscopy* **111**, 1352–1359 (2011).

165. Wang, A. *et al.* 'Direct structure inversion from exit waves. Part II: A practical example'. *Ultramicroscopy* **116**, 77–85 (2012).

166. Lobato, I. & Van Dyck, D. 'MULTEM: A new multislice program to perform accurate and fast electron diffraction and imaging simulations using Graphics Processing Units with CUDA'. *Ultramicroscopy* **156**, 9–17 (2015).

167. Ágoston, P. & Albe, K. 'Disordered reconstructions of the reduced SnO_2-(110) surface'. *Surface Science* **605**, 714–722 (2011).

168. Yang, H. *et al.* 'Electron ptychographic phase imaging of light elements in crystalline materials using Wigner distribution deconvolution'. *Ultramicroscopy* **180**, 173–179 (2017).

169. Gao, C. *et al.* 'Overcoming contrast reversals in focused probe ptychography of thick materials: An optimal pipeline for efficiently determining local atomic structure in materials science'. *Applied Physics Letters* **121**, (2022).

170. Lu, N. *et al.* 'Surface Structure of Zigzag SnO_2 Nanobelts'. *The Journal of Physical Chemistry Letters* **1**, 1468–1471 (2010).

171. Rose, A. 'The sensitivity performance of the human eye on an absolute scale'. *Journal of the Optical Society of America* **38**, 196–208 (1948).

172. Helveg, S. *et al.* 'Observing gas-catalyst dynamics at atomic resolution and single-atom sensitivity'. *Micron* **68**, 176–185 (2015).

173. Egerton, R. F. 'Radiation damage to organic and inorganic specimens in the TEM'. *Micron* **119**, 72–87 (2019).

174. Arai, T. & Adachi, S. 'Synthesis and Photoluminescence Properties of SnO_2 Nanopowder'. *Japanese Journal of Applied Physics* **51**, 105002 (2012).

175. Jansonius, R. P. *et al.* 'Strain Engineering Electrocatalysts for Selective CO_2 Reduction'. *ACS Energy Letters* **4**, 980–986 (2019).

176. Wang, S. *et al.* 'Insights into electrochemical CO_2 reduction on tin oxides from first-principles calculations'. *Green Energy and Environment* **2**, 168–171 (2017).

177. Liu, S. *et al.* 'Efficient Electrochemical Reduction of CO_2 to HCOOH over Sub-2 nm SnO_2 Quantum Wires with Exposed Grain Boundaries'. *Angewandte Chemie - International Edition* **58**, 8499–8503 (2019).

178. King, W. E. *et al.* 'Ultrafast electron microscopy in materials science, biology, and chemistry'. *Journal of Applied Physics* **97**, 111101 (2005).

179. Campbell, G. H. *et al.* 'Time resolved electron microscopy for in situ experiments'. *Applied Physics Reviews* **1**, 041101 (2014).

180. Campbell, G. H. *et al.* 'High-Speed Electron Microscopy'. in 455–486 (2019).

181. Levin, B. D. A. *et al.* 'Tracking the picoscale spatial motion of atomic columns during dynamic structural change'. *Ultramicroscopy* **213**, 112978 (2020).

182. Vargas, A. *et al.* 'Fluxionality of gold nanoparticles investigated by Born-Oppenheimer molecular dynamics'. *Physical Review B* **80**, 195421 (2009).

183. Manzorro, R. *et al.* 'Describing Atomic-Level Fluxional Behavior in Nanoparticles'. *Microscopy and Microanalysis* **27**, 1306–1307 (2021).

184. Bostanjoglo, O. & Rosin, T. 'Ultrasonically Induced Magnetic Reversals Observed by Stroboscopic Electron Microscopy'. *Optica Acta: International Journal of Optics* **24**, 657–664 (1977).

185. Olshin, P. K. *et al.* 'Atomic-Resolution Imaging of Fast Nanoscale Dynamics with Bright Microsecond Electron Pulses'. *Nano Letters* **21**, 612–618 (2021).

186. Merkle, K. L. *et al.* 'In-Situ HREM Studies of Grain Boundary Migration'. *Interface Science* **12**, 277–292 (2004).

187. Zhang, K. 'Gctf: Real-time CTF determination and correction'. *Journal of Structural Biology* **193**, 1–12 (2016).

188. Barton, B. *et al.* 'Atomic Resolution Phase Contrast Imaging and In-Line Holography Using Variable Voltage and Dose Rate'. *Microscopy and Microanalysis* **18**, 982–994 (2012).

189. Oviedo, J. & Gillan, M. J. 'First-principles study of the interaction of oxygen with the SnO_2 (110) surface'. *Surface Science* **490**, 221–236 (2001).

190. Onishi, H. & Iwasawa, Y. 'Reconstruction of TiO_2 (110) surface: STM study with atomic-scale resolution'. *Surface Science* **313**, (1994).

191. Katsube, D. *et al.* 'Atomic-resolution imaging of rutile TiO_2 (110)-(1 × 2) reconstructed surface by non-contact atomic force microscopy'. *Beilstein Journal of Nanotechnology* **11**, 443–449 (2020).

192. Crozier, P. A. 'Vibrational and valence aloof beam EELS: A potential tool for nondestructive characterization of nanoparticle surfaces'. *Ultramicroscopy* **180**, 104–114 (2017).

193. Jinschek, J. R. 'Advances in the environmental transmission electron microscope (ETEM) for nanoscale in situ studies of gas–solid interactions'. *Chem. Commun. Chem. Commun* **50**, 2696–2706 (2014).

194. Moreno, M. S. *et al.* 'Differentiation of tin oxides using electron energy-loss spectroscopy'. *Physical Review B* **69**, 233304 (2004).

195. Rez, P. *et al.* 'Damage-free vibrational spectroscopy of biological materials in the electron microscope'. *Nature Communications* **7**, 1–8 (2016).

196. Prasad, P. D. *et al.* 'Synthesis, Characterization of Tin Oxide (SnO) Nanoparticles via Autoclave synthesis protocol for H_2 sensing'. *International Journal of Nanotechnology and Applications* **11**, 265–276 (2017).

197. Refat, M. S. *et al.* 'Synthesis, characterization, and photocatalytic efficiency of a new smart PdO oxide nanomaterials for using in the

recycling and sustainable wastewater treatment'. *Bulletin of the Chemical Society of Ethiopia* **35**, 107–118 (2021).

198. Yuan, W. *et al.* 'Visualizing H_2O molecules reacting at TiO_2 active sites with transmission electron microscopy'. *Science* **367**, 428–430 (2020).

199. Bugnet, M. *et al.* 'Direct Visualization and Control of Atomic Mobility at {100} Surfaces of Ceria in the Environmental Transmission Electron Microscope'. (2017).

200. Pennycook, T. J. *et al.* 'High dose efficiency atomic resolution imaging via electron ptychography'. *Ultramicroscopy* **196**, 131–135 (2019).

201. Liberti, E. *et al.* 'Three-dimensional Electron Ptychography of Catalyst Nanoparticles using Combined HAADF STEM and Atom Counting'. *Microscopy and Microanalysis* **25**, 8–9 (2019).

202. Liberti, E. *et al.* 'Quantitative Electron Ptychography of Sub-Stoichiometric Metal-Oxide Nanoparticle Catalysts Combined with HAADF STEM Atom Counting'. in '*Proceedings of the European Microscopy Congress 2020*' (Royal Microscopical Society, 2021).

203. Liberti, E. *et al.* 'Quantitative electron ptychography for simultaneous light and heavy elements atom counting'. *Acta Crystallographica Section A Foundations and Advances* **77**, C235–C235 (2021).

204. De Backer, A. *et al.* 'StatSTEM: An efficient program for accurate and precise model-based quantification of atomic resolution electron microscopy images'. 12013 (2017).

205. Mostaed, A. *et al.* 'A New Approach for 3D Quantitative STEM Using Defocus Corrected Electron Ptychography'. *Microscopy and Microanalysis* **28**, 380–381 (2022).

206. Kisielowski, C. *et al.* 'Detecting structural variances of Co_3O_4 catalysts by controlling beam-induced sample alterations in the vacuum of a transmission electron microscope'. *Advanced Structural and Chemical Imaging* **2**, 13 (2016).